Constrained Control for Helicopter Shipboard Operations and Moored Ocean Current Turbine Flight Control

Tri D. Ngo

Dissertation submitted to the faculty of the Virginia Polytechnic Institute and State
University in partial fulfillment of the requirements for the degree of

Doctor of Philosophy
In
Aerospace Engineering

Cornel Sultan, Chair
Craig A. Woolsey
Mayuresh J. Patil
Bernard Ferrier

March 21, 2016
Blacksburg, Virginia

Keywords: Helicopter Shipboard Operations, Ocean Current Turbines, Model Predictive Control, Output Variance Constrained, Mixed Integer Quadratic Programming

Constrained Control for Helicopter Shipboard Operations and Moored Ocean Current Turbine Flight Control

Tri D. Ngo

ABSTRACT

This dissertation focuses on constrained control of two applications: helicopter and ocean current turbines (OCT).

A major contribution in the helicopter application is a novel model predictive control (MPC) framework for helicopter shipboard operations in high demanding sea-based conditions. A complex helicopter-ship dynamics interface has been developed as a system of implicit nonlinear ordinary differential equations to capture essential characteristics of the nonlinear helicopter dynamics, the ship dynamics, and the ship airwake interactions. Various airwake models such as Control Equivalent Turbulence Inputs (CETI) model and Computation Fluid Dynamics (CFD) data of the airwake are incorporated in the interface to describe a realistic model of the shipborne helicopter. The feasibility of the MPC design is investigated using two case studies: automatic deck landing during the ship quiescent period in sea state 5, and lateral reposition toward the ship in different wind-over-deck conditions. To improve the overall MPC performance, an updating scheme for the internal model of the MPC is proposed using linearization around operating points. A mixed-integer MPC algorithm is also developed for helicopter precision landing on moving decks. The performance of this control structure is evaluated via numerical simulations of the automatic deck landing in adverse conditions such as landing on up-stroke, and down-stroke moving decks with high energy indices. Kino-dynamic motion planning for coordinated maneuvers to satisfy the helicopter-ship rendezvous conditions is implemented via mixed integer quadratic programming.

In the OCT application, the major contribution is that a new idea is leveraged from helicopter blade control by introducing cyclic blade pitch control in OCT. A minimum energy, constrained control method, namely Output Variance Constrained (OVC) control is studied for OCT flight control in the presence of external disturbances. The minimum achievable output variance bounds are also computed and a parametric study of design parameters is conducted to evaluate their influence on the OVC performance. The performance of the OVC control method is evaluated both on the linear and nonlinear OCT models. Furthermore, control design for the OCT with sensor failures is also examined. Lastly, the MPC strategy is also investigated to improve the OCT flight control performance in simultaneous satisfaction of multiple constraints and to avoid blade stall.

Acknowledgements

I would like to thank several people who made this research possible. First, I would like to express my deepest gratitude to my advisor Dr. Cornel Sultan for his continued support and guidance. I would like to thank former and current members of my doctoral committee Dr. Craig Woolsey, Dr. Mayuresh Patil, Dr. Bernard Ferrier, Dr. Alexander Leonessa, and Dr. Leigh McCue for their constructive comments. I would like to thank Vietnam Education Foundation for providing me with opportunity and financial support to pursue graduate studies in aerospace engineering in the United States. I would like to thank Institute for Critical Technology and Applied Science (ICTAS) at Virginia Tech for their financial support to my Summer I&II in 2015. I would also like to thank Dr. Nguyen Thien Tong who encouraged and helped me a lot to apply to the Ph.D. program in the U.S.

As a member of the multi-institutional collaborative research group, I would like to thank National Science Foundation (NSF) for their support of the project "Optimized Harvesting of Hydrokinetic Power by Ocean Current Turbines Farms using Integrated Control" under grant number NSF ECCS-1308168. I owe special thanks to Dr. James VanZwieten of the Florida Atlantic University, Dr. Nikolas Xiros of the University of New Orleans for many valuable discussions on the ocean current turbine dynamics model.

I would like to thank Mrs. Rachel Smith of the Department of Aerospace & Ocean Engineering, Virginia Tech for her administrative help. I would also like to thank my labmates Ipar Ferhat, Javier Gonzalez-Rocha, Maria Rye, Praneeth Sudalagunta, and Shu Yang for the friendship. Thanks also to my Vietnamese friends in Blacksburg: Chuong Nguyen, Jerry Nguyen, Van Tran, Hanh Truong, Truong Nguyen, Song Hong, who made my student life in the U.S more colorful and joyful.

Lastly, I am very grateful to my parents for their tremendous amount of love and support over the years.

Dedication to

my Dad, Ngo An,
my Mom, Tran Thi Duom,
my brothers, Ngo Cong Duc, Ngo Chi Nhan

Table of Contents

List of Figures

List of Tables

Nomenclature

u, v, w = Translational velocities of helicopter in aircraft frame (m/s)

p, q, r = Angular velocities of helicopter in aircraft frame (deg/s)

Φ_H, θ_H, ψ_H = Helicopter Euler angles (deg)

β_0, β_c, β_s, β_d = Collective, two cyclic, differential blade flapping angles (deg)

ζ_0, ζ_c, ζ_s, ζ_d = Collective, two cyclic, differential blade lead-lagging angles (deg)

$\lambda_0, \lambda_c, \lambda_s$ = Uniform and two cyclic rotor main inflow components (deg)

χ, ψ = Wake skew angle, blade azimuth angle (deg)

x_N, y_E, z_D = Helicopter's Cartesian coordinates in the inertial frame (NED - North East Down) (m)

θ_0, θ_c, θ_s = Collective, two cyclic blade pitch angles of main rotor (deg)

θ_T = Collective pitch angle of tail rotor (deg)

Ω = Main-rotor angular speed (deg/s)

H_p, H_m = Prediction horizon, control horizon

T_s = Sampling period (s)

u_S, v_S, w_S = Translational velocities of the ship in the ship body-fixed axes (m/s)

p_S, q_S, r_S = Angular velocities of the ship in the ship body-fixed axes (deg/s)

x_S, y_S, z_S = Ship's center of mass Cartesian coordinates in the inertial frame NED (m)

x_d, y_d, z_d = Landing deck's Cartesian coordinates in the inertial frame NED (m)

Φ_S, θ_S, ψ_S = Ship Euler angles (deg)

U_∞, σ_w = Mean wind speed, turbulence intensity (m/s)

R_m, R_t = Main rotor and tail rotor radius (m)

w_n = Zero mean, unity covariance white noise signal

α_B, θ_B = Angle of attack and the pitch angle of the blade (deg)

The following nomenclature is for the OCT system.

$\gamma_1, \gamma_2, \gamma_3$ = Pitch angle of the first, second, and third rotor blades (deg)

γ^{eq} = Collective pitch angle (deg)

γ_a, γ_b = Longitudinal and lateral cyclic pitch angles (deg)

α = Azimuth angle of the first rotor blade (deg)

Ω, or p_r = Angular velocity of the rotor with respect to the OCT main body (deg/s)

τ_{em} = Electro-mechanical torque (Nm)

$\bar{U}_M$ = Averaged flow current velocity (m/s)

u, v, w = Translational velocities of the OCT in the body frame (m/s)

p_b, q_b, r_b = Angular velocities of the OCT in the body frame (deg/s)

X, Y, Z = OCT's Cartesian coordinates in the inertial frame (NED - North East Down) (m)

Φ, θ, ψ = OCT's Euler angles (deg)

R = Rotor blade radius (m)

AR = Swept area of the rotor (m^2)

ρ = Density of seawater (kg/m^3)

Chapter 1: Introduction

Constrained control algorithms such as Model Predictive Control (MPC) [1], Output Variance Constrained (OVC) control have been widely implemented in industrial and aerospace systems to solve highly constrained multivariable control problems. Very recently, the rapid development of high performance computing devices and powerful digital processors led to promising applications of MPC and OVC in fast dynamics aerospace/ocean systems. Moreover, these constrained control algorithms can manage highly coupled motions in large-amplitude/aggressive maneuvers by solving a multivariable optimization problem. These are the main reasons that motivated the selection of MPC and OVC as advanced control algorithms for helicopter shipboard operations and moored ocean current turbines flight control in this dissertation.

Referring to helicopter shipboard operations, these are very challenging mission task elements for a pilot, especially in adverse conditions such as rough seas, severe ship airwake, degraded visual environment, etc. These maneuvers demand enormous workload from the pilot to stabilize the helicopter that is disturbed from its desired trajectory, precisely maneuver the helicopter towards the landing deck, and ensure satisfaction of the operating limits of the helicopter. Hence, the pilot must simultaneously accomplish many difficult tasks in only several seconds during shipboard operations, which increases the likelihood of catastrophic mistakes. When the landing mission is aborted, waiting for improved conditions to repeat the maneuver leads to additional fuel consumption and delays. Therefore, research and development of autonomous shipboard operation systems are essential to improve the performance of rotorcraft operating at rough seas. To achieve this goal several ingredients are critical: a helicopter model that captures significant characteristics of the helicopter dynamics, ship motion simulation, helicopter/ship airwake interface for performance evaluation, and an automatic control system to ensure safe landing. Since helicopter flight is inherently constrained, a multivariable control technique that can handle multiple constraints is mandatory. Moreover, for shipboard operations detailed physics based models of the helicopter, ship and the airwake have been constructed. These models, both in nonlinear and linearized form, can be used in control design for trajectory tracking missions that are typical in shipboard maneuvers. These all facts motivated the selection of MPC for shipboard automated control studies.

Referring to hydrokinetic electricity production from moored ocean current turbines (OCTs), this is emerging as a renewable energy solution that can help meet the increasing energy demand. The flight control system for these moored OCTs involve many challenges not common to rigidly mounted systems such as minimizing OCTs motions, locating them at the desired operating depth, and controlling their positions to avoid negative interactions with other systems. This will be particularly important for OCT farms, where the relative positioning between devices will be critical for maximum energy production. These systems are required to operate at sea for long periods of time without maintenance. Therefore feedback control to ensure that they return rapidly to their nominal operating condition is mandatory. OCTs will operate in highly uncertain environments due to sea states, weather influences, current pattern, etc. Therefore, the control system will have to mitigate uncertainties embedded in the control model. For the purpose of this dissertation the feedback control study is limited to stabilizing control around a nominal condition. The control design will be based on models linearized around a nominal operating condition. These factors motivated the selection of OVC and MPC, constrained control techniques which guarantee that the control energy is minimized while prescribed constraints on certain inputs and outputs are also satisfied.

There is another strong connection between these two application research topics: in order to design a control system for the OCT we leverage helicopter blade control technology. Specifically we propose the introduction of blade cyclic pitch control in OCT control design. This is the first study which investigates the feasibility of such an approach.

1.1 Literature Reviews

1.1.1 Helicopter-Ship Dynamics Interaction

An innovative design of shipboard helicopters in extreme conditions (such as rough sea, adverse weather) is highly demanded for numerous civil/military applications in the next decades. To build a solid background for this design, many studies related to helicopter shipboard technologies have been conducted recently. For examples, meticulous flight test processes such as JSHIP [2] were established to define and evaluate the wind-over-deck (WOD) envelope in which a given helicopter-ship combination can operate within the limits of speed and azimuth angle of the wind conditions. Active rotor is one of the innovative technologies that increase the control authority for the helicopter during shipboard operations by using active flaps on the blade as secondary controls. Moreover, many helicopter-ship dynamic interface tools have been developed to widen the knowledge of the helicopter/ship's airwake interactions. Modeling the ship's airwake and its effects has recently attracted an increased number of helicopter researchers for civil as well as military applications (e.g. [3]-[13]). In this dissertation, several papers on the ship airwake modeling are reviewed and discussed from a control design perspective.

Some key papers in the area of ship airwake modeling are [3]-[4], which describe a model-scale helicopter based on a Merlin AW-101 exposed into headwind and a 45-deg wind-over-deck (WOD) angle in a water tunnel to measure the unsteady forces and moments exerted by the ship airwake at fixed locations along the flight path of a landing maneuver. An unsteady computational fluid dynamics (CFD) analysis of the ship airwake was also used to explain the time-average and unsteady aerodynamic loading characteristics such as headwind thrust deficit, and Green 30, 45 pressure wall effects. Recall that Red (R) and Green (G) terminology refer to port and starboard sides of the ship respectively. CFD and experimental results indicated some degradation of flight-handling qualities and excessive levels of pilot workload due to the airwake.

In [5]-[6], a CFD solver (PUMA2) was used to calculate the time-accurate airwake velocity over a landing helicopter assault (LHA) class ship. Then temporal and spatial varying components of the airwake were stored into computer memory. Linear interpolation was used to calculate the airwake flow field at every simulation time step at every local point of the rotor-blade elements, fuselage, empennage and tail rotor in the helicopter flight simulation. Subsequently, the effects of velocities induced by the airwake flow field were easily incorporated into the blade-element rotor model. Besides the CFD representations of the time-varying ship's airwake, GENHEL model of the UH-60 helicopter and a feedback optimal control model (OCM) of the human pilot are two key elements that contributed to the helicopter-ship dynamic interface development. OCM generated the pilot control inputs for shipboard approach and departure tasks in 0- and 30-deg WOD conditions by solving the linear-quadratic-Gaussian problem. A linear model of the helicopter that was decoupled into 3-state longitudinal model, 5-state lateral-directional model, and 1-state vertical motion model was formulated for the optimal control design. The simulations with the time-varying airwake showed that there were significant oscillations in the helicopter states and a substantial increase in pilot workload, particularly when hovering over the flight deck in 30-deg WOD condition. From these references we infer that memory storage and time-consuming computations can become serious issues, particularly if the simulation is to be run in real time. It takes nearly 1.8h on 12 processors (2.4-GHz P4, 4-GB ECC RAM) to simulate only one second of real flow. These limitations represent major challenges for control system design and implementation that are mitigated via control-oriented modeling procedures.

To overcome the computational and memory issues mentioned in the above, equivalent disturbances can be modeled as stochastic processes. For example, in [7] the airwake is represented as a disturbance vector of 3 translational velocity and 3 angular rate components, in the form of Von Karman turbulence model. The key parameters of this model, such as intensity factor σ, length scale L, and coefficients a_i and b_i, were selected to fit the power spectral density (PSD) derived from CFD simulation over the frequency range of 0.1 to 40 rad/sec. Then, the resulting airwake model was incorporated into a modified stability augmented system (SAS) for the UH-60 helicopter operating on a LHA ship. The results indicated a significant reduction in pilot control activity and in angular motion of the aircraft.

Another approach to empirically derive helicopter response model and control system requirements for flight in turbulence was presented following a process described in [8]-[11]. In this process, flight test data from a UH-60 helicopter in turbulent conditions were used to produce a set of expected aircraft mixed inputs using an inverse model of the test aircraft. Subtracting the measured aircraft mixed inputs from these expected mixer inputs resulted in remnant inputs that were essentially equivalent-gust mixer inputs. The disturbance was then modeled using white-noise-driven shaping filters of a form similar to the Dryden spectral models that are comprised of rational functions and characterized by the power spectral densities (PSD) of the gust disturbances [12]. The model's parameters were thus identified by using the PSD characteristics of the equivalent control gust remnants derived from flight test data. The parameters of these filters (or transfer functions) included turbulence scale length L_i, turbulence intensity σ_w, temporal break frequency α_i, gust transfer function gains K, and coefficients C_i. Therefore, a control equivalent turbulence inputs (CETI) model was constructed so that these inputs could be inserted in parallel with those of the pilot. Although the CETI model could not represent accurately aerodynamic interaction between the ship's airwake and rotor blades, it could produce vehicle responses equivalent to those of a turbulence field. A structural pilot modeling approach was used to simulate the control behavior in tracking the landing deck motions. Estimates of flight control bandwidth for precision hover in turbulence were also compared to the disturbance rejection requirements of ADS-33 in [10].

To use empirically derived gust filters obtained for one rotorcraft to be scaled to another, different vehicle with the same configuration, an approximate and simplified approach for scaling rotorcraft control inputs was described in [11]. The scaling technique was derived from approximating the effects of upwash and sidewash turbulence fields as changes in main and tail rotor blade angle of attack. These changes were then equated to equivalent changes in blade pitch through collective and cyclic inputs. Examples of employing the technique were provided using models of 4 rotorcrafts in hover.

In [13], Simulation of Rotor Blade Element Turbulence (SORBET) model was developed to superimpose the turbulence velocity components in real time to each of the five blade-element stations along each of the four rotor blades. Gaussian statistical characteristics of turbulence filters were preserved over the rotor disc. The rotor blades were divided into 5-stations using the equal-annuli algorithm. The superimposition procedure can be summarized in five steps: First, the turbulent flow was assumed stationary and homogeneous in the longitudinal direction using Taylor's hypothesis. An onset line perpendicular to the vehicle flight path and tangential to the leading edge of the rotor disc was defined. Then two points of applicability were selected along the onset line. Second, Dryden models with Gaussian inputs were used to generate independent turbulence translational and rotational velocity histories at each of these two points in real time and stored in tables, which were updated each cycle time. Third, at each blade station, longitudinal/lateral distributions in the velocity history table were computed by using integer indexes that were proportional to the station's perpendicular distance from the onset line and the lateral proportion from the left-hand side to the station. Fourth, Gaussian interpolation technique that preserved the statistical properties of the turbulence spectra over the rotor disc was used to construct transfer functions of translational velocities at each station of each blade from two onset points. Fifth, these transfer functions were then discretized to produce the velocity components in real time to each of the five blade-element stations along each of the four blades with Gaussian inputs. In a piloted, motion-based simulation of the Sikorsky UH60A Black Hawk at NASA Ames Research Center's Vertical Motion Simulator, SORBET model received pilot's favorable comments concerning the vehicle performance in response to the vertical component of turbulence.

The above discussion was aimed at revealing some major challenges posed by the integration of ship airwake models with the control design process. On one hand in order to capture the complex flow field around the ship's superstructure, the standard approach is to employ complex CFD simulations. On another hand, these simulations generate data that in general cannot be directly integrated with the control system design process. Therefore, they require additional processing for adequate control-oriented models.

1.1.2 Automatic Control for Helicopter Shipboard Operations

Although automatic flight control has been generally studied for rotary unmanned aerial vehicles (RUAV), few works address shipboard operations at rough seas, especially using full-scale helicopters with high-order models and advanced control. Complex models including, at the minimum, blade dynamics and airwake models are desired. Blade dynamics must be captured by the helicopter model because of several reasons. In shipboard operations, the airwake has tremendous influence on the blade, and consequently on the overall helicopter dynamics. A model that ignores blade dynamics misses these critical interactions. For example, one may design a controller ignoring blade dynamics, e.g., using a single rigid body helicopter model, but then the risk of blade failure is high because its dynamics was not taken into account when control design was performed.

Some works that address shipboard operations are summarized next. In [14], a tau flight control based on optical flow theory was developed. The parameter tau, defined as the time to close a gap between the helicopter and landing deck at the current closing rate, is derived using inspiration from the manner in which humans achieve purposeful motion. To demonstrate the tau control, a simulation model of the Bell 412HP helicopter was used. The main rotor system was modeled using a blade element model with rigid blades, with a Peters-He finite state inflow model [15] and quasi-steady aerodynamics. The propulsion system was modeled as a simple state-space model to verify the capability of torque envelope protection of the control algorithm. Automatic landing on a stationary deck was successfully achieved via simulations.

A tether-guided landing approach for an autonomous helicopter was proposed in [16]. The tether was modeled as a zero-mass element that applied a tension as an additional control input to the helicopter. The tether tension was used to couple the translation of the helicopter to the rotation. Then the translation reference rates were derived to achieve a desired controlled behaviors of the attitude and altitude. Lyapunov-based control design was applied to guarantee local exponential stability. Simulations using a 6-DOF rigid body helicopter dynamics model showed good tracking during the tether-guided landing on a stationary deck. However, the control signal history displayed an abrupt behavior that increased the workload of the actuators.

In [17]-[18], a sensing system with data fused from 3-D scanning LADAR and GPS/INS was used to find potential landing zones for the full-scale Boeing Unmanned Little Bird (ULB) helicopter. The sensing system fed the perception data of the landing zones into the planning module to generate feasible and collision-free trajectories sent to the autopilot on ULB. Successful landing was achieved in previously unmapped environments via flight tests.

In [19], a dynamic interface (DI) simulation was performed to calculate deck motion limits for RUAV shipboard launch and recovery. A model of a conventional helicopter was constructed which included the rigid body equations of motion and the effect of airflow distribution across the rotor disk. The airwake about the ship for each frame of the simulation was calculated by a CFD code. Ship motion histories in time domain were generated using Response Amplitude Operators (RAOs). The energy index (EI) was used to predict quiescent periods of the ship motion. Recorded data from the Firescout UAV recovery tests on the USS Denver ship, using the Landing Period Designator (LPD) at sea, showed a tendency to reflect very similar computations of deck motion limits in the simulator. High Level Architecture (HLA) was chosen as the standard for building the simulator, which consisted of component parts in Fig. 1.

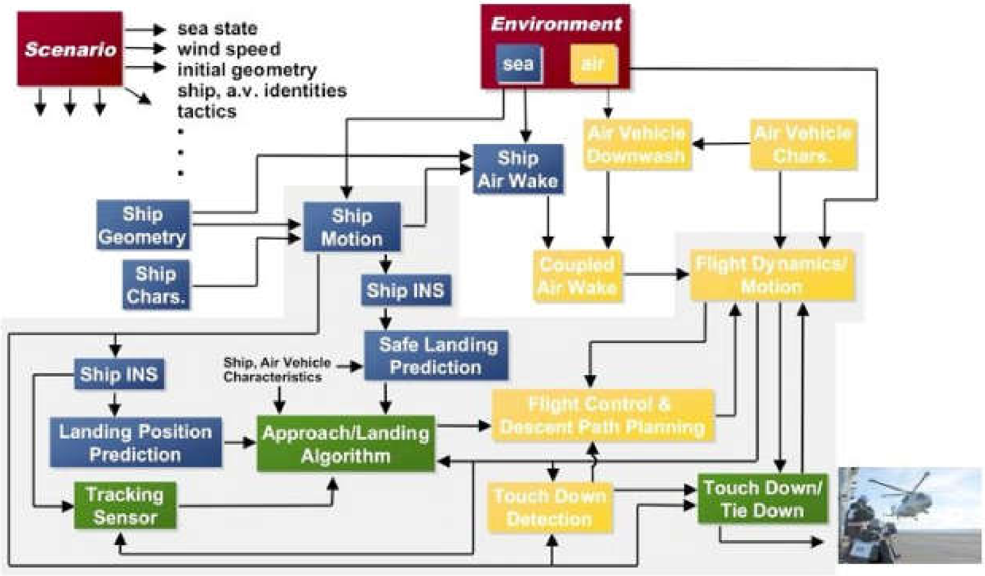

Fig. 1 HLA Federation by Discipline [19]

In [20], a CFD solver was used to calculate the airwake velocity over a landing helicopter assault (LHA) class ship. The GENHEL model of the UH-60 helicopter and a feedback optimal control model (OCM) of the human pilot were employed in the DI simulation. The OCM generated the pilot control inputs for shipboard approach and departure in 0 and 30-deg WOD conditions by solving a Linear Quadratic Gaussian control problem. Three decoupled linear models of the helicopter: 3-state longitudinal model, 5-state lateral-directional model, and 1-state vertical motion model were used. Simulations showed significant helicopter oscillations and a substantial increase in pilot workload, particularly for hover in 30-deg WOD condition.

Restricted landing area on a moving deck at rough seas confines the helicopter movement to a small space with little margins for error. Highly disturbed ship airwake has significant impact on the helicopter flight envelope and pilot workload. Therefore, a critical challenge for shipboard operations is the large number of constraints that must be satisfied. MPC has been widely implemented in industrial systems to solve highly constrained multivariable control problems [1]. The rapid development of high performance computing devices and powerful digital processors led to promising applications of MPC in fast dynamics aerospace systems. Some MPC applications for RUAVs have been reported in [21]-[25].

In [21], a nonlinear MPC algorithm (NMPC) was developed for trajectory tracking of a RUAV modeled as a 6-DOF rigid body with first-order approximation of servomotors. The gradient-descent method was used to implement an online controller to reduce the computational workload and enable real-time applications. Simulations for the spiral ascent maneuver and collision-free trajectory tracking showed the effectiveness of the NMPC in handling system constraints and modeling uncertainties.

In [22]-[23], a distributed MPC algorithm for an autonomous helicopter formation was formulated. A linear cruise model of the Yamaha R-50 helicopter, identified through flight tests, was used. A scaling technique based on Froude number was applied to the R-50's model to create heterogeneous helicopter models. A stable MPC was designed for each individual vehicle. To attenuate the effects of external disturbances that may degrade the performance of individual MPCs, inter-agent coupling terms were introduced in the performance index of each MPC. Simulations of the formation dynamics showed good disturbance rejection of the distributed MPC to longitudinal wind gusts. About an hour of computer time was necessary for 80 seconds of the 8-vehicle formation simulation.

In [24], a modified inverse simulation (IS) scheme that adopted the architecture of MPC was proposed. The modified IS included a predictive step to handle the limits of the real vehicle such as input/output/power constraints. A fast solution of the modified IS was obtained based on a lower-order, simplified model of the helicopter. Simulations for three aggressive maneuvers (hurdle-hop, slalom, and lateral reposition) indicated that the modified IS could handle complex high-order models at a computational cost only marginally higher than necessary for solving the same IS problem based on a less reliable low-order model of the same vehicle. Different assumptions of the main rotor/tail rotor dynamics and inflow models were used to formulate high- and low-order models of the UH-60 helicopter.

In [25], a single-input single-output generalized predictive control (GPC) algorithm was designed to provide inputs to a classical control system, including stability augmentation system (SAS) and control augmentation system of a rotorcraft for a longitudinal/vertical terrain-following flight. SAS guaranteed adequate stability margins, and GPC enabled tracking performance of the system. A low order, linear time-invariant dynamics model of the Bo-105C helicopter enabled the implementation of a simple GPC controller.

The critical ingredient for MPC design is the dynamical model of the system to be controlled. MPC in itself is a complex control framework. Improvements in system performance are expected to come from mixing complex modern control strategies (like MPC) with increasingly complex (high fidelity) models. However, the design process for a preselected control strategy (e.g., MPC) can tolerate only a certain limit of modeling complexity. Therefore, relatively complex control-oriented helicopter models that capture essential flight dynamics (e.g., fuselage dynamics, blade flapping and lead/lagging) developed in the implicit nonlinear ODEs form in [26]-[27] are adopted here. These models were validated via extensive comparisons with trim and eigenmode data available in the literature. In [27], MPC design was illustrated using these models for the tracking of pre-specified trajectories, but landing was not a maneuver studied. In [28]-[30], studies in simultaneous helicopter and control-system design, slung-load system modeling and control, and rotor active morphing with control energy saving were carried out using the same models but MPC was not used. In addition, in these works, linearized models of the helicopter dynamics around certain flight conditions (e.g., hover, straight level flight) were also used for all of the design processes and validations. In [31]-[33], we introduced nonlinear simulations of the helicopter dynamics, the integration of the ship airwake effects into the helicopter dynamics from a control perspective, and some tracking maneuvers achieved using MPC.

1.1.3 Motion Planning for Robotic Vehicles

In the helicopter ship operations, waiting for a quiescent condition leads to additional fuel consumption and delays. Also, in some emergency situations the helicopter must land as quickly as possible. Therefore, automatic landing systems are required to accommodate very challenging landing conditions. One of the key components of this system is the motion planning algorithm in complex and cluttered environments. Some related works in the motion planning techniques for robotic vehicles, especially for helicopters, are summarized next.

In [34], a real-time motion planning algorithm, Closed-loop Rapidly-exploring Random Tree (CL-RRT), was introduced with its application to robotic vehicles operating in urban environments. The CL-RRT algorithm grows a tree of feasible trajectories originating from the current vehicle state to a specified goal set in minimum time to satisfy vehicle and environmental constraints such as obstacle avoidance constraints and rules of the road. Then the best trajectory is chosen for execution, and the cycle is repeated during the next time step. The vehicle model, including 7 states, was used to generate the forward simulation that enabled the expansion of the CL-RRT. The algorithm was demonstrated in the MIT's Team entry for the 2007 DARPA Urban Challenge.

In [35], an incremental randomized motion planner based on the Rapidly-exploring Random Tree (RRT) algorithm for an agile autonomous helicopter in the presence of fixed and moving obstacles was proposed. The helicopter dynamics must be taken into account in the kinodynamic motion planning to make computed trajectories executable, however large dimensional state-space systems can make the randomized motion planning computationally intractable. Therefore, a low dimensional maneuver space of the helicopter was constructed as a combination of appropriate motion primitives (e.g. trim trajectories) and maneuvers (finite-time transitions between trim trajectories). The RRT algorithm operated on the maneuver space and was complemented by a nonlinear tracking control law from [36] to ensure tracking of the computed trajectory. Numerical simulations showed that the algorithm was able to navigate the helicopter through a set of fixed and moving spheres, as well as sliding doors. A maneuver space including 25 trim trajectories and 600 maneuvers was used for motion planning. A 16-state nonlinear helicopter model including 12-state rigid body dynamics, 3-state main rotor dynamics, and 1-state tail rotor dynamics was used [37].

To improve the motion planning technique using maneuver automaton (MA), an efficient procedure was introduced in [38] to construct a library of motion primitives and rules for their concatenation. The size of the library depends on the tradeoff between achievable performance, planning completeness, and computational complexity. A typical library can contain hundreds of primitives. The procedure ensures that the collection of motion primitives is sufficient to steer the system to any configuration from an initial condition. Numerical simulations showed that the helicopter was able to execute acrobatic maneuvers such as ‘ag turn’ using MA. These maneuvers allowed the helicopter to reverse the direction of flight quickly in a very tight space with minor changes in velocity and altitude before and after the maneuver.

In [39], the authors presented a real-time trajectory generation algorithm to move a quadrotor from a large class of initial states to a given target point at rest. This algorithm consists of decoupled planning of trajectories for each of the three translational degrees of freedom (DOF). The feasibility of the algorithm was guaranteed by deriving decoupled constraints and parameters for each DOF. The decoupled planning made the trajectory generation problem more tractable and computationally efficient. Optimal inputs in the bang-singular structure were derived using Pontryagin’s minimum principle. Then the first control interval was applied to the quadrotor at each time step. This process is similar to the infinite-horizon MPC formulation. The control law is stable if the decoupling parameters are chosen to be constant. The procedure’s applicability and robustness were illustrated in the Flight Assembled Architecture project in which a fleet of four quadrotors assembled a 6 m tall tower out of 1500 foam bricks. The quadrotor model has five states (2-D position, 2-D velocity, and the tilt angle). Aerodynamic effects on the quadrotors were neglected in this model.

Mixed-integer programming methods have been widely used in optimal motion planning techniques. In [40], a robust MPC for constrained linear systems was proposed by combining constraint tightening with a variable horizon. Constraint tightening was used to ensure a margin for future feedback action to ensure robustness. A variable horizon was used to enable finite-time arrival within an arbitrary target. This combination was implemented as a mixed integer linear programming (MILP) problem. This also allowed non-convex constraints to be incorporated in the robust MPC by representing the constraints in polyhedral region and using binary variables. Simulations were presented for spacecraft rendezvous control with sensor visibility constraints, and UAV guidance through obstacle fields. In these simulations, the aircraft was modeled as a vehicle moving in the 2-D space with constant speed and limited turning rate. The spacecraft dynamics was approximated by the linearized Hill's equations with 6 states [41].

A homotopy-based, divide-and-conquer strategy for kinodynamic motion planning in 2-D polygonal space was presented in [42]. The general motion planning problem was decomposed into multiple independent problems corresponding to distinct homotopy classes. A homotopy class was defined as a set of multiple locally optimal trajectories corresponding to navigation decisions. The decomposition partitioned the collision-free configuration space into a finite set of convex cells. Then, corresponding motion planning sub-problems were solved using mixed-integer quadratic programming (MIQP) methods, with control inputs represented as continuous optimization variables and the time steps associated with transitions between adjacent cells represented as discrete variables. The strategy was successfully applied in decision making support for vehicle navigation on roadways. Optimal trajectories with minimum effort, minimum required accelerations ensuring satisfaction of driving requirements (e.g., remain within road boundaries, align with the principal direction of the road) were generated for various navigation decisions. The proposed strategy was also combined with a fixed horizon MPC for the bicycle navigation through nonconvex obstacles. A six-state bicycle model with slip was employed in 2-D simulations.

Following these works, motion planning methods can be classified into two main categories: combinational motion planning and sampling-based motion planning. The first category builds a discrete representation that exactly represents the original problem, leading to complete planning approaches. The later category samples the configuration spaces and conducts discrete searches that utilize these samples [47]. In spite of the rapid development of motion planning techniques for robotic vehicles, their application to manned and unmanned helicopters with complex dynamics for high demanding missions is far from straightforward.

1.1.4 Moored Ocean Current Turbines

Hydrokinetic electricity production from river, tidal, and ocean currents is emerging as a renewable energy solution that can help meet the increasing energy demand. Each of these three resources has the potential to impact the U.S. energy portfolio, with feasible U.S. annual electricity production from ocean currents alone estimated at 169 TWh [48]. This resource has time averaged energy densities reaching 3.3 kW/m^3 [49]. The energy density of ocean currents is greatest along the western boundary of the world's oceans, with the primary U.S. ocean current resource located between the southern tip of Florida and North Carolina [50]. While long term tests have not yet been conducted in this resource for commercial scale systems, prototype and experimental system testing of Ocean Current Turbines (OCTs) has been conducted in both towing tanks and the open ocean [51]-[54].

OCTs will most likely operate in water depths from 300 to 400 m (potentially up to 800 m) and within the top 100 m of the water column where the current is strongest [55]. A cross-section of the average energy density of this resource between the U.S. and Bahamas at 27° N is provided (Fig. 2) to highlight the relationship between turbine operating location and resource potential [49]. Because of the location of this resource, OCTs will likely be moored to the sea floor via single-point or multi-point mooring systems. These mooring systems will introduce challenges not common to rigidly mounted systems such as minimizing OCTs motions, locating them at the desired operating depth, and controlling their positions to avoid negative interactions with other systems. This will be particularly important for OCT farms, where the relative positioning between devices will be critical for maximum energy production.

There are very few research works that has been conducted for the OCT flight control. In [55], an OCT simulation was developed which includes a basic rotor model that does not account for wave or current shear loadings on the blades. Flight control systems that use lifting surfaces (wingtips and canard) to control the OCT height, pitch, and roll. Mixed PID/Bang Bang, Mixed LQR/PID/Bang Bang, and Mixed LQG/PID/Bang Bang control approaches were developed and compared using the dynamics simulation in [56]. In this dissertation, cyclic blade pitch control approach is investigated for the 700 kW OCT design with a single 20 meter diameter variable pitch rotor. The design uses a numerical simulation model similar to the one presented in [55] that includes a blade element momentum (BEM) rotor model. Details on the updates made to this numerical simulation are presented in [61]. This model allows for the evaluation of the new control approach.

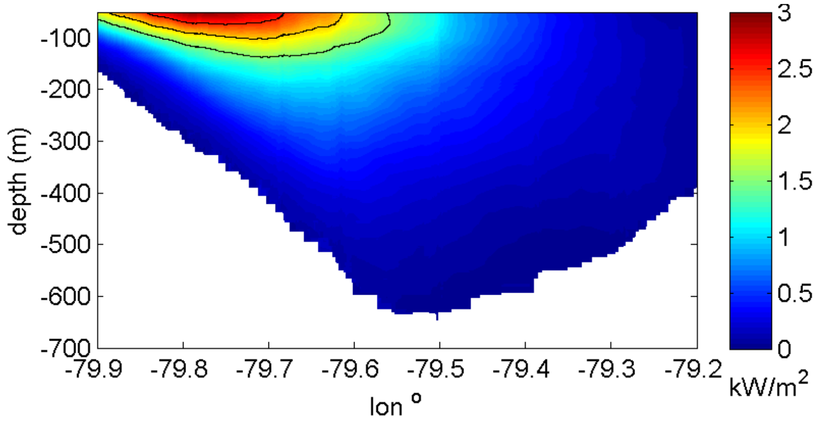

Fig. 2 Average KEF calculated from 35 Transects made at 27°N Latitude. Contour lines are provided at 1.5, 2.0, 2.5 kW/m^2 [61]

1.2 Objectives and Roadmap

In this dissertation, two constrained control algorithms are designed for helicopter shipboard operations under adverse conditions (high sea states, severe ship airwake perturbation) and moored ocean current turbine flight control system. All parameters of the helicopter, ship, and ocean current turbine used in this dissertation were taken from data available in the public domain. A brief roadmap to the dissertation is presented as follows.

Chapter 1 provides an introduction to the research topics, objectives, roadmaps, and contributions of this dissertation. In Chapter 2, the helicopter dynamics model is formulated in the implicit nonlinear ODEs form for control design and evaluation. Parameters of the SA330 Puma helicopter is used for our study. Numerical simulations of the nonlinear and linearized models are performed to explore helicopter responses to various disturbances and control inputs. Chapter 2 also introduces the ship model and shows some motion simulations using RAOs. Ship airwake modeling procedures using a CETI model and available CFD airwake data are performed to investigate their effects on the helicopter. Distribution of the spatial gradient airwake velocities over the rotor disk is implemented in the helicopter-ship airwake interaction.

Chapter 3 presents a MPC framework for the automatic landing during the ship quiescent period with considerations regarding the optimization control problem, system constraints, and stability. The robustness of MPC design is investigated by evaluating stability and performance of the closed-loop helicopter system with various ship airwake models (CETI, CFD). ADS-33E-PRF desired performances for landing and lateral reposition are considered. Comparisons between different assumptions about the uniform/spatial gradient airwake velocities over the main rotor disk of the helicopter are also presented. To improve the prediction accuracy of the MPC's internal model, which can degrade as the helicopter wanders off the trim condition about which the nonlinear system is linearized, a model-updating scheme is proposed in the end of the chapter.

Chapter 4 presents a novel method for helicopter precision landing on moving decks using mixed-integer quadratic programming and model predictive control (MIQP-MPC). The implementation of the MIQP allows the control system to adapt and respond rapidly and precisely to erratic motions of the landing deck via variable prediction horizon. The performance of the control system is evaluated via numerical simulations using the nonlinear helicopter-ship dynamics interaction. The MIQP-MPC can precisely perch the helicopter on moving decks in satisfying rendezvous conditions for helicopter-ship relative attitude, position, and velocities. Simulations of landing on upstroke and downstroke moving decks with the high energy indices are also performed to prove its feasibility under adverse conditions. All operating limits of the helicopter/ship system, and fight deck collision avoidance are respected during the landing maneuvers.

Chapter 5 performs stability analysis and flight control design for a 700 kW moored OCT with a single 20 meter diameter rotor based. The control model used in the control design process is a linear time invariant model of the nonlinear OCT dynamics developed primarily by our collaborators at the Florida Atlantic University. For the OCT flight control design we leverage ideas from helicopter blade control by introducing cyclic blade pitch controls in OCT, similar with the technology used in helicopter control. Output Variance

Constrained (OVC) control is studied for OCT flight control in the presence of external disturbances. The minimum achievable output variance bounds are also computed and a parametric study of design parameters is conducted to evaluate their influence on the OVC performance. The performance of the OVC control method is evaluated both on the linear and nonlinear OCT models. Control design for the OCT with sensor failures is also studied in this dissertation. The MPC strategy is investigated to improve flight control performance in simultaneous satisfaction of multiple constraints and to avoid blade stall. Conclusions and future works are given in Chapter 6.

1.3 Statement of Contributions

The contributions of this dissertation are summarized as follows:

1) A complex helicopter-ship dynamics interface has been developed as a system of implicit nonlinear ordinary differential equations to facilitate shipboard operation simulation, control design, and evaluation. Nonlinear helicopter dynamics model, ship motion simulation, and various ship airwake models are incorporated in this interface to describe realistic helicopter shipboard operations.

2) A model predictive control framework for helicopter shipboard operations during the ship quiescent period is developed and its feasibility is demonstrated via numerical simulations with considerations regarding the optimization control problem, system constraints, and stability.

3) A mixed-integer MPC algorithm for helicopter precision landing on moving decks is proposed. The performance of this control structure is evaluated via numerical simulations of deck landings in adverse conditions (up-stroke, down-stroke moving decks with the high energy indices). Motion planning for coordinated maneuvers to meet the helicopter-ship rendezvous conditions is implemented via mixed integer quadratic programming.

4) A novel method of variance constrained cyclic blade control of moored ocean current turbines is developed for the flight control system to minimize the control energy, to achieve strong exponential stability of the OCT system, and to satisfy prescribed limits on the variances of certain variables. A comprehensive study of the effect of the prescribed

variance bounds and of sensor failures on the OCT closed loop system performance is also presented.

5) Model predictive control is also for the first time investigated for OCT flight control in the presence of external disturbances. The performance and capability of handling system constraints and avoiding blade stall of the OCT flight control with the OVC and MPC strategies are compared using numerical simulations.

A part of the work presented in this dissertation is based on our publications in [31]-[33], and [58]-[62].

Chapter 2: Helicopter-Ship Dynamics Interface

This chapter is intended to construct a realistic helicopter-ship dynamics interface to facilitate the control design and evaluation for helicopter shipboard operations. Three critical modeling components of the interface are the nonlinear helicopter dynamics model, the ship dynamics model, and the helicopter-ship airwake interaction model.

2.1 Nonlinear Helicopter Dynamics Model

If possible, to facilitate control design and minimize pre-control processing, the mathematical model of a system should be directly formulated in ODEs form. This is ideal because ODEs are amendable to control design and both control theory and technology are sufficiently mature for large classes of ODEs. Models based on, for example, partial differential equations or other more complex equations, require significant qualitative and quantitative alteration for control design. Therefore, in [26], a nonlinear helicopter dynamics model was derived using the control-oriented philosophy.

Typical components of a conventional helicopter were incorporated in this model, such as articulated rotor with 4 blades, fuselage, horizontal tail, and tail rotor. The underlying assumptions used throughout the control-oriented modeling process were typical, i.e. the helicopter had a plane of symmetry and constant mass matrix; linear incompressible aerodynamics and the Pitt-Peters linear static inflow model were used; rotor blades were either flexible or rigid. For this study, the blades are assumed rigid and the helicopter model consists of 29 implicit nonlinear ODEs including 9 fuselage equations, 8 blade-flapping equations, 8 blade lead-lagging equations, 1 momentum equation for thrust estimate, and 3 main-rotor Pitt-Peters inflow equations. Three additional navigation equations for the Cartesian coordinates of the helicopter's center of mass in North-East-Down $Ox_Ny_Ez_D$ frame (NED) are included in the model. The origin O of the NED frame is located at a point of interest on the Earth surface, its x_N - y_E plane is tangent to the Earth's surface at O, and axes Ox_Ny_E, Oy_E point in North, East directions, respectively. Configuration parameters used for our study is given in Table A.1 in the Appendix.

2.1.1 Rigid-Body Equations of Motion

The rigid-body equations of motion of the helicopter body can be written as:

$$\dot{\boldsymbol{r}}_G = \boldsymbol{T}_{GA}\boldsymbol{v}_A \tag{1}$$

$$\dot{\boldsymbol{\Theta}} = \boldsymbol{L}_{GA}\boldsymbol{\omega}_A \tag{2}$$

$$\dot{\boldsymbol{v}}_A = \frac{1}{m}\boldsymbol{F}_A + \boldsymbol{T}_{AG}\boldsymbol{g}_G - \tilde{\boldsymbol{\omega}}_A\boldsymbol{v}_A \tag{3}$$

$$\dot{\boldsymbol{\omega}}_A = \boldsymbol{I}_A^{-1}\left(\boldsymbol{M}_A - \tilde{\boldsymbol{\omega}}_A\boldsymbol{I}_A\tilde{\boldsymbol{\omega}}_A\right) \tag{4}$$

where ***r*** is vector of the Cartesian coordinates of the helicopter center of mass with respect to an inertial reference frame, ***Θ*** is the Euler-angle vector, ***v*** is the center of mass translational velocity, ***ω*** is the body-axis angular rate vector, *m* is the helicopter's mass, $\boldsymbol{I}_A$ is the helicopter's inertia matrix, ***g*** is the constant gravitational acceleration, ***F*** and ***M*** are forces and moments applied to the helicopter. The subscripts *A* and *G* denote body axes (fixed to the helicopter body) and inertial axes (fixed to inertial space). Here $\boldsymbol{T}_{GA}$ is the transformation matrix from body axes to inertial axes and $\boldsymbol{L}_{GA}$ matrix connects the Euler-angle rates and body-axis rates.

2.1.2. Rotor dynamics

The force and moment transmitted by a single blade to the rotor hub consist of the integration of infinitesimal aerodynamic and inertial forces and moments acting on the blade elements along the rotor blade in the lead-lagging and flapping frame (*LLF*), and the flapping and lead-lagging spring/damper moments [26]. Flapping and lead-lagging motions are illustrated in Fig. 3. The infinitesimal aerodynamic force and moment are, respectively,

$$d_{LLF}\boldsymbol{F}_{aero} = \frac{\gamma I_\beta}{2R^3}\begin{bmatrix} 0 \\ -\left(\theta\, U_T^2 - U_P\, U_T\right)\dfrac{U_P}{U_T} - \dfrac{1}{a_0}\left(\delta_0 + \delta_2\left(\theta_B - \dfrac{U_P}{U_T}\right)^2\right) \\ \theta\, U_T^2 - U_P\, U_T \end{bmatrix} dx \tag{5}$$

$$d_{LLF}\boldsymbol{M}_{aero} = \begin{bmatrix} 0 & -xR\ (d_{LLF}F_{aero})_{III} & xR\ (d_{LLF}F_{aero})_{II} \end{bmatrix}^T \tag{6}$$

where U_P and U_T are perpendicular and tangential components of the resultant velocity of the airflow to an element located at a generic point P on the rotor blade, x is the non-dimensional location P, θ_B is the blade pitch angle, γ is the Lock number giving the ratio of aerodynamic to inertia forces acting on a rotor blade, I_β is the flap moment of inertia, a_0 is the blade lift curve slope, δ_0 and δ_2 are parasite and induced drag coefficients.

In the helicopter modelling, multi-blade coordinates (MBCs) are used, instead of the individual blade coordinates (IBCs), because IBCs result in periodic terms in the helicopter dynamics model. These periodic terms can be eliminated using the MBCs transformation. Therefore, the flapping and lead-lagging coordinates of a single blade are described in MBCs using (see also [63])

$$\Theta_i(\psi) = \Theta_0 + \Theta_c \cos(\psi_i) + \Theta_s \sin(\psi_i) + \Theta_d (-1)^i \tag{7}$$

where the blade azimuth angle is $\psi_i = \psi_1 - (\pi/2)(i-1),\ i = 1,\ldots,4,$ and Θ is the generic notation for the flapping and lead-lagging angles, while $\Theta_0, \Theta_c, \Theta_s, \Theta_d$ are collective, two cyclic, and differential coordinates, respectively.

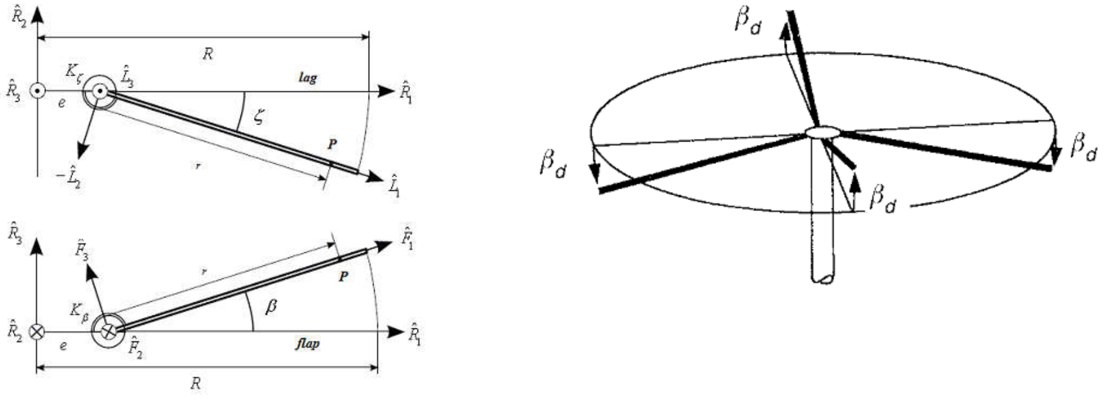

Fig. 3 Flapping, lead-lagging motions, differential coning multi-blade coordinate

Hence, each single blade has two governing second-order ordinary differential equations as follows

$$\begin{aligned} M_y &\triangleq M_{I_1} + M_{S_1} + M_{Aero_1} = 0 \\ M_z &\triangleq M_{I_2} + M_{S_2} + M_{Aero_2} + M_D = 0 \end{aligned} \tag{8}$$

By using state transformation, these two ODEs can be converted into four first-order ODEs. Therefore, we obtain 16 ODEs equations to represent the flapping and lead-lagging dynamics of the main rotor.

2.1.3. Rotor inflow

The flow-field induced by the rotor that contributes to the local blade angle of attack and dynamic pressure, thus changing the aerodynamic load on the rotor disk, can be represented as a linear static inflow model [64]:

$$\lambda_c = \lambda_0 \frac{15\pi}{23} \tan\left(\frac{\chi}{2}\right), \lambda_s = 0, \chi = \tan^{-1}\left(\frac{\hat{u}}{\hat{w} + \lambda_0}\right) \tag{9}$$

where χ is the wake skew angle, λ_0, λ_c, λ_s are collective, and lateral/longitudinal cyclic components of the rotor inflow. λ_0 is calculated using the momentum theory applied to the rotor disk. The induced inflow velocities at station *x* along the blade sections in the body axes system are given by

$$\boldsymbol{v}_i^A = \Omega R[0,\ 0,\ \lambda_0 + x\lambda_c + x\lambda_s]^T \tag{10}$$

The resulting helicopter model consists of 32 implicit nonlinear ODEs: 12 rigid-body equations of motion, 16 blade flapping and lead-lagging equations, 3 main-rotor Pitt-Peters inflow equations, 1 momentum equation applied to the rotor disk. This model can be written formally as

$$\boldsymbol{f}(\boldsymbol{x}, \dot{\boldsymbol{x}}, \boldsymbol{u}) = \boldsymbol{0}, \boldsymbol{x} \in \boldsymbol{R}^{32}, \boldsymbol{u} \in \boldsymbol{R}^4 \tag{11}$$

where

$$\boldsymbol{x} = \Big[\underbrace{u\ v\ w\ p\ q\ r\ \phi_H\ \theta_H\ \psi_H}_{\textit{fuselage states}}\ \underbrace{\beta_0\ \dot{\beta}_0\ \beta_c\ \dot{\beta}_c\ \beta_s\ \dot{\beta}_s\ \beta_d\ \dot{\beta}_d}_{\textit{flapping}}\ \underbrace{\zeta_0\ \dot{\zeta}_0\ \zeta_c\ \dot{\zeta}_c\ \zeta_s\ \dot{\zeta}_s\ \zeta_d\ \dot{\zeta}_d}_{\textit{lead-lagging}}\ \underbrace{\lambda_0\ \lambda_c\ \chi\ \lambda_s}_{\textit{inflow}}\ \underbrace{x_N\ y_E\ z_D}_{\textit{navigation}}\Big]^T$$

$$\boldsymbol{u} = \begin{bmatrix}\theta_0 & \theta_c & \theta_s & \theta_T\end{bmatrix}^T.$$

These notations represent variables that are typical in helicopter literature, for example, the first 9 variables and 3 last variables denote the translational velocities, rotational velocities, Euler angles, and Cartesian coordinates of the rigid-body dynamics. The flapping and lead-lagging coordinates are denoted in 16 variables $\beta_0, ..., \dot{\varsigma}_d$. While λ_0, λ_c, χ, λ_s represent the inflow model states. The input $\boldsymbol{u}$ consists of main rotor collective and cyclic pitch controls, and tail rotor collective pitch control.

2.2 Linearization and Controllability Analysis

If there are some uncontrollable modes, they should be properly identified prior to control design. Linearized models can provide insight into the controllability of the nonlinear system. Hence, the nonlinear system (11) is linearized about trim conditions such as hover and straight level flight, resulting in linear time invariant (LTI) systems:

$$\begin{aligned}\dot{\boldsymbol{x}} &= \boldsymbol{A}_p \boldsymbol{x} + \boldsymbol{B}_p \boldsymbol{u} \\ \boldsymbol{y} &= \boldsymbol{C}_p \boldsymbol{x}\end{aligned} \tag{12}$$

where $\boldsymbol{u} = \left[\theta_0, \theta_c, \theta_s, \theta_T\right]^T \in R^4$, $\boldsymbol{y} = \left[u, v, w,\ p, q, r,\ \Phi_H, \theta_H, \psi_H, x_N, y_E, z_D\right]^T \in R^{12}$

$$\boldsymbol{x} = \left[u, v, w,\ p, q, r,\ \Phi_H, \theta_H, \psi_H,\ \beta_0, \dot{\beta}_0, \beta_c, \dot{\beta}_c, \beta_s, \dot{\beta}_s, \beta_d, \dot{\beta}_d,\ \zeta_0, \dot{\zeta}_0, \zeta_c, \dot{\zeta}_c, \zeta_s, \dot{\zeta}_s, \zeta_d, \dot{\zeta}_d,\ x_N, y_E, z_D\right]^T \in R^{28}$$

As typical in aircraft dynamics, to simplify notation, the same symbols are used for nonlinear states and controls and their deviations from trim (e.g., symbol $\boldsymbol{x}$ in equations (11) is used for the nonlinear state vector and the same symbol, $\boldsymbol{x}$, is used in (12) for perturbations from trim values). Note that the number of states, n, in the linearized model (12) decreases from 32 to 28 because 3 steady state equations of the Pitt-Peters linear static inflow model and 1 equation of the thrust estimate are removed from the set of ODEs during linearization. The state matrix $\boldsymbol{A}_p$ and control matrix $\boldsymbol{B}_p$ in Eq. (12) are calculated as follows:

$$\boldsymbol{E} = \left.\frac{\partial \boldsymbol{f}}{\partial \dot{\boldsymbol{x}}}\right|_{(\boldsymbol{x}_{trim}, \boldsymbol{u}_{trim})},\ \boldsymbol{A}^* = \left.\frac{\partial \boldsymbol{f}}{\partial \boldsymbol{x}}\right|_{(\boldsymbol{x}_{trim}, \boldsymbol{u}_{trim})},\ \boldsymbol{B}^* = \left.\frac{\partial \boldsymbol{f}}{\partial \boldsymbol{u}}\right|_{(\boldsymbol{x}_{trim}, \boldsymbol{u}_{trim})},\ \boldsymbol{A}_p = -\boldsymbol{E}^{-1}\boldsymbol{A}^*,\ \boldsymbol{B}_p = -\boldsymbol{E}^{-1}\boldsymbol{B}^* \tag{13}$$

where $\boldsymbol{u}_{trim}$, $\boldsymbol{x}_{trim}$ are the trim values of the control and state vectors, respectively.

The LTI system (12) is controllable if and only if the controllability matrix $\boldsymbol{C}\left(\boldsymbol{A}_p, \boldsymbol{B}_p\right) = \left[\boldsymbol{B}_p, \boldsymbol{A}_p\boldsymbol{B}_p, \boldsymbol{A}_p^2\boldsymbol{B}_p, \ldots, \boldsymbol{A}_p^{n-1}\boldsymbol{B}_p\right]$ has rank n. To determine the rank of the matrix $\boldsymbol{C}(\boldsymbol{A}_p, \boldsymbol{B}_p)$, a singular value decomposition was performed so that $\boldsymbol{C}(\boldsymbol{A}_p, \boldsymbol{B}_p) = \boldsymbol{U}\Sigma\boldsymbol{V}^*$, where $\boldsymbol{\Sigma} = diag(\sigma_1, \sigma_2, ..., \sigma_r, 0, ..., 0)$, $\boldsymbol{U}$ and $\boldsymbol{V}$ are square unitary matrices and σ_i are the singular values ordered so that $\sigma_1 \geq \sigma_2 \geq ... \geq \sigma_{r-1} \geq \sigma_r$. The rank of the matrix was determined based on the number of singular values greater than a specified tolerance. This criterion led to the conclusion that the rank of matrix $\boldsymbol{C}(\boldsymbol{A}_p, \boldsymbol{B}_p)$ is 24 for a tolerance of 2.389×10^{-6}. Hence, for this tolerance the linear system (12) is uncontrollable. However, the Popov - Belevitch - Hautus (PBH) test, i.e. $rank[\lambda \boldsymbol{I} - \boldsymbol{A}, \boldsymbol{B}] = n$ for every unstable and marginally stable eigenvalue λ, is satisfied, so the linear system (12) is stabilizable. Moreover, the PBH test indicated that the uncontrollable modes are given by eigenvalues (-0.5762 ± 0.7577i; -0.0252 ± 0.3300i) in hover flight, and (-0.5805 ± 0.7800i; -0.0194 ± 0.3364i) in straight level flight. From the eigenvector analysis (see Table A.2 in the Appendix), the dominant motion of these uncontrollable modes is differential coning, which can be visualized as opposite pairs of blades moving in unison, but in opposition to neighboring pairs [63]. Each pair of blades induces equal and opposite loads on the rotor hub, resulting in no effective loading on the rotor hub (see Fig. 3). Therefore, these uncontrollable modes have little effect on the flight dynamics.

2.3 Nonlinear Simulations

The critical ingredient for MPC design is the dynamical model of the system to be controlled. Therefore, in this subsection we investigate the linear model's ability to predict the behavior of the nonlinear system over a future prediction horizon so that MPC can use it as an internal model. Comparisons between responses of the linearized and the nonlinear models are performed. Two scenarios are considered: 1) The controls are fixed to the values corresponding to hover and disturbances in initial conditions are considered; 2) The initial conditions are fixed to those corresponding to straight level flight at 80 knots and the response to control inputs is simulated. We also explain the rationale behind selecting the sampling time, T_s, and prediction horizon, H_p, for MPC design based on the controlled system dynamics.

2.3.1 Response to Initial Disturbances

Fig. 4 shows the response of the helicopter to an initial disturbance in the vertical speed of 5 knots at hover. The controls are fixed to the values corresponding to hover. This figure shows that the disturbance in the vertical speed decays after about 10 seconds for the linearized and the nonlinear models. The disturbance in the vertical speed induces rolling, pitching, and yawing motions that diverge from the trim condition along with time. This behavior is expected because most helicopters, including this one, are inherently unstable in hover [63]. Comparison between simulation results of the behavior of the nonlinear and the linearized models show relatively good agreement for some fuselage states (e.g., u, v, ϕ, ψ) for, approximately, the first two seconds. For other fuselage states (e.g., w, r) and for the blade states the agreement is qualitative rather than quantitative. Nevertheless, the frequencies of oscillations predicted by the linearized model are in good agreement with the nonlinear system's response, which, as discussed shortly, is very important for sampling time selection in MPC design. This indicates that, overall, the linearized model captures the essence on the helicopter dynamics for a few seconds after the disturbance is applied. The ignored dynamics in the linearized model and the unstable hover condition account for the observed discrepancies.

Fig. 5 shows the response of the helicopter to an initial disturbance in the vertical speed of 5 knots in a straight level flight at 80 knots. The controls are fixed to the values corresponding to hover. This figure shows that the disturbance in the vertical speed decays after about 10 seconds for the linearized and the nonlinear models. The disturbance in the vertical speed induces rolling, pitching, and yawing motions. The rolling and pitching motions are slightly damped with a time constants of a few tens of seconds. This is expected because, unlike hover, straight level flight at 80 knots is exponentially stable. However, the yaw motion does not go to zero because it is naturally assumed to be neutrally stable in flight vehicles. Comparison between simulation results of the behavior of the nonlinear and the linearized models show very good agreement for all fuselage states, and blade states.

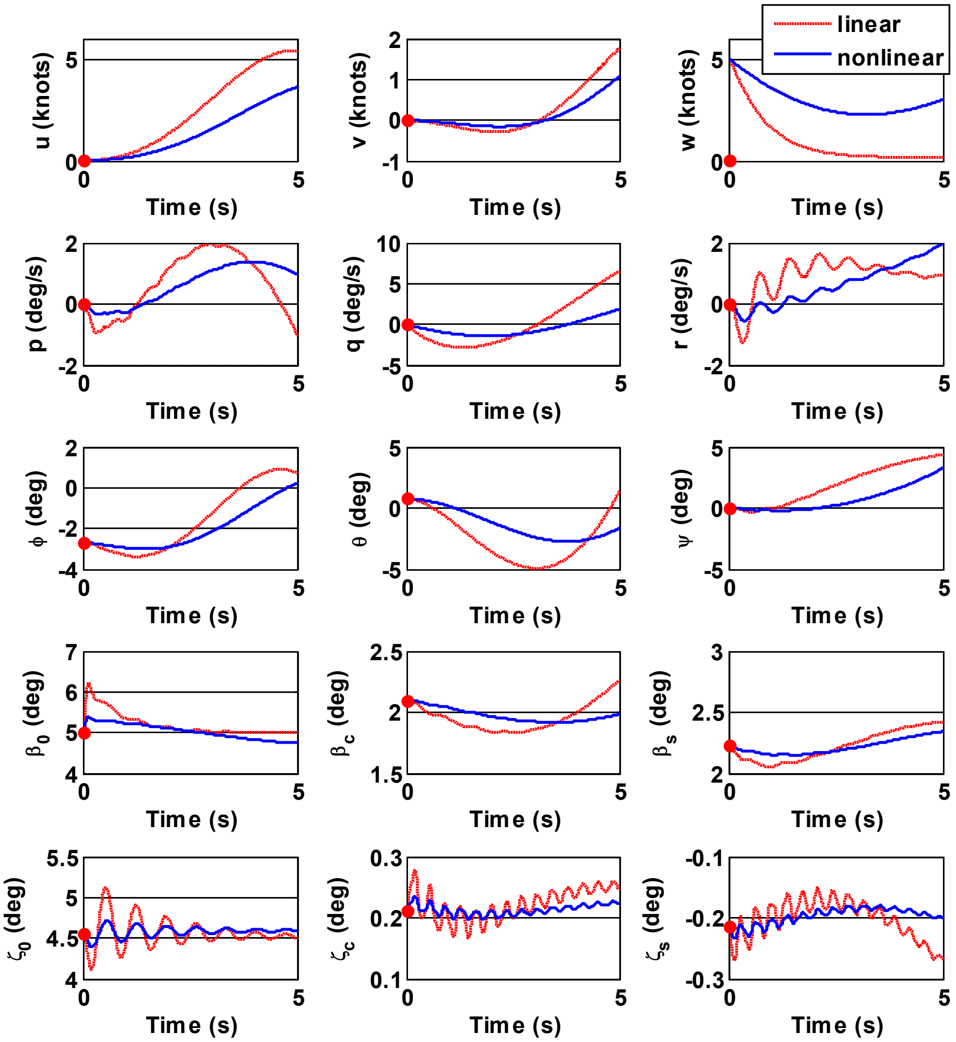

Fig. 4 Response of the helicopter to a disturbance in vertical speed at hover

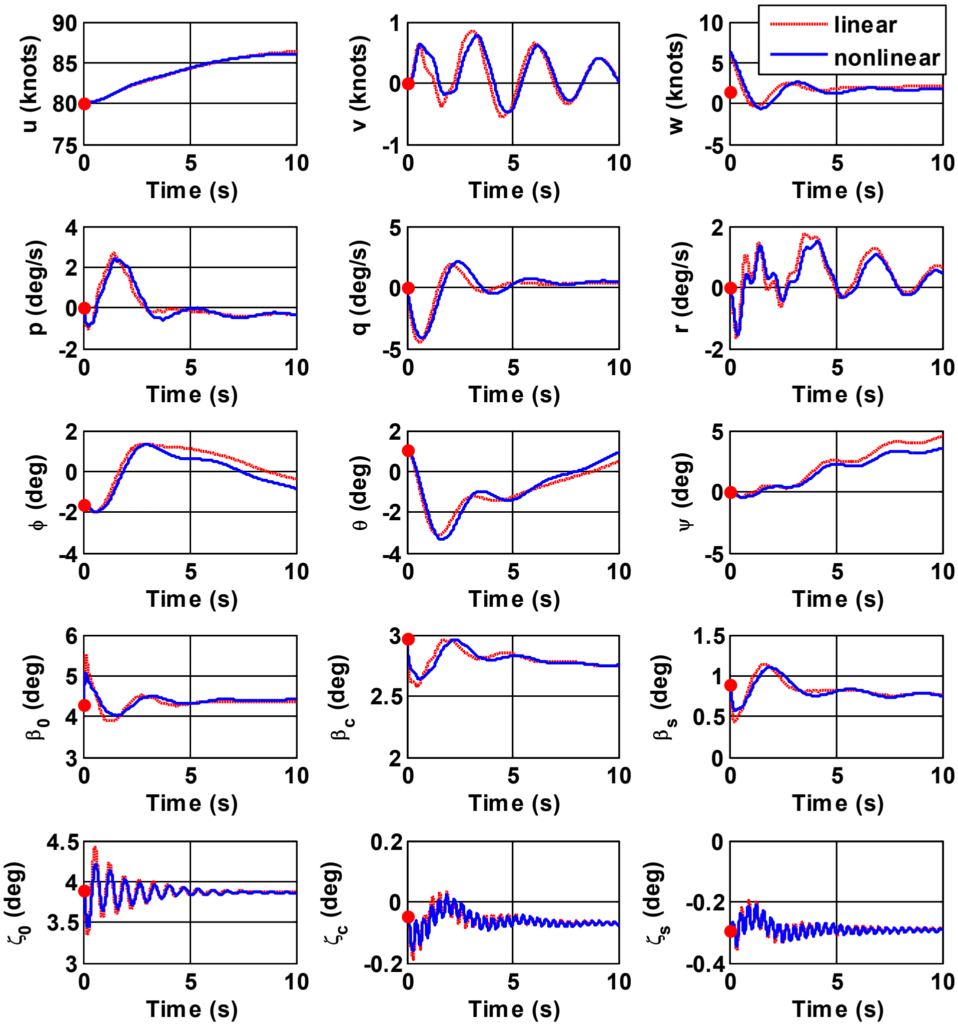

Fig. 5 Response of the helicopter to a disturbance in vertical speed at 80 knots

2.3.2 Response to Controls

Fig. 6 shows the response of the helicopter to a 3-2-1-1 multi-step longitudinal cyclic pitch input applied when the helicopter is initially in a straight level flight at 80 knots. This input, which consists of alternating pulses with time widths in the ratio 3-2-1-1, has much richer frequency content than a doublet so it is a common test input for aircraft system identification. The pulse widths are chosen so that the associated frequencies bracket the expected natural frequency of the dynamic model to be identified [65]. In Fig. 6, the '1' pulse width is 0.7 s, and the magnitude of each pulse is ±2 deg varying around the trim value of the longitudinal cyclic control in straight-level flight at 80 knots. It can be seen from Fig. 6 that there is a direct response in pitch motion with a magnitude of 10 deg after

1 second. Moreover, there is an off-axis roll response due to the cross-coupled control moment that is reinforced by the coupled damping moment. Strong cross couplings are one of the distinguishing features of rotary-wing aircraft compared with most fixed-wing aircraft (for more details, see [63]). As a result of the roll-to-pitch coupling, the helicopter rolls to nearly -7 deg following a pitch angle of 10 deg controlled by the '3' longitudinal cyclic pulse. The next longitudinal cyclic pulses '2', '1', and '1' excite the flight behavior in the same manner as pulse '3' does. We remark that, overall, the nonlinear and linearized systems responses show better agreement for this flight condition. This is expected because, unlike hover, straight level flight at 80 knots is exponentially stable.

Fig. 7 shows the response of the helicopter to the same 3-2-1-1 multi-step longitudinal cyclic pitch input applied when the helicopter is initially in hover. We see that there is no direct response in pitch motion with the 3-2-1-1 input. This can be explained by the fact that unstable modes in hover flight will diverge dramatically under the persistent excitation without the augmented stability systems active. Comparison between simulation results of the behavior of the nonlinear and the linearized models show relatively good agreement for some fuselage states (e.g., u, v, ϕ, θ, ψ) for, approximately, the first two seconds.

From the study of the helicopter responses to perturbations and controls (see Appendix B for more numerical simulations), the observed behaviors of the nonlinear and the linearized models show very good agreement for the fuselage as well as for the main rotor blades, only for the first several seconds (similar agreement patterns were observed for other response simulations). This is not good for long-term simulations but it is actually sufficiently good for MPC design. This conclusion can be explained as follows. In [66], Shannon’s sampling theorem theoretically established that, in order to reconstruct the original function from its samples, the sampling time should be less than half of the period of the fastest dynamic mode. In practice, the sampling time is selected much smaller. In this study, the maximum frequency of the helicopter modes is less than 9 Hz, corresponding to the flapping mode [27], i.e. a period of 0.12 seconds. Thus, an MPC is designed in the next chapters for the sampling period T_s of 0.02 seconds in accordance with the discussion above. The prediction horizon H_p of 25 samples, corresponding to a period of 0.5 seconds, is selected for the MPC design to achieve the desired performance in shipboard operations.

This is 4 times smaller than the two seconds for which the behaviors of the nonlinear and linearized models agree. If the model is updated for control design, agreement between the nonlinear and linearized models for such short time intervals is sufficient. Hence, the linearized model can be used as an internal model to estimate the helicopter behavior during the prediction horizon of the MPC design.

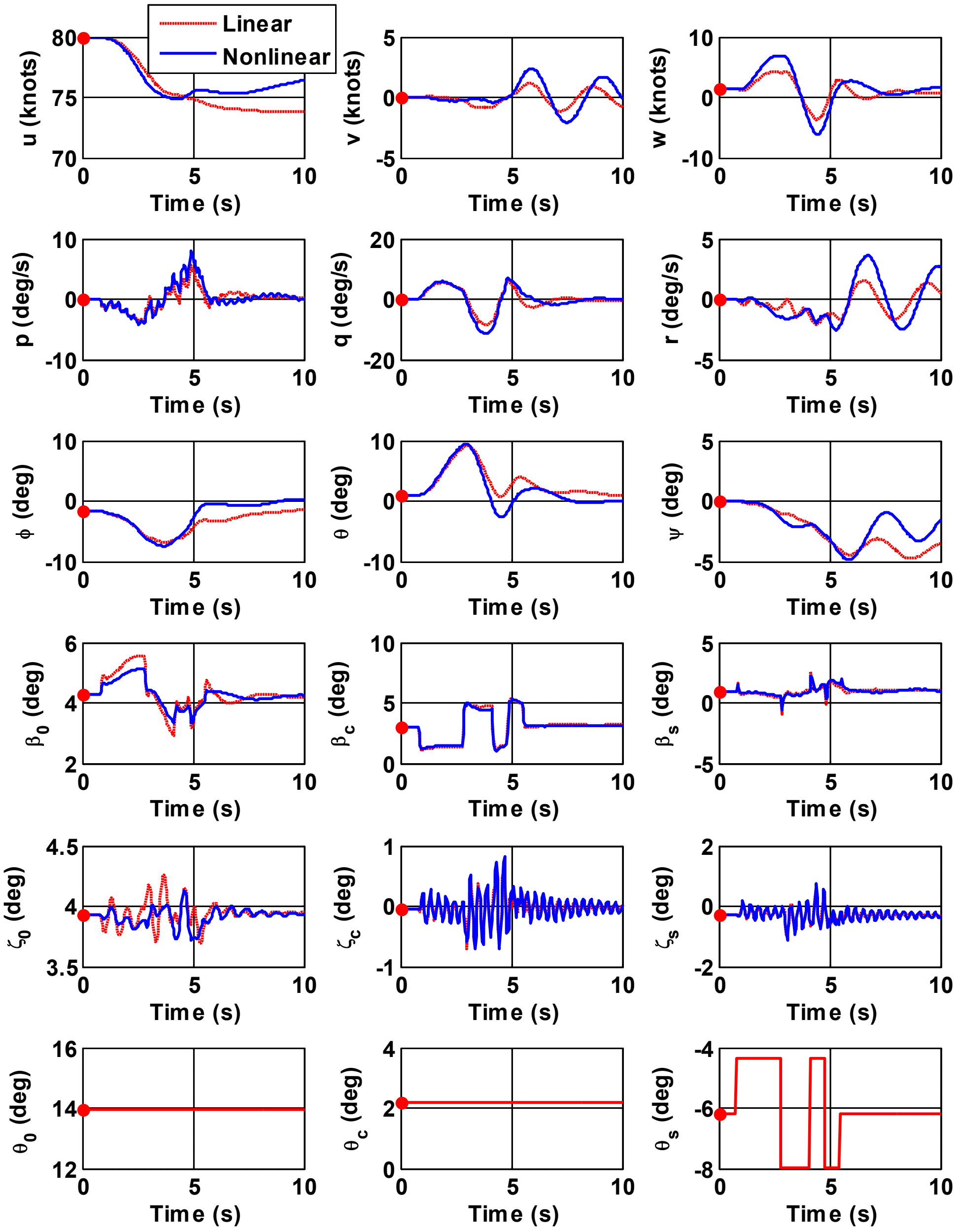

Fig. 6 Response of the helicopter to a 3-2-1-1 longitudinal cyclic pitch at 80 knots

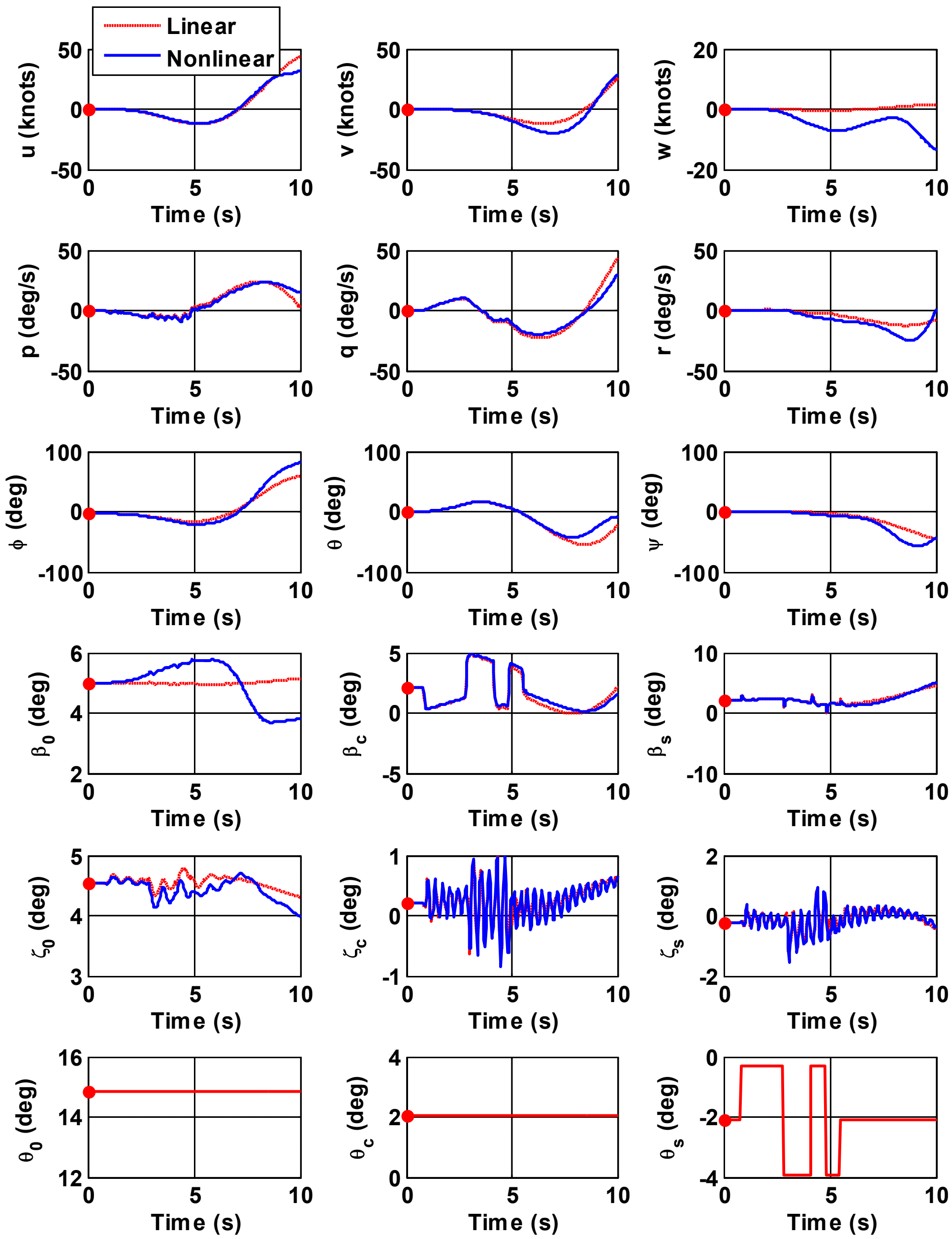

Fig. 7 Response of the helicopter to a 3-2-1-1 longitudinal cyclic pitch at hover

2.4 Ship Modeling and Motion Simulation

Stability and performance are objectives that can often conflict in aircraft operations. For example, strong stability is desired to reject perturbations. In contrast, high maneuverability is required to execute hard maneuvers rapidly and precisely, which may result in a less stable aircraft. Ship-borne helicopters require both stability and maneuverability to achieve safe landing. Understanding the effects of the ship's motion and the ship airwake on helicopter dynamics is essential for stability and performance evaluations.

A ship with Motora Model C body plan [67] and specification data in Table A.3 in the Appendix, is modeled as a single rigid body system with 6 DOFs, i.e., surge, heave, sway, pitch, roll and yaw motions. The 6-DOF equations of motion can be formulated based on the Newton-Euler laws as follows [68]:

$$\begin{aligned} &(\boldsymbol{M}_S+\boldsymbol{A}_S)\dot{\boldsymbol{\upsilon}}+\boldsymbol{C}_S(\boldsymbol{\upsilon})\boldsymbol{\upsilon}+\boldsymbol{B}_S(\boldsymbol{\upsilon})\boldsymbol{\upsilon}+\boldsymbol{g}(\boldsymbol{\eta})=\boldsymbol{\tau}+\boldsymbol{F}_{D\&I} \\ &\dot{\boldsymbol{\eta}}=\boldsymbol{J}(\boldsymbol{\eta})\,\boldsymbol{\upsilon} \end{aligned} \tag{14}$$

where $\boldsymbol{v} = [u_S, v_S, w_S, p_S, q_S, r_S]^T$ is the translational and angular velocity vector decomposed in the ship body-fixed axes ($Ox_by_bz_b$), in which x_b is the longitudinal coordinate, positive forward, y_b is the transverse coordinate, positive to the right, z_b is the vertical coordinate, positive downward. The vector $\boldsymbol{\eta} = [x_S, y_S, z_S, \Phi_S, \theta_S, \psi_S]^T$ is the position and orientation vector of the ship in the inertial reference frame, $\boldsymbol{\tau}$ is the vector of control forces and moments, and $\boldsymbol{F}_{D\&I}$ is the vector of wave-exciting incident and diffraction forces and moments calculated using the flow potential theory and superposition principle. The added mass $\boldsymbol{A}_S$ and damping matrix $\boldsymbol{B}_S$ can be estimated using the linear strip theory. In this theory, the hull is divided into a number of transverse sections or strips with 2 dimensional added mass coefficients estimated using available analytical solutions [69]. Eq. (14) is integrated to produce the ship motion in response to wave-exciting forces and moments in time domain.

In the frequency domain, response amplitude operators (RAOs) have been widely published by Denis and Pierson [70] (see Fig. 8). The RAO corresponding to a particular motion (surge, heave, pitch, etc.) is obtained by calculating the motion amplitude and phase in a series of regular, small-amplitude waves of various frequencies. To validate our ship model RAOs for the Model C are computed and compared with those obtained from the PDSTRIP software [71], and those reproduced from [72] for the Destroyer 26 ship that has similar dimensions. We observe good agreements for the RAOs of heave, sway, pitch, and yaw motions between the linear strip theory, PDSTRIP, and Destroyer 26 results. These RAOs are acceptable in the dominant frequency span 0-2 Hz where the sea wave has a significant effect on the ship dynamics. Fig. 9 shows the deck motion simulation of the Model C generated by the RAO technique in response to Pierson-Moskowitz sea state 5 wave spectrum [72] and wave heading of 150 deg.

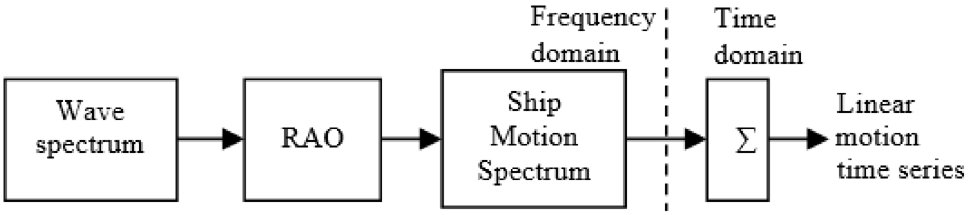

Fig. 8 RAO Technique

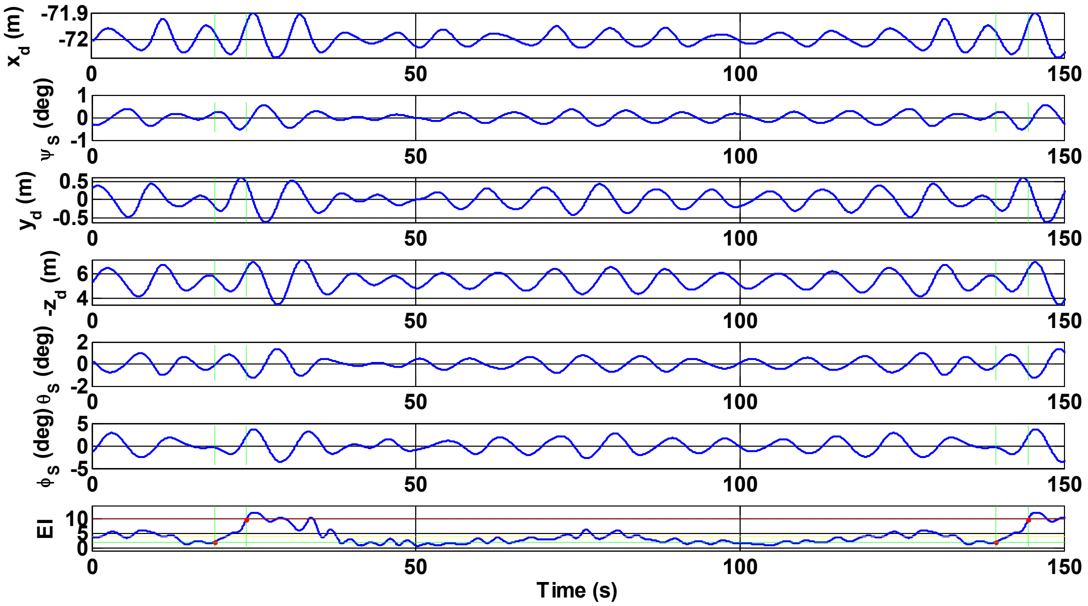

Fig. 9 Ship motion time history and energy index

To predict the ship's quiescent periods, O'Reilly introduced the EI index that gives indication of the motion a ship can travel in the near future for safe landings [72]. The EI aggregates information about linear/angular displacements, velocities and accelerations to predict the quiescent ship motion periods. In [73], the EI is defined as

$$EI = s_1 \dot{y}_d^2 + s_2 \ddot{y}_d^2 + s_3 \dot{z}_d^2 + s_4 \ddot{z}_d^2 + s_5 \phi_S^2 + s_6 \dot{\phi}_S^2 + s_7 \theta_S^2 + s_8 \dot{\theta}_S^2 \tag{15}$$

where $s_1 \ldots s_8$ are constant coefficients. Coefficients s_i of the EI index in Eq. (15) were selected by normalizing each measured quantity using its maximum value:

$$\begin{aligned} s_i &= \frac{\max\limits_{i=1,\ldots,8}\{scale(i)\}}{scale(i)}, \\ scale &= \left\{ \max(\dot{y}_d^2), \max(\ddot{y}_d^2), \max(\dot{z}_d^2), \max(\ddot{z}_d^2), \max(\phi_S^2), \max(\dot{\phi}_S^2), \max(\theta_S^2), \max(\dot{\theta}_S^2) \right\} \Big|_{T_{sim}} \end{aligned} \tag{16}$$

In three simulations with duration T_{sim} of 10 hours, weights were obtained as $s = [5, 57, 1, 20, 197, 468, 3623, 7486]^T$.

The EI status describes the relationship between the ship motion and its effect on helicopter operating limits. In [73], the EI status for the Merlin helicopter/FFG-7 combination was defined as Danger (red): 10→∞, Caution (amber): 4→10, Safe (green): 1.8→4, Very safe (flashing green): 0→1.8. The time required to raise the deck from minimal motion (negative side of flash green *EI* line) to unacceptable motion (positive side of the red *EI* line) is called rise-time. The minimum rise-time is an inherent characteristic of a ship/helicopter combination independent of the sea level or direction. To estimate the minimum rise-time, 40 trial simulations with a simulation period of 1 hour each were executed, indicating that the minimum rise-time is 4.5 s for Model C/generic helicopter combination (Fig. 10). The result is consistent with, but a litter lower than, other similar ship/helicopter combinations in [74]. An automatic deck landing controller should be designed so that a safe landing is rapidly accomplished in less than the minimum rise-time.

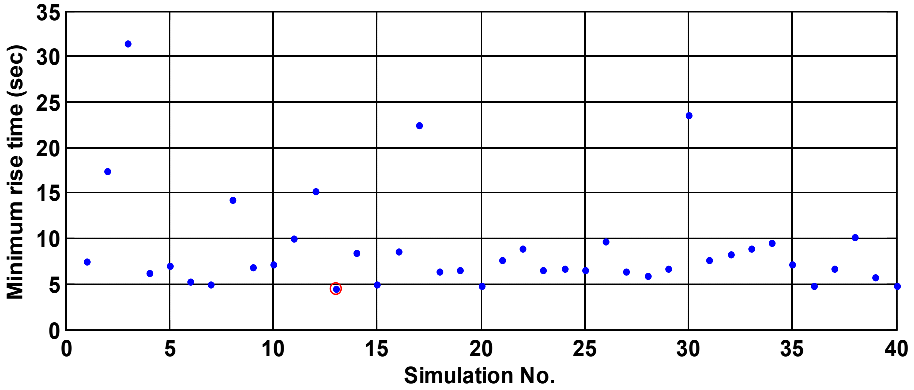

Fig. 10 Minimum rise-times in 40 simulations
(T_{sim} = 1 hour for each simulation, H_s=4 m, χ=150 deg)

2.5 Ship Airwake Modeling

Two popular ship airwake models that are used in shipboard operations are CETI and CFD based models. The CETI model consists of a set of transfer functions parameterized by main-rotor diameter, turbulence intensity, and mean wind speed. These transfer functions determine the control inputs that should be inserted in parallel with those of the pilot to produce vehicle responses equivalent to those in a turbulence field. In [8]-[11], a CETI model was identified using the flight test data from a UH-60 rotorcraft hovering in the atmospheric turbulence downwind of a large, cube-like hangar. Since this scenario is relatively similar to a deck landing, the CETI model is used for automatic landing in this dissertation. On the another hand, experimental and CFD data of the ship airwake were generated in [3]-[4] for a model-scale helicopter based on a Merlin AW-101 exposed into headwind and a 30-deg WOD. Those data were used to explain well-known phenomena in the helicopter lateral reposition, i.e., headwind thrust deficit and 30-deg WOD pressure wall effects. For that reason, CFD data for modeling the ship airwake is used to take into account its aerodynamic effect on the helicopter for lateral reposition. Fig. 11 shows a typical approach and landing maneuver. The following section describes the procedure that embeds interactional aerodynamic effects of the ship airwake into the nonlinear helicopter model.

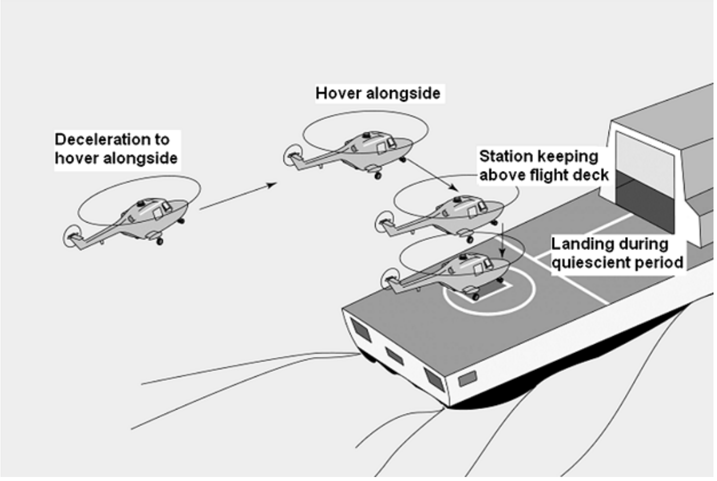

Fig. 11 A typical approach and landing [63]

2.5.1 Control Equivalent Turbulence Inputs (CETI)

The CETI model derived in [9] for the UH-60/hangar combination is given by the following transfer functions:

$$\begin{aligned}
\frac{\theta_c}{w_n} &= 0.837\sigma_w^{-0.6265}\sqrt{\frac{\sigma_w^2 U_\infty}{\pi R_m}}\left[\frac{1}{s+(2U_\infty/R_m)}\right] \\
\frac{\theta_s}{w_n} &= 1.702\sigma_w^{-0.6265}\sqrt{\frac{\sigma_w^2 U_\infty}{\pi R_m}}\left[\frac{1}{s+(2U_\infty/R_m)}\right] \\
\frac{\theta_0}{w_n} &= 0.1486\sigma_w^{-0.7069}\sqrt{\frac{3\sigma_w^2 U_\infty}{\pi R_m}}\times\left[\frac{s+33.91(U_\infty/R_m)}{\left[s+1.46(U_\infty/R_m)\right]\left[s+9.45(U_\infty/R_m)\right]}\right] \\
\frac{\theta_T}{w_n} &= 1.573\sigma_w^{-0.6493}\sqrt{\frac{\sigma_w^2 U_\infty}{\pi R_t}}\left[\frac{1}{s+(U_\infty/R_t)}\right]
\end{aligned} \tag{17}$$

where σ_w is turbulence intensity, U_∞ is mean wind speed, R_m is main rotor radius, R_t is tail rotor radius, w_n is white-noise signal. The turbulence was modeled using white-noise-driven shaping filters of a form similar to the Dryden spectral models that are comprised of rational functions and characterized by the power spectral densities (PSD) of the gust disturbances [12]. The model's parameters were identified by using the PSD characteristics of the equivalent control gust remnants derived from flight test data. However, PSD data in [9] showed that collective gust autospectrum was more consistent with a second-order filter than the first-order filter. Then the second-order filter was constructed based on the reduced order filter of the Von Karman model for the equivalent collective control input in (17). This can be physically explained based on the fact that the conventional helicopter is naturally unstable in the phugoid mode in hover (see Fig. 12). When the helicopter hovers behind a cube-shaped hangar, gust disturbances excite much more complex behavior in the phugoid mode than in other modes. Therefore, the equivalent collective control input must have much more complex action than other control inputs to produce longitudinal mode responses equivalent to those in the turbulence field.

The CETI model empirically created for one rotorcraft can be scaled to another vehicle that has the same configuration by using the scaling technique developed in [11]. This technique was derived from approximating the effects of upwash and sidewash turbulence fields as changes in the angles of attack of the main rotor and tail rotor blades. These changes were then made equal to equivalent changes in blade pitch angles through collective and cyclic inputs. Turbulence intensity of 3 m/s and mean wind speed of 15 m/s are chosen to generate the equivalent control inputs for the disturbance in Fig. 13. Then the nonlinear helicopter model that includes the effects of the disturbance can be formally rewritten as

$$\boldsymbol{f}(\boldsymbol{x},\dot{\boldsymbol{x}},\boldsymbol{u}+\delta\boldsymbol{u}_{CETI})=\boldsymbol{0},\ \boldsymbol{x}\in\boldsymbol{R}^{32},\ \boldsymbol{u}\in\boldsymbol{R}^{4} \tag{18}$$

where $\delta\boldsymbol{u}_{CETI}$ are the control equivalent turbulence inputs.

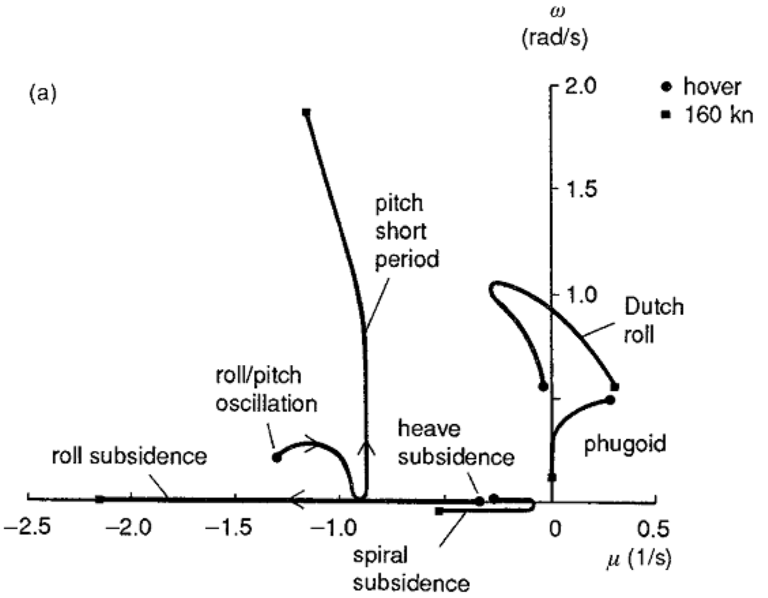

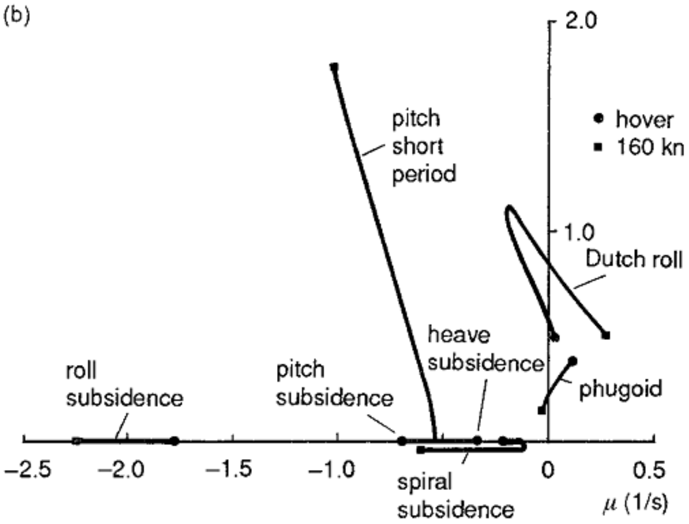

Fig. 12 Loci of Puma eigenvalues as a function of forward speed [63]: (a) coupled; (b) uncoupled

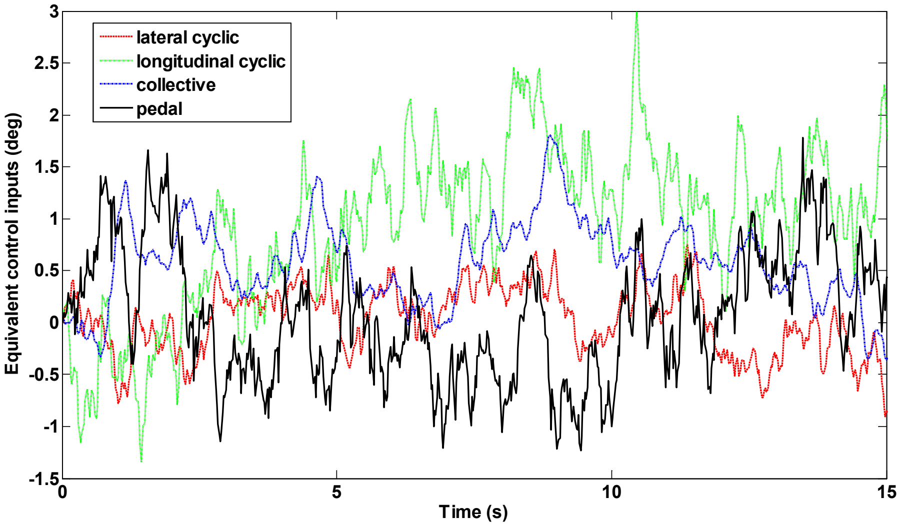

Fig. 13 Equivalent control inputs for the disturbance

2.5.2 CFD model of the ship airwake

In [3]-[4], a model-scale helicopter based on a Merlin AW-101 was exposed into headwind and 30-deg WOD conditions in a water tunnel to measure the unsteady forces and torques exerted by the ship airwake at fixed locations along the flight path of a landing maneuver. An unsteady CFD analysis of the ship airwake was performed to estimate the time-average and unsteady aerodynamic loading on the helicopter. Those experimental and CFD results explained two well-known phenomena in helicopter ship operations: headwind thrust deficit and 30-deg pressure wall effects. Accordingly, when the helicopter makes a lateral reposition towards the landing deck of a ship with medium to large-scale hangars in headwind condition, the collective pitch control must be increased to balance the helicopter's altitude out of the thrust deficit. On the other hand, for the same maneuver in 30-deg WOD, there is a noticeable increase in thrust and a severe deceleration in sideslip velocity as the helicopter translates toward the deck due to the spatial velocity gradients in the airwake. Consequently, the pressure wall effect can divert the helicopter away from the landing deck. Hence, a control strategy that is different from the one in headwind must be applied, i.e. reducing the collective pitch control and increasing the lateral cyclic control input.

In this dissertation, CFD data of the ship airwake reproduced from [4] is incorporated into the nonlinear helicopter model (1). The airwake has an important effect on the main rotor blade angle of attack, mathematically captured by Eq. (19). Consequently, the aerodynamic loading of the flow field over the rotor disk will be modified compared with the one used in our previous work [32] as

$$\alpha_B = \theta_B - \frac{U_P}{U_T},\ U_T = \overset{LLF}{\boldsymbol{v}}_{air}[2], U_P = \overset{LLF}{\boldsymbol{v}}_{air}[3],\ \overset{LLF}{\boldsymbol{v}}_{air} = \boldsymbol{T}_{LLF-A}\left(\overset{A}{\boldsymbol{v}}_{induced} - \overset{A}{\boldsymbol{v}}_{A} + \overset{A}{\boldsymbol{v}}_{airwake}\right) - \overset{LLF}{\boldsymbol{v}}_{P} \tag{19}$$

where α_B, θ_B are the angle of attack and the pitch angle of the blade (Fig. 14), $\overset{LLF}{\boldsymbol{v}}_{air}$, $\overset{LLF}{\boldsymbol{v}}_{P}$ are the resultant velocity of the airflow to a strip located at a generic point P on the rotor blade and the inertial velocity of this strip in the lead-lagging frame, $\boldsymbol{T}_{LLF\text{-}A}$ is the transformation matrix from the aircraft frame to the lead-lagging frame, $\overset{A}{\boldsymbol{v}}_{induced}$, $\overset{A}{\boldsymbol{v}}_{A}$, $\overset{A}{\boldsymbol{v}}_{airwake}$ are induced velocity, helicopter fuselage velocity, and airwake velocity in the aircraft frame, respectively.

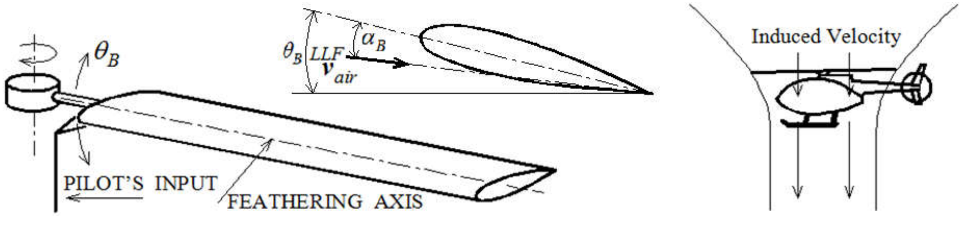

Fig. 14 Main rotor blade angle of attack

Components of ship airwake velocities that are present in the ODEs of flapping and lead-lagging motions are then interpolated with piecewise polynomial functions from CFD data extracted from [4]. Time-varying implicit ODEs (20) for the helicopter model are formally obtained due to the time varying distribution of the airwake over the rotor blades:

$$\begin{aligned}&\boldsymbol{f}(\boldsymbol{x},\dot{\boldsymbol{x}},\boldsymbol{u},\boldsymbol{a}_{jnki},t)=\mathbf{0},\ \boldsymbol{x}\in\boldsymbol{R}^{32},\ \boldsymbol{u}\in\boldsymbol{R}^{4},\\&j=1..n_{seg},n=1..n_{cof},k=1..n_{vel},i=1..n_{bla}\end{aligned} \tag{20}$$

where each of the main rotor blades is divided into n_{seg} segments, the airwake velocity components are interpolated with piecewise (n_{cof} - 1)th order polynomial functions with time-varying coefficients $\boldsymbol{a}_{jnki}$, $n_{vel} = 3$ is the number of components of the airwake velocity vector, $n_{bla} = 4$ is the number of main rotor blades. Fig. 15 shows the normalized mean vertical velocity contours of the airwake reproduced from [4] and the main rotor blades divided into 4 segments. The circle in Fig. 15 traces the main rotor's blade tip and the curved line represents this rotor's trajectory during a typical lateral reposition maneuver. We can see the varying distribution of the airwake over the rotor blades at each instant.

Linear Interpolation

The non-dimensional k^{th} velocity component of the ship's airwake along the j^{th} segment of the i^{th} rotor blade is approximated by a linear interpolation from CFD data (Fig. 16):

$$\overline{w}_g(j,k,i)=a_{j1ki}\overline{x}+a_{j2ki} \tag{21}$$

where $\overline{x}$ is a non-dimensional coordinate in the lead-lagging frame ($\overline{x}$ = r/R).

Cubic Spline Interpolation

The non-dimensional k^{th} velocity component of the ship's airwake along the j^{th} segment of the i^{th} rotor blade is approximated by a cubic spline interpolation from CFD data (Fig. 16):

$$\overline{w}_g(j,k,i)=a_{j1ki}(\overline{x}-\overline{x}_j)^3+a_{j2ki}(\overline{x}-\overline{x}_j)^2+a_{j3ki}(\overline{x}-\overline{x}_j)+a_{j4ki} \tag{22}$$

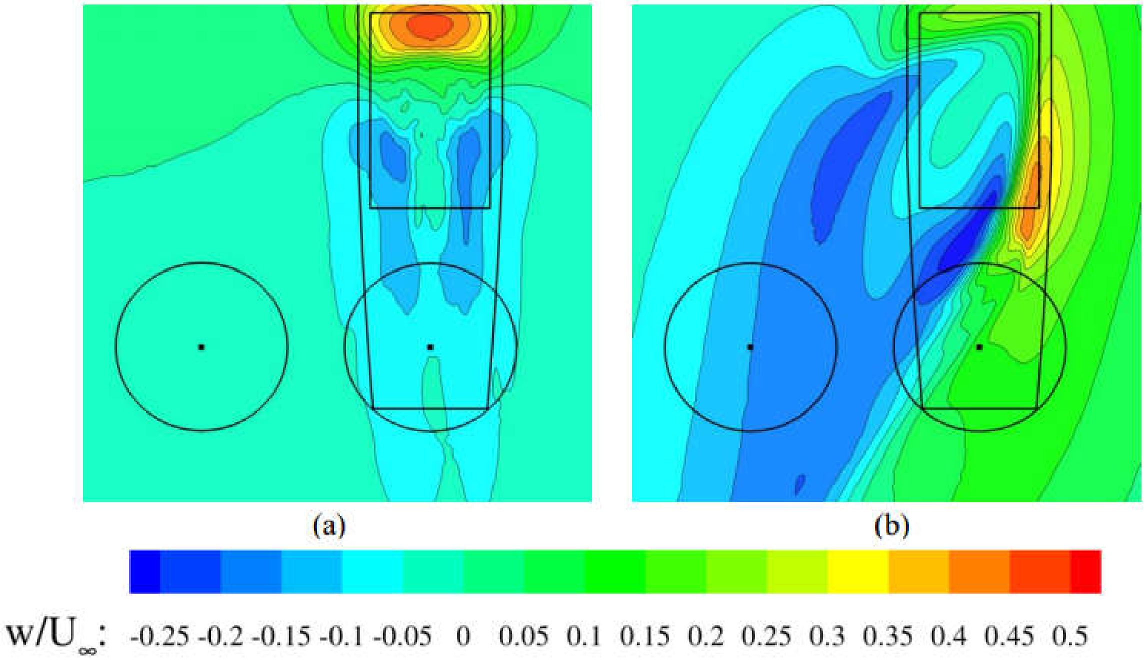

Fig. 15 Normalized mean vertical velocity contours for a headwind (a), 30-deg WOD condition (b) [4]

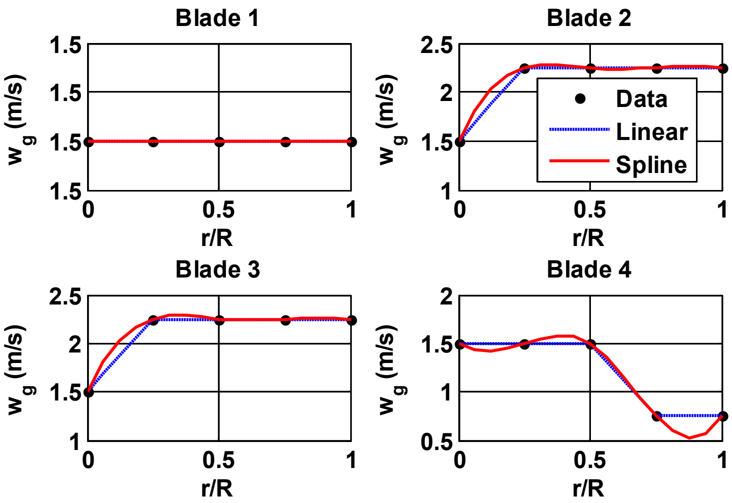

Fig. 16 Linear & spline interpolations of the vertical velocity component of the ship's airwake along each of four rotor blades at the instant in Fig. 15

2.5.3 Helicopter-ship airwake interaction simulations

For the same CFD data of the ship's airwake disturbance in 30-deg WOD condition, various interpolations of the spatial-gradient velocity components over the rotor disk are incorporated into the nonlinear helicopter dynamics model to obtain the time-varying implicit ODE (20). Then the controls are fixed to the values corresponding to hover and responses of the helicopter to these disturbance approximations are simulated to investigate their effects on the open-loop flight. A comparison is illustrated in Fig. 17-18 to select a good approximation of the ship's airwake interaction for control design and evaluation.

Initially, the helicopter hovers at the position 20 m portside of the ship. Then the spatial velocity gradients in the ship's airwake produce a large degree of asymmetric aerodynamic loading over the main rotor disk that causes the rolling, pitching, yawing motions of the fuselage. Consequently, the helicopter's flight path is deviated in close proximity to the ship (Fig. 17). In Fig. 18 we see that the ship's airwake also results in noticeable rotor flapping and lead-lagging motions at high frequency. Therefore, helicopter shipboard operations in the ship's airwake require significant workload from the pilot.

All simulations in Fig. 17-18 show that the quality of the linear interpolation of the airwake velocity components to each of the four segments along each blade is adequate to represent the turbulence effect of such a CFD data used in this dissertation. Obviously, we can incorporate a high-order accurate interpolation with a larger number of blade segments for more complex flow-field of the ship's airwake into the nonlinear ODEs (20) of the helicopter.

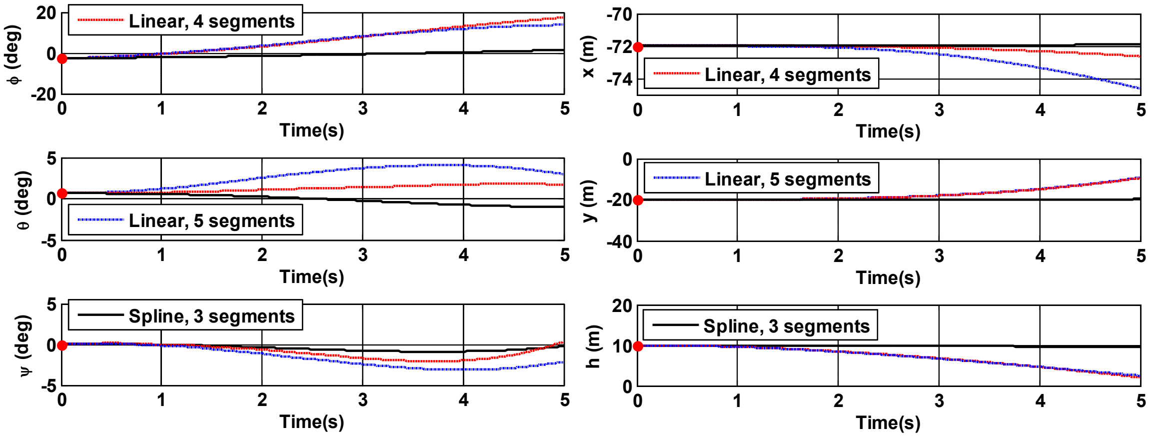

Fig. 17   Euler angles and position of the helicopter in response to the ship airwakes

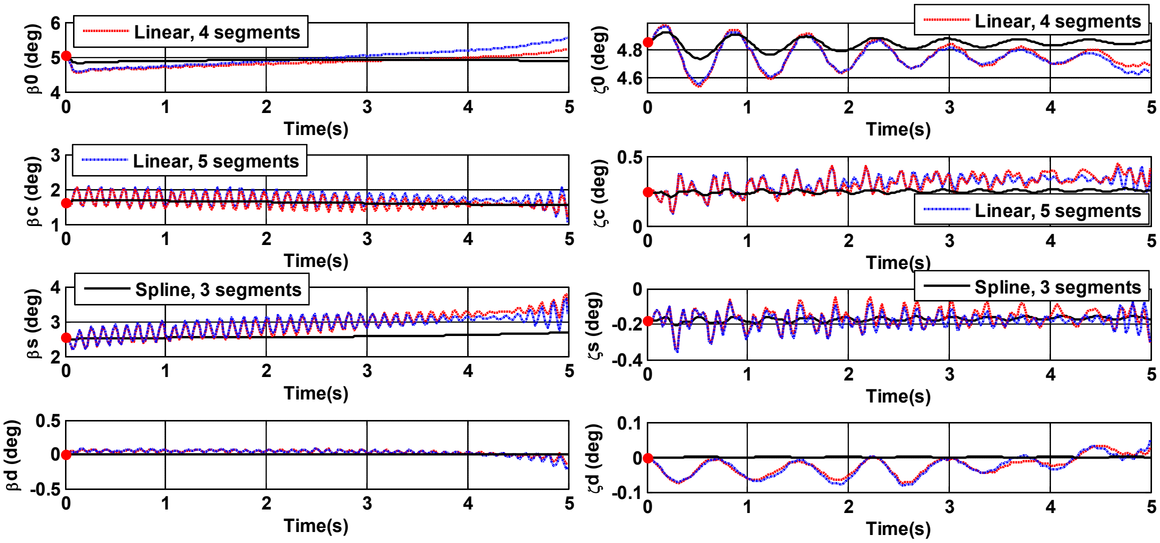

Fig. 18   Time history of the flapping, lead-lagging states of the main rotor blades in response to the ship airwakes

Chapter 3: MPC for Helicopter Shipboard Operations

Traditional flight control systems consist of an inner loop for attitude stabilization and an outer loop for trajectory tracking. The idea behind this design strategy is that the inner loop should control aircraft's attitude and the outer loop should control desired translational motions. The inner loop and the outer loop can be designed separately by control techniques that are primarily based on reducing control model complexity. This separated design idea works best if the outer loop bandwidth is significantly lower than that of the inner loop. However, the performance of this control structure can degrade in highly coupled dynamic systems and/or in large-magnitude/aggressive maneuvers required for an agile helicopter. In this dissertation, the separation of inner and outer loops is abandoned because all control modes are governed by MPC. It is believed that this is more appropriate for the highly coupled system used in shipboard operations.

In the MPC approach, an optimization problem is solved in which an internal model predicts the behavior of the system over a future prediction horizon starting at each time step, then an optimization algorithm generates the optimal control sequence to minimize the performance measure (e.g., tracking error, control effort) and satisfy the system constraints. Only the first element of the control sequence is applied as the input signal to the system at the current step. Then a new output measurement is obtained and the technique is repeated at the new time step [75]. This chapter presents a MPC design for helicopter shipboard operations at rough seas. Simulations of the automatic landing on a moving ship in sea state 5 in the CETI model airwake, and the automatic lateral reposition from the portside towards the landing deck at 30-deg WOD condition in the CFD airwake are performed to evaluate the feasibility of the MPC.

3.1 MPC Design

3.1.1 Optimization Problem

Following the standard MPC design, a performance measure *V(k)* is defined as:

$$V(k)=\sum_{i=0}^{H_p-1}\left(\sum_{j=1}^{p} w_{i+1,j}^{y}\left|\left(y_j(k+i+1\,|\,k)-r_j(k+i+1)\right)\right|^2 + \sum_{j=1}^{m} w_{i+1,j}^{u}\left|u_j(k+i\,|\,k)\right|^2 + \sum_{j=1}^{m} w_{i+1,j}^{\Delta u}\left|\Delta u_j(k+i\,|\,k)\right|^2\right) \tag{23}$$

The MPC action at time step k is obtained by solving the optimization problem $\underset{\Delta u(k|k),\ldots,\Delta u(k+H_m-1|k)}{minimize}\; V(k)$ subjected to the helicopter dynamic equations (12) discretized with the sampling time T_s selected as discussed in Section 2.3.2:

$$\begin{aligned} \boldsymbol{x}(k+1)&=\boldsymbol{A}\boldsymbol{x}(k)+\boldsymbol{B}\boldsymbol{u}(k)\\ \boldsymbol{y}(k)&=\boldsymbol{C}\boldsymbol{x}(k)+\boldsymbol{D}\boldsymbol{u}(k) \end{aligned} \tag{24}$$

In Eqs. (23) & (24), $\boldsymbol{x},\boldsymbol{r},\boldsymbol{u},\Delta\boldsymbol{u}$ represent vectors of system states, reference, inputs, and input increments, respectively, and $\boldsymbol{y}$ represents the controlled outputs vector, e.g., $\boldsymbol{y}=\left[u,v,w,\,p,q,r,\,\Phi_H,\theta_H,\psi_H,x_N,\,y_E,\,z_D\right]^T$. The subscript $()_j$ denotes the j component of a vector, $(k+i|k)$ denotes the value predicted for time $k+i$ using the values at time k, while p, m, H_p, H_m represent number of outputs, number of inputs, prediction horizon, and control horizon, respectively, and $w_{i+1,j}^{y}, w_{i+1,j}^{u}, w_{i+1,j}^{\Delta u}$ represent nonnegative weights for the corresponding variable. The optimization problem also includes constraints on the inputs and the outputs of the system such as control saturations obtained from the Puma helicopter's parameters [76] and main-rotor blade pitch control rate limits (slew rates). These are chosen based on the fact that operating frequencies for blade pitch control are limited by the bandwidth of the actuators that is typically between 10 and 40 rad/s [48]. In addition, output constraints are derived from the requirement for large-amplitude attitude changes in hover and low-speed flight for the moderate agility level [77]. Based on this information, for the numerical examples herein, the following values were chosen:

$$\begin{aligned} &\left[0,-7,-15,-20\right]\le\left[\theta_0,\theta_c,\theta_s,\theta_T\right]\le\left[25,7,15,20\right]\ \text{deg}\rightarrow \textit{input saturation}\\ &\left[\left|\dot\theta_0\right|,\left|\dot\theta_c\right|,\left|\dot\theta_s\right|,\left|\dot\theta_T\right|\right]\le\left[40,40,40,40\right]\ \text{deg}/\,s\rightarrow \textit{slew rates}\\ &-30\le\theta_H\le 20\,\text{deg},\left|\Phi_H\right|\le 60\,\text{deg},\ \left[\left|p\right|,\left|q\right|,\left|r\right|\right]\le\left[50,13,22\right]\text{deg}/\,s\rightarrow \textit{output saturation} \end{aligned} \tag{25}$$

For MPC design and implementation, the continuous constraints (e.g., slew rate constraints) were discretized. Matrices $\boldsymbol{A}$, $\boldsymbol{B}$, $\boldsymbol{C}$, $\boldsymbol{D}$ are obtained from Eq. (12) from Chapter 2 via discretization (note that $\boldsymbol{D}$ = 0). Assumed sensor measurements in this study are translational/angular velocities, Euler angles, and Cartesian coordinates of the helicopter in the NED frame. Because we cannot have true measurements, in this dissertation we mimic them: the values generated by the implicit nonlinear model of the helicopter are considered as measurements for the state observer described below. In practice, of course these measurements are delivered by sensors.

3.1.2 State Observer

In practice, not all of the states of the helicopter are directly measurable. Therefore, estimations are necessary using a state observer. Consider the linear helicopter model in the discrete form

$$\begin{aligned} \boldsymbol{x}(k+1) &= \boldsymbol{A}\boldsymbol{x}(k) + \boldsymbol{B}_u\boldsymbol{u}(k) + \boldsymbol{B}_d\boldsymbol{d}(k) \\ \boldsymbol{y}_m(k) &= \boldsymbol{C}\boldsymbol{x}(k) + \boldsymbol{D}_u\boldsymbol{u}(k) + \boldsymbol{D}_d\boldsymbol{d}(k) + \boldsymbol{n}(k) \end{aligned} \tag{26}$$

where $\boldsymbol{d}(k)$ is the plant noise, $\boldsymbol{n}(k)$ is the measurement noise, $\boldsymbol{y}_m$ is the measurement vector. Note that here $\boldsymbol{B}_u = \boldsymbol{B}_d = \boldsymbol{B}$, $\boldsymbol{D}_u = \boldsymbol{D}_d = \boldsymbol{D} = \mathbf{0}$. The plant noise $\boldsymbol{d}(k)$ is modeled as a LTI system with a zero-mean, unit covariance, random Gaussian input $\boldsymbol{n}_d(k)$:

$$\begin{aligned} \boldsymbol{x}_d(k+1) &= \bar{\boldsymbol{A}}\boldsymbol{x}_d(k) + \bar{\boldsymbol{B}}\boldsymbol{n}_d(k) \\ \boldsymbol{d}(k) &= \bar{\boldsymbol{C}}\boldsymbol{x}_d(k) + \bar{\boldsymbol{D}}\boldsymbol{n}_d(k) \end{aligned} \tag{27}$$

where $\bar{\boldsymbol{A}} = \mathbf{I}_{m\times m}, \bar{\boldsymbol{B}} = T_s^{ndm}\mathbf{I}_{m\times m}, \bar{\boldsymbol{C}} = \mathbf{I}_{m\times m}, \bar{\boldsymbol{D}} = \mathbf{0}_{m\times m}, T_s^{ndm} = T_s / \Omega$, m is the number of inputs, T_s^{ndm} is the non-dimensional sampling time. States $\boldsymbol{x}(k)$, $\boldsymbol{x}_d(k)$ are estimated using the measurement $\boldsymbol{y}_m(k)$ by a state observer that can be considered as a linear feedback system with equations as follows [78]:

$$\hat{\boldsymbol{y}}(k) = \boldsymbol{C}\hat{\boldsymbol{x}}(k\,|\,k-1) + \boldsymbol{D}_u\boldsymbol{u}(k) + \boldsymbol{D}_d\bar{\boldsymbol{C}}\,\hat{\boldsymbol{x}}_d(k\,|\,k-1) \tag{28}$$

$$\begin{bmatrix} \hat{\boldsymbol{x}}(k\,|\,k) \\ \hat{\boldsymbol{x}}_d(k\,|\,k) \end{bmatrix} = \begin{bmatrix} \hat{\boldsymbol{x}}(k\,|\,k-1) \\ \hat{\boldsymbol{x}}_d(k\,|\,k-1) \end{bmatrix} + \boldsymbol{M}\left(\boldsymbol{y}_m(k) - \hat{\boldsymbol{y}}(k)\right) \tag{29}$$

$$\begin{bmatrix} \hat{\boldsymbol{x}}(k+1|k) \\ \hat{\boldsymbol{x}}_d(k+1|k) \end{bmatrix} = \begin{bmatrix} \boldsymbol{A}\hat{\boldsymbol{x}}(k|k) + \boldsymbol{B}_u\boldsymbol{u}(k) + \boldsymbol{B}_d\bar{\boldsymbol{C}}\hat{\boldsymbol{x}}_d(k|k) \\ \bar{\boldsymbol{A}}\hat{\boldsymbol{x}}_d(k|k) \end{bmatrix} \tag{30}$$

Here $\hat{\boldsymbol{x}}(k|k-1)$, $\hat{\boldsymbol{x}}_d(k|k-1)$ denote the values of plant states and noise states estimated for time *k* using the values at time *k-1*, respectively. At the current step *k*, the predicted output $\hat{\boldsymbol{y}}(k)$ is calculated using Eq. (28) based on the state estimates $\hat{\boldsymbol{x}}(k|k-1)$, $\hat{\boldsymbol{x}}_d(k|k-1)$ at the previous step *k-1*. Then the observer gain $\boldsymbol{M}$ updates the state estimations $\hat{\boldsymbol{x}}(k|k-1)$, $\hat{\boldsymbol{x}}_d(k|k-1)$ using the new measurement $\boldsymbol{y}_m(k)$ to obtain $\hat{\boldsymbol{x}}(k|k)$ and $\hat{\boldsymbol{x}}_d(k|k)$ in Eq. (29). Finally, a one-step prediction of the states $\hat{\boldsymbol{x}}(k+1|k)$, $\hat{\boldsymbol{x}}_d(k+1|k)$ is formulated in Eq. (30). The steady-state observer gain $\boldsymbol{M}$ in Eq. (29) is designed using the Kalman filtering technique on the following extended model [78]:

$$\begin{gathered} \begin{bmatrix} \boldsymbol{x}(k+1) \\ \boldsymbol{x}_d(k+1) \end{bmatrix} = \begin{bmatrix} \boldsymbol{A} & \boldsymbol{B}_d\bar{\boldsymbol{C}} \\ \boldsymbol{0} & \bar{\boldsymbol{A}} \end{bmatrix} \begin{bmatrix} \boldsymbol{x}(k) \\ \boldsymbol{x}_d(k) \end{bmatrix} + \begin{bmatrix} \boldsymbol{B}_u \\ \boldsymbol{0} \end{bmatrix} \boldsymbol{u}(k) + \begin{bmatrix} \boldsymbol{B}_d\bar{\boldsymbol{D}} & \boldsymbol{0} \\ \bar{\boldsymbol{B}} & \boldsymbol{0} \end{bmatrix} \begin{bmatrix} \boldsymbol{n}_d(k) \\ \boldsymbol{n}(k) \end{bmatrix} \\ \boldsymbol{y}_m(k) = \begin{bmatrix} \boldsymbol{C} & \boldsymbol{D}_d\bar{\boldsymbol{C}} \end{bmatrix} \begin{bmatrix} \boldsymbol{x}(k) \\ \boldsymbol{x}_d(k) \end{bmatrix} + \boldsymbol{D}_u\boldsymbol{u}(k) + \begin{bmatrix} \boldsymbol{D}_d\bar{\boldsymbol{D}} & \boldsymbol{I} \end{bmatrix} \begin{bmatrix} \boldsymbol{n}_d(k) \\ \boldsymbol{n}(k) \end{bmatrix} \end{gathered} \tag{31}$$

which can be concisely written as:

$$\begin{gathered} \boldsymbol{x}_{ext}(k+1) = \boldsymbol{A}_{ext}\boldsymbol{x}_{ext}(k) + \boldsymbol{B}_{ext}\boldsymbol{u}(k) + \boldsymbol{G}_{ext}\boldsymbol{w}(k) \\ \boldsymbol{y}_m(k) = \boldsymbol{C}_{ext}\boldsymbol{x}_{ext}(k) + \boldsymbol{D}_{ext}\boldsymbol{u}(k) + \boldsymbol{H}_{ext}\boldsymbol{w}(k) \end{gathered} \tag{32}$$

where $\boldsymbol{x}_{ext}(k) = \begin{bmatrix} \boldsymbol{x}(k) \\ \boldsymbol{x}_d(k) \end{bmatrix}$, $\boldsymbol{w}(k) = \begin{bmatrix} \boldsymbol{n}_d(k) \\ \boldsymbol{n}(k) \end{bmatrix}$, $\boldsymbol{A}_{ext} = \begin{bmatrix} \boldsymbol{A} & \boldsymbol{B}_d\bar{\boldsymbol{C}} \\ \boldsymbol{0} & \bar{\boldsymbol{A}} \end{bmatrix}$, $\boldsymbol{B}_{ext} = \begin{bmatrix} \boldsymbol{B}_u \\ \boldsymbol{0} \end{bmatrix}$,

$\boldsymbol{G}_{ext} = \begin{bmatrix} \boldsymbol{B}_d\bar{\boldsymbol{D}} & \boldsymbol{0} \\ \bar{\boldsymbol{B}} & \boldsymbol{0} \end{bmatrix}$, $\boldsymbol{C}_{ext} = \begin{bmatrix} \boldsymbol{C} & \boldsymbol{D}_d\bar{\boldsymbol{C}} \end{bmatrix}$, $\boldsymbol{D}_{ext} = \boldsymbol{D}_u$, $\boldsymbol{H}_{ext} = \begin{bmatrix} \boldsymbol{D}_d\bar{\boldsymbol{D}} & \boldsymbol{I} \end{bmatrix}$.

The observer gain $\boldsymbol{M}$ is computed as $\boldsymbol{M} = \boldsymbol{P}\boldsymbol{C}_{ext}^T\left(\boldsymbol{C}_{ext}\boldsymbol{P}\boldsymbol{C}_{ext}^T + \bar{\boldsymbol{R}}\right)^{-1}$, where $\bar{\boldsymbol{R}} = \boldsymbol{R}_n + \boldsymbol{H}_{ext}\boldsymbol{Q}_n\boldsymbol{H}_{ext}^T, \boldsymbol{Q}_n = \boldsymbol{I}$, $\bar{\boldsymbol{Q}} = \boldsymbol{B}_{ext}\boldsymbol{Q}_n\boldsymbol{B}_{ext}^T, \boldsymbol{R}_n = \boldsymbol{I}$, while $\boldsymbol{P}$ is determined by solving a discrete algebraic Riccati (DARE) equation:

$$\boldsymbol{A}_{ext}\boldsymbol{P}\boldsymbol{A}_{ext}^T - \boldsymbol{P} - \boldsymbol{A}_{ext}\boldsymbol{P}\boldsymbol{C}_{ext}^T\left(\boldsymbol{C}_{ext}\boldsymbol{P}\boldsymbol{C}_{ext}^T + \bar{\boldsymbol{R}}\right)^{-1}\boldsymbol{C}_{ext}\boldsymbol{P}\boldsymbol{A}_{ext}^T + \bar{\boldsymbol{Q}} = \boldsymbol{0} \tag{33}$$

We note that the extended system must be at least detectable for the state estimation design to succeed. The extended system (32) is observable if and only if the observability matrix $\boldsymbol{O}(\boldsymbol{A}_{ext}, \boldsymbol{C}_{ext})$ has rank equal to n. Observability of (32) was verified using SVD decomposition of the observability matrix. This analysis revealed that for a tolerance of 5.742×10^{-3} the rank of the observability matrix was 28. Hence, the extended system (32) is unobservable. However, the PBH test, i.e., $rank[\lambda\boldsymbol{I} - \boldsymbol{A}_{ext}; \boldsymbol{C}_{ext}] = n$ for every unstable or marginally stable eigenvalue λ, is satisfied, so the extended system (32) is detectable.

3.1.3 Stability of the MPC design

Stability of the closed-loop system in which MPC is embedded is a major issue especially for inherently unstable systems. The parameters in the MPC formulation (such as prediction horizon, control horizon, sampling time, and system constraints) should be tuned to obtain stability. Furthermore, achieving stability may require a re-estimation of the plant model followed by an online redesign of the controller [75]. The prediction horizon H_p is chosen to ensure that the horizon is not too short to "short-sight" the system dynamics, in which the MPC does not take into account the flight dynamic behavior beyond the prediction horizon. This could put the plant (especially an unstable plant) into such a state that may be impossible to stabilize [75]. For "short-sight" prediction horizons, we obtained simulation results in which the states of the nonlinear system such as body angular velocities become extremely large and one of the control actuators rapidly saturates causing the optimization scheme to be unfeasible in the next horizon. A horizon prediction of 25 time steps (H_pxT_s = 25x0.02 = 0.5 s) was found to be adequate for MPC to achieve a good performance.

Due to its look ahead ability, MPC has had exceptional success in the process control industry where the dynamic performance demanded from the controller is relatively slow. For an available time history of a reference for the output throughout the prediction horizon of several seconds, the controller will compensate for the forthcoming reference variations and hence improve tracking performance. However, in aerospace applications, especially in helicopter ship landings, the reference (such as helideck motion) is not accurately known beforehand due to unpredictable sea states. To solve this problem, the reference throughout the prediction horizon (0.5 s) was generated using a second-order polynomial approximation as follows:

$$r_j(k+i) = r_j(k) + \dot{r}_j(k)T_s i + \frac{1}{2}\ddot{r}_j(k)\left(T_s i\right)^2,\ i = 1,2,\ldots,H_p \tag{34}$$

where $r_j(k), \dot{r}_j(k), \ddot{r}_j(k)$ are magnitude, rate of change, and acceleration of the j^{th} coordinate of the landing deck at the current time. These values are numerically generated using the ship model in Eq. (14) at each current time step. In the landing maneuver, the reference ***r*** is composed of a time series of the heading angle and Cartesian coordinates of the landing deck in the NED frame throughout the prediction horizon. The horizon 0.5 s is a short time so that the reference approximation does not diverge dramatically from the actual landing deck motion generated by ship motion simulation in Section 2.4. This approximation guarantees that the prediction capability of MPC is not degraded due to the lack of future reference information. The following subsections present numerical simulations of the automatic shipboard operations using MPC in the presence of the ship airwake and rough seas.

3.2 Simulation of the Automatic Deck Landing with the CETI Airwake Model

In this section, the nonlinear dynamic model of the helicopter described in Section 2.1, the ship model described in Section 2.4, the CETI model of the ship airwake reproduced from [9], and the MPC design presented above are combined together to develop a helicopter/ship dynamic interface for automatic landing. A landing gear deck contact model is not used in this simulation. Mission task elements (MTEs) for the MPC evaluation are summarized as follows: a) maintain the hover condition at 3m above the landing deck, b) wait for a quiescent period of the ship motion, c) land on the deck with nearly zero touchdown velocity. Besides the prediction horizon H_p = 25 and the sampling time T_s = 0.02 s, the control horizon H_u and the weights $\boldsymbol{w}^y, \boldsymbol{w}^u, \boldsymbol{w}^{\Delta u}$ in the performance measure (23) are important design parameters for the stability and performance of MPC. The control horizon was selected as $H_u = 2$.

To perform deck tracking, firstly, the controlled output weights corresponding to helicopter's flight path coordinates (x_N, y_E, z_D) and heading angle ψ_H must be specified in the performance measure (23). The flight path is influenced by the rotor thrust vector whose orientation is heavily impacted by the longitudinal/lateral cyclic pitch inputs. These controls also influence the helicopter attitude, so we should assign non-zero weights on the attitude variables (Φ_H, θ_H) in Eq. (23) to coordinate the translational-rotational motions. Furthermore, the velocity weights effectively contribute to the system damping to avoid harsh, oscillatory motions of the helicopter, and to enhance soft touchdown (nearly zero translational velocities). Following this rationale, we select $\boldsymbol{w}^y$ = [50, 50, 10, 0, 0, 0, 1, 2, 1, 5, 7, 1]$^{\mathrm{T}}$, $\boldsymbol{w}^u$= [1, 1, 1, 1]$^{\mathrm{T}}$, $\boldsymbol{w}^{\Delta u}$= [1, 1, 1, 1]$^{\mathrm{T}}$, for $\boldsymbol{y} = \left[u, v, w, p, q, r, \Phi_H, \theta_H, \psi_H, x_N, y_E, z_D\right]^T$. These values are very effective in our MPC design. The MPC is designed using the helicopter model augmented with a CETI airwake model described in Section 2.1.1. Then the design is evaluated when different CETI data series are included. Moreover, the design is also evaluated in the benign condition when the ship airwake is absent. The weights $\boldsymbol{w}^y, \boldsymbol{w}^u, \boldsymbol{w}^{\Delta u}$ are selected to ensure good performance and disturbance rejection in the presence of the airwake. Turbulence intensity of 3 m/s and mean wind speed of 15 m/s are chosen for the CETI model of the ship airwake in Fig. 13. The origin of the inertial NED frame is located at the initial position of the ship's center of mass. The landing deck's coordinates (x_D, y_D, z_D) are -72 m longitudinal, 0 m lateral, and -5 m vertical with respect to the origin, respectively. The ship operates in sea state 5 and 150-deg heading wave. The output reference $\boldsymbol{r}$ in (23) is $\boldsymbol{r} = \left[u_{trim}, v_{trim}, w_{trim}, p_{trim}, q_{trim}, r_{trim}, \Phi_{H_{trim}}, \theta_{H_{trim}}, \psi_{H_{trim}}, x_{N_{trim}}, y_{E_{trim}}, z_{D_{trim}}\right]^T$ for the first several seconds when the helicopter hovers above the landing deck, and $\boldsymbol{r} = \left[\psi_S, x_d, y_d, z_d\right]^T$ when the helicopter initiates the landing maneuver. The subscript *trim* denotes the trim value of the corresponding variable of the helicopter at hover.

Some explanatory notes regarding the simulations shown in Fig. 19-21 are given: **Trim** means the value at trim condition, **Heli. w/ AWK** or **Heli. w/o AWK** mean the nonlinear helicopter model including the ship airwake model or not, **Deck motion** means the deck motion simulation, **Constraints** means the input saturations. Fig. 19 shows that the helicopter is first maintained in a hover condition above the deck for 10 seconds waiting for a quiescent period in the ship motion. At Time=40 s, the helicopter initiates the landing maneuver and ends with a soft touchdown (surge velocity less than 0.1 knots, sway velocity less than 0.1 knots, heave velocity less than 1.1 knots) at Time=43 s. Recall that the helicopter only tracks the moving deck after Time=40 s. The ADS-33E-PRF specifications [77] require the helicopter to land gently, with a smooth descent with no objectionable oscillations, complete landing within 10 seconds once the altitude is below 10 ft (i.e., 3.048 m), touch down within ±1 ft (i.e., ±0.304 m) longitudinally, ±0.5 ft (i.e., ±0.152 m) laterally of the designated reference point, and attain a heading at touchdown that is aligned with the reference heading within ±5 deg. It can be seen in Fig. 19 that the landing maneuver, with and without the ship airwake, satisfies the ADS-33E-PRF specifications. From the helicopter's altitude of 3 m relative to the deck at Time=40 seconds, the MPC accomplishes a gentle landing without objectionable oscillations within 3 seconds. The touchdown point is within ±0.1 meters longitudinally and ± 0.1 meters laterally on the deck. The helicopter's heading at touchdown is aligned with the ship's longitudinal axis within ±2 deg. However, when the ship airwake model is included, the autopilot workload is higher than when the ship airwake is ignored, as illustrated in Fig. 19.

Fig. 19-21 show that MPC can handle the system constraints and external disturbances, and track the moving deck for safe landing simultaneously. The linear model (24) around the trim condition (hover) was employed as the internal model for MPC design in these simulations. The helicopter trajectory was solved for to optimize the MPC performance measure (23) subject to the system constraints (25). Fig. 21 shows the time histories of the flapping and lead-lagging states of the main rotor. The fuselage and main rotor states display only small oscillations during the landing maneuver in the presence of the ship airwake. We remark that the blade differential coning angles are zero throughout the maneuver. A possible explanation is that the landing maneuver investigated here assumes a uniform flow distribution over the rotor disc. As seen shortly, in the lateral repositioning maneuver the CFD model distributes the spatial velocity gradient of the ship’s airwake over the rotor disk resulting in an asymmetric aerodynamic loading of the rotor, which leads to small variations in the blade differential coning angles.

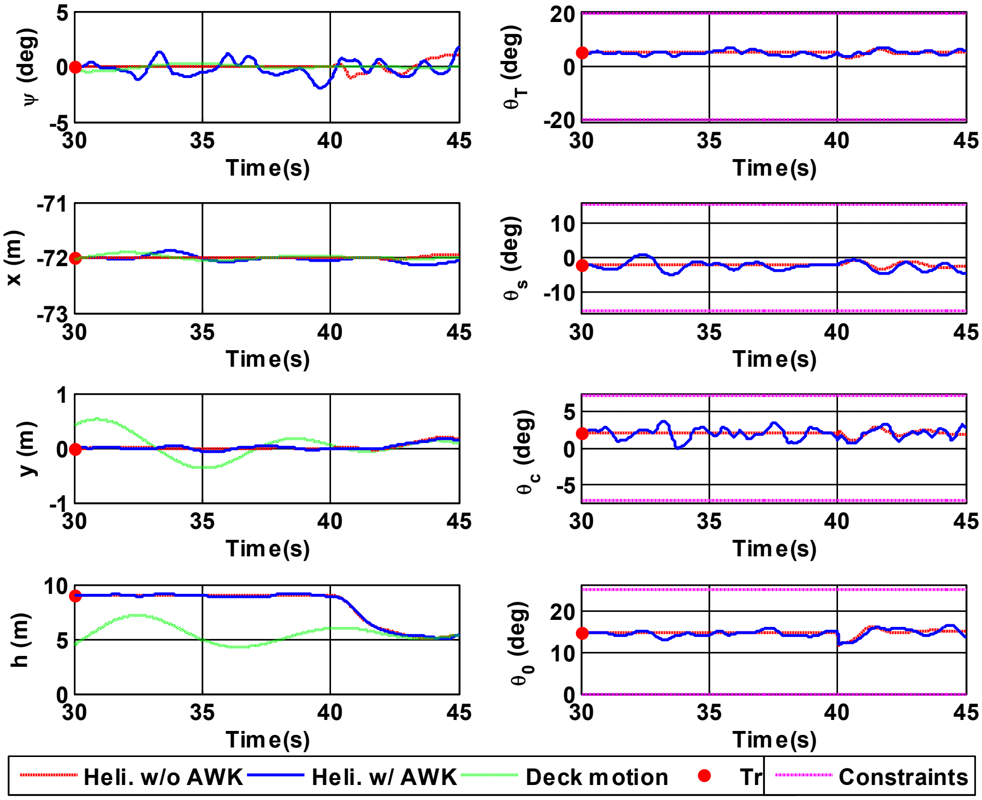

Fig. 19 Heading angle, position and control time histories of the helicopter during the landing maneuver

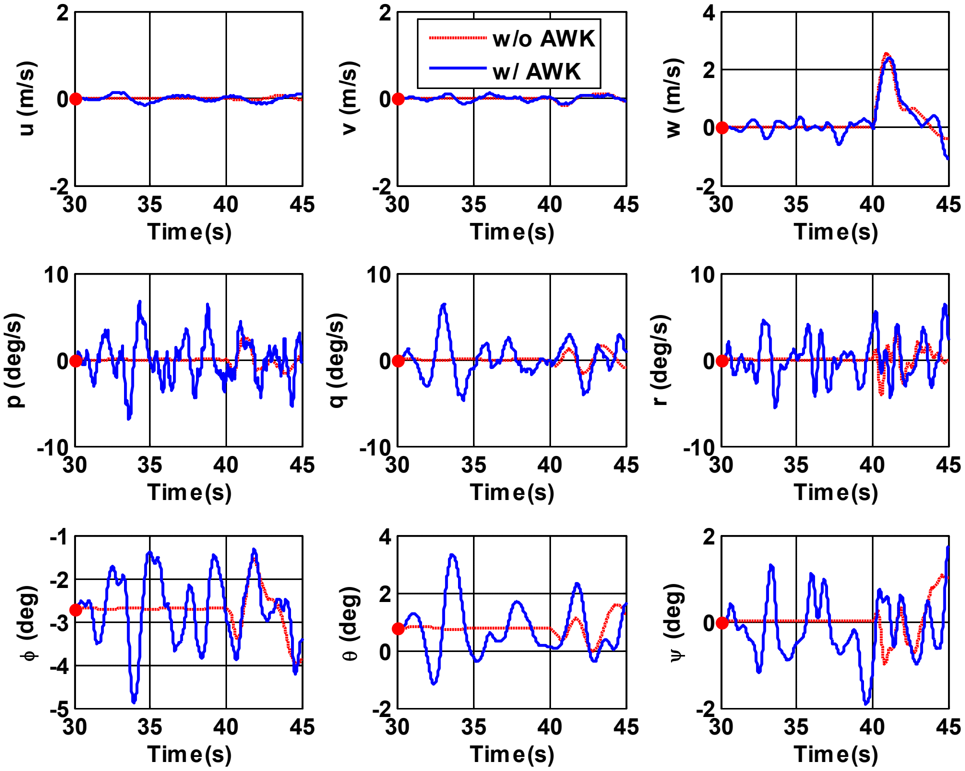

Fig. 20 Fuselage state responses of the helicopter during the landing maneuver

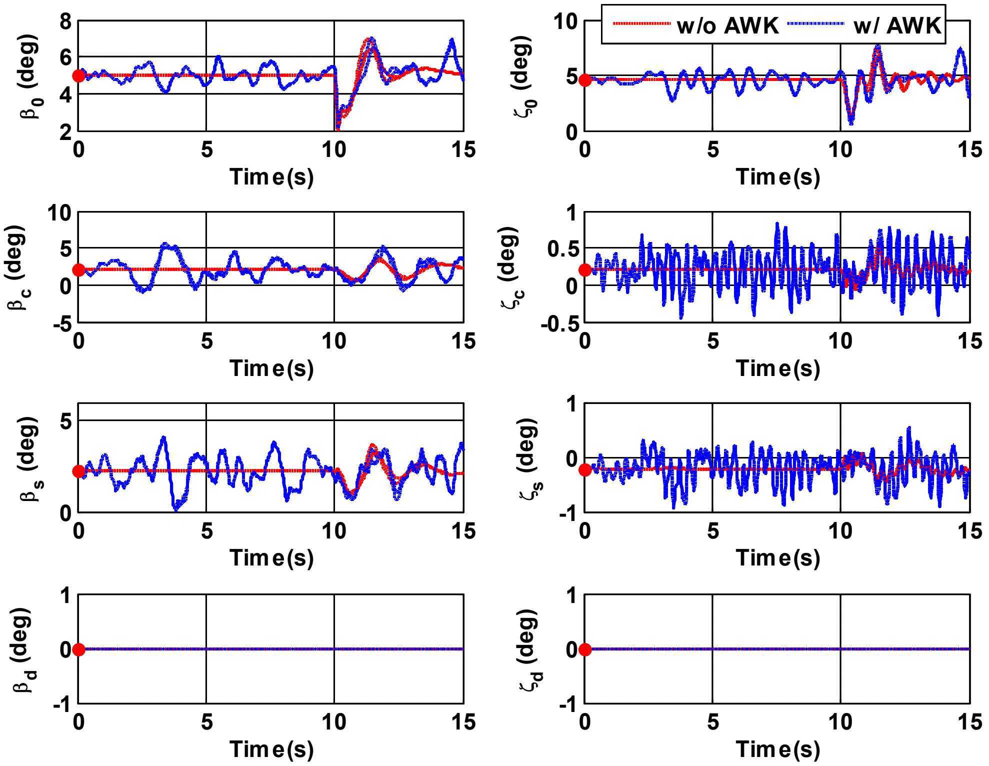

Fig. 21 Time history of the flapping, lead-lagging states of the main rotor

3.3 Simulation of the Automatic Lateral Reposition with the CFD Airwake Data

In shipboard landing, the pilot is required to bring the helicopter to hover alongside the ship, perform a lateral reposition toward and land onto the deck [63]. In this dissertation, lateral reposition is automatically accomplished using MPC, designed using a model that includes the ship airwake model.

We first remark that, when attempting to use the same controller's parameters as in the previous design and simulations (i.e. subsection 3.2), the performance of the MPC during the lateral reposition maneuver was not sufficiently good, i.e., the system did not satisfy ADS-33-PRF specifications. The fact that the controller which performed well in the previous simulations does not perform as well in the lateral reposition maneuver can be explained by the fact that the lateral reposition maneuver is totally different from the landing maneuver. Also, for the landing maneuver a CETI model is used, whereas for the lateral repositioning a CFD based model is used. Lastly, note that the ADS-33-PRF desired specifications are also different. Therefore, we modified the weights in MPC design until these specifications were met. We report here the results obtained for the following weights, $\boldsymbol{w}^{y}$ = [90, 40, 90, 0, 0, 0, 1, 2, 2, 3, 2, 1]^{T}, which resulted in very good performance. The resulting controller is applied to the nonlinear helicopter dynamics model augmented with the CFD airwake model in Eq. (20). The reference vector $\boldsymbol{r}$ in (23) is $\boldsymbol{r} = \left[\psi_S, x_d, y_d, z_d\right]^T$. MPC simulations are performed for three scenarios: 1) The helicopter operates in the absence of the ship airwake; 2) The helicopter operates in the 30-deg WOD condition with the uniform airwake velocity distribution over the main rotor disk; 3) The helicopter operates in the 30-deg WOD condition (Fig. 15) with spatial velocity gradient distribution over the main rotor disk. The free stream velocity magnitude is 15 m/s in these simulations. The linear model (24) around the trim condition at hover was employed as the internal model for MPC design.

3.3.1 Lateral reposition in the headwind WOD

In Fig. 22-25, from the stabilized hover off 20 meters portside of the ship, the helicopter endowed with MPC initiates a lateral translation toward the landing deck at Time=5 sec. Fig. 22 gives the time histories of the heading & position deviations, and control inputs of the helicopter during the landing maneuver. We see that even though the altitude is maintained with a slight reduction of 0.07 m in the headwind compared to the situation when the airwake model is not included, the collective pitch control is increased during the maneuver. This simulation result agrees with the headwind thrust deficit phenomenon reported in the literature.

Remark that Fig. 23 illustrates exceptional performance of the closed-loop system to close the 20 meters gap between the initial position of the helicopter and the landing deck. The helicopter maintains altitude within ±0.2 meters, maintains heading within -10 to 1 deg, accomplishes acceleration and deceleration phases in single smooth maneuvers to reach the flight deck during the deceleration, and terminates in a hover condition. This satisfies the ADS-33E-PRF desired performance for lateral reposition specified in [77] in which the helicopter is required to maintain longitudinal track within ±10 feet (i.e., ±3.048 meters), altitude within ±10 feet (i.e., ±3.048 meters), heading within ±10 deg, and complete the maneuver within 18 seconds. From Fig. 22-24, we can see that severe spatial velocity gradients of the ship airwake can increase the control workload to accomplish the mission, as well as the rotor blade loading and oscillations.

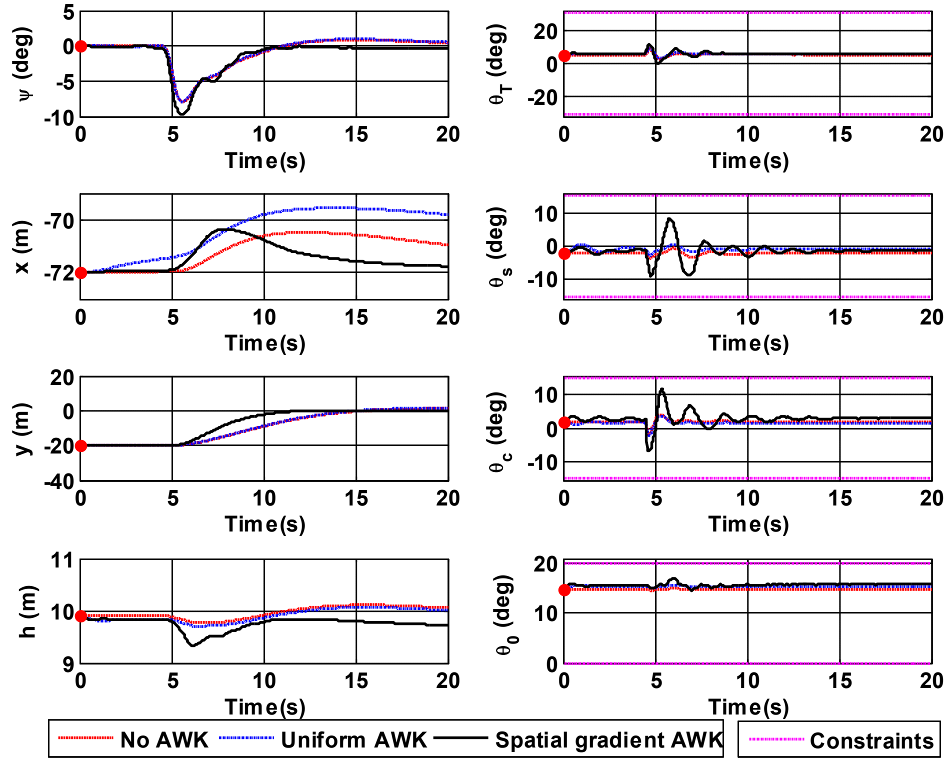

Fig. 22 Time history of the heading angle, position and controls during the lateral reposition in the headwind WOD

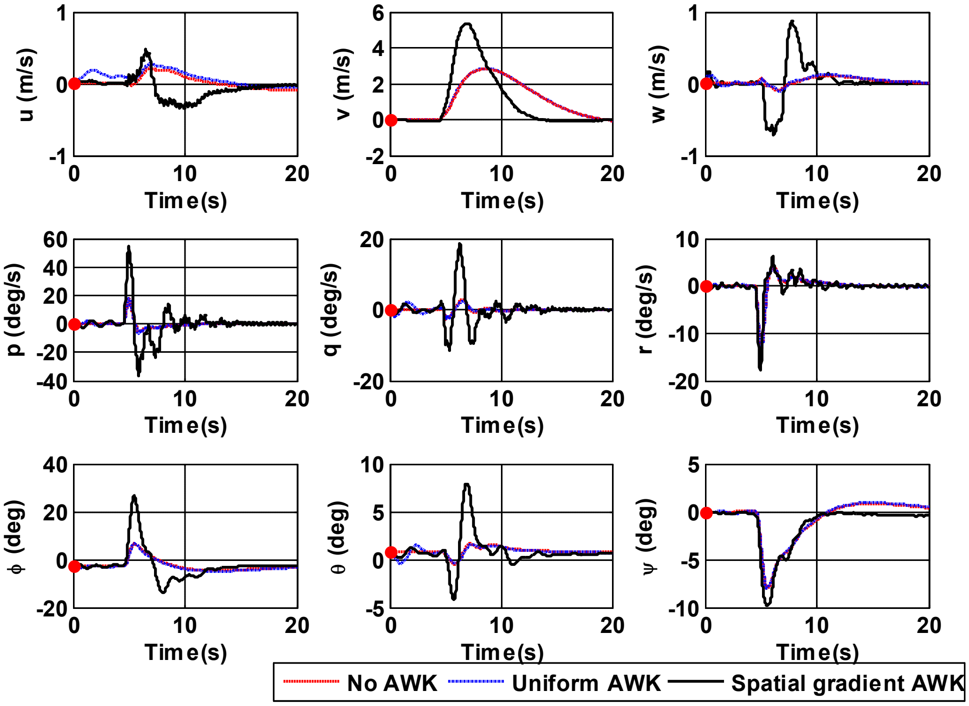

Fig. 23 Fuselage state responses of the helicopter during the lateral reposition in the headwind WOD

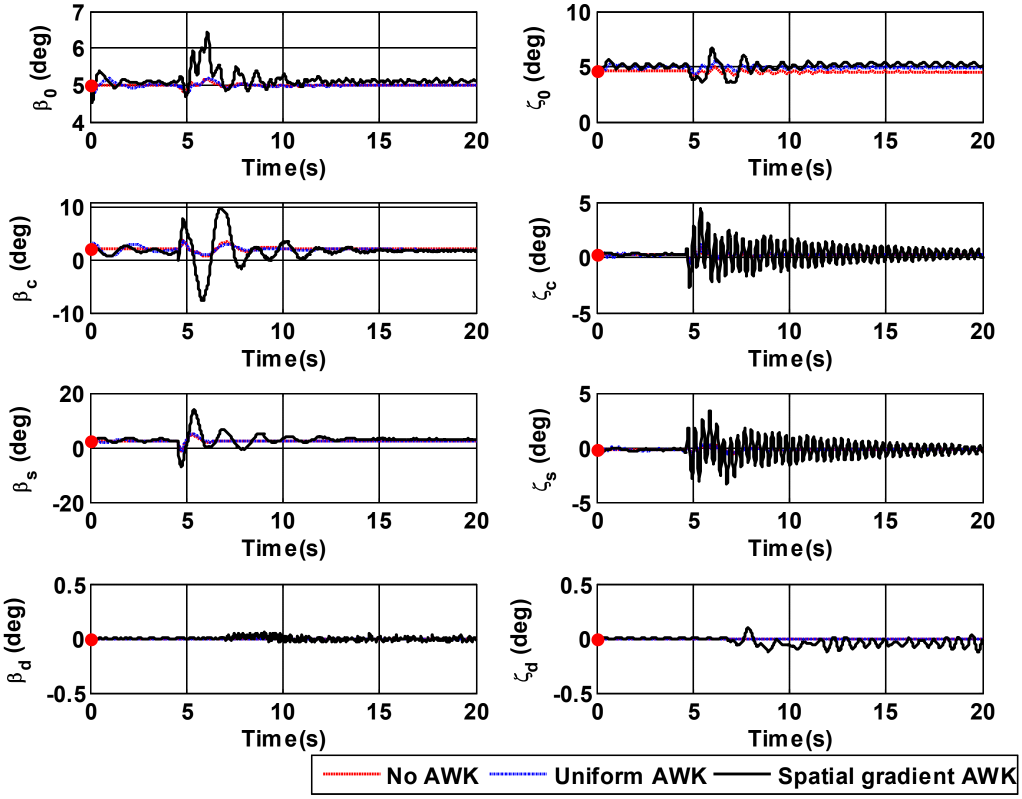

Fig. 24 Time history of the flapping, lead-lagging states of the main rotor during lateral reposition in the headwind WOD

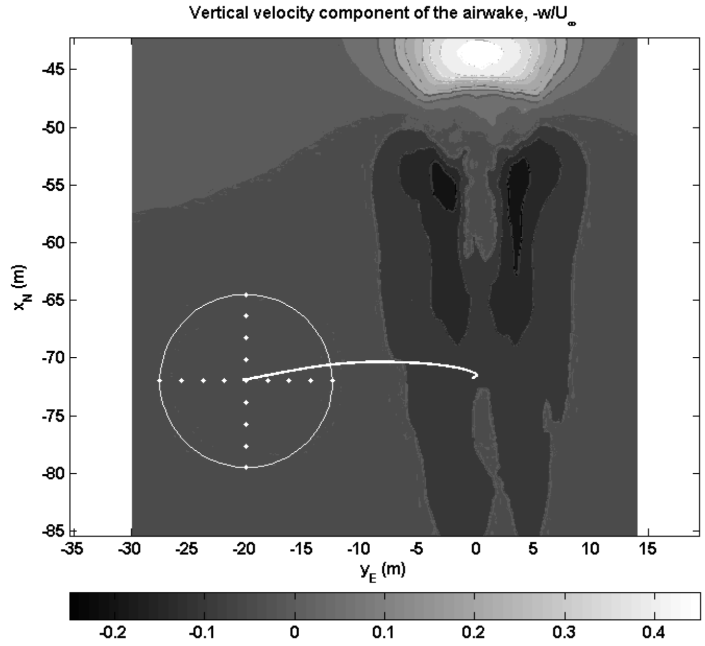

Fig. 25 Flight trajectory of the helicopter during lateral reposition in the headwind WOD

3.3.2 Lateral reposition in the 30-deg WOD

Fig. 26-29 show that from a stabilized hover position 20 meters portside of the ship, the helicopter initiates a lateral reposition maneuver toward the landing deck at Time=5 seconds. There is a minor loss (less than 0.7 meters) in altitude that is compensated for by increasing the collective input in all three scenarios. The helicopter regains the initial altitude as it arrives over the deck. In the time span 6-8 seconds, the lateral cyclic pitch control θ_c produces a positive rolling moment to increase the sideslip velocity toward the landing deck in order to compensate for the pressure wall effect when the helicopter moves into the area of most significant airwake disturbance (see Fig. 15). This behavior of the lateral cyclic control is not observed in the case with the uniform velocity in the airwake over the rotor disk (see Fig. 26). There needs a greater degree of control workload for the deck landing in 30-deg WOD than for the headwind case (see Fig. 22). These results agree with the 30-deg pressure wall phenomenon reported in the literature [3]. In the lateral reposition maneuver, at Time=7.6 seconds, the helicopter has a longitudinal deviation of magnitude about 1.3 meters from the landing deck position due to its roll-to-pitch cross-coupling characteristic. Fig. 26 shows the time history of the longitudinal cyclic pitch control to maintain the desired flight path toward the landing deck. Fig. 27 also shows that all other helicopter fuselage states are well behaved during the maneuver.

Severe spatial velocity gradients of the ship airwake can increase the control workload to accomplish the mission, as well as the rotor blade loading and oscillations. Fig. 28 shows high-frequency flapping and lead-lagging motions of the main rotor due to the effects of the non-uniform airwake over the rotor disk. This is expected because the states of the main rotor are not measurable outputs available for control design. Inclusion of a state observer for the rotor state and/or active rotor blade control may be promising solutions to mitigate these oscillations. We also notice that severe spatial velocity gradients induce differential coning flapping and lead-lagging motions (β_d , ς_d) with relatively small magnitudes of 0.3 deg. These motions do not exist in the case with uniform airwake over the rotor disk.

All simulations in Fig. 26-29 illustrate exceptional performance of the closed-loop system to close the 20 meters gap between the initial position of the helicopter and the landing deck. The helicopter maintains altitude within ±0.3 meters, maintains heading within -8 to 1 deg, accomplishes acceleration and deceleration phases in single smooth maneuvers to reach the flight deck during the deceleration, and terminates in a hover condition. This satisfies the ADS-33E-PRF desired performance for lateral reposition specified in [77] in which the helicopter is required to maintain longitudinal track within ±10 feet (i.e., ±3.048 meters), altitude within ±10 feet (i.e., ±3.048 meters), heading within ±10 deg, and complete the maneuver within 18 seconds.

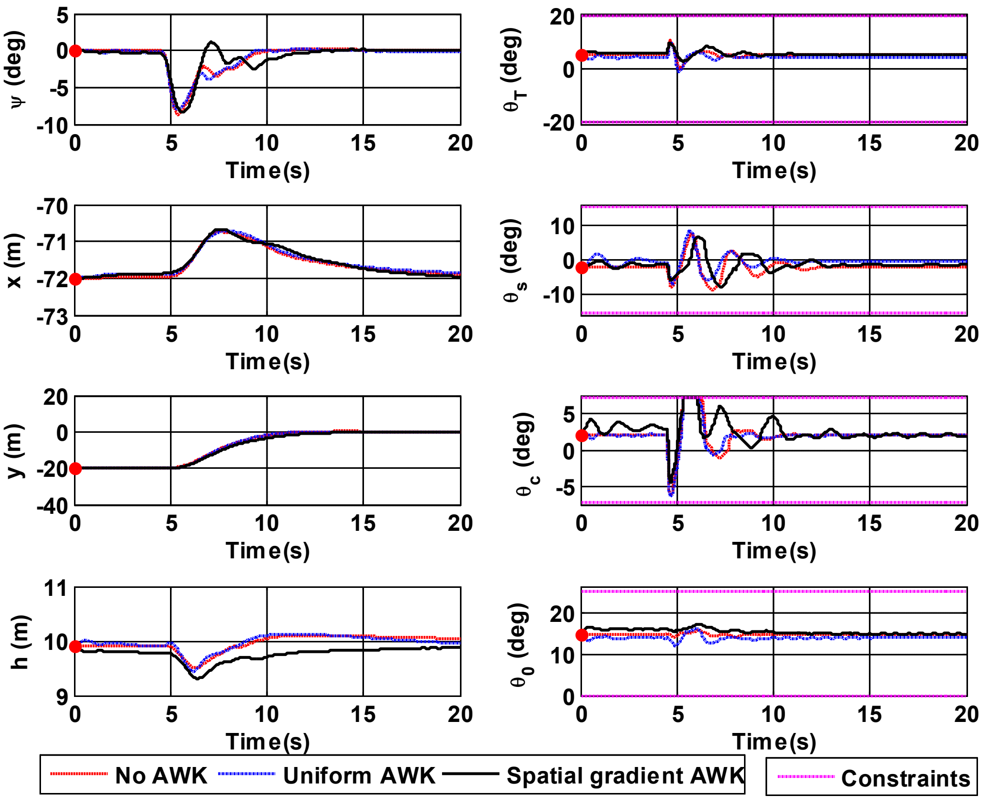

Fig. 26 Time history of the heading angle, position and controls during the lateral reposition in the 30-deg WOD

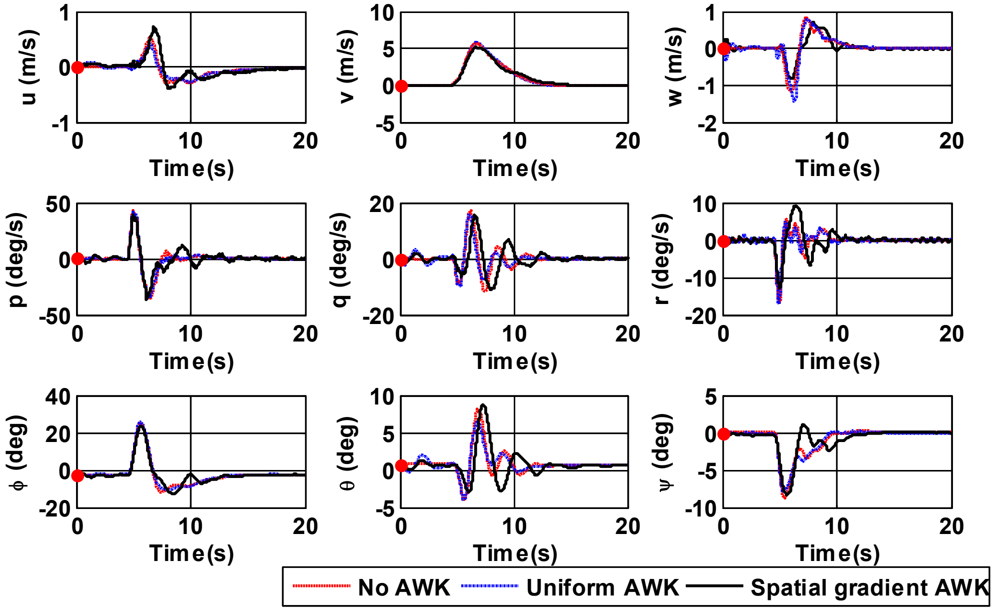

Fig. 27 Fuselage state responses of the helicopter during the lateral reposition in the 30-deg WOD

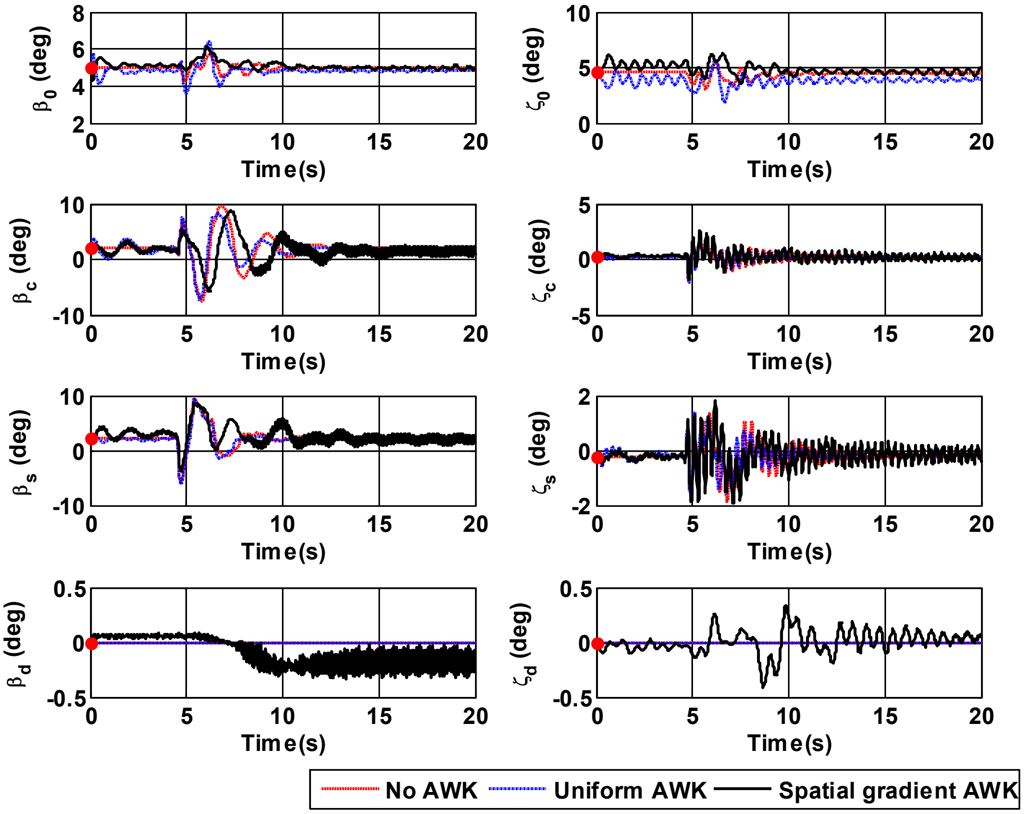

Fig. 28 Time history of the flapping, lead-lagging states of the main rotor during lateral reposition in the 30-deg WOD

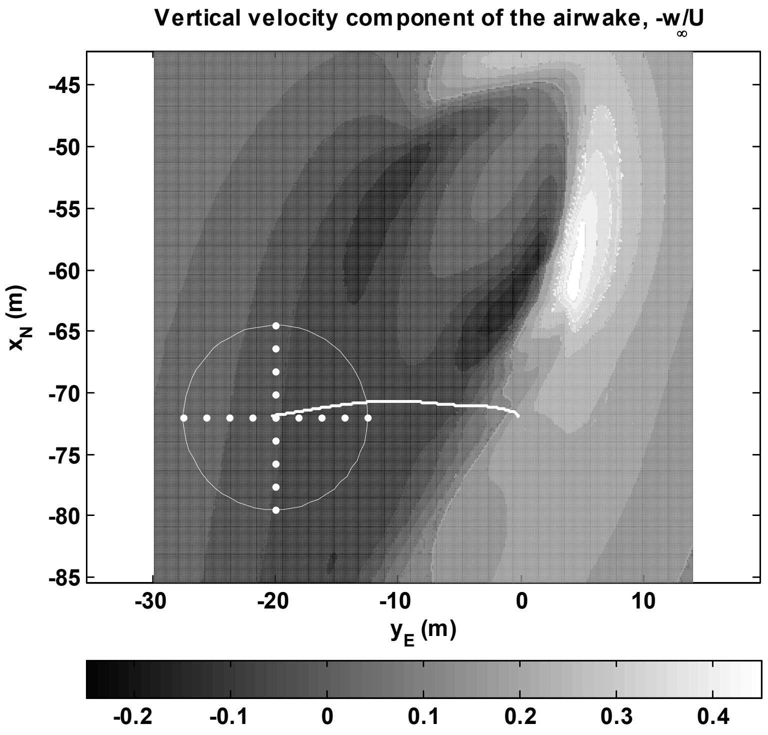

Fig. 29 Flight trajectory of the helicopter during lateral reposition in the 30-deg WOD

Lastly, by exposing the helicopter to the non-uniform ship airwake, the MPC design can be evaluated not only with respect to its disturbance rejection capability but also with respect to system constraint handling. From Fig. 26, we can see that even though the lateral cyclic pitch control was saturated within the time span 5 - 7 seconds (i.e., this control reached the dashed line value), MPC performs a smooth translation towards the flight deck within 5 seconds.

3.4 Internal Model Updating Scheme of MPC

The critical ingredient for MPC design is the dynamical model of the system to be controlled (e.g., the helicopter). The helicopter is a complex dynamic system mathematically described by nonlinear equations that are highly coupled. Therefore, the linear model (24) may not be able to predict accurately the dynamic behavior of the system when the helicopter wanders off the trim condition about which the nonlinear system (11) is linearized. To improve the prediction capability of MPC, the nonlinear model (11) should be used directly as the internal model. However, this results in significant computational difficulties. Therefore, we also develop an MPC design process with a model-updating scheme, which can be more practical for helicopter shipboard operations. This idea is conceptually captured in Fig. 30. In this scheme, the nonlinear model (11) is linearized around the operating points on the flight trajectory to obtain linearized models. This process provides linear approximations of the nonlinear helicopter dynamics in the neighborhood of the operating points. Matrices $\boldsymbol{A}_p$, $\boldsymbol{B}_p$ in Eq. (12) are obtained from Eq. (13) using the current values of the states $\boldsymbol{x}$ and inputs $\boldsymbol{u}$, which are $\boldsymbol{x} = \boldsymbol{x}(t_c)$, $\boldsymbol{u} = \boldsymbol{u}(t_c)$, with t_c being the current time. As not all states of the system are measureable, the estimates obtained from the same state observer described in Section 3.1.2 are used in the linearization process.

An important feature of the updating scheme is the frequency with which model updating via linearization is performed. This frequency depends on the various flight regimes the helicopter exhibits during shipboard operations. There are two different ways to choose the updating frequency. The first one requires updating the internal model only if the perturbations in states of the system are far from their values at the operating point. The second one requires updating the internal model periodically with a period of several seconds. In this dissertation, the latter is selected because it ensures that the internal model in MPC remains valid throughout the shipboard operations. The main drawback of the latter approach may be high computational cost with respect to the former.

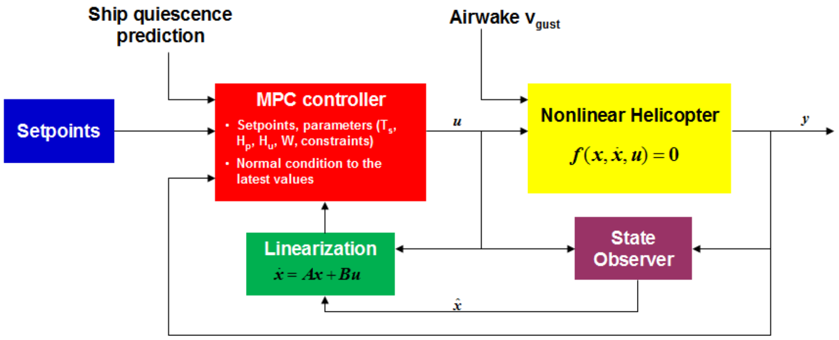

Fig. 30 MPC diagram with the internal model updated along the operating points

Comparisons between MPC performances with and without the model-updating scheme applied to the automatic deck landing in the CETI airwake are illustrated in Fig. 31-33. In these simulations, the model is updated every $1\times T_s$ seconds. When model updating is used in MPC design, a smoother landing on the deck is achieved compared to the situation when the model is not updated. We note that the helicopter only tracks the ship deck during the quiescent period of the ship motion, i.e., after Time = 40 seconds. Moreover, Fig. 32-33 show that a remarkable reduction in the fuselage state perturbations and main rotor flapping oscillations due to the ship airwake effect are achieved by using the model-updating scheme with respect to the situation when model updating is not used (see Fig. 20).

One major disadvantage of the model-updating scheme is the computational cost if the model is updated too frequently. To alleviate this disadvantage one may try to decrease the model updating frequency. However, our experience indicates that when the updating frequency is significantly decreased (e.g., updates happen every $5\times T_s$), the system's stability deteriorates rapidly. This is because detectability is not guaranteed for the extended model in Eq. (32) at the operating points. This issue could be investigated in future work.

Shipboard operations and landing regardless of ship quiescence prediction should be explored. Ensuring safe landing in non-quiescent conditions will result in significant reductions in maneuver time and fuel consumption. Clearly, the problem of autonomous landing in general non-quiescent conditions will require satisfaction of rapidly changing constraints dictated primarily by the ship motion and sea state. Landing procedures different than the standard one, used for landing in quiescent conditions, as well as alternative control problem formulations will be investigated in the next Chapter to determine the extent to which ship quiescence prediction can be ignored in the landing decision process.

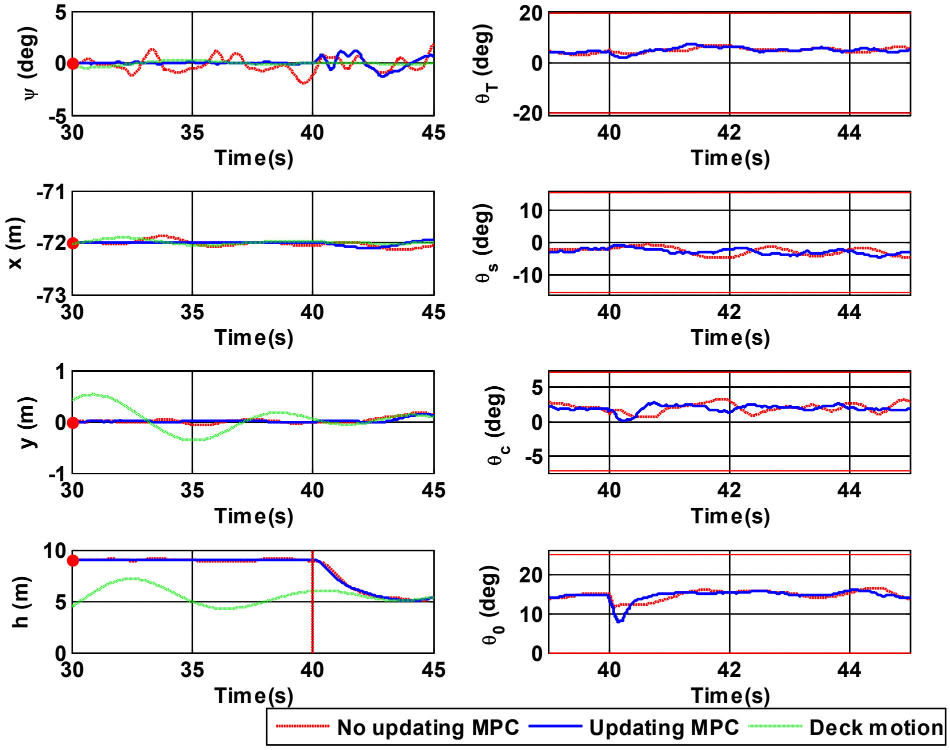

Fig. 31 Heading angle, position and control time histories of the helicopter

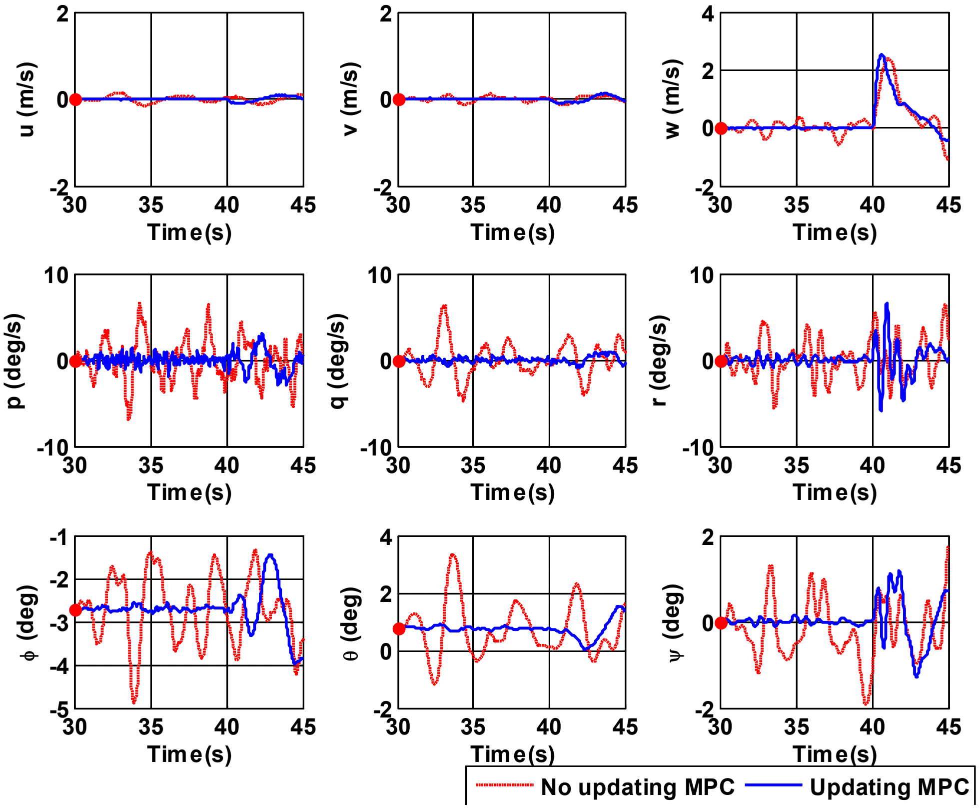

Fig. 32 Fuselage state responses of the helicopter during the landing maneuver

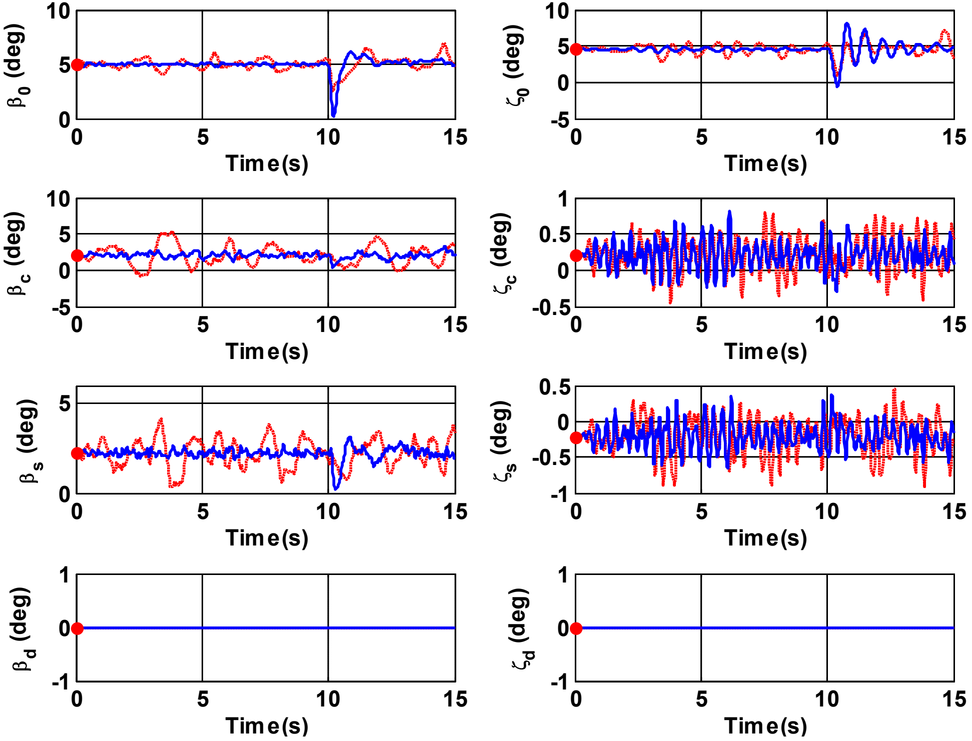

Fig. 33 Time history of the flapping, lead-lagging states of the main rotor during landing maneuver

Chapter 4: Mixed Integer MPC for Shipboard Precision Landing

4.1 Landing in High Energy Index Conditions

It is often desired that the landing maneuver is executed in high demanding sea-based conditions. Landing in such a scenario is particularly difficult due to limitations on the flight safety and on the capability to rapidly perform multiple mission task elements. In the first phase, during the flight path control to bring the helicopter close to the ship, it is reasonable to assume that the helicopter can precisely track only the position and heading angle of the ship using 4 primary control inputs, but it is not reasonable to request that difficult approach-and-land maneuvers are simultaneously executed. For example, the helicopter cannot perform simultaneously a lateral reposition to the right and a bank maneuver to the left in the slope landing. The helicopter must execute coordinated movements to achieve desired attitude, position, and velocities (see Fig. 34).

To deal with these difficulties, shipboard landing on moving decks is proposed to be accomplished by a sequential control process called flight path control and rendezvous control. First, the helicopter is brought closer to the flight deck by a flight path controller in the approaching phase. Second, the helicopter performs coordinated movements to align its attitude, position, and velocities with those of the landing deck in the phase of rendezvous. If underestimated/unexpected deck motions occur which prevent safe landing, the helicopter can rapidly abort the mission. Ideally, all flight phases (approaching, rendezvous, and abort) must satisfy ship-helicopter operating limits and ADS-33-PRF specifications for the landing maneuver [77]. Moreover, safety considerations such as flight envelope protection and control authority need to be considered.

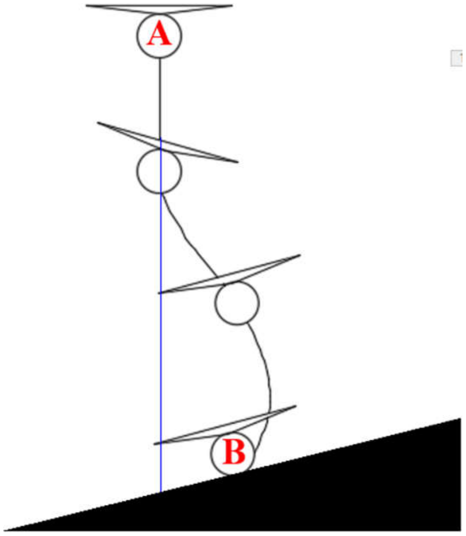

Fig. 34 Slope landing

4.2 Rendezvous Controller

4.2.1 Mixed Integer Model Predictive Control

A moving deck is a time-varying target whose attitude, position, and velocities cannot, in general, be simultaneously tracked through a fixed prediction horizon via standard MPC. However, if the prediction horizon is not fixed but determined by how long before the helicopter-ship rendezvous takes place from each current information of the deck motion, tracking a moving deck via MPC becomes possible. This approach is inspired by the manner in which human pilots operate. Practically they make instantaneous estimations of the time horizon over which their actions will be effective.

To enable the variable prediction horizon, a binary variable is introduced as a decision variable in the optimization problem in Section 3.1.1. This additional variable determines the right time at which rendezvous conditions for the helicopter-ship attitude, position, and velocities are satisfied. This powerful optimization framework, which includes both integer variables for decision making and continuous variables for optimal trajectory finding, is mathematically challenging. The description of the optimization problem is given next.

At a given time step k, the problem of receding horizon motion planning can be formulated in the form of mixed integer quadratic programming. The optimal flight trajectory $\boldsymbol{x}$(t), control input $\boldsymbol{u}$(t), and the variable horizon N* are obtained by minimizing the R-weighted control energy and the arrival time:

$$\underset{\boldsymbol{x},\boldsymbol{u},N^*}{minimize}\ J(k)=\sum_{j=1}^{H_p} ja(j)\quad+\quad\sum_{j=1}^{H_p}\left\|\boldsymbol{u}(k+j-1\,|\,k)\right\|_{\boldsymbol{R}}^{2} \tag{35}$$

subject to

- System dynamics

$$\boldsymbol{x}(k+j\,|\,k)=\boldsymbol{A}\boldsymbol{x}(k+j-1\,|\,k)+\boldsymbol{B}\boldsymbol{u}(k+j-1\,|\,k),\ j=1,\ldots,N_f \tag{36}$$

- Initial condition

$$\boldsymbol{x}(k\,|\,k)=\boldsymbol{x}_0(k) \tag{37}$$

- Input and output constraints

$$\begin{aligned}
&\left[0,-7,-15,-20\right]\le\left[\theta_0,\theta_c,\theta_s,\theta_T\right]\le\left[25,7,15,20\right]\ \text{deg}\\
&\rightarrow \textit{input saturation}\\
&\left[\left|\theta_0(i+1)-\theta_0(i)\right|,\left|\theta_c(i+1)-\theta_c(i)\right|,\left|\theta_s(i+1)-\theta_s(i)\right|,\left|\theta_T(i+1)-\theta_T(i)\right|\right]\\
&\qquad\le\left[40,40,40,40\right]\ \text{deg}/\,s\times T_s\\
&\rightarrow \textit{slew rates}\\
&-30\le\theta_H\le 20\,\text{deg},\left|\Phi_H\right|\le 60\,\text{deg},\ \left[\left|p\right|,\left|q\right|,\left|r\right|\right]\le\left[50,13,22\right]\text{deg}/\,s,\ w\le 3m/s\\
&\rightarrow \textit{output saturation}
\end{aligned} \tag{38}$$

- Rendezvous condition

$$\sum_{j=1}^{H_p}a(j)=1,\ \ a(j)\in\{0,1\} \tag{39}$$

$$\begin{aligned}
T_{DG}\boldsymbol{r}_{heli}(k+j\,|\,k)&\le\ \ T_{DG}\boldsymbol{r}_{deck}(k+j\,|\,k)+\boldsymbol{r}_{tol}+M(1-a(j))\boldsymbol{I}_{3\times1}\\
-T_{DG}\boldsymbol{r}_{heli}(k+j\,|\,k)&\le -T_{DG}\boldsymbol{r}_{deck}(k+j\,|\,k)+\boldsymbol{r}_{tol}+M(1-a(j))\boldsymbol{I}_{3\times1}\\
\boldsymbol{\Theta}_{heli}(k+j\,|\,k)&\le\ \ \boldsymbol{\Theta}_{deck}(k+j\,|\,k)+\boldsymbol{\Theta}_{tol}+M(1-a(j))\boldsymbol{I}_{3\times1}\\
-\boldsymbol{\Theta}_{heli}(k+j\,|\,k)&\le -\boldsymbol{\Theta}_{deck}(k+j\,|\,k)+\boldsymbol{\Theta}_{tol}+M(1-a(j))\boldsymbol{I}_{3\times1}\\
\boldsymbol{\vartheta}_{heli}(k+j\,|\,k)&\le\ \ \boldsymbol{\vartheta}_{deck}+\boldsymbol{\vartheta}_{tol}+M(1-a(j))\boldsymbol{I}_{3\times1}\\
-\boldsymbol{\vartheta}_{heli}(k+j\,|\,k)&\le -\boldsymbol{\vartheta}_{deck}+\boldsymbol{\vartheta}_{tol}+M(1-a(j))\boldsymbol{I}_{3\times1}\\
\boldsymbol{r}_{heli}&=[x,y,z]^T,\ \boldsymbol{r}_{tol}=[x_{tol},y_{tol},z_{tol}]^T\\
\boldsymbol{\Theta}_{heli}&=[\phi,\theta,\psi]^T,\boldsymbol{\Theta}_{tol}=[\phi_{tol},\theta_{tol},\psi_{tol}]^T,\\
\boldsymbol{\vartheta}_{heli}&=[w,p,q]^T,\boldsymbol{\vartheta}_{tol}=[w_{tol},p_{tol},q_{tol}]^T,j=1,\ldots,N_f
\end{aligned} \tag{40}$$

- Collision avoidance

$$\begin{aligned}&a_p(k+j)(x_N(k+i\,|\,k)-x_{deck}(k+j\,|\,k))+b_p(k+j)(y_E(k+i\,|\,k)\\&-y_{deck}(k+j\,|\,k))+c_p(k+j)(z_D(k+i\,|\,k)-z_{deck}(k+j\,|\,k))<M(1-a(i)) \qquad (41)\\&(i=1,\ldots,j,\quad j=1,\ldots,N_f)\end{aligned}$$

The first and second terms in the performance measure (35) ensure minimization of the time and control effort required to land the helicopter on the moving deck. When the rate of descent exceeds the normal downward induced inflow rate of the inner blade sections, the inflow is upward relative to the disk. Then, a secondary vortex is produced in addition to the normal tip vortices. Consequently, unsteady turbulent flow over a large area of the rotor disk is developed and the rotor efficiency is substantially diminished [80]. Therefore, the rate of descend, *w*, during landing must be limited in (38). This constraint is in addition to the input saturation, the slew rates, and the output saturation constraints in (25). For the results presented in this dissertation an upper limit of 3 m/s on the rate of descent *w* was found sufficient to achieve satisfactory landing.

The equality constraint (39) ensures that there exists an *N**-th step at which the rendezvous conditions in (40) are satisfied within rendezvous tolerances $\boldsymbol{r}_{tol}, \boldsymbol{\Theta}_{tol}, \boldsymbol{\vartheta}_{tol}$ ($\boldsymbol{r}_{tol}$ defines a 3D tolerance box around the landing deck center). Here *a*(*j*) = 1 when *j* = *N**, otherwise, *a*(*j*) = 0, and constraints on the helicopter attitude, $\boldsymbol{\Theta}_{tol}$, position, $\boldsymbol{r}_{tol}$, and velocities, $\boldsymbol{\vartheta}_{tol}$, are relaxed using a large positive number *M* in (40). The vertical speed *w* is included in (40) to enhance soft touchdown (nearly zero relative vertical speed), and therefore to alleviate the negative effects of the translational acceleration transferred from the ship deck to the landing gear. For simplicity, the landing gear deck contact is not modelled in this study. When the helicopter-ship rendezvous occurs, a landing-aided equipment aboard the ship (e.g., harpoon tip locking-pin) automatically engages to anchor the helicopter to the grid deck. This device prevents the helicopter from drifting due to large amplitude deck motions in high sea states.

It is known that the helicopter can develop a high roll rate that occurs typically in aggressive maneuvers. It can roll over on its side with one wheel or skid on the ground (see Fig. 35). Hence, the helicopter should have a small roll rate *p* at touch down to avoid rollover in (40). The pitch rate q must also be kept small to be able to avoid an excessively high nose and to prevent the tail rotor from striking the landing deck in (40).

The inequality constraint (41) prevents collisions between the helicopter and the deck. Here ($a_p(k+j)$, $b_p(k+j)$, $c_p(k+j)$) denote the components of the normal direction of the flight deck at step $k+j$. Fig. 36 illustrates the general idea of constructing the collision avoidance constraint (41). Since not all of the helicopter states are directly measurable, a state observer is implemented in Fig. 37 (see Section 3.1.2 for details where the extended system was proved at least detectable so the state estimation is guaranteed to succeed).

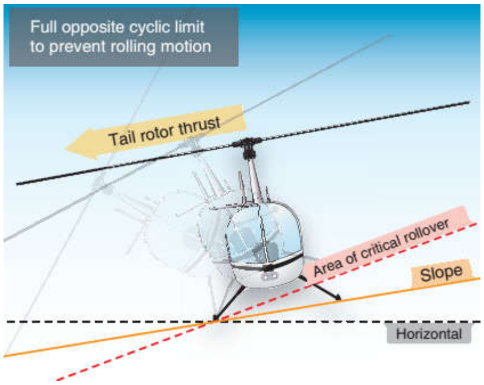

Fig. 35 Critical rollover in slope landing [80]

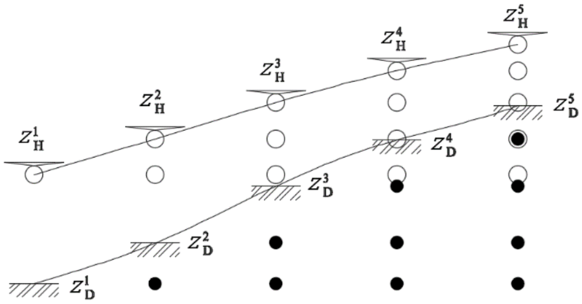

Fig. 36 Flight deck collision avoidance

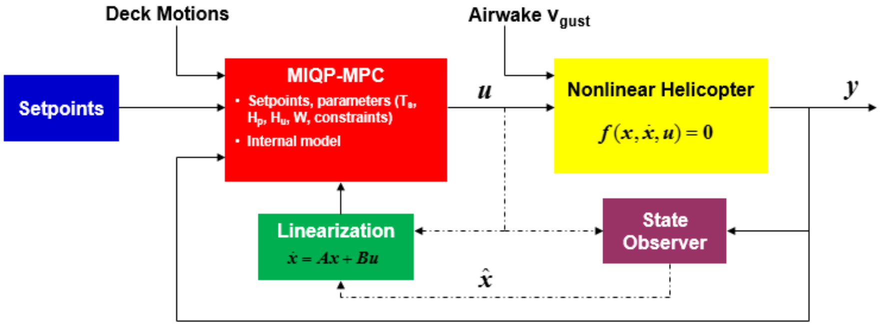

Fig. 37 MIQP-MPC implementation

4.2.2 Choice of Design Parameters

a) Maximum prediction horizon: The effectiveness of the MPC to handle multivariable constrained problems relies on its prediction capability. Accordingly, the controller will compensate for the upcoming reference variations. The reference over the maximum prediction horizon H_p is generated using a second-order polynomial as follows:

$$r_i(k+j\,|\,k) = r_i(k) + \dot{r}_i(k)T_s i + \frac{1}{2}\ddot{r}_i(k)\left(T_s j\right)^2,\ \ j = 1,2,\ldots,N_f \tag{42}$$

where $r_i(k), \dot{r}_i(k), \ddot{r}_i(k)$ are magnitude, rate of change, and acceleration of the i^{th} coordinate of the landing deck at the current time *k*. These values are numerically generated using the ship model in Chapter 2 at each time step. In the ship landing problem, the reference is composed of time series of the Euler angles and Cartesian coordinates of the landing deck in the NED frame over the prediction horizon H_p. This reference is updated at every sampling period $T_s = 0.02$ s.

b) *Minimum altitude for MIQP-MPC*: The final phase of the landing maneuver requires that the helicopter is sufficiently close to the deck to engage the MIQP-MPC controller.

c) *Rendezvous tolerances*: The linear model (36) is used as an internal model to estimate the helicopter behavior during the prediction horizon. Then, the MIQP-MPC generates the optimal control policy to accomplish the rendezvous maneuver within pre-defined tolerances. There are some differences between the dynamic responses of the linear model and the nonlinear model used in the evaluation of the closed-loop performance, due to unmodeled dynamics, elimination of nonlinearities due to linearization, and also due to strong dynamic couplings in aggressive maneuvers. Consequently, some of the helicopter states do not converge to the rendezvous condition in due time. The helicopter and the ship will miss the rendezvous and need plenty of time to reschedule another set of coordinated movements. To solve this problem, tolerances for each states are modified as described in algorithm 1 with the values selected as follows:

$$\begin{aligned}&x_{tol} = y_{tol} = z_{tol} = 0.1\,\text{m}, w_{tol} = 0.1\ \text{m/s}, p_{tol} = q_{tol} = 4.5\,\text{deg}/\,s, \phi_{tol} = \theta_{tol} = \psi_{tol} = 0.5\,\text{deg},\\ &\gamma_x = \gamma_y = 2, \gamma_z = 1,\ \gamma_\phi = \gamma_\phi = \gamma_\psi = 2, \gamma_w = 5, \gamma_p = \gamma_q = 1.1.\end{aligned} \tag{43}$$

This algorithm results in trajectories which satisfy ADS-33-PRF specifications for slope landing [77]. ADS-33-PRF provide established industry standards which require the helicopter to touch down and maintain a final position within an area that is 1.8 m longer (i.e., $x_{tol} = \pm 0.9$ m), and 1.2 m wider (i.e., $y_{tol} = \pm 0.6$ m) than the landing gear and maintain the heading at touchdown aligned with the reference heading within ±5 deg. Fig. 38 shows the achieved task performance in helicopter/ship landing MTE in terms of touchdown velocities and landing scatter from the flight test results of a Sea King helicopter [79]. We can see that the rendezvous tolerances in (43) are much smaller (i.e., more demanding) than the corresponding values of the touchdown velocity and the landing scatter in Fig. 38.

It is assumed that the harpoon tip-locking pin must anchor the helicopter to the deck structure before the critical rollover angle is reached (5-8 deg depending on helicopter type, winds, and loading [32]). For a period of 1 s of the harpoon deployment, the MPC should keep the absolute values of the roll and pitch rates at touch down below 5 deg/s in (26).

Algorithm 1 *Arrival Check*

```
At the beginning of each time step k, do the following
    if $(|x_N - x_{deck}| \le \gamma_x x_{tol})$ & $(|y_E - y_{deck}| \le \gamma_y y_{tol})$ & $(|z_D - z_{deck}| \le \gamma_z z_{tol})$ &
       $(|\phi - \phi_{deck}| \le \gamma_\phi \phi_{tol})$ & $(|\theta - \theta_{deck}| \le \gamma_\theta \theta_{tol})$ & $(|\psi - \psi_{deck}| \le \gamma_\psi \psi_{tol})$ &
       $(|w - w_{deck}| \le \gamma_w w_{tol})$ & $(|p - p_{deck}| \le \gamma_p p_{tol})$ & $(|q - q_{deck}| \le \gamma_q q_{tol})$,
    then  $x_{tol} \equiv \gamma_x x_{tol}, y_{tol} \equiv \gamma_y y_{tol}, z_{tol} \equiv \gamma_z z_{tol}$
          $\phi_{tol} \equiv \gamma_\phi \phi_{tol}, \theta_{tol} \equiv \gamma_\theta \theta_{tol}, \psi_{tol} \equiv \gamma_\psi \psi_{tol}$
          $w_{tol} \equiv \gamma w_{tol}, p_{tol} \equiv \gamma_p p_{tol}, q_{tol} \equiv \gamma_q q_{tol}$
```

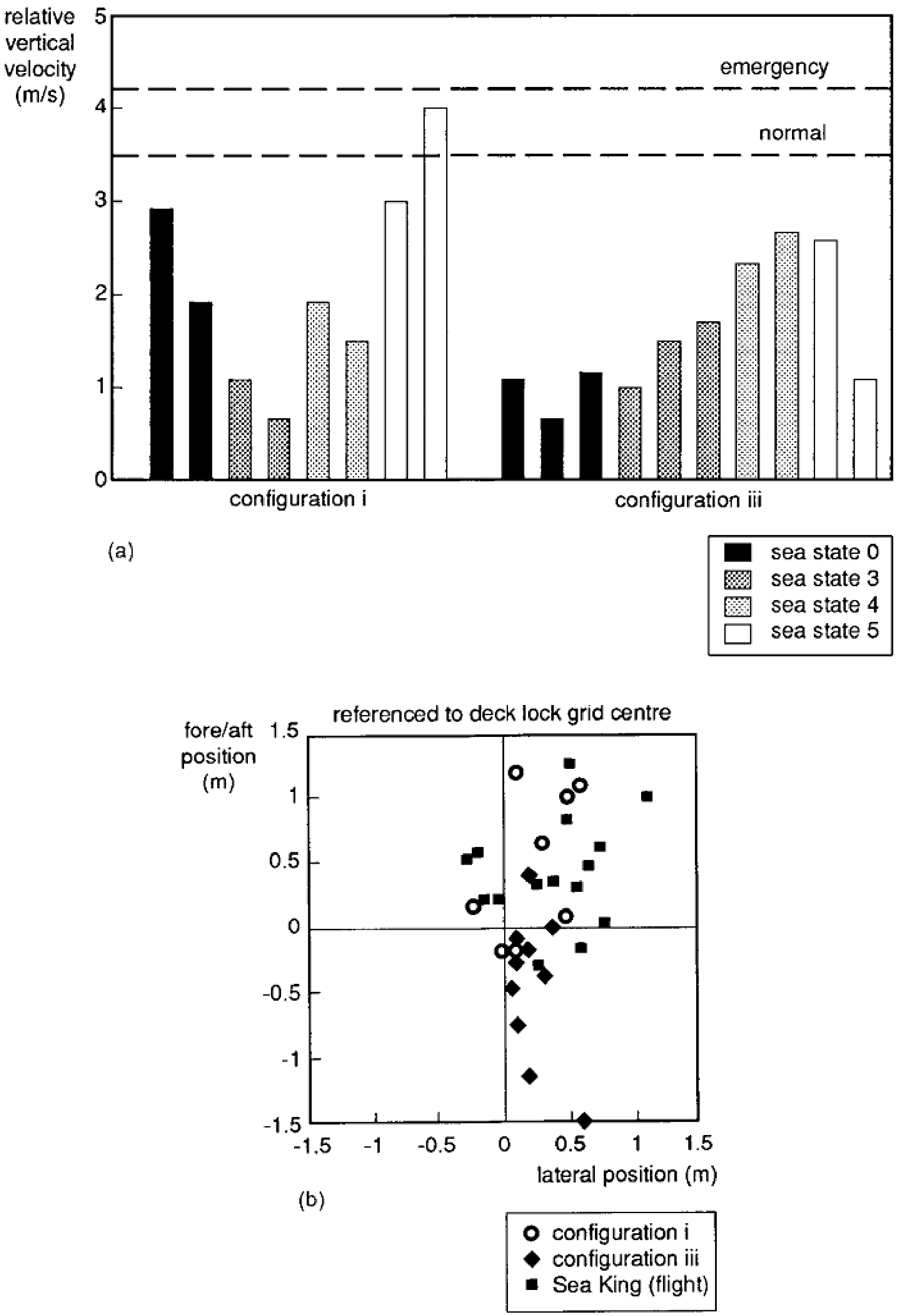

Fig. 38 Task performance in helicopter/ship landing MTE [79]: (a) touchdown velocity; (b) landing scatter

4.3 Performance Evaluation

4.3.1 Implementation of the Rendezvous Controller

To achieve landing on moving decks, algorithm 2 described in this section was been developed. The algorithm represents the implementation of the MIQP-MPC method. The helicopter is brought to a certain altitude (1.5 m in the examples presented herein) above the flight deck by the flight path MPC controller. Then, coordinated movements are calculated and implemented by the MIQP-MPC controller to meet the rendezvous conditions for relative attitude, position, and velocities.

In the tracking measure (23), the weights $\boldsymbol{w}^{y}$ = [50, 50, 10, 0, 0, 0, 1, 2, 1, 5, 7, 1]$^{\mathrm{T}}$, $\boldsymbol{w}^{u}$ = [1, 1, 1, 1]$^{\mathrm{T}}$, $\boldsymbol{w}^{\Delta u}$ = [1, 1, 1, 1]$^{\mathrm{T}}$ are selected to ensure good performance and disturbance rejection in the presence of the ship airwake. Turbulence intensity of 3 m/s and mean wind speed of 15 m/s are chosen for the CETI model of the ship airwake in Fig. 13. The origin of the inertial NED frame is located at the initial position of the ship's center of mass. The landing deck's coordinates (x_D, y_D, z_D) are -72 m longitudinal, 0 m lateral, and -5 m vertical with respect to the origin, respectively. The ship operates in sea state 5 and 150-deg heading wave. The output reference $\boldsymbol{r}$ in (23) is $\boldsymbol{r}=\left[u_{trim}, v_{trim}, w_{trim}, p_{trim}, q_{trim}, r_{trim}, \Phi_{H_{trim}}, \theta_{H_{trim}}, \psi_{H_{trim}}, x_{N_{trim}}, y_{E_{trim}}, z_{D_{trim}}\right]^{T}$ for the first several seconds when the helicopter hovers above the landing deck, and when the helicopter initiates the approaching maneuver. The subscript trim denotes the trim value of the corresponding variable of the helicopter at hover. In (23), the control horizon H_u is much smaller than the prediction horizon H_p = 25 to promote faster computations due to fewer variables computed in the optimization scheme. Moreover, there are delays in the system dynamics so that some control moves do not affect the system outputs before the end of the prediction horizon. Therefore, H_u is chosen to be 2.

For the rendezvous maneuver, numerical simulations are performed to compute dynamically feasible trajectories of the helicopter at each time step. As opposed to kinematic motion planning algorithms, the system dynamics and constraints are taken into account in the motion planning using MIQP-MPC. Therefore, the motion plan is executable and the discrepancies between the planned trajectory and the trajectory actually executed by the system are minimal. The key attributes of the MIQP-MPC for helicopter landing that will be evaluated in this section are as follows:

(1) Rapid: The algorithm rapidly performs a set of coordinated maneuvers for the ship landing in the shortest arrival time. This attribute comes from the optimization described in (35).

(2) Precise: The rendezvous conditions (40) on the helicopter-ship relative attitude, position and velocities are precisely tracked within the tolerance boxes in (43).

(3) Safety: All of the system constraints (38) and the flight deck collision avoidance condition (41) are strictly satisfied. During the last phase of the rendezvous, there is still adequate control authority for the helicopter to execute new maneuvers in case of emergencies.

(4) Adapt: The algorithm continuously updates awareness of the operational situation such as erratic motions of the landing deck in different scenarios (upstroke, downstroke motions with high energy indices) to adapt and respond rapidly with possible control efforts. This attribute comes from the ability of the predictive control and the variable prediction horizon.

Algorithm 2 shows how MIQP-MPC performs helicopter landing on decks experiencing high energy index motions. First, parameters of the MIQP-MPC problem, such as maximum prediction horizon H_p, arrival time $N^* = H_p/1.2$, control horizon H_u, sampling time T_s, system constraints in (38), rendezvous tolerances in (43), and large positive number M for the relaxation purpose, are initialized. Second, the helicopter and flight deck measurements are updated at the current time k, then the helicopter-deck relative position is computed, the maximum prediction horizon $H_p = 1.2N^*$ and the control horizons $H_u = 0.8H_p$ are updated. Third, the Euler angles, Cartesian coordinates, and velocities of the flight deck over the maximum prediction horizon H_p are estimated using (42), the rendezvous tolerances are updated using Algorithm 1. Fourth, if the helicopter-deck relative altitude is larger than a certain altitude ALT ($ALT = 1.5$ m in the examples presented herein) above the landing deck, the helicopter is brought to this altitude by the flight path MPC controller. Otherwise, a rendezvous MIQP-MPC controller generates an optimal control sequence to minimize the performance measure (arrival time, control effort), satisfy the rendezvous conditions (40) in N^* steps, manage system constraints (38) and flight deck collision avoidance (41). Fifth, if the rendezvous conditions are satisfied at the current step k (i.e., $N^* = 1$), the landing mission is accomplished. Otherwise, only the first element of the control sequence is applied as the input signal to the system, then a new output measurement is obtained and the technique is repeated at the new time step.

Algorithm 2 Precision Landing Algorithm

```
1:  Initialize parameters: $H_p$, $H_u$, $T_s$, $M$, rendezvous tolerances (43), system constraints
    (38), $N^* = H_p/1.2$, $k_1=1$, $k = 1$.
repeat
2:  Update the helicopter and flight deck measurements at the current time $k$. Compute the
    helicopter-deck relative position. Update the maximum prediction horizon $H_p = 1.2N^*$,
    $H_u = 0.8H_p$.
3:  Estimate the flight deck attitude, position, and velocities over the maximum prediction
    horizon $H_p$ using (42). Run Algorithm 1 to update the rendezvous tolerances.
4:  If ($ALT > 1.5$ m) and ($k_1 = 1$) then
        Find optimal control sequence to bring the helicopter close to the deck using the
        flight path MPC controller.
    elseif ($ALT \leq 1.5$ m) then
        Find optimal control sequence, arrival time $N^*$ using the rendezvous MIQP-MPC
        controller. Set $k_1 = 0$.
    end
5:  Apply the first element of the optimal control sequence to the nonlinear helicopter
    dynamics system (18). Goto line 2.
until $N^* = 1$ (Mission Accomplished)
```

4.3.2 Landing on Inclined Platforms

This section shows the feasibility of the MIQP-MPC controller in landing on a platform initially pitching up by 10 degrees and rolling to the right by 10 degrees. The controller is applied to the nonlinear helicopter dynamics model in Eq. (11). Fig. 39-42 show the flight trajectory, fuselage states, and control input time histories of the helicopter. The helicopter initially rolls to the left to compensate for lateral displacement, then performs a positive bank turn to the right to align itself with the positive inclination angle of the platform. These maneuvers are automatically coordinated to accomplish precision landing with soft touch down at the right place and time. The vertical velocity at touch down is nearly zero. The final tracking errors satisfy the ADS-33-PRF requirements, i.e. 0.06-m longitudinal, 0.08-m lateral, 0.13-deg roll, 0.67-deg pitch, 0-deg heading error. In Fig. 40, we see that the MIQP-MPC performs the aggressive maneuvers required for this difficult landing with control efforts satisfying the system constraints (38). During the last phase of the rendezvous, there is still adequate control authority for the helicopter to execute new maneuvers in case of emergency.

In Fig. 41, the roll rate and pitch rate at touch down are 3.16 deg/s, 4.69 deg/s respectively, thus satisfying the rendezvous tolerances in (43) to avoid the dynamic rollover and the tail striking the ground. Fig. 42 shows that the rate of descent during landing is much smaller than the induced inflow of the inner blade sections computed using (10) to avoid the adverse secondary vortex ring.

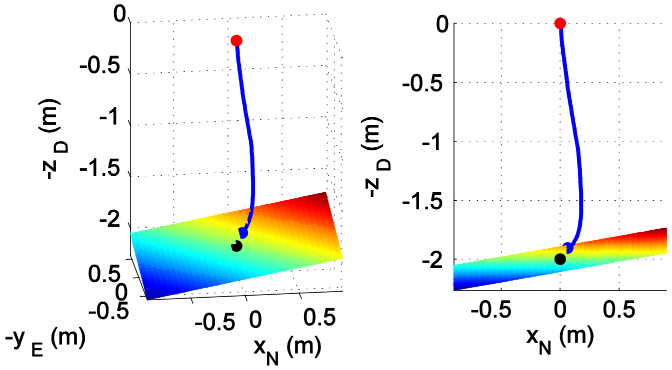

Fig. 39 Helicopter trajectory toward the 10-deg pitching & 10-deg rolling platform

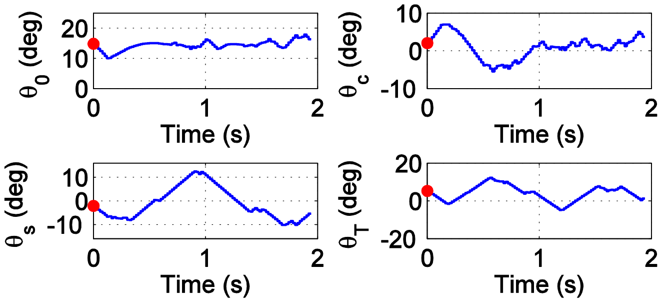

Fig. 40 Control input histories of the helicopter

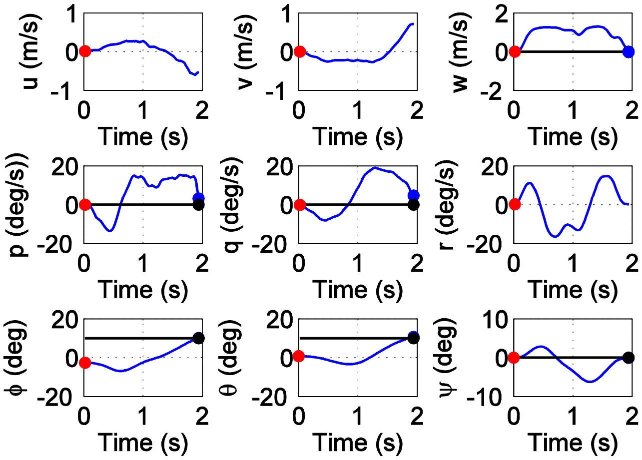

Fig. 41 Fuselage state responses of the helicopter

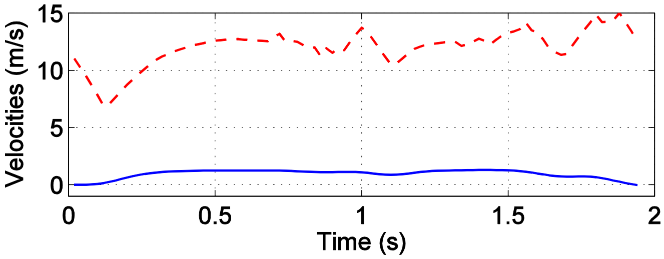

Fig. 42 Induced inflow (dashed line) and rate of descend (solid line)

4.3.3 Landing during Down-Stroke Deck Motions

This section demonstrates a successful landing on the moving deck during downstroke motions at ‘danger’ EI index. The controller is applied to the nonlinear helicopter dynamics model augmented with the CETI airwake disturbance model with the mean wind speed of 15 m/s in Eq. (18). The helicopter is brought to the hover condition 1.5 m above the landing deck using the flight path MPC controller. Then the MIQP-MPC executes the rendezvous maneuver at time = 3 s in the ship motion simulation in Fig. 43. Only the rendezvous maneuver is simulated in this subsection. Fig. 44-46 show the helicopter attitude, position, velocities, control inputs and main-rotor states during the maneuver. It takes 1.16 s and 1.182 s to accomplish the mission when the airwake effects are not included and included, respectively. Blue and black solid circles at the end of the maneuver highlight the precision tracking of the helicopter-ship attitude, position, and velocities. It satisfies all rendezvous tolerances defined in (43), as well as the ADS-33-PRF specifications for slope landing in [77]. All control saturation and slew rate limits are satisfied. In Fig. 44, there are no large rapid movements of the controls during landing. In Fig. 45, the relative vertical speed is reduced to less than 0.1 m/s by the time the helicopter has a soft touchdown on the moving deck. Moreover, the roll and pitch rates absolute values are smaller than 5 deg/s to avoid the dynamic rollover and the tail striking the ground.

It can be seen that the MIQP-MPC is able to execute rapid maneuvering so that the airwake does not have enough time to take effect on the overall performance. From Fig. 46, we can see that the flapping, lead-lagging states of the main rotor are well-behaved during the landing in the presence of the ship airwakes. This can be explained by the fact that the rotor blade dynamics is taken into account in the control design phase by including it into the control model.

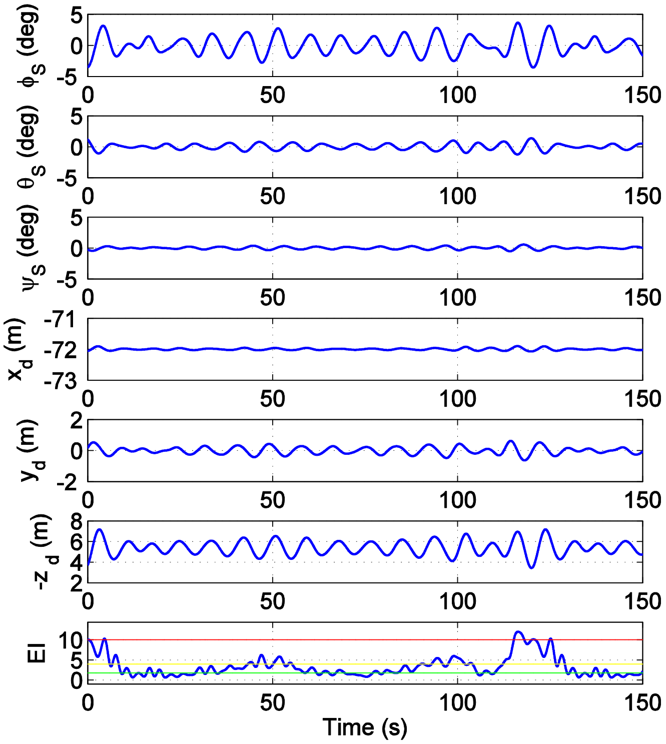

Fig. 43 Ship motion time history and energy index

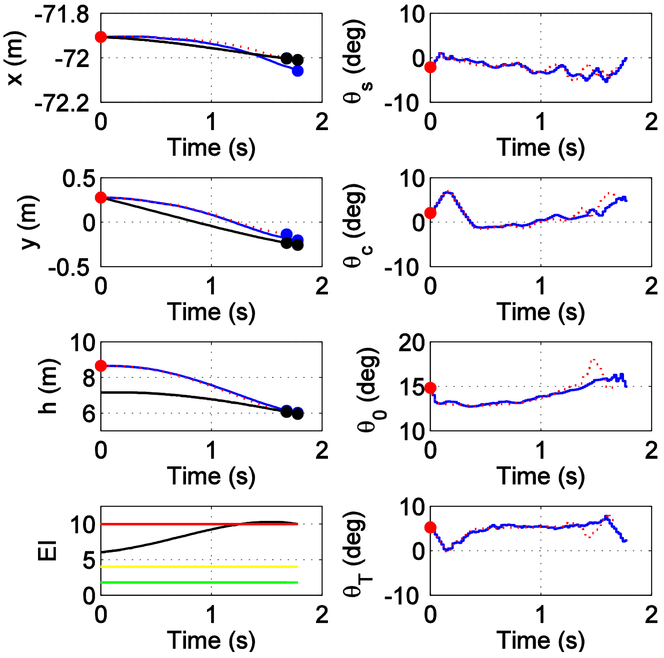

Fig. 44 Position and control input histories of the helicopter during the landing without airwakes (dotted line), with airwakes (solid line) on the moving deck (black lines)

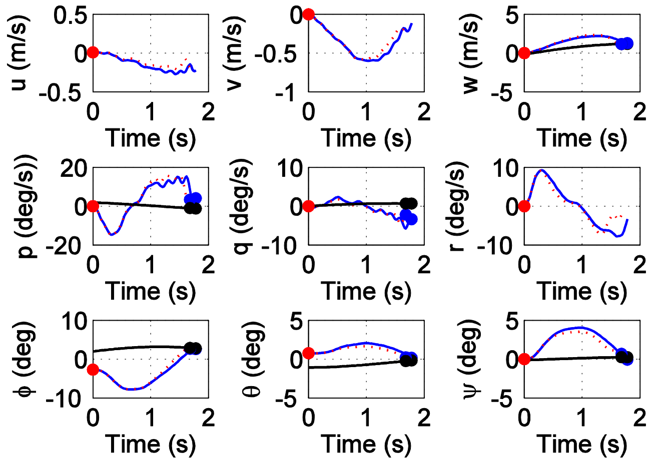

Fig. 45 Fuselage state responses of the helicopter during the landing without airwakes (dotted line), with airwakes (solid line)

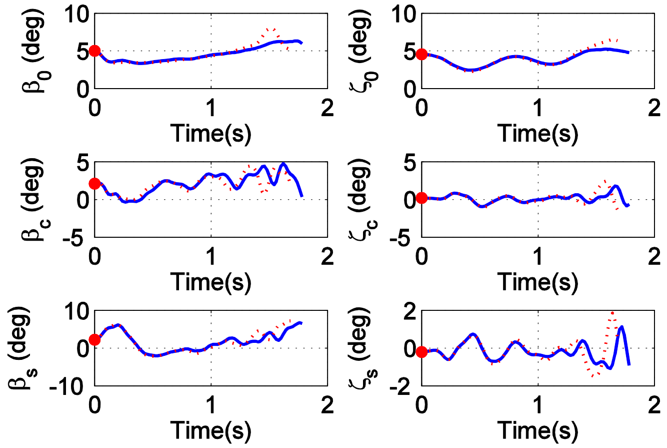

Fig. 46 Flapping, lead-lagging states of the main rotor during the landing without airwakes (dotted line), with airwakes (solid line)

4.3.4 Landing during the Up-Stroke Deck Motions

An example to illustrate the capability of landing on upstroke moving decks at 'danger' EI index using MIQP-MPC control is given in Fig. 47-49. The controller is applied to the nonlinear helicopter dynamics model augmented with the CETI airwake disturbance model with the mean wind speed of 15 m/s in Eq. (18). The helicopter is brought to the hover condition at 1.5 m above the landing deck using the flight path controller. Then the MIQP-MPC controller executes the rendezvous maneuver. Only the rendezvous maneuver is simulated in this subsection. Fig. 47-49 show the helicopter attitude, position, velocities, control inputs and main-rotor states during the maneuver. The closed loop system achieves a very good performance, similar as for the deck landing during downstroke deck motions.

However, it takes a slightly longer length of time to accomplish the mission, i.e. 2.24 s and 2.56 s when the airwake effects are not included and included in the model, respectively. Moreover, the airwake has enough time to take effect on the overall performance.

Despite the fact that the system works harder to control the relative vertical velocity to obtain a soft landing during the upstroke motion in Fig. 47, and more control effort is needed to mitigate the airwake effects in Fig. 48, there are still sufficient control margins of the collective, cyclic, and pedal controls to react quickly in case of emergency. Fig. 49 shows considerable oscillations in the main rotor states under the airwake effects. However, the magnitudes of the flapping, lead-lagging motions are the same for both downstroke and upstroke landing scenarios. We observe that the rate of descent has much lower magnitude than the normal downward induced inflow rate of the inner blade sections to avoid the appearance of the adverse secondary vortex ring. Interest readers may consult Appendix C for more numerical simulations of the precision landing on moving decks.

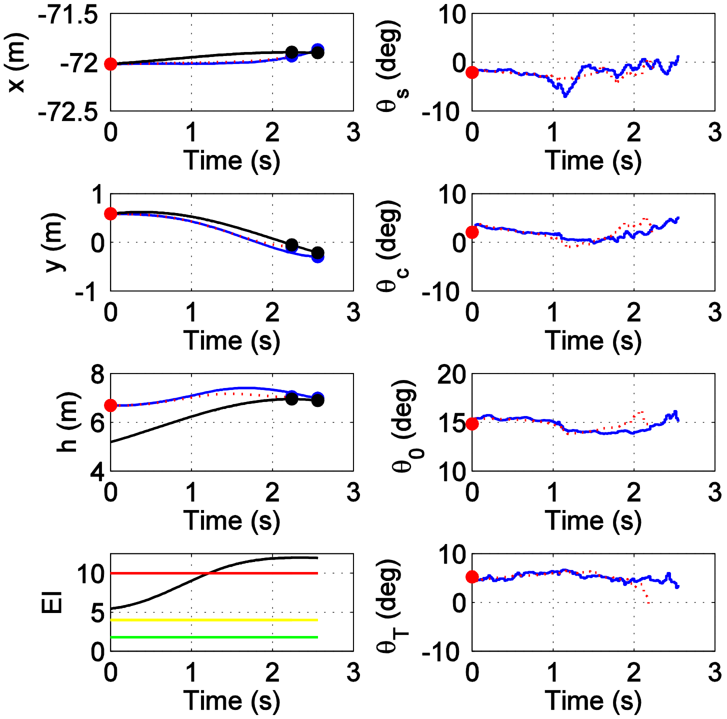

Fig. 47 Position and control input histories of the helicopter during the landing without airwakes (dotted line), with airwakes (solid line)

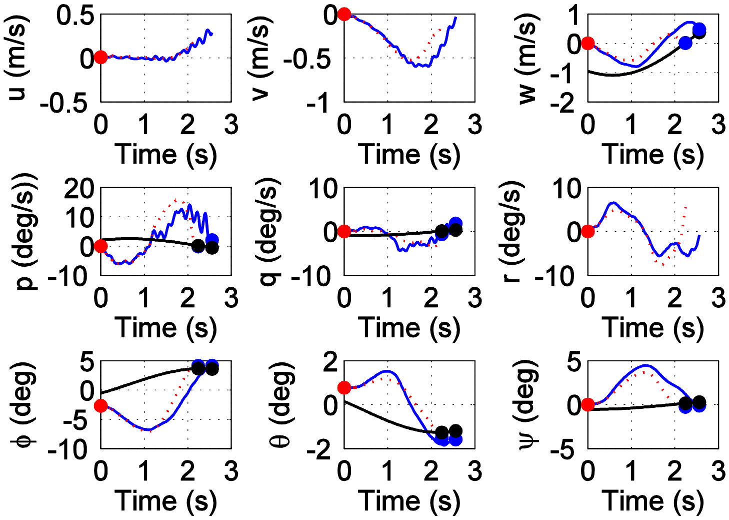

Fig. 48 Fuselage state responses of the helicopter during the landing without airwakes (dotted line), with airwakes (solid line)

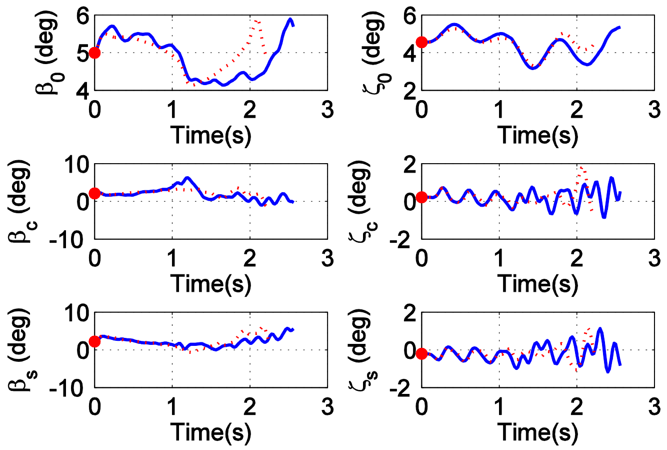

Fig. 49 Flapping, lead-lagging states of the main rotor during the landing without airwakes (dotted line), with airwakes (solid line)

4.4 Maneuverability and Agility Enhancement

Some of the ideas arising from this study to enhance maneuverability and agility of the shipborne helicopter using the MIQP-MPC algorithm are summarized as follows. First, typical helicopter flight control systems are designed with the assumption that rotor speed is constant during the operating condition. Continuous variable rotor speed control can be incorporated into the MIQP programming as an additional variable to optimally increase the control authority of the system and guarantee the engine torque limit protection. Second, for high performance shipborne helicopters, high gain/high authority active control is required to achieve the consistent performance in high demanding operating conditions. For examples, the control saturation and slew rates in (38) can be feasibly increased by innovative rotorcraft design using advanced CFD techniques for high efficient rotor blades and advanced technologies for helicopter rotor blade actuators.

Chapter 5: Constrained Control for Ocean Current Turbines

In this Chapter we address the Ocean Current Turbine (OCT) flight control problem. For the OCT flight control system design, we leverage ideas from helicopter blade control by introducing cyclic blade pitch controls in OCT, in analogy with the blade pitch cyclic controls used in helicopter control. Then Output Variance Constrained (OVC) control and Model Predictive Control (MPC) are investigated as advanced constrained control algorithms for the OCT flight control system design. The effect of prescribed output variance constraint values on the performance of the OVC control system is evaluated, as well as the effect of sensor failures. Extensive linear and nonlinear simulations are used to evaluate the performance of the closed loop OCT systems. Regardless of the strategy used (OVC or MPC), cyclic blade pitch control proves to effectively regulate the OCT's position and rotor angular speed when disturbed from the nominal operating condition.

5.1 OCT System Description

5.1.1 Nonlinear Ocean Current Turbine Model

The OCT design used in this dissertation is a nearly neutrally buoyant conceptual design developed by SNMREC [81] and modified according to [61]. Configuration data of the OCT is given in Table A.4 in the Appendix. This horizontal axis OCT (Fig. 50) has a single 20 m diameter rotor that is designed to produce up to approximately 700 kW of shaft power when operating in the Florida Current. Two elliptically shaped floats counteract the hydrodynamic torque of the rotor [81]. The rotor uses airfoil shapes that range from nearly cylindrical at the hub to an FX-83W airfoil with a thickness ratio of 21% at 20% of the rotor radius and FX-83W with a thickness ratio of 10.8% at the blade tip [61]. The airfoils at these locations have maximum two-dimensional (2D) lift coefficients of 1.4 and 1.62 at angles of attack of 16° and 17° respectively (Calculated using X-Foil, [82]). These 2D coefficients are modified to account for 3D effects using the Selig Du and Eggars corrections, resulting in maximum coefficient lift values of 2.02 and 1.54 at angles of attack of 32° and 16.5° respectively (Corrections made using AirfoilPrep, [83]).

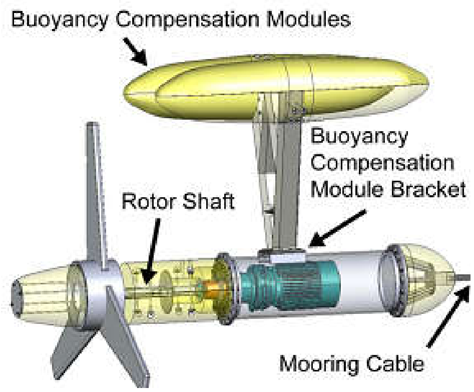

Fig. 50 Artist rendering of the turbine with some of the major components listed. The rotor blades are not accurately drawn in this rendering [55]

The envisioned testing configuration for this OCT design is attaching it, via a cable, to a flounder plate connected to a main mooring line that runs from a surface buoy to the sea floor [81]. The rigid body dynamics of this turbine, including the effects of the mooring cable that attaches it to the flounder plate, are considered in the developed nonlinear simulation. However, for computational efficiency the flounder plate is assumed to be stationary for these analyses.

The hydrodynamic rotor modeling process is summarized for completeness of this dissertation (also see [55]). The rotor is assumed to be a single rigid body and hydrodynamic forces are calculated using the blade element momentum (BEM) approach, similar to the approach in [81]. This model uses a grid fixed to the swept area of the rotor blade to calculate impeded flow values using a dynamic wake approach. Impeded flow values at each rotor blade element are then calculated each time step from values on this grid at the adjacent radial grid points. The motion of the rotor elements, free stream flow velocities, and calculated impeded flow values are then used to calculate the relative flow velocity and angle of attack of each finite blade element. Forces on each blade element are numerically integrated to calculate the hydrodynamic forces and moments on the rotor.

The hydrodynamic and cable models are described in detail in [55]. Hydrodynamic forces that act on the rotor, the main body that houses the generator and rotor shaft, two buoyancy compensations modules, and the tow cable elements, are calculated at each time step. These hydrodynamic forces, along with gravity, buoyancy, and elastic cable forces, are utilized to calculate the motion of the OCT. The seven-degrees of freedom (DOF) of the turbine, including the relative rotation of the rotor, are calculated as suggested in [61].

A finite element lumped mass model is used for the 607 meter long cable that attaches the turbine to the flounder plate. This model adds 3 degrees of freedom (DOF) per cable node (besides the nodes that are attached to the turbine and flounder plate) to the 7-DOF of the OCT. For the nonlinear simulation results presented in this dissertation five linear elastic cable elements were used, adding 12 degrees of freedom to the non-linear simulation. These were not included in the linear model. For more details of these nonlinear and linear OCT models, developed by the Florida Atlantic University researchers, interest readers may consult [55]-[57], and [61].

5.1.2 Individual Blade Pitch Control (IBC)

Individual blade control, which is very popular in helicopter technology, will be used in this dissertation for OCT control. In a simple implementation, which is the focus in this dissertation, IBC consists of three blade pitch angle controls achieved primarily via collective and cyclic (or differential) controls. IBC can be used to generate forces and moments that affect the position and orientation of the OCT [85]. In this dissertation, IBC oscillates harmonically the root pitch angle of each individual rotor blade as a function of the azimuth angle, α, about the collective pitch angle, γ^{eq}, which produces maximum power when the system is operating at the optimal tip speed ratio in a steady axial flow. In analogy with the physical mechanism of the helicopter rotor control [63], the cyclic blade pitch angles are controlled through a swashplate which consists of a non-rotating plate attached to the control actuators, and a rotating plate attached to blades with pitch link rods (Fig. 51). For three blades rotating in a synchronous manner, the resulting blade pitch root angles are:

$$\begin{bmatrix}\gamma_1\\ \gamma_2\\ \gamma_3\end{bmatrix}=\begin{bmatrix}1\\1\\1\end{bmatrix}\gamma^{eq}+\begin{bmatrix}\sin(\alpha) & \cos(\alpha)\\ \sin\left(\alpha+\frac{2\pi}{3}\right) & \cos\left(\alpha+\frac{2\pi}{3}\right)\\ \sin\left(\alpha+\frac{4\pi}{3}\right) & \cos\left(\alpha+\frac{4\pi}{3}\right)\end{bmatrix}\begin{bmatrix}\gamma_a\\ \gamma_b\end{bmatrix} \tag{44}$$

where γ_a, γ_b are longitudinal and lateral cyclic pitch control inputs. The electromechanical control torque, labeled τ_{em} and applied directly to the rotor shaft, is the third control input of the OCT dynamics model.

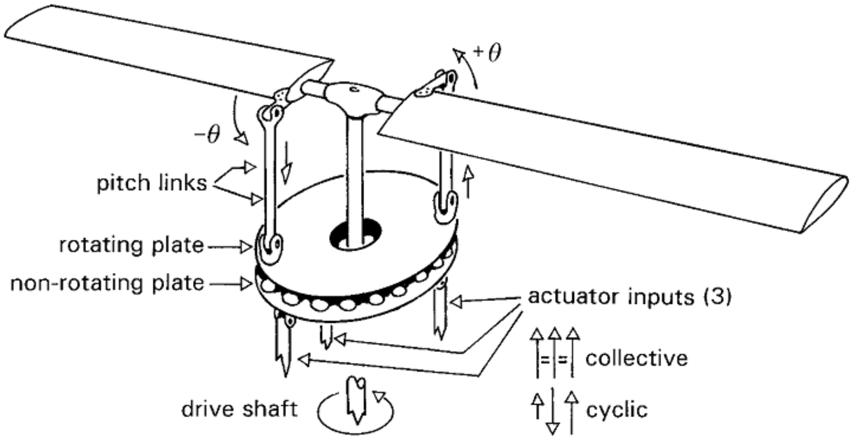

Fig. 51 Rotor control through a swash plate [63]

5.2 Linearization and Stability Analysis

5.2.1 Linearized Model

The nonlinear model of a moored OCT was linearized around an operating condition corresponding to maximum power output produced by the OCT placed in a steady axial flow. Its main parameters are: averaged flow current velocity $\bar{U}_M$ = 1.6 *m/s*, angular rotor speed $\dot{\alpha}^{eq} = \Omega = 14.169\,\text{rpm}$, rotor blade angles $\gamma_0^{eq} = \gamma_a^{eq} = \gamma_b^{eq} = 0\,deg$, and electromechanical torque $\tau_{em}^{eq} = -246.48\,kNm$. The corresponding linearized model, calculated under the quasi-static assumption that intermediate cable node states are in equilibrium to purposely remove these states from the linear model, has 7 DOFs. In fact, our preliminary numerical simulations indicated that the cable dynamics has little influence on the OCT dynamics and thus it may be reasonable to ignore it in preliminary studies. The states used to describe the dynamics of the OCT system are: the linear and angular velocities of the OCT main body in the body fixed reference frame, labeled u, v, w, p_b, q_b, r_b; the angular velocity of the rotor with respect to the OCT main body, labeled p_r; the Cartesian coordinates of the OCT's rotor attachment point to the blade hub with respect to an inertial reference frame, labeled X, Y, Z; the azimuth angle α of the first rotor blade measured with respect to a fixed direction in the plane of the rotor; three Euler angles describing the orientation of the OCT main body with respect to the inertial reference frame, labeled ϕ, θ, ψ (for illustration of these variables, interested readers may consult [68]). The OCT state and control vectors are

$$\boldsymbol{x} = \begin{bmatrix} u & v & w & p_b & p_r & q_b & r_b & X & Y & Z & \phi & \alpha & \theta & \psi \end{bmatrix}^T, \boldsymbol{u} = \begin{bmatrix} \gamma_a & \gamma_b & \tau_{em} \end{bmatrix}^T,$$

and the corresponding linearized model can be formally written as

$$\delta \dot{\boldsymbol{x}} = \boldsymbol{A} \delta \boldsymbol{x} + \boldsymbol{B} \delta \boldsymbol{u} \tag{45}$$

where δ denotes the difference between the state or control vectors and the equilibrium values about which the system is linearized. For notational simplicity, δ has been omitted from the linearized model in subsequent sections. Matrices ***A*** and ***B*** are given below.

A	u	v	w	pb	pr	qb	rb	X	Y	Z	phi	alpha	theta	psi
u	-0.3129	-0.0790	-0.0060	-0.2181	-0.2207	-0.3659	0.1828	-0.0580	0.0001	-0.0030	-0.0103	0.0000	-1.1747	-0.0029
v	0.0031	-0.1563	0.6025	0.1750	-0.0007	1.5805	1.9023	0.0000	0.0011	0.0000	1.1503	0.0000	-0.0713	0.9402
w	-0.0673	-0.4601	-0.1937	-0.0565	-0.0575	-0.8337	1.1684	-0.0178	0.0000	-0.0005	-0.0023	0.0000	-3.7736	-0.0499
pb	0.0001	-0.0473	-0.0084	-0.6591	-0.0001	-0.0302	-0.3790	0.0000	0.0002	0.0000	-1.4587	0.0000	-0.0052	0.2220
pr	0.5455	0.0000	-0.0001	-0.2570	-0.2559	-0.0266	-0.0039	0.0000	0.0000	0.0000	-0.4707	0.0000	0.0280	-0.0003
qb	-0.0117	-0.0435	-0.0046	-0.0088	-0.0090	-0.2420	0.1043	-0.0026	0.0000	0.0001	-0.0001	0.0000	-0.6318	-0.0076
rb	-0.0004	0.0122	-0.0635	0.0213	0.0002	-0.1582	-0.3068	0.0000	-0.0004	0.0000	0.2376	0.0000	0.0121	-0.2522
X	0.9989	-0.0011	-0.0462	0.0000	0.0000	0.0000	0.0000	0.0000	0.0000	0.0000	0.0000	0.0000	0.0000	0.0000
Y	0.0004	0.9999	-0.0135	0.0000	0.0000	0.0000	0.0000	0.0000	0.0000	0.0000	0.0000	0.0000	0.0000	0.0000
Z	0.0462	0.0134	0.9988	0.0000	0.0000	0.0000	0.0000	0.0000	0.0000	0.0000	0.0000	0.0000	0.0000	0.0000
phi	0.0000	0.0000	0.0000	1.0000	0.0000	-0.0006	-0.0463	0.0000	0.0000	0.0000	0.0000	0.0000	0.0000	0.0000
alpha	0.0000	0.0000	0.0000	0.0000	1.0000	0.0000	0.0000	0.0000	0.0000	0.0000	0.0000	0.0000	0.0000	0.0000
theta	0.0000	0.0000	0.0000	0.0000	0.0000	0.9999	-0.0134	0.0000	0.0000	0.0000	0.0000	0.0000	0.0000	0.0000
psi	0.0000	0.0000	0.0000	0.0000	0.0000	0.0134	1.0010	0.0000	0.0000	0.0000	0.0000	0.0000	0.0000	0.0000

B	gamma_a	gamma_b	tau_em
u	-0.2943	-0.0357	0.0000
v	-0.1378	1.4902	0.0000
w	-1.0459	-0.1100	0.0000
pb	0.0014	0.0647	0.0000
pr	-0.0229	-0.0026	0.0000
qb	-0.1634	-0.0112	0.0000
rb	0.0151	-0.2511	0.0000
X	0.0000	0.0000	0.0000
Y	0.0000	0.0000	0.0000
Z	0.0000	0.0000	0.0000
phi	0.0000	0.0000	0.0000
alpha	0.0000	0.0000	0.0000
theta	0.0000	0.0000	0.0000
psi	0.0000	0.0000	0.0000

5.2.2 Stability Analysis

After linearization around the nominal operating condition, a trivial kinematic equation that relates the time derivative of the rotor blade azimuth angle to the rotor angular velocity is obtain, $\dot{\alpha} = p_r$. Also after linearization the blade azimuth angle has no significant on the other equations. Therefore, for further studies this kinematic equation, which decouples from the other equations, along with the rotor blade azimuth angle are removed from the set of linearized equations and variables reducing the dimension of matrix $\boldsymbol{A}$ in (45) to 13x13 [62]. Its eigenvalues are:

$$\begin{array}{ll} -0.2737 \pm 1.1842i, & -0.1242 \pm 0.1751i \\ -0.2372 \pm 0.9944i, & -0.0012 \pm 0.0016i \\ -0.2344 \pm 0.3942i, & -0.0656. \\ -0.1599 \pm 0.4446i, & \end{array}$$

All the complex eigenvalues are clearly stable so they give rise to exponentially decaying oscillatory modes. However the open loop system does not display a desired eigenvalue pattern. Specifically, there are three very lightly damped eigenvalues (-0.0012±0.0016i, -0.0656) that are very close to the imaginary axis. Our eigenvalue-eigenvector analysis showed that the dominant motions corresponding to the very lightly damped eigenvalues affects the Cartesian coordinates of the OCT, *X*, *Y*, *Z* (see Table A.5 in the Appendix). Because of the very lightly damped eigenvalues, if the Cartesian position of the OCT is perturbed, the OCT will need a lot of time to return to the trim condition. This may become a critical issue for OCTs not equipped with an appropriate feedback flight control system, because OCTs are not intended for regular maintenance for large periods of time. Also OCTs are subject to numerous uncertainties, so OCT flight control which ensures rapid return to the unperturbed position in the presence of uncertainties is mandatory.

5.2.3 Controllability Analysis

This system is relatively easy to control. Specifically, it was also discovered via standard linear controllability analysis (i.e. using the PBH controllability test) that, if two cyclic blade controls and the electromechanical torque are assumed as inputs, the modes that are of major concern in this OCT system are stabilizable.

The LTI system (45) is controllable if and only if the controllability matrix $\boldsymbol{C}\left(\boldsymbol{A}_p, \boldsymbol{B}_p\right) = \left[\boldsymbol{B}_p, \boldsymbol{A}_p\boldsymbol{B}_p, \boldsymbol{A}_p^2\boldsymbol{B}_p, ..., \boldsymbol{A}_p^{n-1}\boldsymbol{B}_p\right]$ has rank *n*. To determine the rank of the matrix $\boldsymbol{C(A_p, B_p)}$, a singular value decomposition was performed so that $\boldsymbol{C}(\boldsymbol{A}_p, \boldsymbol{B}_p) = \boldsymbol{U}\Sigma\boldsymbol{V}^*$, where $\boldsymbol{\Sigma} = diag(\sigma_1, \sigma_2, ..., \sigma_r, 0, ..., 0)$, $\boldsymbol{U}$ and $\boldsymbol{V}$ are square unitary matrices and σ_i are the singular values ordered so that $\sigma_1 \geq \sigma_2 \geq ... \geq \sigma_{r-1} \geq \sigma_r$. The rank of the matrix was determined based on the number of singular values greater than a specified tolerance. This criterion led to the conclusion that the rank of matrix $\boldsymbol{C}(\boldsymbol{A}_p, \boldsymbol{B}_p)$ is 14 for a tolerance of 1.395×10^{-6} (see Fig. 52). Moreover, the Popov - Belevitch - Hautus (PBH) test, i.e. $rank[\lambda \boldsymbol{I} - \boldsymbol{A}, \boldsymbol{B}] = n$ for every unstable and marginally stable eigenvalue λ (-0.0012±0.0016i, -0.0656) is satisfied, so the linear system (45) is stabilizable. Therefore, effective flight control design for OCT using only these three controls is possible.

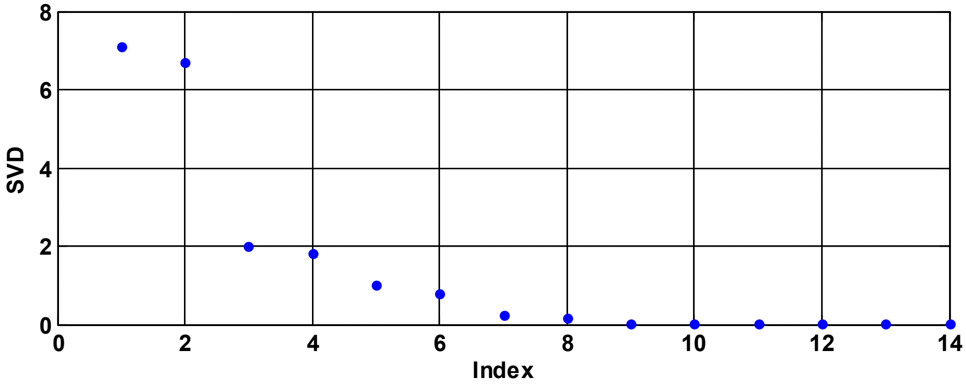

Fig. 52 Singular Value Decomposition (SVD) of the Controllability Matrix

5.2.4 Nonlinear Simulations

We also performed extensive comparisons between the nonlinear and linearized model responses. For example, Fig. 53-55 show the OCT model responses to the electromechanical torque τ_{em}, and to the cyclic pitch control inputs γ_a, γ_b, respectively. The system behaviors predicted by the linearized model are in relatively good agreement with the nonlinear OCT responses for the position states of the OCT. There is some disagreement for the response of the rotor speed to the blade cyclic control, which deserves further investigation. However, very good agreement is obtained for the rotor speed response to a step change in the shaft torque (Fig. 53).

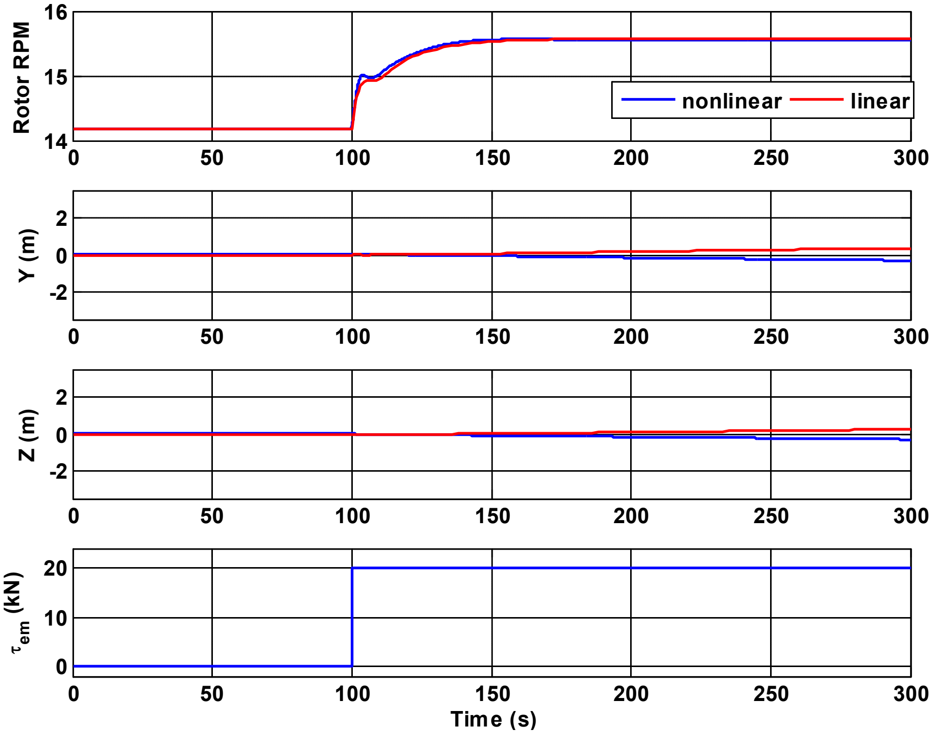

Fig. 53 Response of the OCT to 20kN step torque input

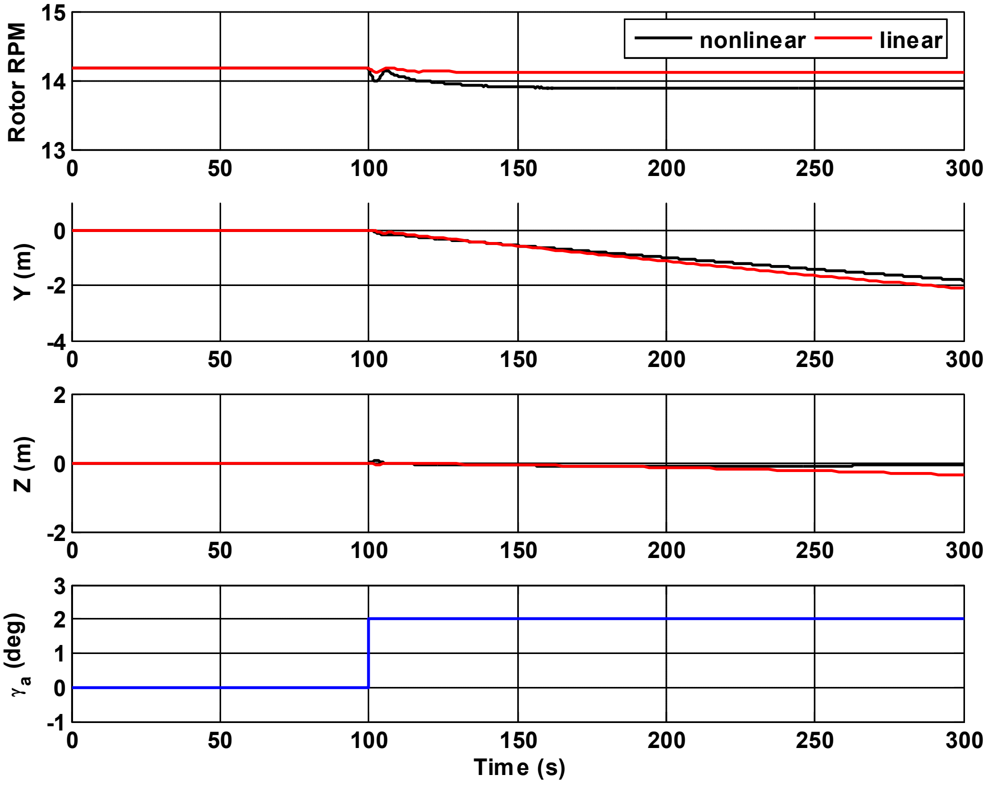

Fig. 54 Response of the OCT to 2^0 step longitudinal cyclic pitch control input

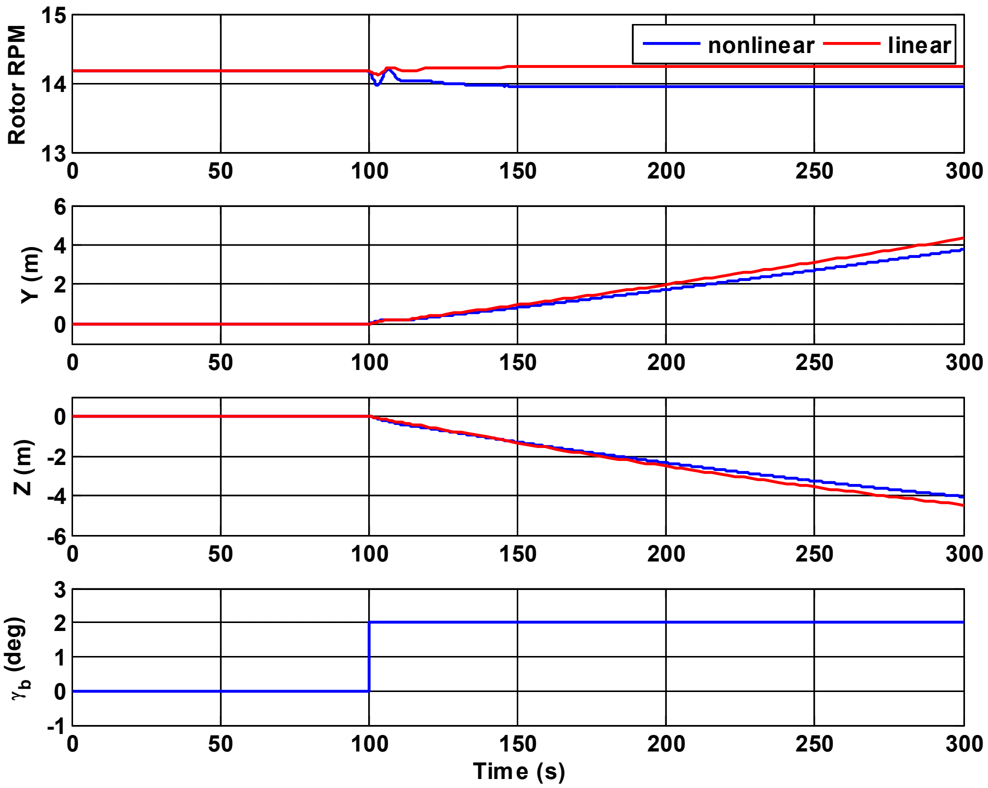

Fig. 55 Response of the OCT to 2^0 step lateral cyclic pitch control input

5.3 Output Variance Constrained Control

OVC control has been used before in aerospace vehicles and structures control (see for example [86]-[90]). It is a dynamic controller which minimizes the control energy subject to variance constraints on specified outputs. OVC control is very effective in exponentially stabilizing a linear system around a nominal operating condition, while guaranteeing constraint satisfaction in the presence of uncertainties [90]. The design of an OVC controller reduces to the selection of the output penalty matrix $\boldsymbol{Q}$ in standard LQG design such that the output variance constraints are satisfied. In this dissertation, an OVC flight control system is designed for the OCT system.

5.3.1 OVC Control Design

The OVC control problem is briefly described here for completeness (see also [91]-[92]). Consider the LTI system:

$$\dot{\boldsymbol{x}}_p(t) = \boldsymbol{A}_p \boldsymbol{x}_p(t) + \boldsymbol{B}_p \boldsymbol{u}(t) + \boldsymbol{D}_p \boldsymbol{w}_p(t)\,,\ \boldsymbol{y}_p(t) = \boldsymbol{C}_p \boldsymbol{x}_p(t)\,,$$

$$\boldsymbol{z}(t) = \boldsymbol{M}_p \boldsymbol{x}_p(t) + \boldsymbol{v}(t) \qquad (46)$$

and a strictly proper output feedback control law given by:

$$\dot{\boldsymbol{x}}_c(t) = \boldsymbol{A}_c\boldsymbol{x}_c(t) + \boldsymbol{F}\boldsymbol{z}(t), \quad \boldsymbol{u}(t) = \boldsymbol{G}\boldsymbol{x}_c(t) \tag{47}$$

where $\boldsymbol{y}_p$ is the vector of size n_y of system outputs, $\boldsymbol{z}$ the vector of sensor measurements of size n_z, $\boldsymbol{w}_p$ and $\boldsymbol{v}$ are zero-mean uncorrelated process and measurement Gaussian white noises with intensities $\boldsymbol{W}_p$ and $\boldsymbol{V}$ respectively, $\boldsymbol{x}_c$ is the controller state vector, and $\boldsymbol{x}_p$ is the plant state vector. Matrices $\boldsymbol{F}$ and $\boldsymbol{G}$ are state estimator and controller gains, respectively. Then, the resulting closed-loop system is

$$\dot{\boldsymbol{x}}(t) = \boldsymbol{A}_{cl}\boldsymbol{x}(t) + \boldsymbol{D}_{cl}\boldsymbol{w}(t), \quad \boldsymbol{y}(t) = \boldsymbol{C}_{cl}\,\boldsymbol{x}(t) \tag{48}$$

where $\boldsymbol{x}(t) = \begin{bmatrix} \boldsymbol{x}_p^T(t) & \boldsymbol{x}_c^T(t) \end{bmatrix}^T$, $\boldsymbol{A}_{cl} = \begin{bmatrix} \boldsymbol{A}_p & \boldsymbol{B}_p\boldsymbol{G} \\ \boldsymbol{F}\boldsymbol{M}_p & \boldsymbol{A}_c \end{bmatrix}$, $\boldsymbol{D}_{cl} = \begin{bmatrix} \boldsymbol{D}_p & 0 \\ 0 & \boldsymbol{F} \end{bmatrix}$, $\boldsymbol{y}(t) = \begin{bmatrix} \boldsymbol{y}_p(t) \\ \boldsymbol{u}(t) \end{bmatrix} = \begin{bmatrix} \boldsymbol{C}_y \\ \boldsymbol{C}_\mathrm{u} \end{bmatrix}\boldsymbol{x}(t)$,

$\boldsymbol{C}_y = \begin{bmatrix} \boldsymbol{C}_p & 0 \end{bmatrix}, \boldsymbol{C}_u = \begin{bmatrix} 0 & \boldsymbol{G} \end{bmatrix}$.

If the plant matrix $\boldsymbol{A}_{cl}$ of the closed-loop system (48) is exponentially stable, the closed-loop controllability Grammian $\boldsymbol{X}$ satisfies the Lyapunov equation

$$0 = \boldsymbol{A}_{cl}\boldsymbol{X} + \boldsymbol{X}\boldsymbol{A}_{cl}^T + \boldsymbol{D}\boldsymbol{W}\boldsymbol{D}^T \tag{49}$$

where $\boldsymbol{W} = \begin{bmatrix} \boldsymbol{W}_p & 0 \\ 0 & \boldsymbol{V} \end{bmatrix}$.

The OVC problem, of finding the controller (47) which minimizes the control energy J_{OVC} and satisfies the output variance constraints $\overline{Y}_i$, can be written as follows:

$$\underset{\boldsymbol{F},\boldsymbol{G}}{\mathit{minimize}} \; J_{OVC} = E_\infty \boldsymbol{u}^T \boldsymbol{R}\boldsymbol{u} = \mathit{trace}(\boldsymbol{R}\boldsymbol{C}_\mathrm{u}\boldsymbol{X}\boldsymbol{C}_\mathrm{u}^T) \tag{50}$$

$$\mathit{subject\ to}\, Y_i = \boldsymbol{C}_i\boldsymbol{X}\boldsymbol{C}_i^T \le \overline{Y}_i, \quad i = 1,2,\ldots,n_y \tag{51}$$

where $\boldsymbol{R}$ is the control penalty matrix, $E_\infty = \lim_{t\to\infty} E$ with E the expectation operator and $\boldsymbol{C}_i$ is the i^{th} row in the $\boldsymbol{C}_p$ matrix. In the interest of completeness, the OVC algorithm used for OCT's flight control design is given next [91]-[92].

Algorithm 3: *OVC algorithm*

For the given data $(\boldsymbol{A}_p, \boldsymbol{B}_p, \boldsymbol{C}_p, \boldsymbol{D}_p, \boldsymbol{M}_p, \overline{Y}_i, \boldsymbol{W}_p, \boldsymbol{V}, \boldsymbol{R}, \boldsymbol{Q}_0, n, N_{\max}, \epsilon)$

where $\boldsymbol{Q}_0$ is the initial guess of the state penalty matrix, $N_{\max}$ is the number of allowed iterations, and ϵ is the convergence tolerance, proceed as follows:

(1) Compute $\boldsymbol{F}$ using the continuous-time algebraic Riccati equation (CARE):

$$\boldsymbol{A}_p\tilde{\boldsymbol{X}} + \tilde{\boldsymbol{X}}\boldsymbol{A}_p^T - \tilde{\boldsymbol{X}}\boldsymbol{M}_p^T\boldsymbol{V}^{-1}\boldsymbol{M}_p\tilde{\boldsymbol{X}} + \boldsymbol{D}_p\boldsymbol{W}_p\boldsymbol{D}_p^T = 0$$

then $\boldsymbol{F} = \tilde{\boldsymbol{X}}\boldsymbol{M}_p^T\boldsymbol{V}^{-1}$.

(2) Compute $\boldsymbol{K}_j$ and $\boldsymbol{G}_j$ at the *j*th iteration step using the CARE:

$$\boldsymbol{A}_p^T\boldsymbol{K}_j + \boldsymbol{K}_j\boldsymbol{A}_p - \boldsymbol{K}_j\boldsymbol{B}_p\boldsymbol{R}^{-1}\boldsymbol{B}_p^T\boldsymbol{K}_j + \boldsymbol{C}_p^T\boldsymbol{Q}(j)\boldsymbol{C}_p = 0$$

then $\boldsymbol{G}_j = -\boldsymbol{R}^{-1}\boldsymbol{B}_p^T\boldsymbol{K}_j$.

(3) Compute $\boldsymbol{X}_j$ using the Lyapunov equation

$$(\boldsymbol{A}_p + \boldsymbol{B}_p\boldsymbol{G}_j)\boldsymbol{X}_j + \boldsymbol{X}_j(\boldsymbol{A}_p + \boldsymbol{B}_p\boldsymbol{G}_j)^T + \boldsymbol{F}\boldsymbol{V}\boldsymbol{F}^T = 0.$$

Set $Y_i(j) = \boldsymbol{C}_i(\tilde{\boldsymbol{X}} + \boldsymbol{X}_j)\boldsymbol{C}_i^T, i = 1, 2 \ldots, n_y$,

If $\sum_{i=1}^{n_y} \left\| \left(\overline{Y}_i - Y_i(j)\right) Q_{ii}(j) \right\| \le \epsilon$ or $j = N_{\max}$, stop tuning $\boldsymbol{Q}(j)$. Otherwise,

(4) Update $\boldsymbol{Q}(j)$ with

$$\boldsymbol{Q}_{ii}(j+1) = \left[\frac{\boldsymbol{C}_i(\boldsymbol{X}_j + \tilde{\boldsymbol{X}})\boldsymbol{C}_i^T}{\overline{Y}_i}\right]^n \boldsymbol{Q}_{ii}(j),$$

set *j*=*j*+*1* and go to step **(2)**.

The state matrix of the controller (47) is then

$$A_c = A_p + B_pG - FM_p \tag{52}$$

It is important to note that the minimum achievable output variance bounds can be computed a-priori, before OVC design is performed. These are given by

$$\left\{\bar{Y}_{i_{min}}\right\}_{i=1,2,\dots,n_y} = diag\left[C_p\tilde{\boldsymbol{X}}C_p^T\right] \tag{53}$$

Therefore, $\bar{Y}_i$ can be selected such that

$$\left\{\bar{Y}_i\right\}_{i=1,2,\dots,n_y} = a \times diag\left[C_p\tilde{\boldsymbol{X}}C_p^T\right],\ a > 1 \tag{54}$$

where *a* is a scaling factor of the minimum achievable output variance bounds. This enables investigation of the influence of these bounds on the OVC performance.

5.3.2 Selection of Design Parameters

Note that all states and control inputs have different units and a wide range of magnitudes. Therefore, the linearized system (45) has been normalized as follows: all linear velocities have been divided through by the tip blade velocity, ΩR, angular velocities by dividing them through the nominal angular rate of the rotor, Ω, and all lengths by dividing them through by the blade radius, *R*. In this dissertation the rotor diameter is 20 m, the swept area is 314 m^2, the turbine mass is 4.98x10^5 kg, the turbine displaces 5.07x105 kg mass of seawater, the rotor mass is 6.16x10^4 kg, and the rotor mass moment of inertia about rotor axis is 5.39x10^5 kg.m^2. Eq. (46) is rewritten in the form of the normalized LTI system:

$$\begin{bmatrix} \dot{\bar{u}}\,R\Omega^2 \\ \dot{\bar{v}}\,R\Omega^2 \\ \dot{\bar{w}}\,R\Omega^2 \\ \dot{\bar{p}}_b\,\Omega^2 \\ \dot{\bar{p}}_r\,\Omega^2 \\ \dot{\bar{q}}_b\,\Omega^2 \\ \dot{\bar{r}}_b\,\Omega^2 \\ \dot{\bar{X}}\,R\Omega \\ \dot{\bar{Y}}\,R\Omega \\ \dot{\bar{Z}}\,R\Omega \\ \dot{\bar{\phi}}\,\Omega \\ \dot{\bar{\theta}}\,\Omega \\ \dot{\bar{\psi}}\,\Omega \end{bmatrix} = \boldsymbol{A}\begin{bmatrix} \bar{u}\,R\Omega \\ \bar{v}\,R\Omega \\ \bar{w}\,R\Omega \\ \bar{p}_b\,\Omega \\ \bar{p}_r\,\Omega \\ \bar{q}_b\,\Omega \\ \bar{r}_b\,\Omega \\ \bar{X}\,R \\ \bar{Y}\,R \\ \bar{Z}\,R \\ \bar{\phi} \\ \bar{\theta} \\ \bar{\psi} \end{bmatrix} + \boldsymbol{B}\begin{bmatrix} \gamma_a \\ \gamma_b \\ \bar{\tau}_{em}\,0.5\rho R\bar{U}_M^2 AR \end{bmatrix} + \boldsymbol{Dw} \tag{55}$$

where *ρ* is the density of seawater, *R* is the rotor radius, and *AR* is the swept area of the rotor. Eq. (55) is rewritten in the form of the normalized LTI system:

$$\begin{aligned} \dot{\bar{\boldsymbol{x}}}_p(t) &= \bar{\boldsymbol{A}}_p\dot{\bar{\boldsymbol{x}}}_p(t) + \bar{\boldsymbol{B}}_p\bar{\boldsymbol{u}}(t) + \bar{\boldsymbol{D}}_p\bar{\boldsymbol{w}}_p(t) \\ \bar{\boldsymbol{y}}_p(t) &= \bar{\boldsymbol{C}}_p\bar{\boldsymbol{x}}_p(t) \\ \bar{\boldsymbol{z}}(t) &= \bar{\boldsymbol{M}}_p\bar{\boldsymbol{x}}_p(t) + \bar{\boldsymbol{v}}(t) \end{aligned} \tag{56}$$

where $\bar{\boldsymbol{x}}_p, \bar{\boldsymbol{u}}, \bar{\boldsymbol{y}}_p, \bar{\boldsymbol{z}}, \bar{\boldsymbol{w}}_p, \bar{\boldsymbol{v}}$ are non-dimensional plant states, control inputs, outputs, sensor measurements, process noise, and measurement noise, respectively.

The vector of measurements, $\boldsymbol{z}$, was formed by translational/angular velocities, Euler angles, Cartesian coordinates of the OCT in the North-East-Down $Ox_N y_E z_D$ frame, rotor angular speed, and azimuth angle of a certain blade which is usually referred to as the first (or leading) rotor blade. The control inputs are longitudinal/lateral cyclic pitch angles and electromechanical torque. The vector of outputs, $\boldsymbol{y}$, consists of two OCT Cartesian coordinates, y_E and z_D, and the rotor angular speed Ω. Zero-mean uncorrelated process and measurement Gaussian white noises, $\boldsymbol{w}_p$ and $\boldsymbol{v}$ with intensities $\bar{\boldsymbol{W}}_p = \bar{\boldsymbol{V}} = 10^{-6}\boldsymbol{I}_{13}$ were added to the corresponding equations in agreement with (56), taking $\boldsymbol{D}_p = \boldsymbol{I}$. Here $\boldsymbol{I}$ is the identity matrix of the corresponding size.

The minimum achievable output variance bounds were computed first and then the OVC design algorithm applied for various values of the scaling factor *a* in (54). This generated a family of OVC controllers numerically parameterized by *a*, which enabled an analysis of the variation of the control energy with *a*. Fig. 56 shows the control energy variation with the scaling factor *a*. We can see that the larger the scaling factor is (i.e. the output variance constraints are softened), less control energy is required. When *a* approaches 1 the control energy becomes very large because the theoretically achievable output variance bounds are approached. Thus a trade-off must be made between the output variance constraints that need to be satisfied and the control energy necessary to satisfy these constraints.

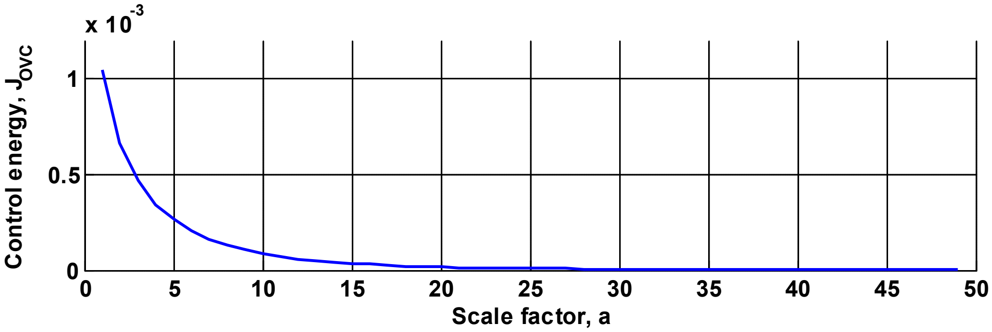

Fig. 56 Control energy of the normalized system J_{OVC} with the scale factor

In the Algorithm 3, the control input weighting matrix $\boldsymbol{R}$ and process noise covariance matrix $\boldsymbol{W_p}$ can be properly tuned to meet the performance requirements, such as: the rotor angular speed and position regulation errors are small, the external disturbances should be as high as possible while the closed-loop system still satisfy the desired output variance constraints and avoid blade stall.

Process Noise Covariance Matrix

The process noise covariance characterizes how much the external disturbances change around their mean values. There is a trade-off between the output variance constraints and the process noise covariance the system can tolerate. For example, the increase of the process noise covariance can lead to a large blade pitch control to mitigate the disturbance effects in satisfying the output variance constraints. However, the large pitch control can cause the blades to stall and then dramatically reduce the rotor efficiency as well as the power generation efficiency of the OCTs. In this dissertation, the blade pitch angles are limited to magnitudes of 10 deg to avoid blade stall.

Fig. 57-58 present an investigation of the maximum blade pitch angles for different process noise covariance values at a given scale factor, *a*, and control input weighting matrix, $\boldsymbol{R} = \boldsymbol{I}_{3x3}$. In Fig. 57, we can see that the closed-loop system can tolerate any disturbances with noise covariance less than $1.44x10^{-6}\boldsymbol{I}$. The control system regulates the OCT position and the rotor angular speed with maximum deviations of 6.9 m lateral, 6.5 m vertical, and 0.5 rpm from the trim values respectively. When the OVC control disengages, the OCT is disturbed by 21.5 m lateral and 12.1 m vertical with respect to the original position over the simulation period of 30 minutes.

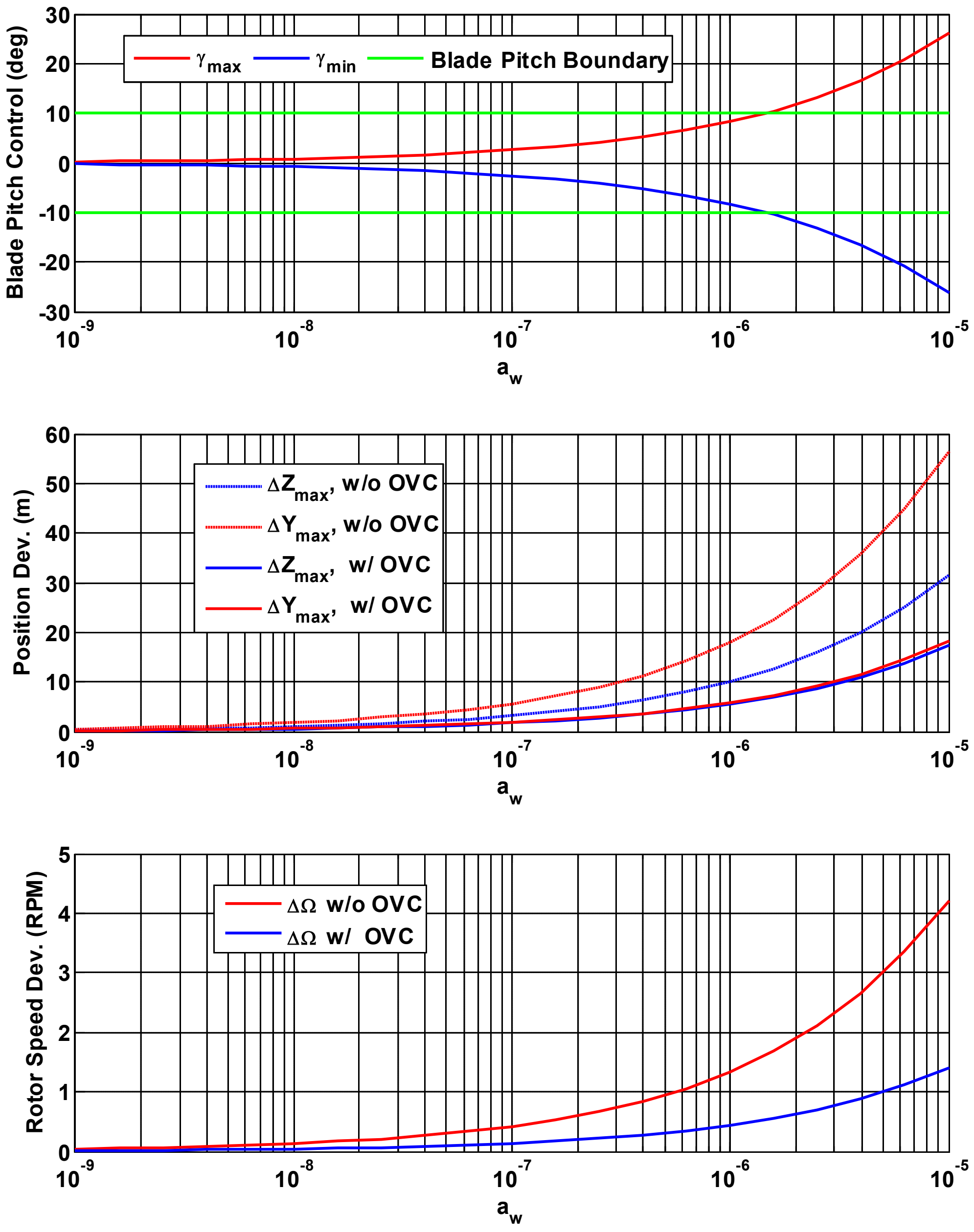

Fig. 57 Minimum and maximum blade pitch control, maximum position deviation, and maximum rotor angular speed deviation for different process noise covariance magnitudes, $a = 5$, $R = I_{3x3}$

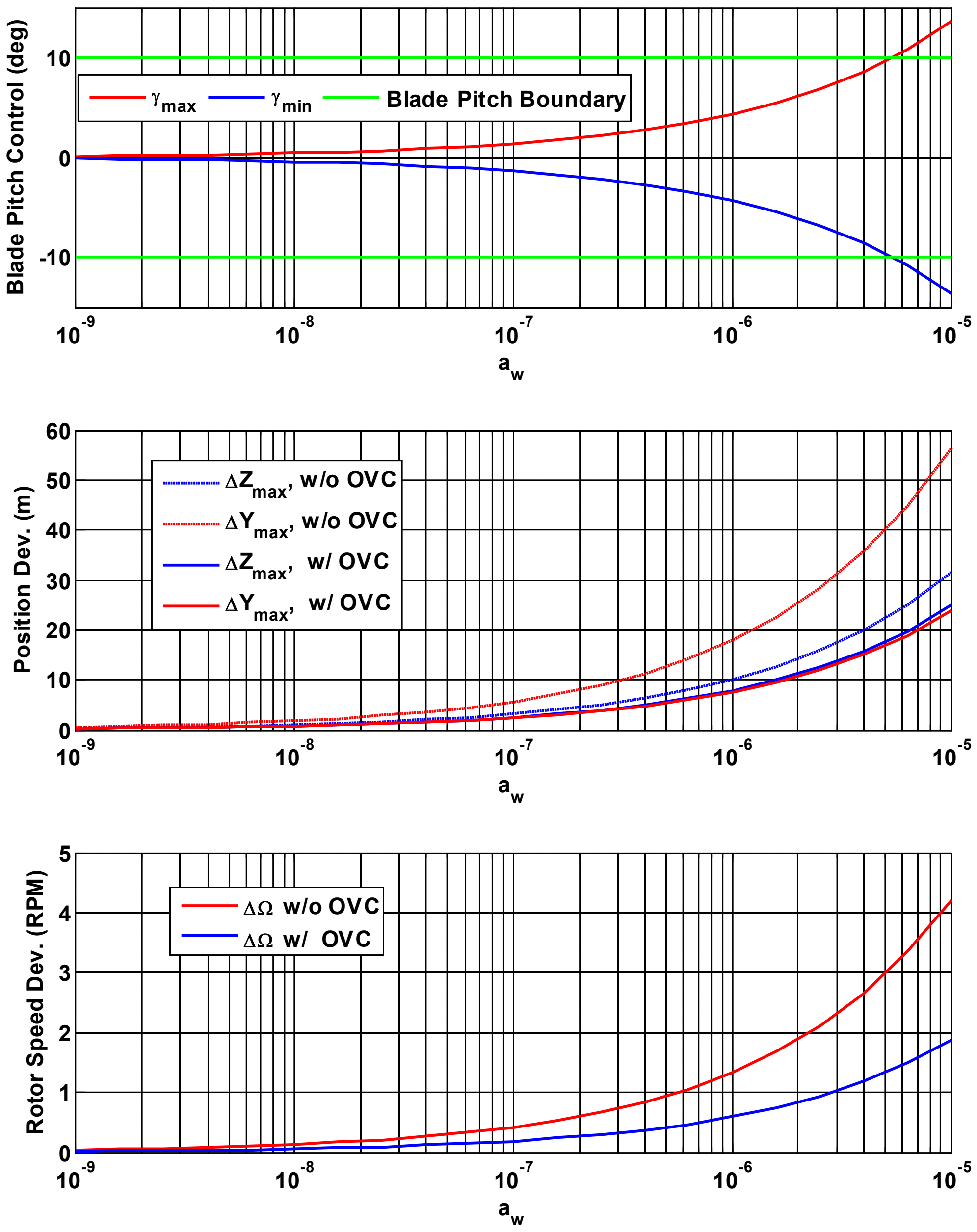

Fig. 58 Minimum and maximum blade pitch control, maximum position deviation, and maximum rotor angular speed deviation for different process noise covariance magnitudes, $a = 10$, $R = I_{3x3}$

Control Input Weighting Matrix

In OVC control design, the output penalty matrix $\boldsymbol{Q}$ is optimally tuned to satisfy the output variance constraints in comparison with the standard LQG design. However, the control weighting matrix $\boldsymbol{R}$ in (57) must be defined before the OVC design is performed.

The CARE2 equation and the control gain matrix $\boldsymbol{G}_j$ in the Algorithm 3 are regenerated as follows

$$\boldsymbol{A}_p^T \boldsymbol{K}_j + \boldsymbol{K}_j \boldsymbol{A}_p - \boldsymbol{K}_j \boldsymbol{B}_p \boldsymbol{R}^{-1} \boldsymbol{B}_p^T \boldsymbol{K}_j + \boldsymbol{C}_p^T \boldsymbol{Q}(j) \boldsymbol{C}_p = 0 \tag{57}$$

$$\boldsymbol{G}_j = -\boldsymbol{R}^{-1} \boldsymbol{B}_p^T \boldsymbol{K}_j \tag{58}$$

We must tune positive weights on the control input to avoid blade stall while the control system achieves the desired output variance constraints. A simple tuning approach is to scale up the $\boldsymbol{R}$ matrix by a factor α, i.e. $\boldsymbol{R} = \lambda \boldsymbol{R}_0$. However,

$$\max(svd(\boldsymbol{A}_p^T \boldsymbol{K})) \approx 1.99 \times 10^4 \max(svd(\boldsymbol{C}_p^T \boldsymbol{Q} \boldsymbol{C}_p)),\ \ \lambda = 1,10,\ldots,100$$

Hence, the equation (57) is equivalent to

$$\begin{aligned}
0 &\approx \boldsymbol{A}_p^T \boldsymbol{K} + \boldsymbol{K}\boldsymbol{A}_p - \boldsymbol{K}\boldsymbol{B}_p \boldsymbol{R}^{-1} \boldsymbol{B}_p^T \boldsymbol{K} \\
0 &\approx \boldsymbol{A}_p^T \boldsymbol{K} + \boldsymbol{K}\boldsymbol{A}_p - \boldsymbol{K}\boldsymbol{B}_p \left(\lambda \boldsymbol{R}_0\right)^{-1} \boldsymbol{B}_p^T \boldsymbol{K} \\
0 &\approx \boldsymbol{A}_p^T \left(\boldsymbol{K}\lambda^{-1}\right) + \left(\boldsymbol{K}\lambda^{-1}\right)\boldsymbol{A}_p - \left(\boldsymbol{K}\lambda^{-1}\right)\boldsymbol{B}_p \boldsymbol{R}_0^{-1} \boldsymbol{B}_p^T \left(\boldsymbol{K}\lambda^{-1}\right) \\
0 &\approx \boldsymbol{A}_p^T \boldsymbol{K}_0 + \boldsymbol{K}_0 \boldsymbol{A}_p - \boldsymbol{K}_0 \boldsymbol{B}_p \boldsymbol{R}_0^{-1} \boldsymbol{B}_p^T \boldsymbol{K}_0
\end{aligned}$$

Therefore, the control matrix $\boldsymbol{G}$ does not change significantly when tuning the scale factor α. Another tuning approach is proposed for the $\boldsymbol{R}$ matrix as follows:

$$\boldsymbol{R} = \begin{array}{c} \begin{array}{ccc} \gamma_a & \gamma_b & \tau_{em} \end{array} \\ \begin{bmatrix} \lambda & 0 & 0 \\ 0 & \lambda & 0 \\ 0 & 0 & 1 \end{bmatrix} \end{array} \tag{59}$$

Fig. 59 presents an investigation of the maximum blade pitch angles for different control input weighting matrices at a given scale factor $a = 5$ and noise covariance $\boldsymbol{W} = 1.4\text{x}10^{-6}\boldsymbol{I}$. We select $\lambda = 0.25$ to ensure the maximum blade pitch angles in the range of ±10 deg to avoid blade stall.

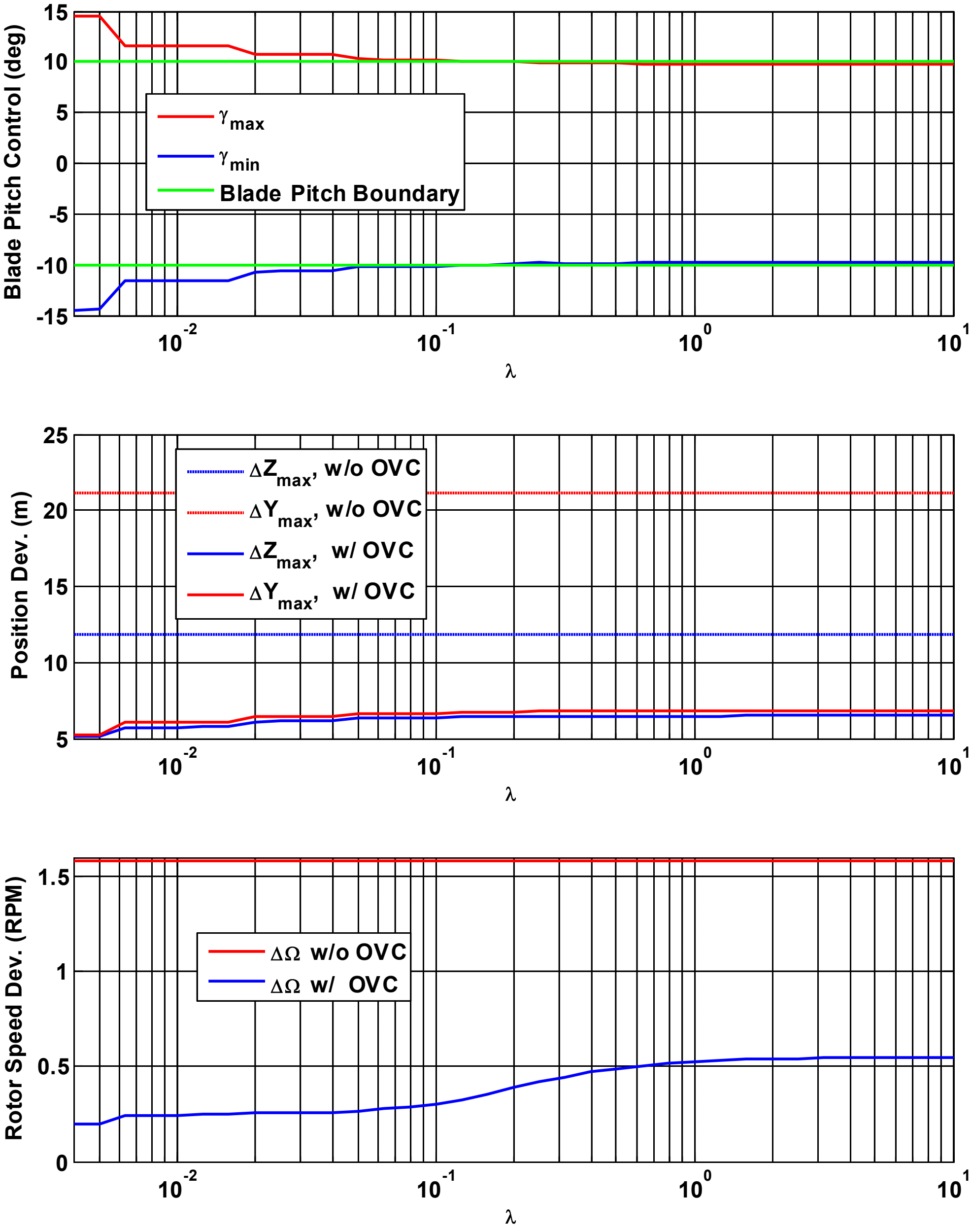

Fig. 59 Minimum and maximum blade pitch control, maximum position deviation, and maximum rotor angular speed deviation for different process noise covariance magnitudes, *a* = 5, $W_p = 1.4\text{x}10^{-6}\boldsymbol{I}$

5.3.3 Numerical Simulations

5.3.3.1 Linear Simulations

For illustrative purposes, an OVC control design with parameters $a = 5$, $\alpha = 0.25$, $\boldsymbol{W} = 1.4\text{x}10^{-6}\boldsymbol{I}$ is selected. Fig. 60 shows that all eigenvalues of the linear closed loop system have negative real parts, as expected because OVC is an exponentially stabilizing controller. Note that the data reported next refers to the linear system's performances for 2 scenarios in which the closed loop responses to initial perturbation and white noise disturbances are investigated.

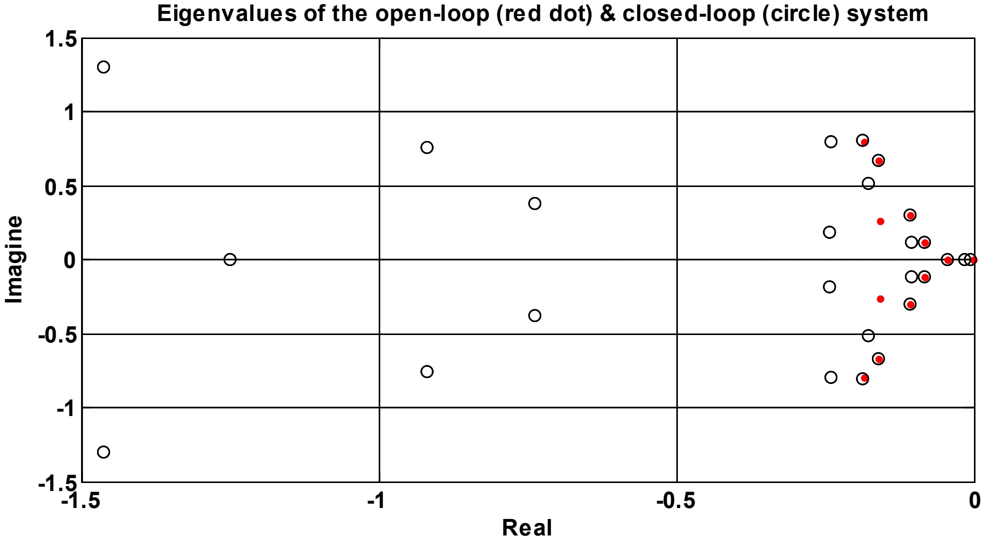

Fig. 60 Eigenvalues of the open loop (red dot) and the closed loop (circle) normalized system

Fig. 61 shows the OVC performance when the OCT is initially disturbed by 5 m lateral and 5 m vertical with respect to the original position. The OVC controller restores the OCT to its original position 10 minutes after the perturbation is applied. By comparison, if the OCT is not equipped with the OVC controller, i.e. in the open loop simulations, it takes 1.67 hours for the perturbed lateral and vertical positions to return to their values. In the closed-loop, the rotor blades experience individual pitch angles in the range of ±8 deg. The maximum deviation from the trim value of the electromechanical torque is 11%. The rotor angular speed variation during the maneuver is very small, with a maximum deviation of about 0.35 rpm.

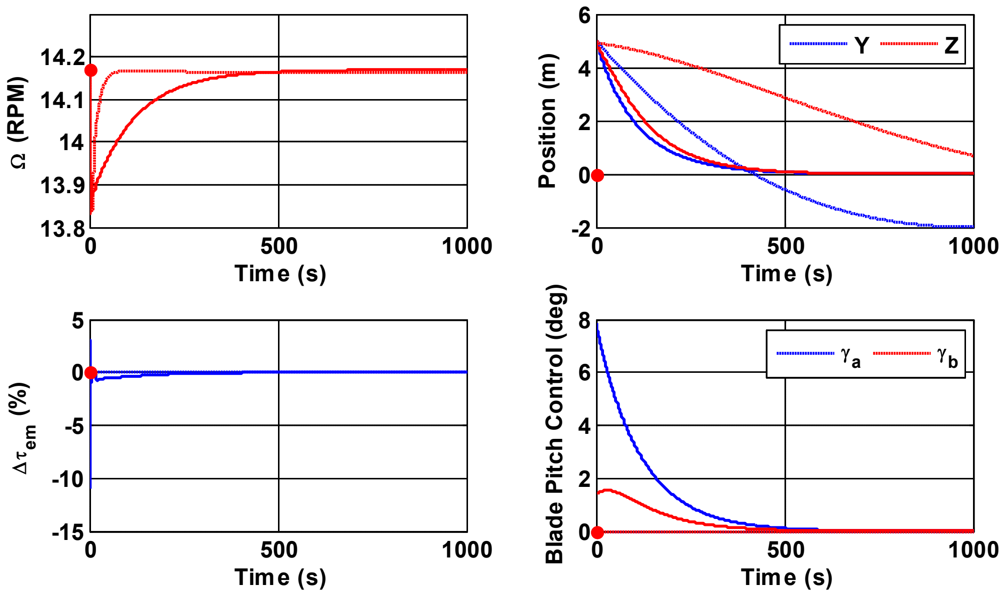

Fig. 61 Time histories of the OCT's angular speed, position, and control input

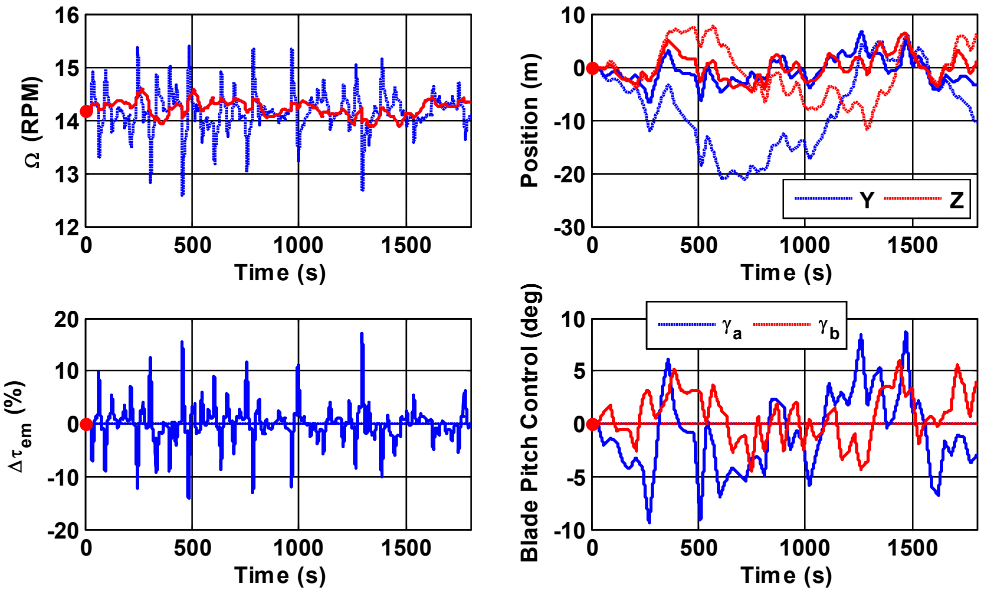

Fig. 62 Time histories of the OCT's angular speed, position, and control inputs in the presence of disturbances (solid lines: closed loop, dash lines: open loop), *a* = 5

Fig. 62 shows time histories of the closed loop OCT system in the presence of white noise disturbances with the same intensity as the one used in the OVC control system design process. The simulations display expected bounded behavior with numerous frequencies because the white noise signal excites all system modes. The maximum deviation from the trim value of the OCT position is 6.7 m in the lateral direction, 6.5 m in the vertical one.

The rotor angular speed variation during the maneuver is very small, with a maximum deviation of about 0.4 rpm.

We remark that in Fig. 61-62, the angles labeled "blade control" refer to values of the blade pitch root angle with respect to the value of this angle corresponding to the operation in which maximum power production for the designed tip speed ratio is achieved. The airfoils on this blade are twisted with respect to the blade root section along the blade with twist angles varying between 18.5° near the rotor hub and 0.6° at the blade tip. The blade pitch root angles displayed in Fig. 61-62 exhibit large variations, which may cause the airfoils to stall in some cases. The angles of attack of the individual airfoil sections, which determine the onset of stall, are functions of the blade twist, particular blade design, operating conditions, etc. Therefore, further research should investigate if blade stall truly occurs and how blade stall may be avoided at all points along the blade. This investigation should be carried out in the context of the global nonlinear OCT dynamics. In fact, our extensive numerical investigations using other values of the parameter a (for examples, Fig. 63-64) revealed that the blade pitch root angles variation increase. This shows that the danger of stall increases when more stringent OVC constraints are imposed, i.e. when smaller values of the parameter a are used in OVC control design. This is in agreement with the observation that the control energy also increases when small values of the parameter a are used and can be physically explained by the fact that to achieve large control energy large deflections of the blade pitch angles are required. A potential solution for this problem is to include collective blade pitch control in the vector of active controls used to design the OVC controller for OCT, in analogy with the same control action used on helicopter blade control. This may also lead to lower achievable output variance bounds. It is also possible that a different control strategy that is inherently more constrained such as Model Predictive Control may yield improved performance in simultaneous satisfaction of multiple constraints.

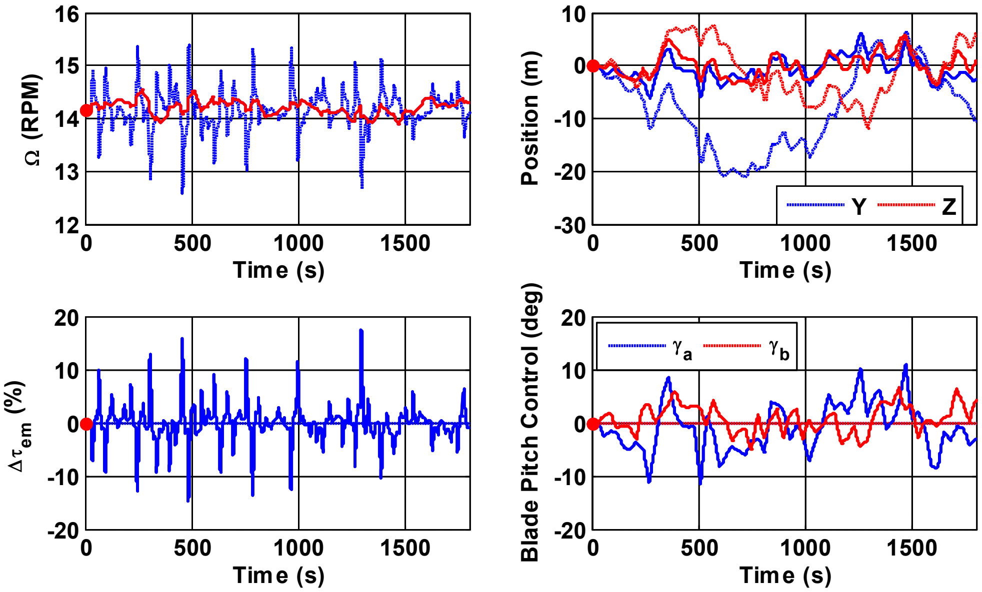

Fig. 63 Time histories of the OCT's angular speed, position, and control inputs in the presence of disturbances (solid lines: closed loop, dash lines: open loop), $a = 4$

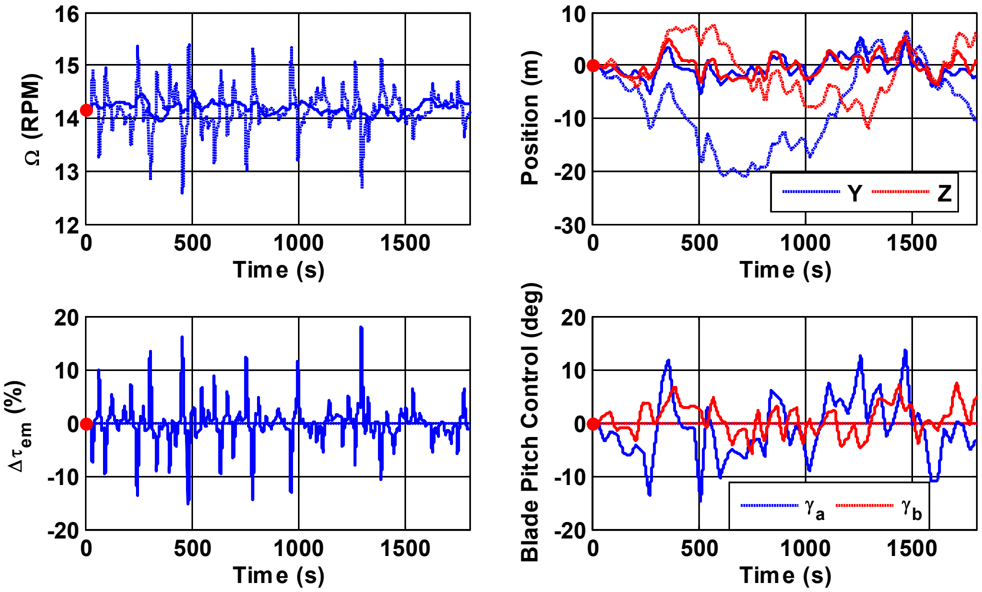

Fig. 64 Time histories of the OCT's angular speed, position, and control inputs in the presence of disturbances (solid lines: closed loop, dash lines: open loop), $a = 3$

5.3.3.2 Nonlinear Simulations

This section presents a comparison of the OVC performance evaluations with the nonlinear model in Section 5.1.1 and the linear model in Section 5.2.1. The OCT is initially disturbed by 5 m lateral and 2 m vertical from the original position. Fig. 65-66 show that the OVC controller restores the OCT to its original position within 8 minutes in the linear and nonlinear responses.

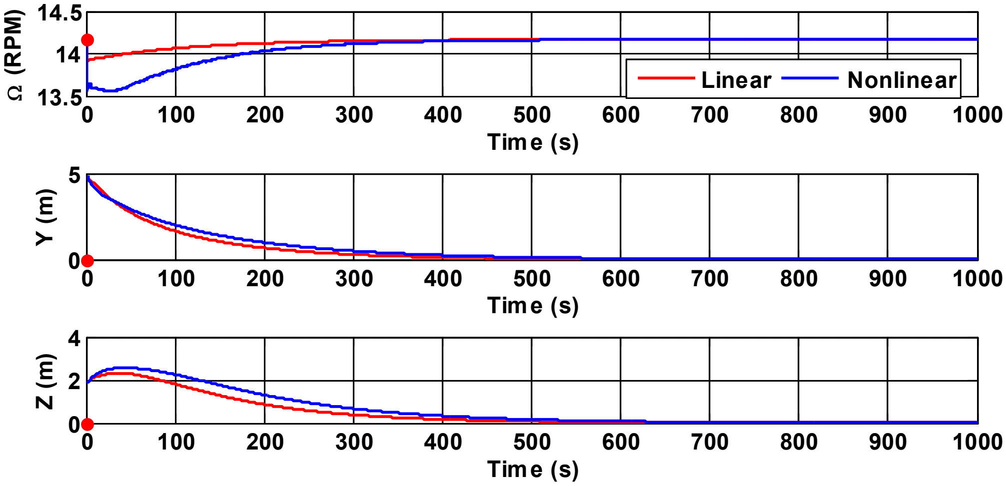

Fig. 65 Time histories of the OCT's angular speed and position in response to initial disturbances in Y and Z coordinates

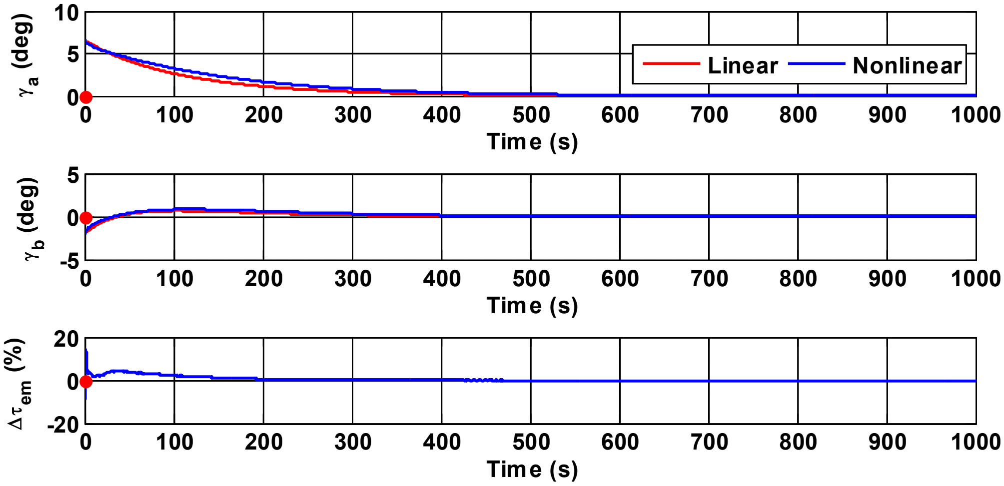

Fig. 66 Time histories of the OCT's control inputs in response to initial disturbances in Y and Z coordinates

5.4 OVC Design for Sensor Failures

5.4.1 Positioning sensor failure

In the previous section, the states used to describe the dynamics of the OCT system were: the linear and angular velocities of the OCT main body in the body fixed reference frame, labeled u, v, w, p_b, q_b, r_b; the angular velocity of the rotor with respect to the OCT main body, labeled p_r; the Cartesian coordinates of the OCT with respect to an inertial reference frame, labeled X, Y, Z; the azimuth angle α of the 1st rotor blade measured with respect to a fixed direction in the plane of the rotor; three Euler angles describing the orientation of the OCT main body with respect to the inertial reference frame, labeled ϕ, θ, ψ. In an ideal situation all these states are assumed to be measurable for example using inertial sensors and the GPS. In reality, the Cartesian coordinates of the OCT are difficult to measure due to the lack of GPS signal in deep water. An inertial navigation system (INS) can be a practical substitute for the GPS, by using inertial sensors and a Kalman observer to estimate the OCT position. However, INS may result in large errors because of the large uncertainties associated with OCT drift, ocean currents, etc. The use of several transponders on the seabed, in combination with the INS, can increase the accuracy of the positioning system. Nevertheless, sensor failure can easily occur and affect the operation of OCTs. Therefore, in this dissertation, the OVC control system is also designed in the case the positioning sensor failures occur. Then, the measured outputs in (46) is rewritten as

$$\boldsymbol{z} = [u\ v\ w\ p_b\ p_r\ q_b\ r_b\ \phi\ \theta\ \psi]^T + \boldsymbol{v}(t) \tag{60}$$

As we mentioned in Section 5.3, the design of an OVC controller reduces to the selection of the output penalty matrix $\boldsymbol{Q}$ in standard LQG design such that the output variance constraints are satisfied. As a requirement of the LQG-based control, stabilizability and detectability are required for the OVC control design for the OCT with sensor failures to succeed. We note that the system (45) with the positioning sensor failure (60) is detectable. This has been ascertained using the PBH test. Therefore, OVC design can proceed in the same manner as when all measurements were available.

In this subsection, the OVC control system is re-designed using the reduced set of sensors (60) and its performance is evaluated using the linearized OCT model. Two scenarios are considered: 1) The OCT is initially disturbed by 5 m lateral and 5 m vertical with respect to the original position; 2) The OCT is persistently disturbed by white noise disturbances with the same intensity used in the nominal OVC control design. The same controller's parameters as in the previous design and simulations (i.e. subsection 5.3) are used. Fig. 67 shows a comparison of the closed loop simulations for the sensor failure case (solid lines) with the nominal case (dotted lines) subjected to an initial perturbation in position. Fig. 68 shows a comparison of the closed loop simulations for the sensor failure case (solid lines) with the nominal case (dotted lines) in the presence of the white noise disturbances. It can be seen that there are negligible degrading effects of the sensor failures on the system performance. In Fig. 68, the rotor blades experience individual pitch angles in the range of ±8 deg. The maximum value of the electromechanical torque is about 18% of the trim value. The rotor angular speed variation during the maneuver is very small, with a maximum deviation of about 0.5 rpm. The OCT's position is regulated around the magnitude of 8 m from the original position. Fig. 69 shows that the Euler angles of the OCT are stabilized around their trim values. The closed-loop system with the positioning sensor failure still achieves good performance because it uses the information from rate gyros and accelerometers to estimate the OCT's position. In the next simulation, the failure of both the positioning sensor and the accelerometers are investigated.

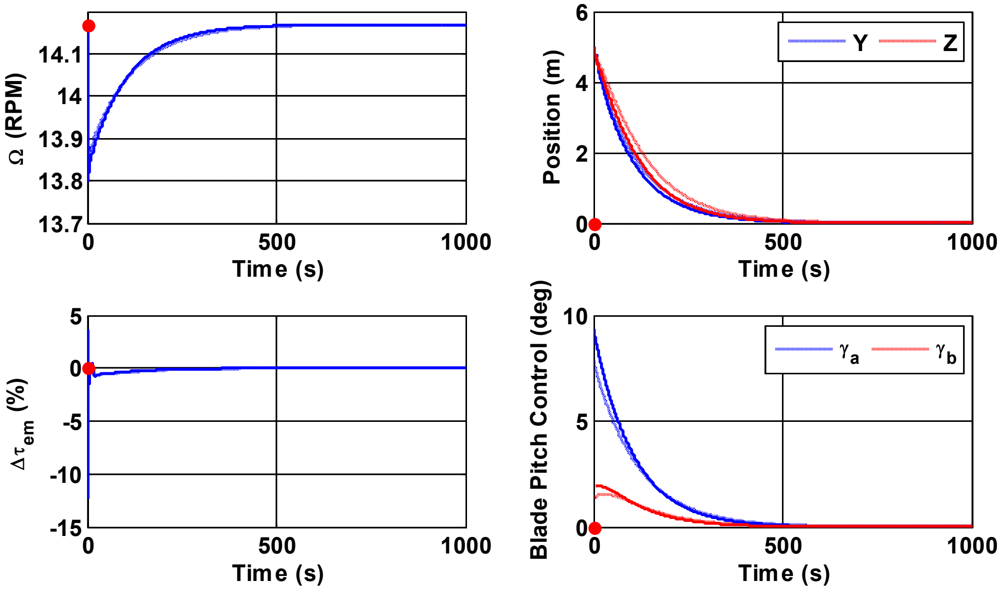

Fig. 67 Time histories of the OCT's angular speed, position, and control input (solid lines: sensor failures, dotted lines: no failure)

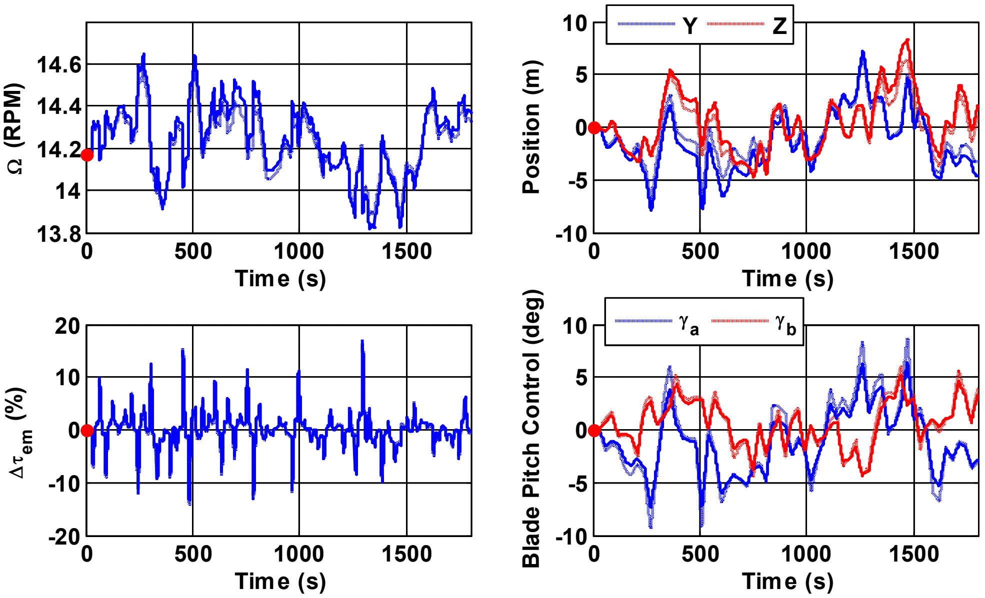

Fig. 68 Time histories of the OCT's angular speed, position, and control inputs in the presence of disturbances (solid lines: sensor failures, dotted lines: no failure)

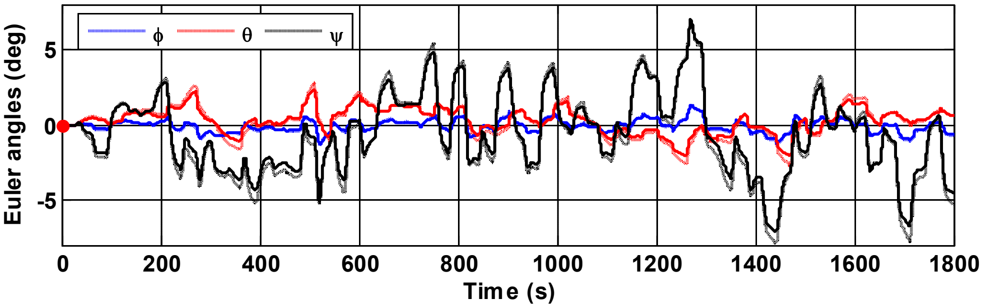

Fig. 69 Euler angles of the OCT in the presence of disturbances (solid lines: sensor failures, dotted lines: no failure)

5.4.2 Positioning sensor and accelerometer failure

In this subsection the OVC control system is re-designed in case of the positioning sensor and accelerometer failure. Then, the measured outputs in (46) is rewritten as $\boldsymbol{z} = [p_b\ p_r\ q_b\ r_b\ \phi\ \ \theta\,\psi]^T + \boldsymbol{v}(t)$. We note that the resulting system is detectable. Fig. 70-71 shows the time history of the closed-loop responses of the OCT for the rate gyros failure case. From Fig. 70, the maximum deviation of the OCT is about 9 m, larger than the value of 6.7 m for the nominal case. The OVC employs more torque (18%), and large blade pitch control input (9 deg) to stabilize the system in the same white noise disturbance used for the nominal case.

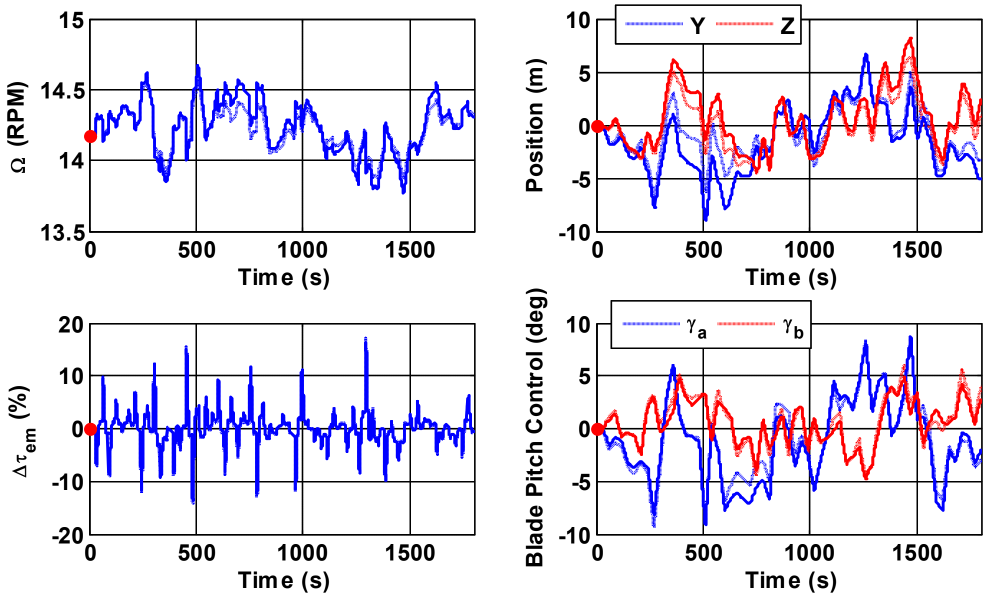

Fig. 70 Time histories of the OCT's angular speed, position, and control inputs in the presence of disturbances (solid lines: sensor failures, dotted lines: no failure)

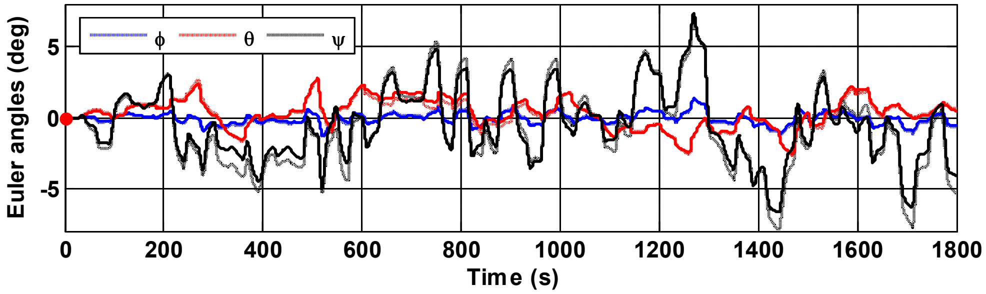

Fig. 71 Euler angles of the OCT in the presence of disturbances, sensor failures

Our investigations using other values of the parameter *a* revealed that the danger of stall increases when more stringent OVC constraints are imposed, i.e. when smaller values of *a* are used in OVC design. This is in agreement with the observation that the control energy also increases when small values of *a* are used and can be physically explained by the fact that to achieve larger control energy large deflections of the blade angles are required. Of course this has two major consequences: stall conditions may be reached and the linearized model based on which control design was performed is no longer valid. A potential solution for this problem is to include collective blade pitch control in the vector of active controls used to design the OVC controller for OCT, in analogy with the same control action used on helicopter blade control. This may lead to lower achievable output variance bounds as well to a reduced danger of stall. It is also possible that a different control strategy that is inherently more constrained such as MPC may yield improved performance.

5.5 Model Predictive Control

In the MPC approach, the behavior of the OCT system over a future prediction horizon starting at each time step is predicted by an internal model, then an optimization algorithm finds a control sequence that minimizes the performance measure (e.g., tracking error, control effort) while satisfying the system constraints. Only the first element of the control sequence is implemented as the input signal to the system at the current step. Then a new output measurement is updated and the technique is repeated at the new time step [75]. This section proposes a MPC design for the OCT flight control. Simulations of the automatic flight control of the OCT in the presence of white noise disturbances are performed to evaluate the feasibility of the MPC.

5.5.1 MPC Design

Following the standard MPC design, an objective function $V(k)$ is defined as:

$$V(k)=\sum_{i=0}^{H_p-1}\left(\sum_{j=1}^{p}w_{i+1,j}^{y}\left|\left(y_j(k+i+1\mid k)-r_j(k+i+1)\right)\right|^2+\sum_{j=1}^{m}w_{i+1,j}^{u}\left|u_j(k+i\mid k)\right|^2+\sum_{j=1}^{m}w_{i+1,j}^{\Delta u}\left|\Delta u_j(k+i\mid k)\right|^2\right) \tag{61}$$

The MPC action at time step k is obtained by solving the optimization problem subjected to the OCT dynamic equations (56) discretized with the sampling time T_s:

$$\begin{aligned}\boldsymbol{x}(k+1)&=\boldsymbol{A}\boldsymbol{x}(k)+\boldsymbol{B}\boldsymbol{u}(k)\\ \boldsymbol{y}(k)&=\boldsymbol{C}\boldsymbol{x}(k)+\boldsymbol{D}\boldsymbol{u}(k)\end{aligned} \tag{62}$$

In Eqs. (61) & (62), $\boldsymbol{x},\boldsymbol{r},\boldsymbol{u},\Delta\boldsymbol{u}$ represent vectors of system states, reference, inputs, and input increments, respectively, and represents the controlled outputs vector, e.g., $\boldsymbol{y}=\left[\Omega,Y,Z\right]^T$. The subscript ()*j* denotes the *j* component of a vector, (*k*+*i*|*k*) denotes the value predicted for time *k*+*i* using the values at time *k*, while *p*, *m*, H_p, H_u represent number of outputs, number of inputs, prediction horizon, and control horizon, respectively, and $w_{i+1,j}^{y}$, $w_{i+1,j}^{u}$, $w_{i+1,j}^{\Delta u}$ represent nonnegative weights for the corresponding variable.

The optimization problem also includes constraints on the inputs and the outputs of the system such as control saturations, and cyclic pitch control rate limits (slew rates). These are chosen based on the fact that the airfoils at the hub and the blade tip have the maximum coefficient lift values of 2.02 and 1.54 at angles of attack of 32° and 16.5° respectively (see Subsection 5.1.1). The electromechanical torque is allowed to vary its magnitude in the range of 20% of the nominal operating value so that the power characteristics of the OCT does not vary much in maneuvers. Operating frequencies for cyclic pitch control are limited by the bandwidth of the actuators that is typically between 10 and 40 rad/s [63]. In addition, output constraints are derived to maintain the OCT level flight in the ocean current. Based on this information, for the numerical examples herein, the following values were chosen:

$$\begin{aligned} &\left[|\gamma_a|,|\gamma_b|,|\tau_{em}|\right] \le \left[10\deg, 10\deg, 20\%\,\tau_{em}^{eq}\ Nm\right] \rightarrow \textit{input saturation} \\ &\left[|\dot{\gamma}_a|,|\dot{\gamma}_b|\right] \le \left[40, 40\right] \ \deg/s \rightarrow \textit{slew rates} \\ &\left[|\phi|,|\theta|,|\psi|\right] \le \left[10, 10, 10\right] \ \deg \rightarrow \textit{output constraints} \end{aligned} \tag{63}$$

Assumed sensor measurements in this dissertation for MPC design for OCT are translational/angular velocities, Euler angles, Cartesian coordinates of the OCT in the NED frame, rotor angular speed, and azimuth angle of the first rotor blade. The prediction horizon H_p = 50, the sampling time T_s = 0.01 s, the control horizon H_u = 10, and the weights $\boldsymbol{w}^{y} = \left[2/\Omega \quad 10/R \quad 25/R\right]^{T}$, $\boldsymbol{w}^{u} = \left[4 \quad 2 \quad 2/\left(0.5\rho R\bar{U}_{M}^{2}AR\right)\right]^{T}$, $\boldsymbol{w}^{\Delta u} = \left[1 \quad 1 \quad 1\right]^{T}$ in the performance measure (61) were selected to ensure good performance and disturbance rejection in the presence of external perturbations.

5.5.2 Linear Simulation

The MPC performance is evaluated and compared with the OVC control system using the linearized OCT model. The OCT is persistently disturbed by white noise disturbances with the intensity $\boldsymbol{W}$=2x10^{-6}$\boldsymbol{I}$. Fig. 72-73 show time histories of the OCT in response to the disturbance in a period of 30 minutes. Fig. 72 shows that the MPC and OVC strategies has the same performance. The maximum deviation from the original position is 8 m laterally and 8 m vertically. The rotor angular speed variation during the maneuver is very small, with a maximum deviation of about ±0.5 rpm. In contrast with the OVC strategy, the cyclic pitch angles in the MPC strategy displayed in Fig. 73 satisfy the control saturation when the process noise covariance exceeds the design value $\boldsymbol{W} < 1.44\text{x}10^{-6}\boldsymbol{I}$ in the subsection 5.3.2.

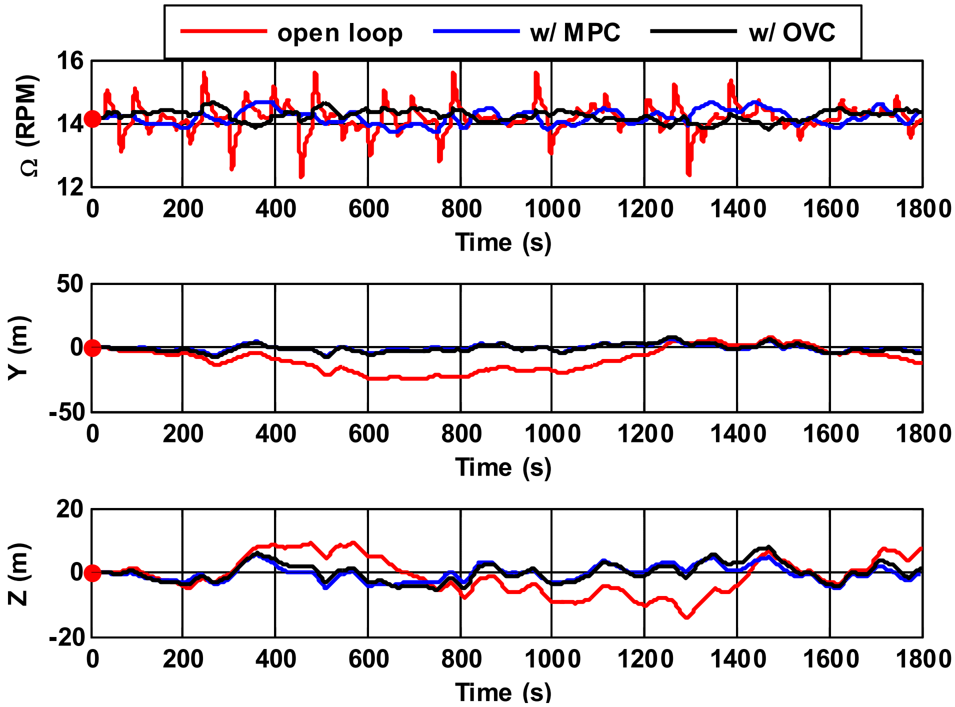

Fig. 72 Time histories of the OCT's angular speed and position in response to white noise disturbances $\boldsymbol{W} = 2\text{x}10^{-6}\boldsymbol{I}$

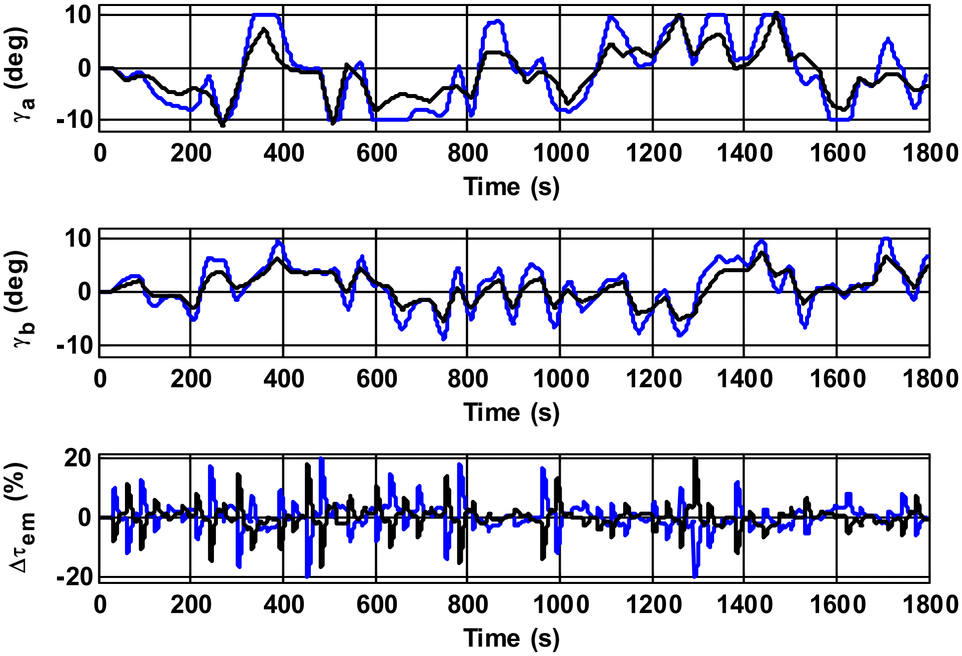

Fig. 73 Time histories of the OCT's control inputs in response to white noise disturbances $\boldsymbol{W} = 2\text{x}10^{-6}\boldsymbol{I}$

5.5.3 Nonlinear Simulation

The MPC performance is evaluated using the nonlinear OCT model. The OCT is initially disturbed by 5 m lateral and 2 m vertical with respect to the original position. Fig. 74-75 show a comparison of the MPC evaluations with the nonlinear model in Section 5.1.1 and the linear model in Section 5.1.2. The MPC controller restores the OCT to its original position within 6 minutes in the linear and nonlinear responses. Fig. 75 shows that more control effort is needed to regulate the nonlinear system after the initial disturbance is applied. All control constraints are satisfied in the MPC strategy.

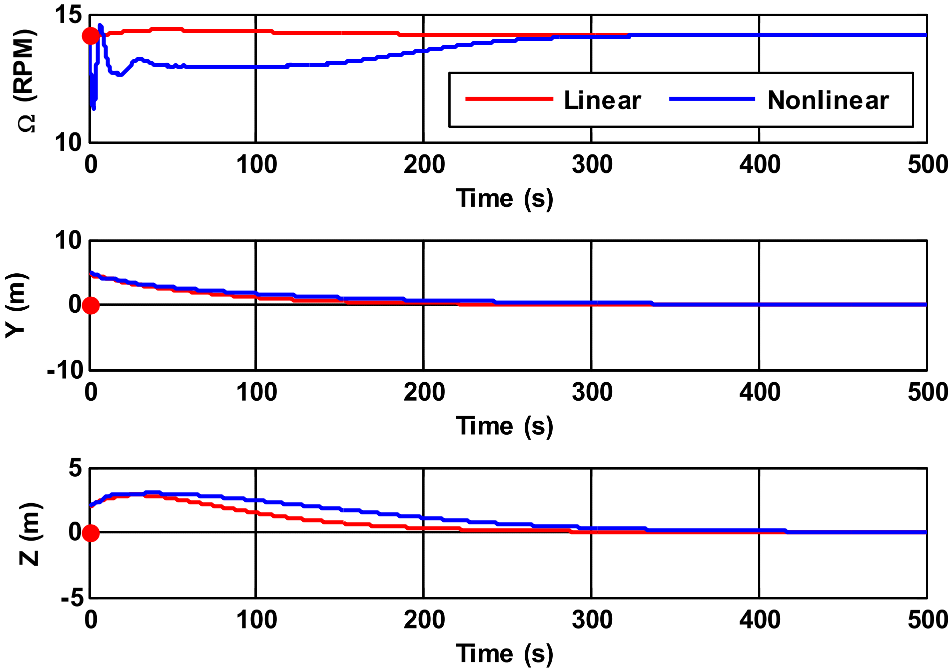

Fig. 74 Time histories of the OCT's angular speed and position in response to a perturbation in Y and Z direction

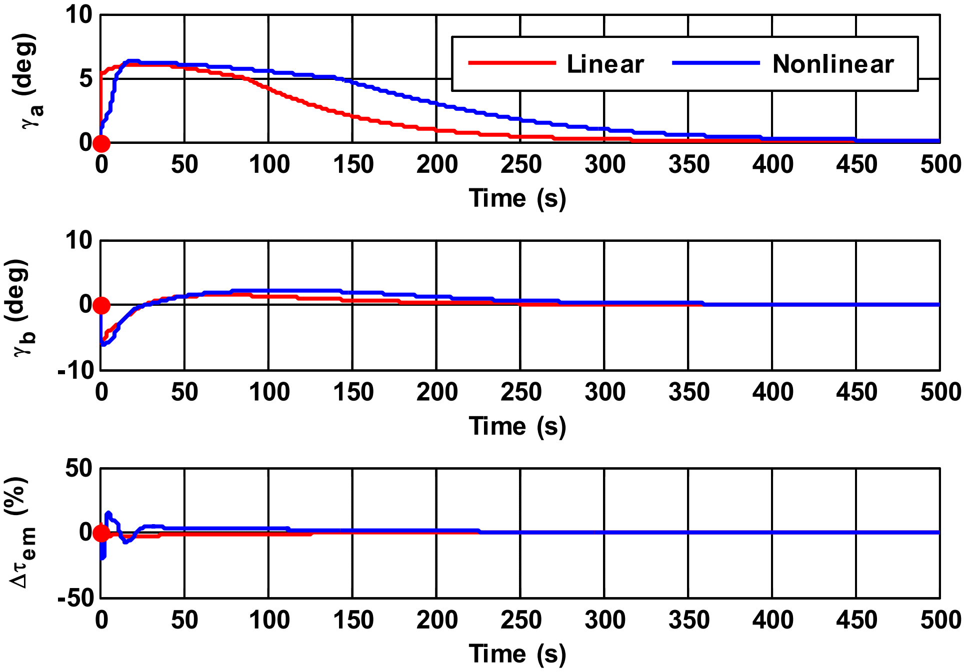

Fig. 75 Time histories of the OCT's control inputs in response to a perturbation in Y and Z direction

Chapter 6: Conclusions and Future Works

This dissertation focuses on advanced constrained control of two applications: helicopter and ocean current turbines (OCT). In the helicopter application, a complete helicopter/ship dynamic interface was developed and entirely implemented as a system of implicit nonlinear ordinary differential equations to facilitate shipboard operation control design, simulation, and evaluation. The interface includes control-oriented nonlinear helicopter and ship dynamics models and is versatile, accommodating various airwake models such as Control Equivalent Turbulence Inputs (CETI) model and Computational Fluid Dynamics (CFD) based model. The aerodynamic effects of both models were successfully embedded in the nonlinear helicopter dynamics. Hence, this interface generates realistic models of the ship-borne helicopter that can capture essential dynamics (e.g., fuselage dynamics, blade flapping, and lead-lagging) as well as aerodynamic effects induced by the ship environmental disturbances. The ship motion simulation using Response Amplitude Operators can also be generated for various sea states and different wave headings.

As a major contribution, Model Predictive Control (MPC) design for automatic shipboard operations was proposed and its feasibility demonstrated via numerical simulations for ship landing and lateral reposition maneuvers. Numerical simulations of helicopter dynamics showed good agreement between nonlinear and linearized helicopter models responses for several seconds. Therefore, linearized helicopter models were used as internal models in MPC design, whereas the nonlinear model was used for evaluation of MPC performance. Simulations were conducted to evaluate the MPC capability to satisfy the ADS-33E-PRF desired performance and specifications. In simulations of the automatic landing on a moving ship at rough sea (sea state 5) in the CETI airwake model, and the automatic lateral reposition toward the flight deck in various WOD conditions using CFD data, MPC showed excellent performance in handling system constraints, flight deck tracking, and rejection of disturbances caused by ship airwakes. Moreover, to improve the prediction accuracy of the internal model of the MPC, which can degrade as the helicopter wanders off the trim condition about which the nonlinear system is initially linearized, a model-updating MPC scheme was proposed for shipboard operations. Model updating consists of periodically re-computing the linear helicopter model based on its current position along the trajectory. Consequently, a better deck-tracking performance and a remarkable reduction in fuselage state oscillations due to the ship airwake were achieved. The main drawback of model updating is computational burden for high model updating frequencies and loss of stability for low ones.

For helicopter precision landing on moving decks in high sea states, a novel MIQP-MPC scheme for helicopter precision landing on moving decks is developed and evaluated using a nonlinear helicopter-ship dynamics interaction model. The variable prediction horizon in the MIQP-MPC scheme mimics the manner in which human pilots act in determining how long ahead they look forward during ship landing to accomplish the mission. Effectively, their actions allow to think ahead to compensate for upcoming reference variations, to handle multivariable constraints, and to react quickly in aggressive maneuvers. Results of the numerical simulations show that the helicopter uses the current knowledge of the deck states to land precisely in difficult conditions characterized by sea state 5 and ship airwake disturbances with the mean wind speed of 15 m/s. The rendezvous or docking conditions include the helicopter-ship relative attitude, position, and velocities constraints. These conditions simultaneously align the helicopter states with those of the ship to achieve soft touchdown, to avoid dynamic rollover, tail striking the landing deck, and adverse secondary ring vortex accompanied with high rate of decent. Downstroke, and upstroke deck motions with EI index lager than 10 are employed in the evaluation of the landing performance. The closed-loop system satisfies the ADS-33-PRF specifications for slope landing. The rendezvous phase of the landing maneuver requires that the helicopter is sufficiently close to the deck landing point to initially engage the MIQP-MPC controller.

In MPC design, the optimization process included elements of the ship motion and ship airwake models. An example of a helicopter-ship combination was used to show feasibility of MPC in shipboard operations. Of course, portability to other helicopter-ship combinations is an issue that can be addressed in other works. Also, guaranteeing robustness for MPC is a difficult problem (even in simpler settings than the one in this work). Simulations were used to gain some confidence in the stability and robustness properties of the MPC designed herein. Classical robustness measures such as stability margins are inappropriate for the kind of models and controllers we use in this dissertation.

For further work, it is essential to quantify the set of initial conditions from which a precision landing on a moving deck can be achieved, and/or the set of reachable states from which the mission can be safely aborted as soon as underestimated deck motions occur. Moreover, there needs a further work to address the collision avoidance problem with complex ship's superstructures. Some of the ideas arising from the control design process that can enhance maneuverability and agility of the future shipborne rotorcraft will be considered: increase of the control saturation and slew rates to increase the agility of the helicopter during the shipboard landing; variable rotor speed control as a decision variable in the MIQP-MPC algorithm to increase the control authority for high demanding maneuvers and guarantee the engine torque limit protection.

In the OCT application, this is the first work which investigates cyclic blade control to the best of our knowledge. The linear stability analysis of the open loop system revealed the existence of three very lightly damped modes which impact primarily the Cartesian position of the OCT. The corresponding very slowly decaying open loop behavior associated with these modes is not desired because OCTs are not envisioned to undergo frequent maintenance. The linear controllability analysis showed that the system is controllable if blade cyclic pitch angle controls and the electromechanical torque are used as controls. An investigation into OVC control design for OCT was carried out, showing that rapid stabilization of the OCT is possible using only two blade longitudinal/lateral cyclic controls and electromechanical torque control. For OVC control design, a parametric study with respect to the prescribed variance constraint bounds showed that for relatively large values of these bounds the control energy and blade pitch angle variations are reasonable. However, if the prescribed bounds are close to the minimum achievable bounds the required control energy is very large and, consequently, the blade pitch angles may reach large values that may result in blade stall. Control system for the OCT with the failures of sensors (e.g., positioning sensor, acceleration sensors) was also designed in this dissertation and its performance was evaluated using the linearized OCT model. The closed-loop system with the sensor failure still achieves good performance in comparison with the nominal closed-loop system.

MPC design was also for the first time performed for OCT flight control to handle the system constraints and avoid blade stall. Simulations were conducted to evaluate the MPC capability to regulate the OCT's position and rotor angular speed when disturbed from the nominal operating condition. MPC yielded improved performance in handling system constraints and rejection of white noise disturbances. In contrast with the OVC strategy, the cyclic pitch angles in the MPC strategy satisfied the control saturation when the process noise covariance exceeded the OVC design value. Nonlinear simulation were also used to evaluate the MPC performance. Regardless of the strategy used (OVC or MPC), cyclic blade pitch control proved to effectively regulate the OCT's position and rotor angular speed when disturbed from the nominal operating condition.

For further work, a realistic model of highly uncertain environments due to sea states, weather influences, ocean current pattern, etc., should be incorporated into the OCT dynamics model for control design and evaluation. Further research should investigate if blade stall truly occurs and how blade stall may be avoided at all points along the blade. This investigation should be carried out in the context of the global nonlinear OCT dynamics. Moreover, advanced constrained control using OVC and/or MPC strategies should be designed for OCT farms, where the relative positioning between devices will be critical for maximum energy production.

Appendix A

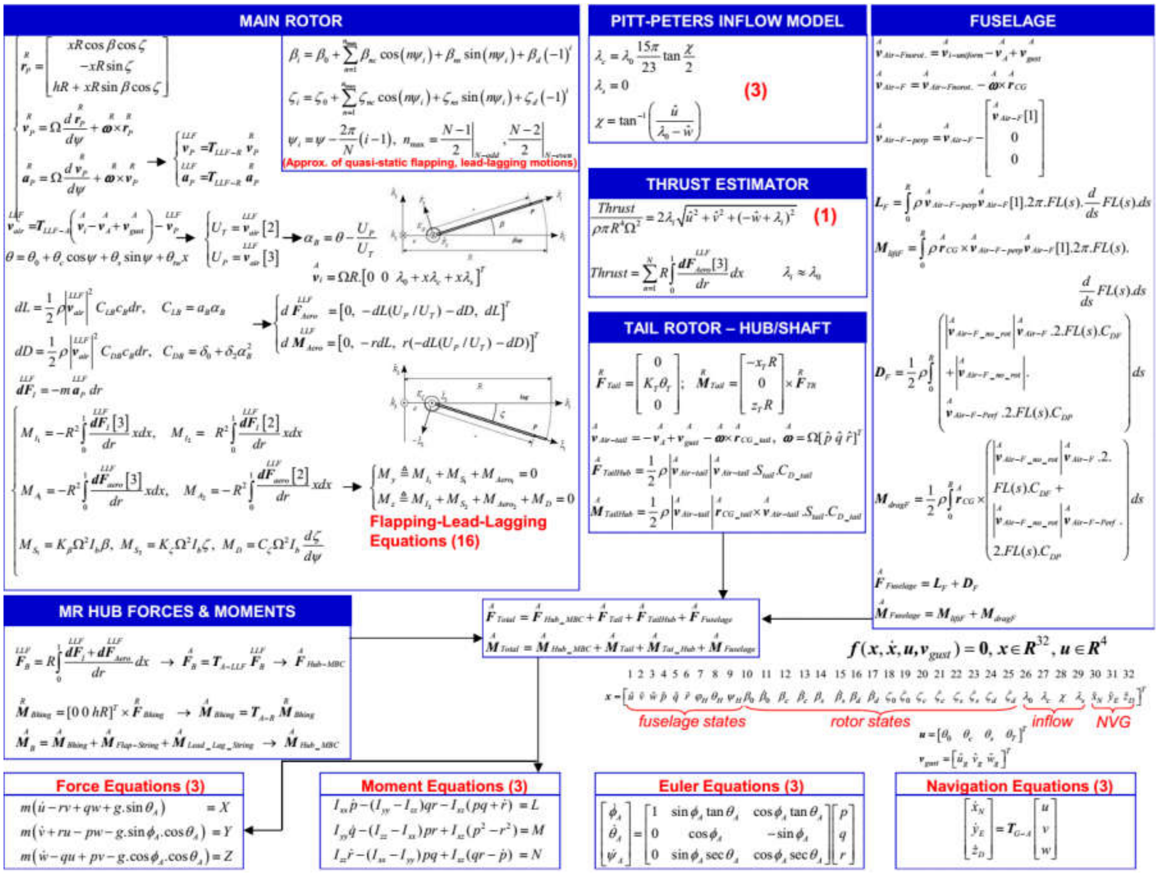

MAIN ROTOR

$$\overset{R}{\boldsymbol{r}}_P = \begin{bmatrix} xR\cos\beta\cos\zeta \\ -xR\sin\zeta \\ hR + xR\sin\beta\cos\zeta \end{bmatrix}$$

$$\overset{R}{\boldsymbol{v}}_P = \Omega\frac{d\,\overset{R}{\boldsymbol{r}}_P}{d\psi} + \overset{R}{\boldsymbol{\omega}}\times\overset{R}{\boldsymbol{r}}_P$$

$$\overset{R}{\boldsymbol{a}}_P = \Omega\frac{d\,\overset{R}{\boldsymbol{v}}_P}{d\psi} + \overset{R}{\boldsymbol{\omega}}\times\overset{R}{\boldsymbol{v}}_P \rightarrow \begin{cases} \overset{LLF}{\boldsymbol{v}}_P = \boldsymbol{T}_{LLF-R}\,\overset{R}{\boldsymbol{v}}_P \\ \overset{LLF}{\boldsymbol{a}}_P = \boldsymbol{T}_{LLF-R}\,\overset{R}{\boldsymbol{a}}_P \end{cases}$$

$$\beta_i = \beta_0 + \sum_{n=1}^{n_{\max}} \beta_{nc}\cos(n\psi_i) + \beta_{ns}\sin(n\psi_i) + \beta_d(-1)^i$$

$$\zeta_i = \zeta_0 + \sum_{n=1}^{n_{\max}} \zeta_{nc}\cos(n\psi_i) + \zeta_{ns}\sin(n\psi_i) + \zeta_d(-1)^i$$

$$\psi_i = \psi - \frac{2\pi}{N}(i-1),\ n_{\max} = \left.\frac{N-1}{2}\right|_{N-odd},\ \left.\frac{N-2}{2}\right|_{N-even}$$

(Approx. of quasi-static flapping, lead-lagging motions)

$$\overset{LLF}{\boldsymbol{v}}_{air} = \boldsymbol{T}_{LLF-A}\left(\overset{A}{\boldsymbol{v}}_i - \overset{A}{\boldsymbol{v}}_A + \overset{A}{\boldsymbol{v}}_{gust}\right) - \overset{LLF}{\boldsymbol{v}}_P \rightarrow \begin{cases} U_T = \overset{LLF}{\boldsymbol{v}}_{air}[2] \\ U_P = \overset{LLF}{\boldsymbol{v}}_{air}[3] \end{cases} \rightarrow \alpha_B = \theta - \frac{U_P}{U_T}$$

$$\theta = \theta_0 + \theta_c\cos\psi + \theta_s\sin\psi + \theta_{tw}x$$

$$\overset{A}{\boldsymbol{v}}_i = \Omega R.[0\ \ 0\ \ \lambda_0 + x\lambda_c + x\lambda_s]^T$$

$$dL = \frac{1}{2}\rho\left|\overset{LLF}{\boldsymbol{v}}_{air}\right|^2 C_{LB}c_B dr,\quad C_{LB} = a_B\alpha_B$$

$$dD = \frac{1}{2}\rho\left|\overset{LLF}{\boldsymbol{v}}_{air}\right|^2 C_{DB}c_B dr,\quad C_{DB} = \delta_0 + \delta_2\alpha_B^2$$

$$\rightarrow \begin{cases} d\,\overset{LLF}{\boldsymbol{F}}_{Aero} = [0,\ -dL(U_P/U_T) - dD,\ dL]^T \\ d\,\overset{LLF}{\boldsymbol{M}}_{Aero} = [0,\ -r\,dL,\ r(-dL(U_P/U_T) - dD)]^T \end{cases}$$

$$\overset{LLF}{\boldsymbol{dF}}_I = -m\,\overset{LLF}{\boldsymbol{a}}_P\,dr$$

$$M_{I_1} = -R^2\int_0^1 \frac{\overset{LLF}{\boldsymbol{dF}}_I[3]}{dr}x\,dx,\quad M_{I_2} = R^2\int_0^1 \frac{\overset{LLF}{\boldsymbol{dF}}_I[2]}{dr}x\,dx$$

$$M_{A_1} = -R^2\int_0^1 \frac{\overset{LLF}{\boldsymbol{dF}}_{aero}[3]}{dr}x\,dx,\quad M_{A_2} = -R^2\int_0^1 \frac{\overset{LLF}{\boldsymbol{dF}}_{aero}[2]}{dr}x\,dx \rightarrow \begin{cases} M_y \triangleq M_{I_1} + M_{S_1} + M_{Aero_1} = 0 \\ M_z \triangleq M_{I_2} + M_{S_2} + M_{Aero_2} + M_D = 0 \end{cases}$$

$$M_{S_1} = K_\beta\Omega^2 I_b\beta,\ M_{S_2} = K_\zeta\Omega^2 I_b\zeta,\ M_D = C_\zeta\Omega^2 I_b\frac{d\zeta}{d\psi}$$

Flapping-Lead-Lagging Equations (16)

PITT-PETERS INFLOW MODEL

$$\lambda_c = \lambda_0\frac{15\pi}{23}\tan\frac{\chi}{2}$$

$$\lambda_s = 0$$

$$\chi = \tan^{-1}\left(\frac{\hat{u}}{\lambda_0 - \hat{w}}\right)$$

(3)

THRUST ESTIMATOR

$$\frac{Thrust}{\rho\pi R^4\Omega^2} = 2\lambda_1\sqrt{\hat{u}^2 + \hat{v}^2 + (-\hat{w} + \lambda_1)^2}\quad (1)$$

$$Thrust = \sum_{n=1}^{N} R\int_0^1 \frac{\overset{LLF}{\boldsymbol{dF}}_{Aero}[3]}{dr}dx \qquad \lambda_1 \approx \lambda_0$$

TAIL ROTOR – HUB/SHAFT

$$\overset{R}{\boldsymbol{F}}_{Tail} = \begin{bmatrix} 0 \\ K_T\theta_T \\ 0 \end{bmatrix};\quad \overset{R}{\boldsymbol{M}}_{Tail} = \begin{bmatrix} -x_T R \\ 0 \\ z_T R \end{bmatrix}\times\overset{R}{\boldsymbol{F}}_{TR}$$

$$\overset{A}{\boldsymbol{v}}_{Air-tail} = -\overset{A}{\boldsymbol{v}}_A + \overset{A}{\boldsymbol{v}}_{gust} - \overset{A}{\boldsymbol{\omega}}\times\overset{A}{\boldsymbol{r}}_{CG\_tail},\quad \overset{A}{\boldsymbol{\omega}} = \Omega[\hat{p}\ \hat{q}\ \hat{r}]^T$$

$$\overset{A}{\boldsymbol{F}}_{TailHub} = \frac{1}{2}\rho\left|\overset{A}{\boldsymbol{v}}_{Air-tail}\right|\overset{A}{\boldsymbol{v}}_{Air-tail}.S_{tail}.C_{D\_tail}$$

$$\overset{A}{\boldsymbol{M}}_{TailHub} = \frac{1}{2}\rho\left|\overset{A}{\boldsymbol{v}}_{Air-tail}\right|\overset{A}{\boldsymbol{r}}_{CG\_tail}\times\overset{A}{\boldsymbol{v}}_{Air-tail}.S_{tail}.C_{D\_tail}$$

FUSELAGE

$$\overset{A}{\boldsymbol{v}}_{Air-Fnorot.} = \overset{A}{\boldsymbol{v}}_{i-uniform} - \overset{A}{\boldsymbol{v}}_A + \overset{A}{\boldsymbol{v}}_{gust}$$

$$\overset{A}{\boldsymbol{v}}_{Air-F} = \overset{A}{\boldsymbol{v}}_{Air-Fnorot.} - \overset{A}{\boldsymbol{\omega}}\times\overset{A}{\boldsymbol{r}}_{CG}$$

$$\overset{A}{\boldsymbol{v}}_{Air-F-perp} = \overset{A}{\boldsymbol{v}}_{Air-F} - \begin{bmatrix} \overset{A}{\boldsymbol{v}}_{Air-F}[1] \\ 0 \\ 0 \end{bmatrix}$$

$$\boldsymbol{L}_F = \int_0^R \rho\,\overset{A}{\boldsymbol{v}}_{Air-F-perp}\overset{A}{\boldsymbol{v}}_{Air-F}[1].2\pi.FL(s).\frac{d}{ds}FL(s).ds$$

$$\boldsymbol{M}_{liftF} = \int_0^R \rho\,\overset{A}{\boldsymbol{r}}_{CG}\times\overset{A}{\boldsymbol{v}}_{Air-F-perp}\overset{A}{\boldsymbol{v}}_{Air-F}[1].2\pi.FL(s).\frac{d}{ds}FL(s).ds$$

$$\boldsymbol{D}_F = \frac{1}{2}\rho\int_0^R \begin{pmatrix} \left|\overset{A}{\boldsymbol{v}}_{Air-F\_no\_rot}\right|\overset{A}{\boldsymbol{v}}_{Air-F}.2.FL(s).C_{DF} \\ +\left|\overset{A}{\boldsymbol{v}}_{Air-F\_no\_rot}\right|. \\ \overset{A}{\boldsymbol{v}}_{Air-F-Perf}.2.FL(s).C_{DP} \end{pmatrix} ds$$

$$\boldsymbol{M}_{dragF} = \frac{1}{2}\rho\int_0^R \overset{A}{\boldsymbol{r}}_{CG}\times\begin{pmatrix} \left|\overset{A}{\boldsymbol{v}}_{Air-F\_no\_rot}\right|\overset{A}{\boldsymbol{v}}_{Air-F}.2. \\ FL(s).C_{DF} + \\ \left|\overset{A}{\boldsymbol{v}}_{Air-F\_no\_rot}\right|\overset{A}{\boldsymbol{v}}_{Air-F-Perf}. \\ 2.FL(s).C_{DP} \end{pmatrix} ds$$

$$\overset{A}{\boldsymbol{F}}_{Fuselage} = \boldsymbol{L}_F + \boldsymbol{D}_F$$

$$\overset{A}{\boldsymbol{M}}_{Fuselage} = \boldsymbol{M}_{liftF} + \boldsymbol{M}_{dragF}$$

MR HUB FORCES & MOMENTS

$$\overset{LLF}{\boldsymbol{F}}_B = R\int_0^1 \frac{\overset{LLF}{\boldsymbol{dF}}_I + \overset{LLF}{\boldsymbol{dF}}_{Aero}}{dr}dx \rightarrow \overset{A}{\boldsymbol{F}}_B = \boldsymbol{T}_{A-LLF}\,\overset{LLF}{\boldsymbol{F}}_B \rightarrow \overset{A}{\boldsymbol{F}}_{Hub-MBC}$$

$$\overset{R}{\boldsymbol{M}}_{Bhing} = [0\ 0\ hR]^T\times\overset{R}{\boldsymbol{F}}_{Bhing} \rightarrow \overset{A}{\boldsymbol{M}}_{Bhing} = \boldsymbol{T}_{A-R}\,\overset{R}{\boldsymbol{M}}_{Bhing}$$

$$\overset{A}{\boldsymbol{M}}_B = \overset{A}{\boldsymbol{M}}_{Bhing} + \overset{A}{\boldsymbol{M}}_{Flap-String} + \overset{A}{\boldsymbol{M}}_{Lead\_Lag\_String} \rightarrow \overset{A}{\boldsymbol{M}}_{Hub\_MBC}$$

$$\overset{A}{\boldsymbol{F}}_{Total} = \overset{A}{\boldsymbol{F}}_{Hub\_MBC} + \overset{A}{\boldsymbol{F}}_{Tail} + \overset{A}{\boldsymbol{F}}_{TailHub} + \overset{A}{\boldsymbol{F}}_{Fuselage}$$

$$\overset{A}{\boldsymbol{M}}_{Total} = \overset{A}{\boldsymbol{M}}_{Hub\_MBC} + \overset{A}{\boldsymbol{M}}_{Tail} + \overset{A}{\boldsymbol{M}}_{Tail\_Hub} + \overset{A}{\boldsymbol{M}}_{Fuselage}$$

$$\boldsymbol{f}(\boldsymbol{x}, \dot{\boldsymbol{x}}, \boldsymbol{u}, \boldsymbol{v}_{gust}) = \boldsymbol{0},\ \boldsymbol{x}\in\boldsymbol{R}^{32},\ \boldsymbol{u}\in\boldsymbol{R}^4$$

$$\boldsymbol{x} = \big[\underbrace{\overset{1}{\hat{u}}\ \overset{2}{\hat{v}}\ \overset{3}{\hat{w}}\ \overset{4}{\hat{p}}\ \overset{5}{\hat{q}}\ \overset{6}{\hat{r}}\ \overset{7}{\varphi_H}\ \overset{8}{\theta_H}\ \overset{9}{\psi_H}}_{\text{fuselage states}}\ \underbrace{\overset{10}{\beta_0}\ \overset{11}{\dot{\beta}_0}\ \overset{12}{\beta_c}\ \overset{13}{\dot{\beta}_c}\ \overset{14}{\beta_s}\ \overset{15}{\dot{\beta}_s}\ \overset{16}{\beta_d}\ \overset{17}{\dot{\beta}_d}\ \overset{18}{\zeta_0}\ \overset{19}{\dot{\zeta}_0}\ \overset{20}{\zeta_c}\ \overset{21}{\dot{\zeta}_c}\ \overset{22}{\zeta_s}\ \overset{23}{\dot{\zeta}_s}\ \overset{24}{\zeta_d}\ \overset{25}{\dot{\zeta}_d}}_{\text{rotor states}}\ \underbrace{\overset{26}{\lambda_0}\ \overset{27}{\lambda_c}\ \overset{28}{\chi}\ \overset{29}{\lambda_s}}_{\text{inflow}}\ \underbrace{\overset{30}{\hat{x}_N}\ \overset{31}{\hat{y}_E}\ \overset{32}{\hat{z}_D}}_{\text{NVG}}\big]^T$$

$$\boldsymbol{u} = [\theta_0\ \ \theta_c\ \ \theta_s\ \ \theta_T]^T$$

$$\boldsymbol{v}_{gust} = [\hat{u}_g\ \hat{v}_g\ \hat{w}_g]^T$$

Force Equations (3)

$$m(\dot{u} - rv + qw + g.\sin\theta_A) = X$$

$$m(\dot{v} + ru - pw - g.\sin\phi_A.\cos\theta_A) = Y$$

$$m(\dot{w} - qu + pv - g.\cos\phi_A.\cos\theta_A) = Z$$

Moment Equations (3)

$$I_{xx}\dot{p} - (I_{yy} - I_{zz})qr - I_{xz}(pq + \dot{r}) = L$$

$$I_{yy}\dot{q} - (I_{zz} - I_{xx})pr + I_{xz}(p^2 - r^2) = M$$

$$I_{zz}\dot{r} - (I_{xx} - I_{yy})pq + I_{xz}(qr - \dot{p}) = N$$

Euler Equations (3)

$$\begin{bmatrix} \dot{\phi}_A \\ \dot{\theta}_A \\ \dot{\psi}_A \end{bmatrix} = \begin{bmatrix} 1 & \sin\phi_A\tan\theta_A & \cos\phi_A\tan\theta_A \\ 0 & \cos\phi_A & -\sin\phi_A \\ 0 & \sin\phi_A\sec\theta_A & \cos\phi_A\sec\theta_A \end{bmatrix}\begin{bmatrix} p \\ q \\ r \end{bmatrix}$$

Navigation Equations (3)

$$\begin{bmatrix} \dot{x}_N \\ \dot{y}_E \\ \dot{z}_D \end{bmatrix} = \boldsymbol{T}_{G-A}\begin{bmatrix} u \\ v \\ w \end{bmatrix}$$

Table A.1 Configuration data of the generic helicopter

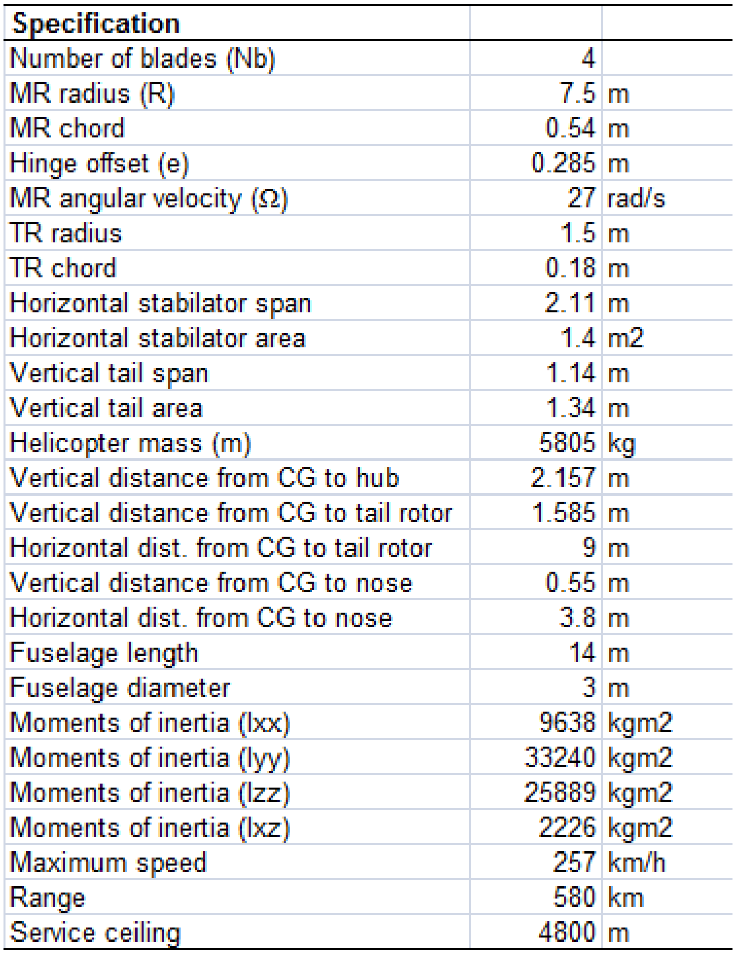

Specification		
Number of blades (Nb)	4	
MR radius (R)	7.5	m
MR chord	0.54	m
Hinge offset (e)	0.285	m
MR angular velocity (Ω)	27	rad/s
TR radius	1.5	m
TR chord	0.18	m
Horizontal stabilator span	2.11	m
Horizontal stabilator area	1.4	m2
Vertical tail span	1.14	m
Vertical tail area	1.34	m
Helicopter mass (m)	5805	kg
Vertical distance from CG to hub	2.157	m
Vertical distance from CG to tail rotor	1.585	m
Horizontal dist. from CG to tail rotor	9	m
Vertical distance from CG to nose	0.55	m
Horizontal dist. from CG to nose	3.8	m
Fuselage length	14	m
Fuselage diameter	3	m
Moments of inertia (Ixx)	9638	kgm2
Moments of inertia (Iyy)	33240	kgm2
Moments of inertia (Izz)	25889	kgm2
Moments of inertia (Ixz)	2226	kgm2
Maximum speed	257	km/h
Range	580	km
Service ceiling	4800	m

Table A.2 Eigenvector analysis of the linearized helicopter model (polar form)

Eigenmodes		-0.5805 ± 0.7800i			-0.0194 ± 0.3364i	
States		Magnitude	Phase		Magnitude	Phase
1	$\hat{u}$	1.30E-17	81.1303	$\hat{u}$	1.83E-18	-99.7
2	$\hat{v}$	4.37E-18	-147.6	$\hat{v}$	3.37E-16	-127.6
3	$\hat{w}$	1.21E-17	145.138	$\hat{w}$	8.24E-17	-90.26
4	$\hat{p}$	2.89E-17	59.0892	$\hat{p}$	1.24E-16	150.5
5	$\hat{q}$	3.10E-18	115.335	$\hat{q}$	1.06E-17	-148.6
6	$\hat{r}$	1.44E-17	165.728	$\hat{r}$	5.67E-16	145.27
7	ϕ_A	1.54E-15	35.0842	ϕ_A	4.55E-16	93.231
8	θ_A	3.50E-16	-179.51	θ_A	1.01E-16	36.115
9	ψ_A	1.74E-17	25.5073	ψ_A	1.68E-15	51.976
10	β_0	2.86E-16	116.735	β_0	9.62E-16	-159.6
11	$\dot{\beta}_0$	2.95E-16	-115.86	$\dot{\beta}_0$	3.26E-16	-66.04
12	β_c	8.72E-17	131.701	β_c	4.00E-16	41.446
13	$\dot{\beta}_c$	9.16E-17	-117.09	$\dot{\beta}_c$	1.31E-16	134.45
14	β_s	6.90E-17	-32.231	β_s	2.17E-16	-36.46
15	$\dot{\beta}_s$	6.63E-17	107.237	$\dot{\beta}_s$	7.33E-17	55.212
16	β_d	0.7104	180	β_d	0.0937	-38.79
17	$\dot{\beta}_d$	0.6908	-53.341	$\dot{\beta}_d$	0.0316	54.517
18	ζ_0	4.64E-16	-24.301	ζ_0	8.35E-15	-125.6
19	$\dot{\zeta}_0$	2.52E-16	-19.641	$\dot{\zeta}_0$	2.82E-15	-31.52
20	ζ_c	9.65E-18	129.784	ζ_c	1.53E-16	-84.74
21	$\dot{\zeta}_c$	7.10E-18	129.934	$\dot{\zeta}_c$	4.83E-17	9.2749
22	ζ_s	4.86E-17	-93.372	ζ_s	9.43E-17	177.79
23	$\dot{\zeta}_s$	4.53E-17	59.126	$\dot{\zeta}_s$	3.30E-17	-88.79
24	ζ_d	0.0965	-131.72	ζ_d	0.9430	0
25	$\dot{\zeta}_d$	0.0939	-5.0567	$\dot{\zeta}_d$	0.3178	93.304

Table A.3 Ship's specifications

Length (m)	170	C_M	0.943	z_G (m)	-0.3
Beam (m)	22.8	C_P	0.599	z_B (m)	3.6
Draught (m)	9.3	C_B	0.565	I_{xx} (kg-m^2)	1.05E+09
U (m/s)	5.15	x_{CF} (m)	3.1	I_{yy} (kg-m^2)	3.70E+10
m (ton)	20876	$x_G = x_B$ (m)	0.6658	I_{zz} (kg-m^2)	3.70E+10

Table A.4 Configuration Data of the OCT

Parameters	Values	Units
Turbine mass	4.98E+05	kg
Turbine displacement mass	5.07E+05	kg
Rotor diameter	20	m
Rotor mass	6.16E+04	kg
Rotor displacement mass	4.73E+04	kg
Rotor moment of intertia about the rotor axis	5.39E+05	kg*m2
Rotor swept area	314	m2
Cable length	91	m
Total cable mass	1.93E+04	kg

Table A.5 Eigenvector analysis of the linearized OCT model (polar form)

Eigenmodes		0		-0.0656		-0.0012 ± 0.175i	
States		Magnitude	Phase	Magnitude	Phase	Magnitude	Phase
1	**u**	9.64E-22	180	2.14E-02	180	1.31E-05	-41
2	**v**	1.28E-19	180	2.63E-03	180	1.64E-03	55
3	**w**	3.46E-20	0	8.99E-04	180	1.12E-03	133
4	**pb**	5.71E-23	0	9.47E-06	180	3.32E-07	-159
5	**pr**	5.69E-12	180	6.18E-02	180	1.59E-04	141
6	**qb**	2.15E-23	0	8.63E-06	180	6.10E-07	126
7	**rb**	4.04E-22	0	1.34E-05	180	2.99E-06	-134
8	**X**	3.47E-10	180	3.26E-01	0	3.28E-02	78
9	**Y**	2.23E-08	180	4.00E-02	0	8.21E-01	-180
10	**Z**	5.66E-09	0	2.94E-02	0	5.65E-01	-102
11	**phi**	5.78E-12	0	1.35E-04	0	1.08E-04	-49
12	**alpha**	1.00E+00	180	9.42E-01	0	7.97E-02	-93
13	**theta**	5.26E-12	0	1.29E-04	0	3.10E-04	-112
14	**psi**	7.13E-11	0	2.06E-04	0	1.50E-03	-8

Appendix B

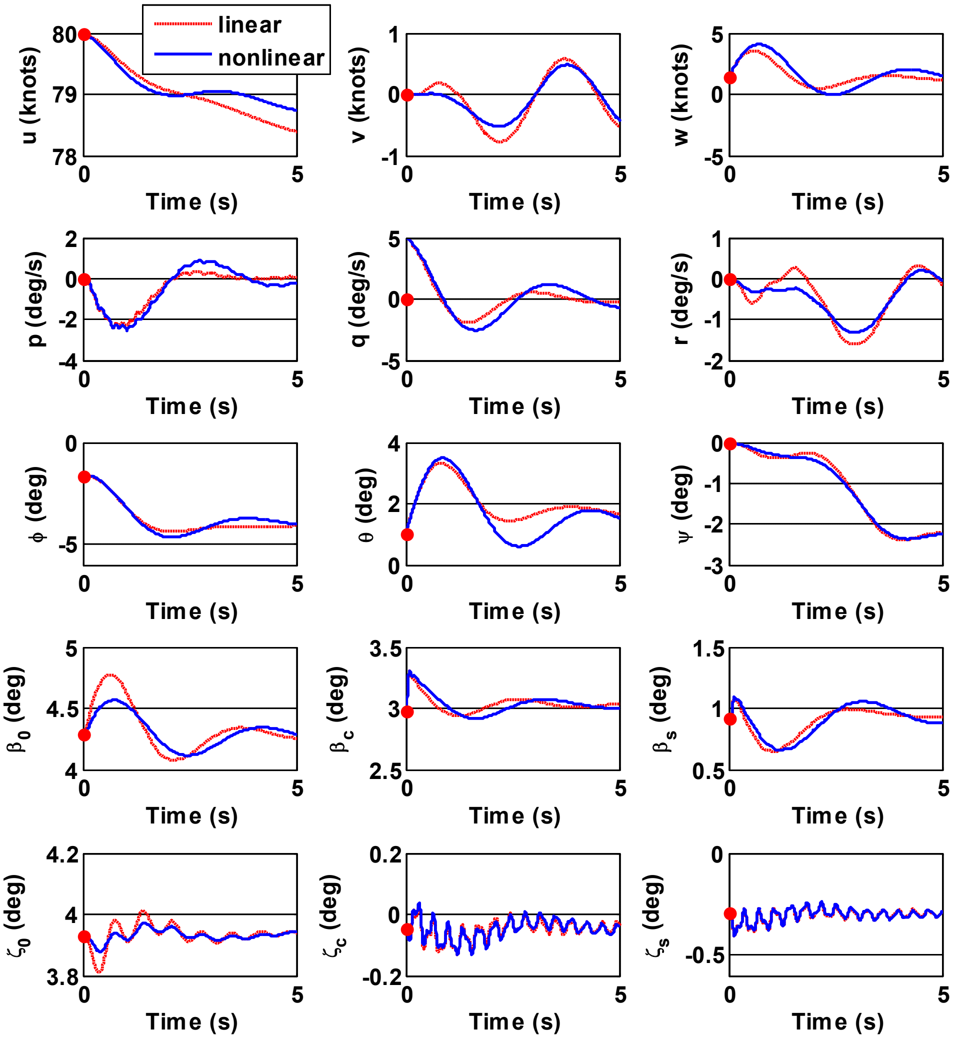

Fig. B. 1 Response of the helicopter to a disturbance in pitch rate at 80 knots

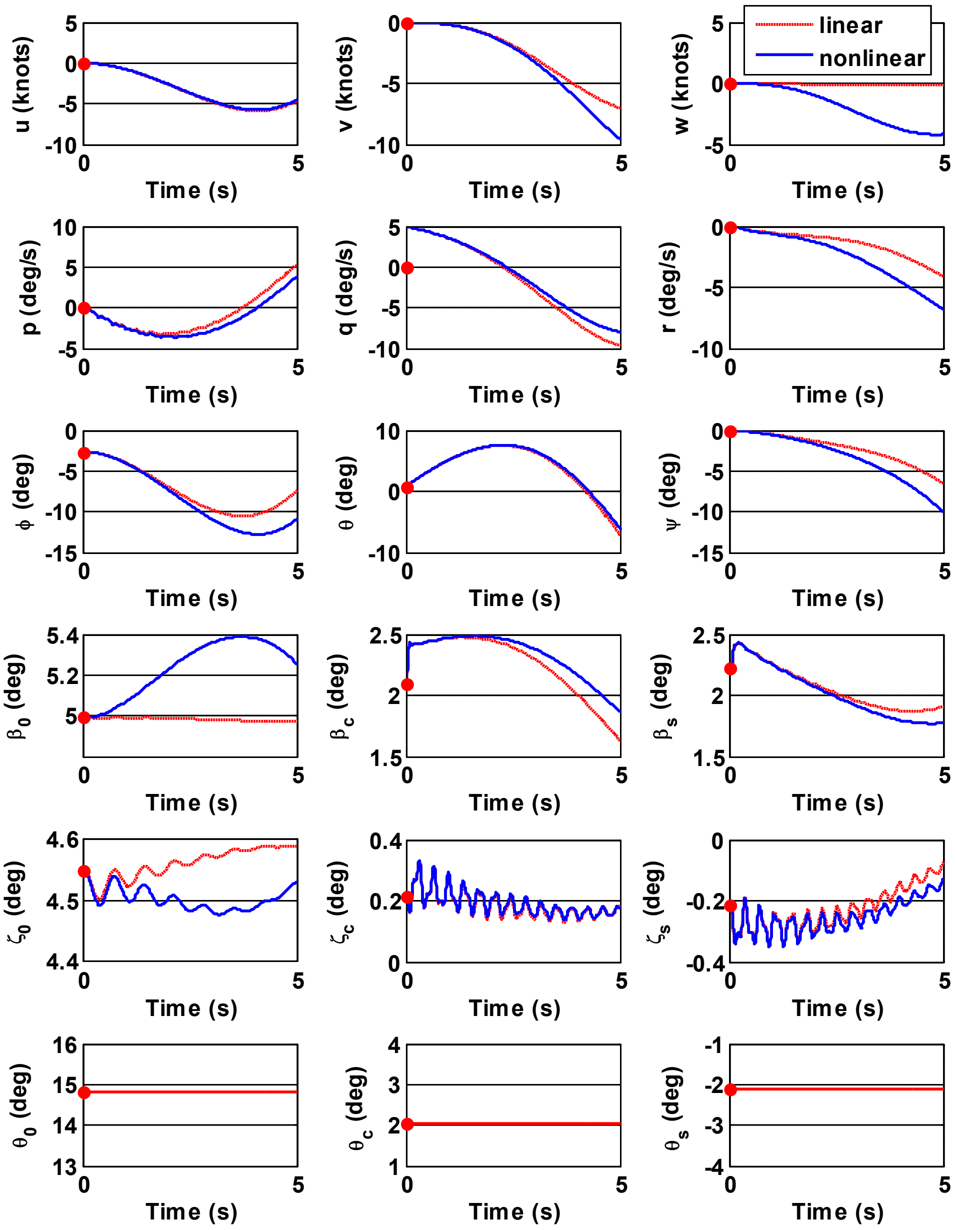

Fig. B.2 Response of the helicopter to a disturbance in pitch rate at hover

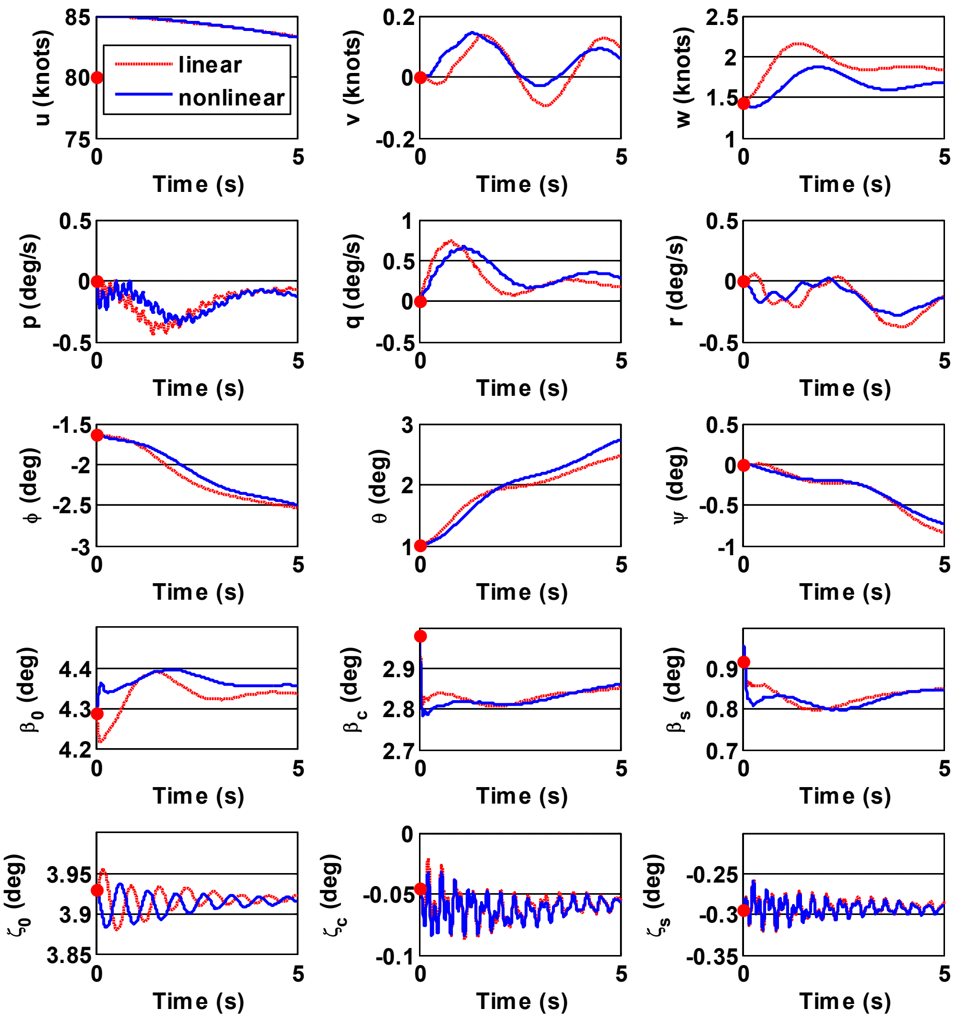

Fig. B.3 Response of the helicopter to a disturbance in forward speed at 80 knots

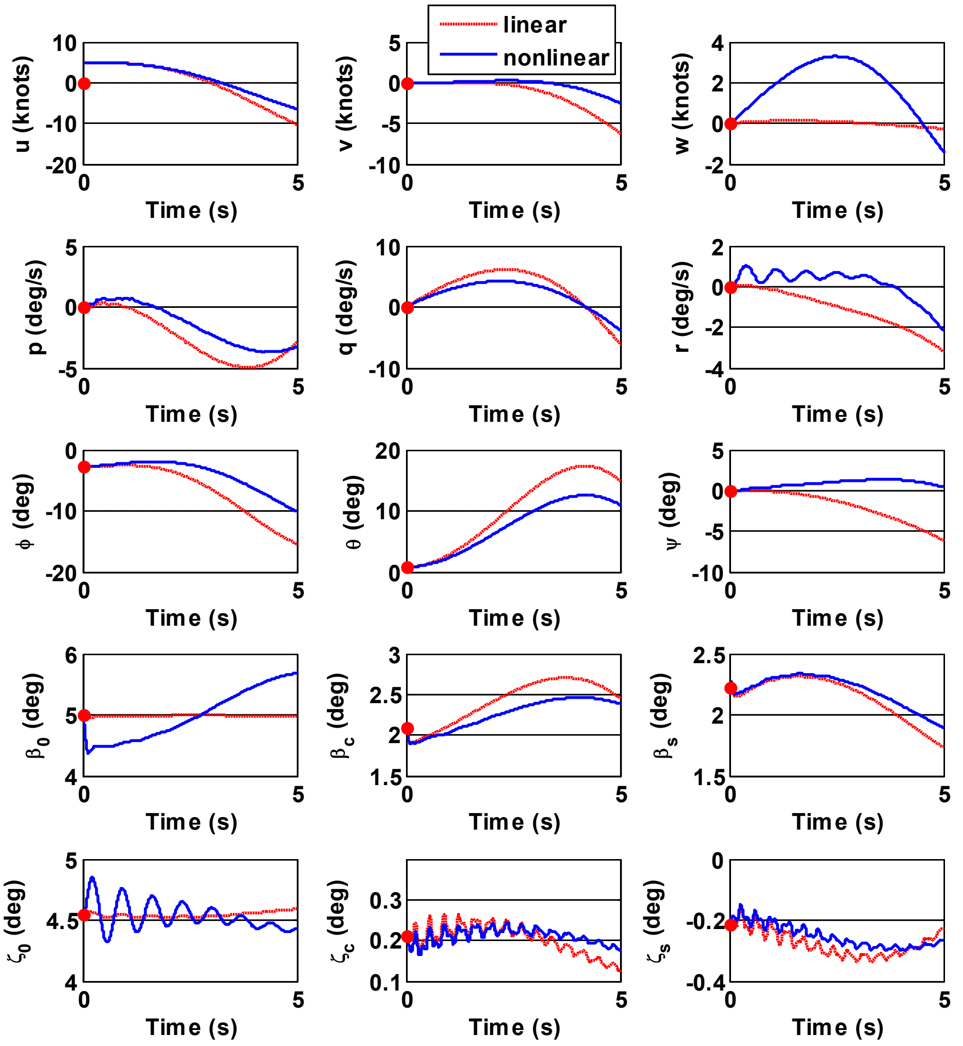

Fig. B.4 Response of the helicopter to a disturbance in forward speed at hover

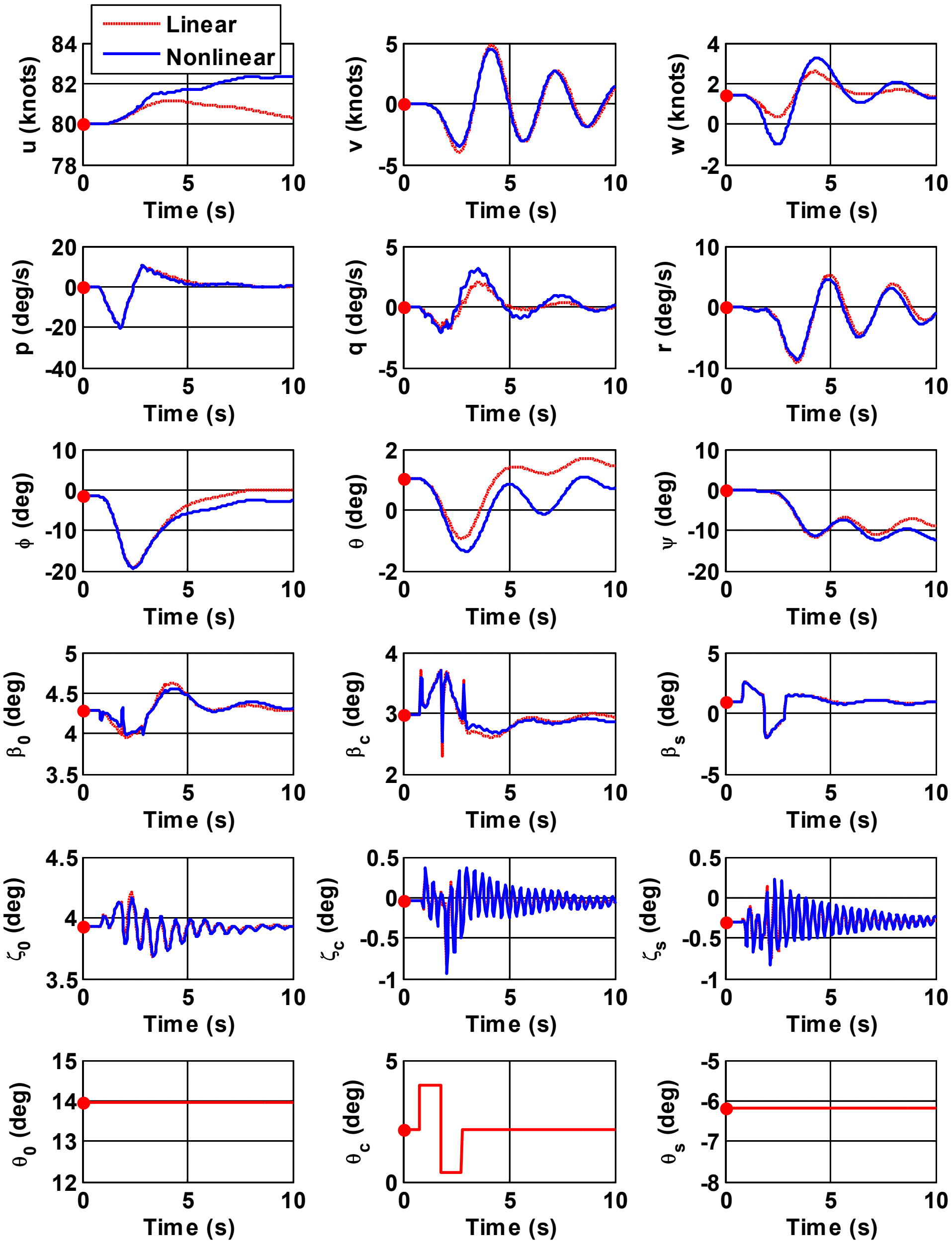

Fig. B.5 Response of the helicopter to a doublet lateral cyclic pitch at 80 knots

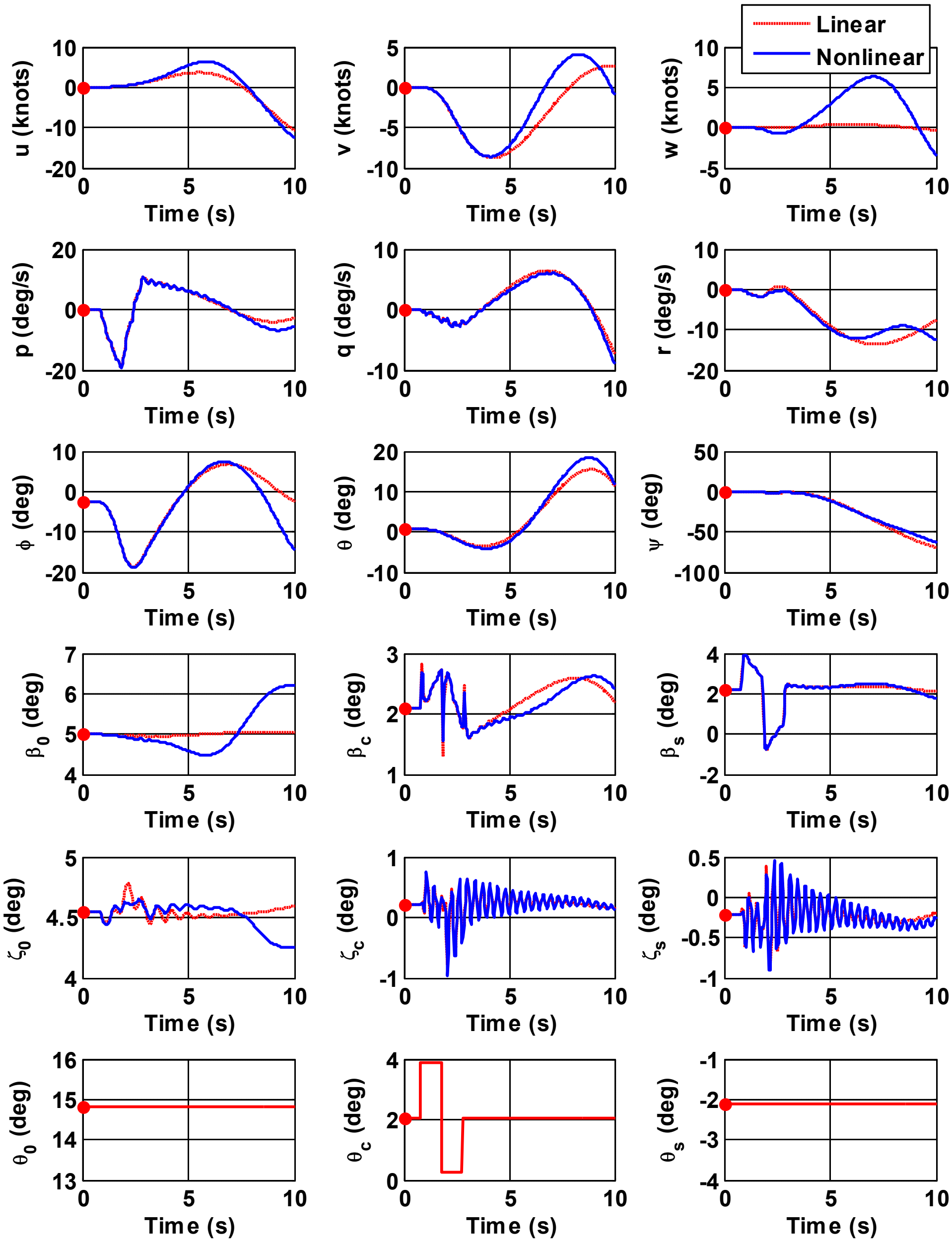

Fig. B.6 Response of the helicopter to a doublet lateral cyclic pitch at hover

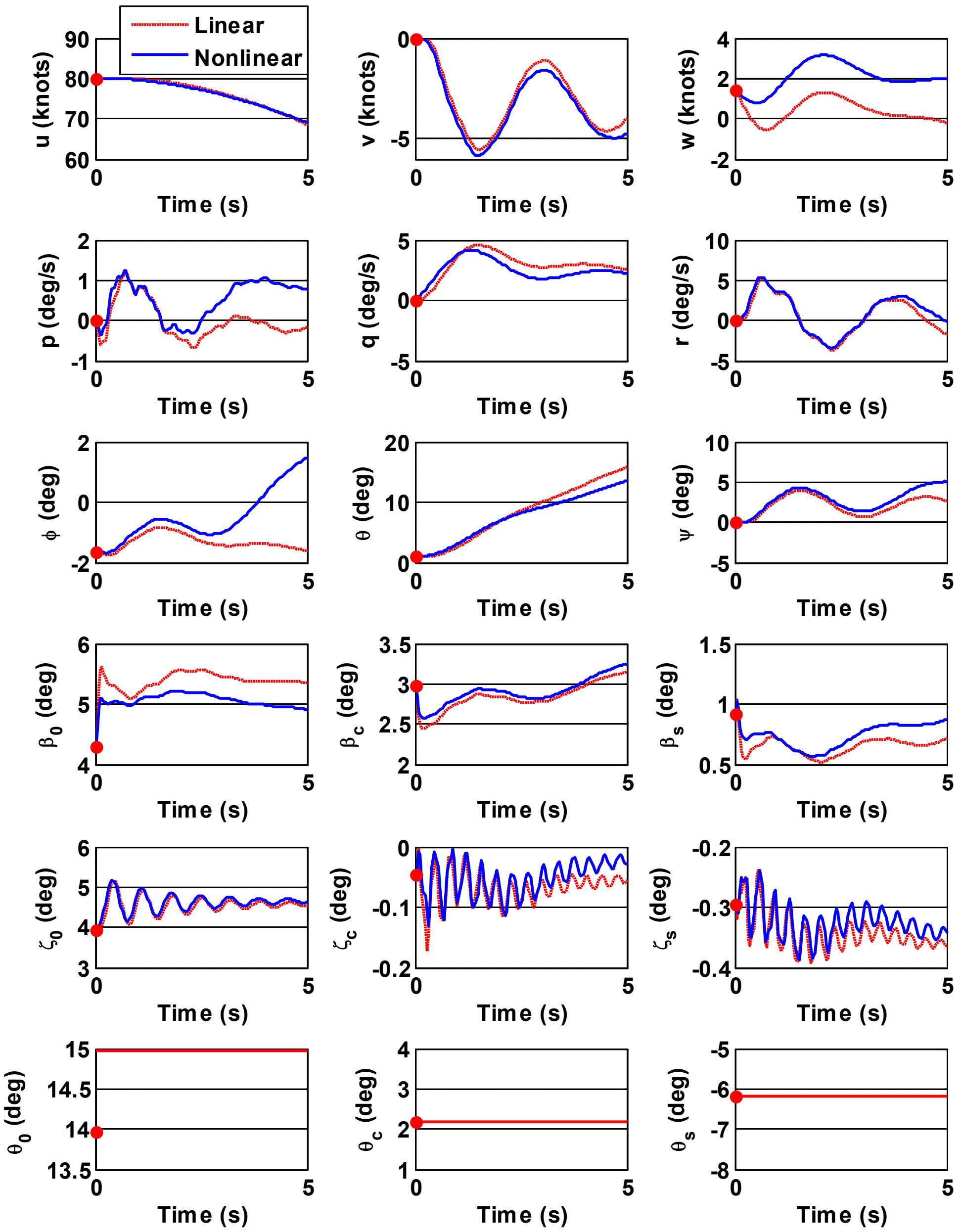

Fig. B.7 Response of the helicopter to a step collective input at 80 knots

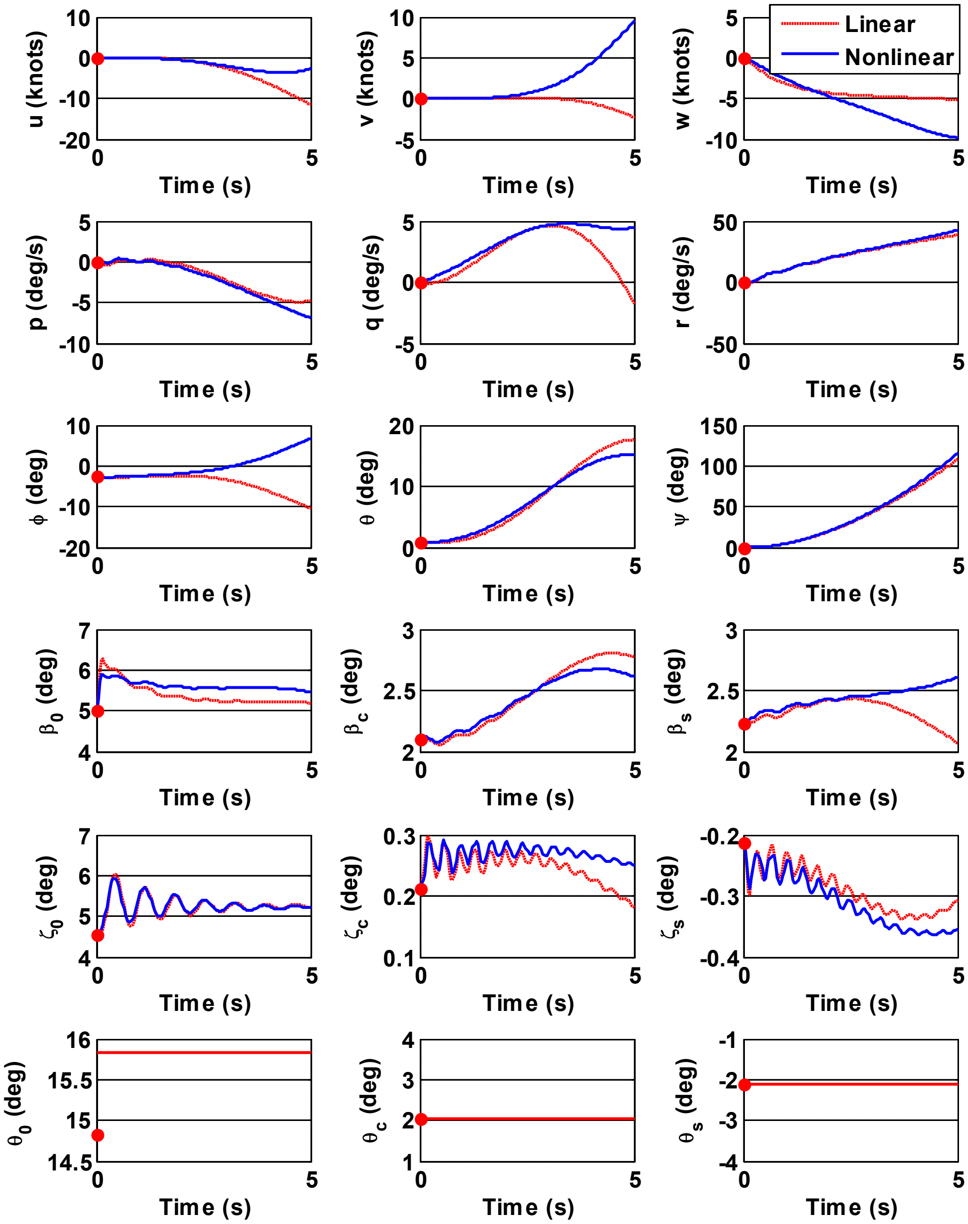

Fig. B.8 Response of the helicopter to a step collective input at hover

Appendix C

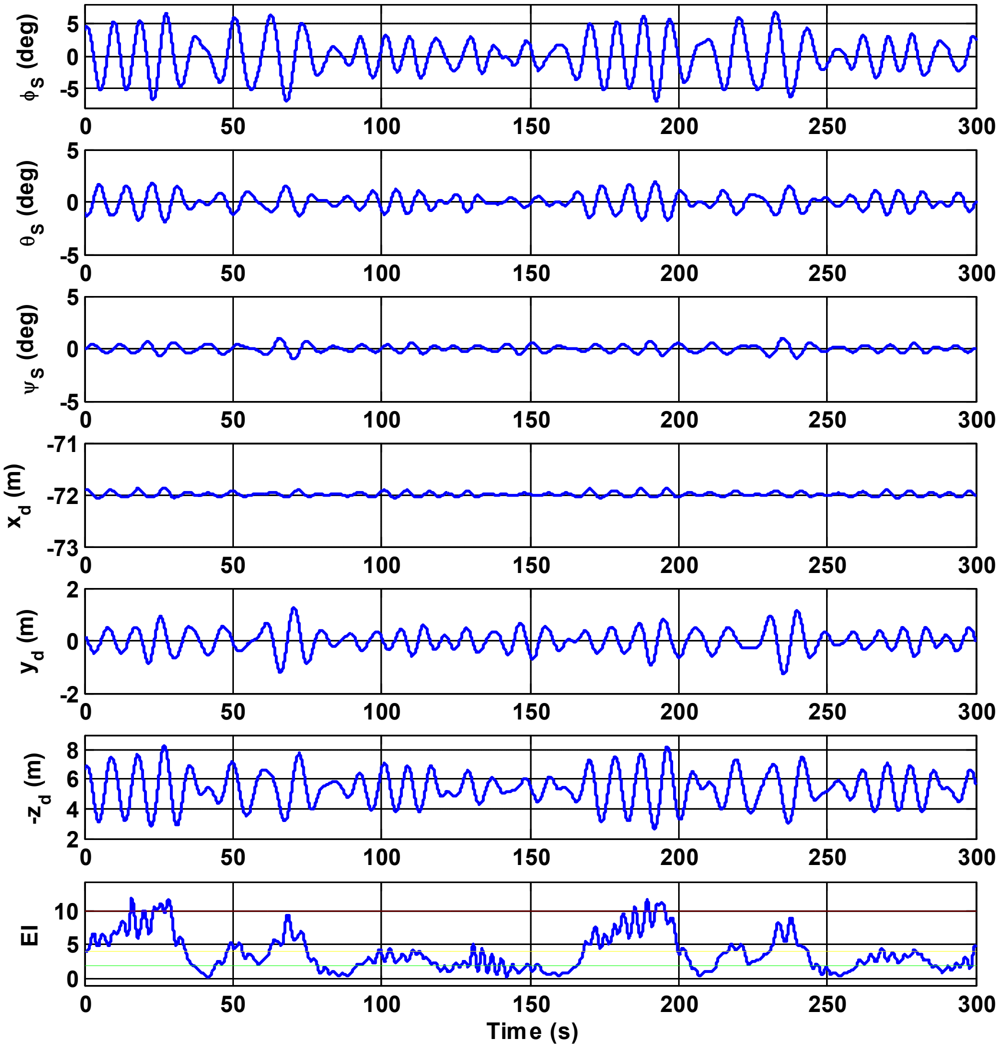

Fig. C.1 Third sample of the ship motion time history and energy index

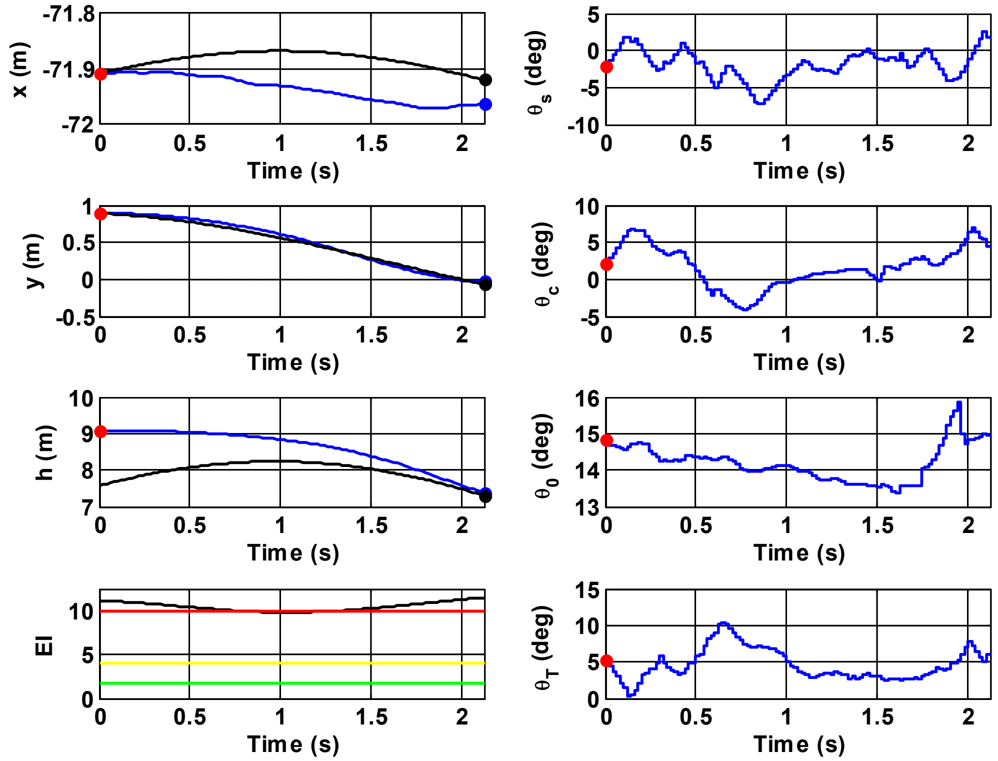

Fig. C.2 Position and control input histories (blue lines) of the helicopter during the landing on the downstroke moving deck (black lines) starting from Time = 26 s in the third sample of the ship motion, airwake is included

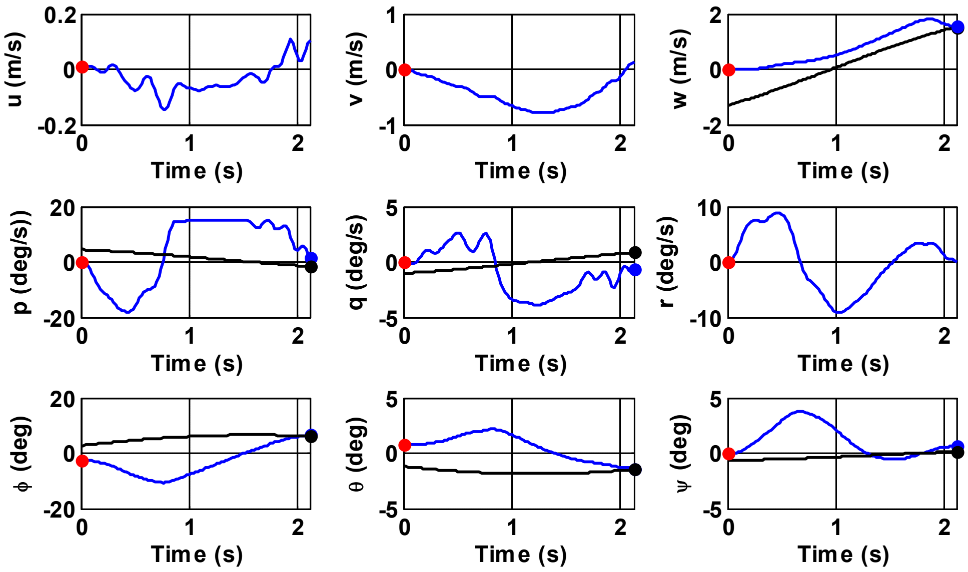

Fig. C.3 Fuselage state responses of the helicopter during the landing starting from Time = 26 s

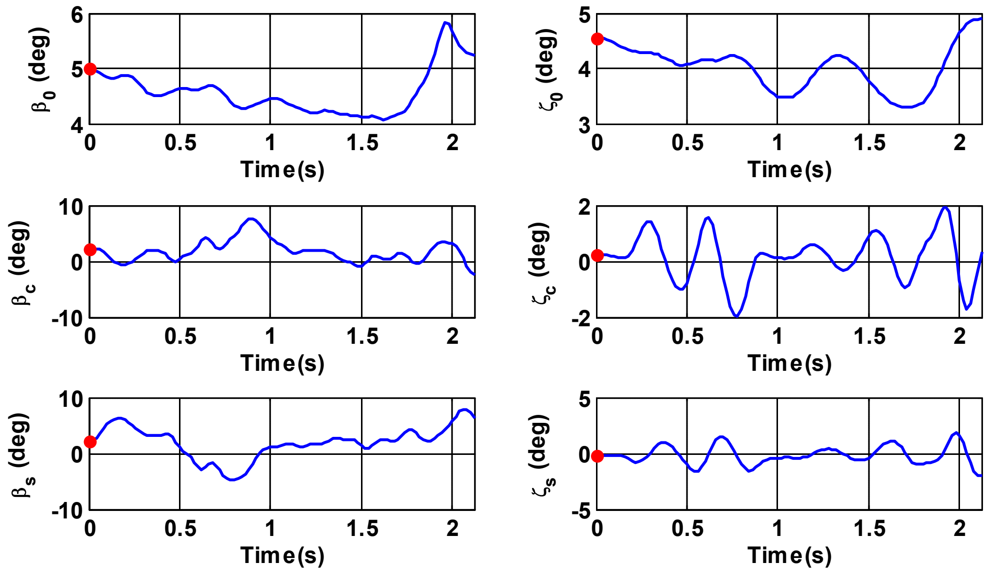

Fig. C.4 Flapping, lead-lagging states of the main rotor during the landing starting from Time = 26 s

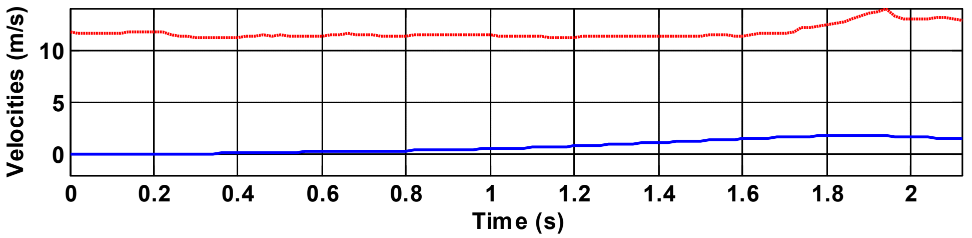

Fig. C.5 Induced inflow (dashed line) and rate of descend (solid line) during the landing starting from Time = 26 s

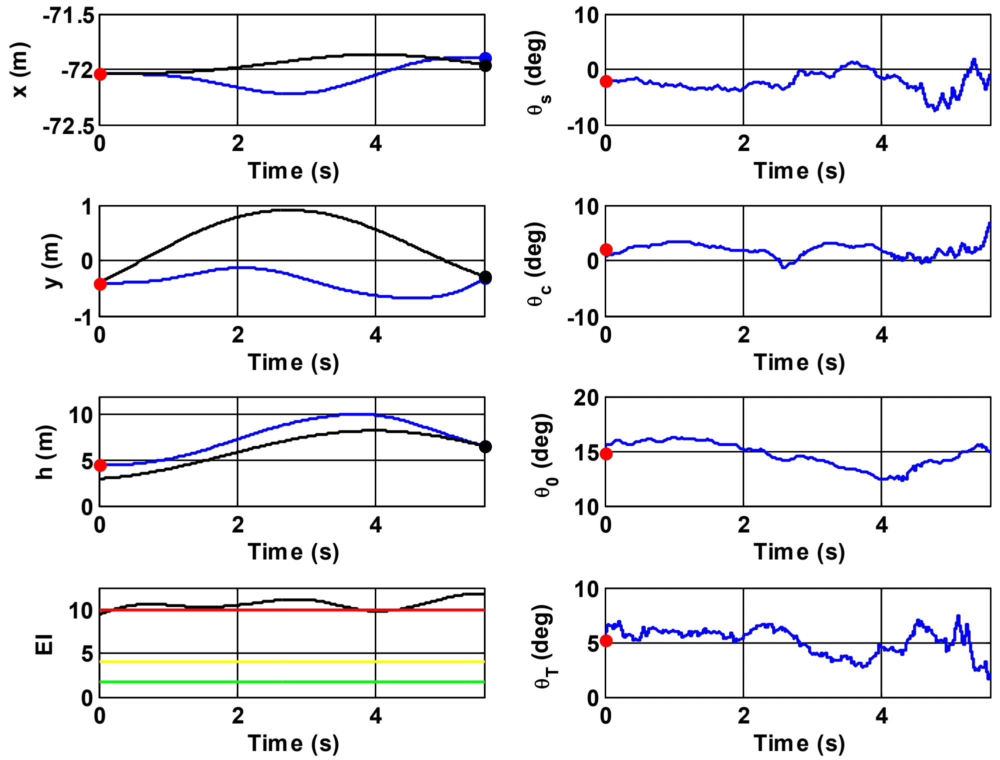

Fig. C.6 Position and control input histories (blue lines) of the helicopter during the landing on the upstroke moving deck (black lines) starting from Time = 23 s in the third sample of the ship motion, airwake is included

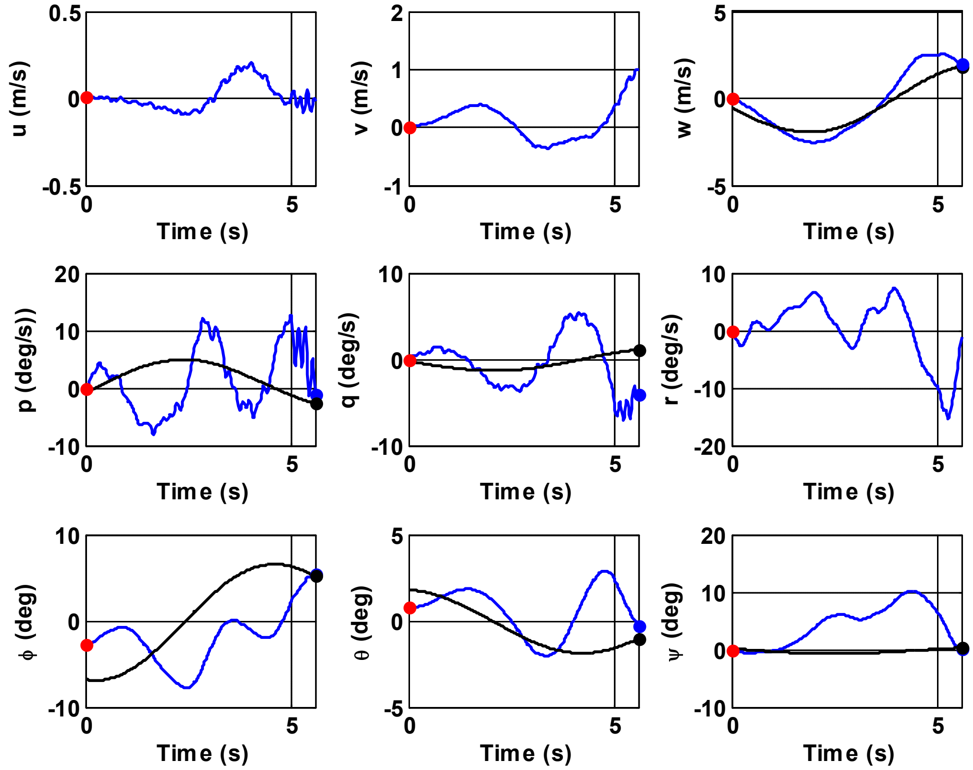

Fig. C.7 Fuselage state responses of the helicopter during the landing starting from Time = 23 s

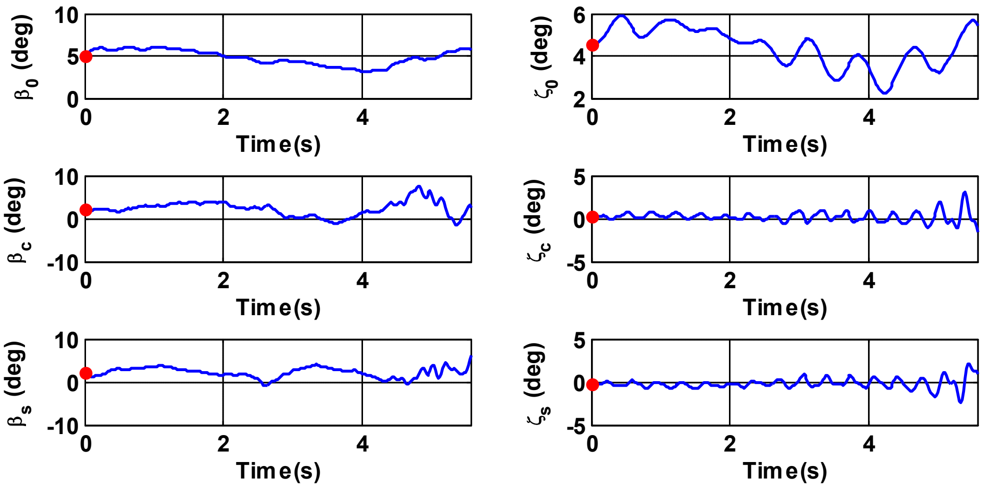

Fig. C.8 Flapping, lead-lagging states of the main rotor during the landing starting from Time = 23 s

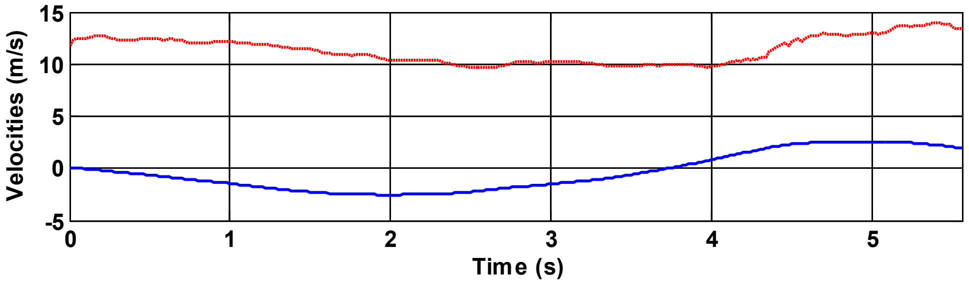

Fig. C.9 Induced inflow (dashed line) and rate of descend (solid line) during the landing starting from Time = 23 s

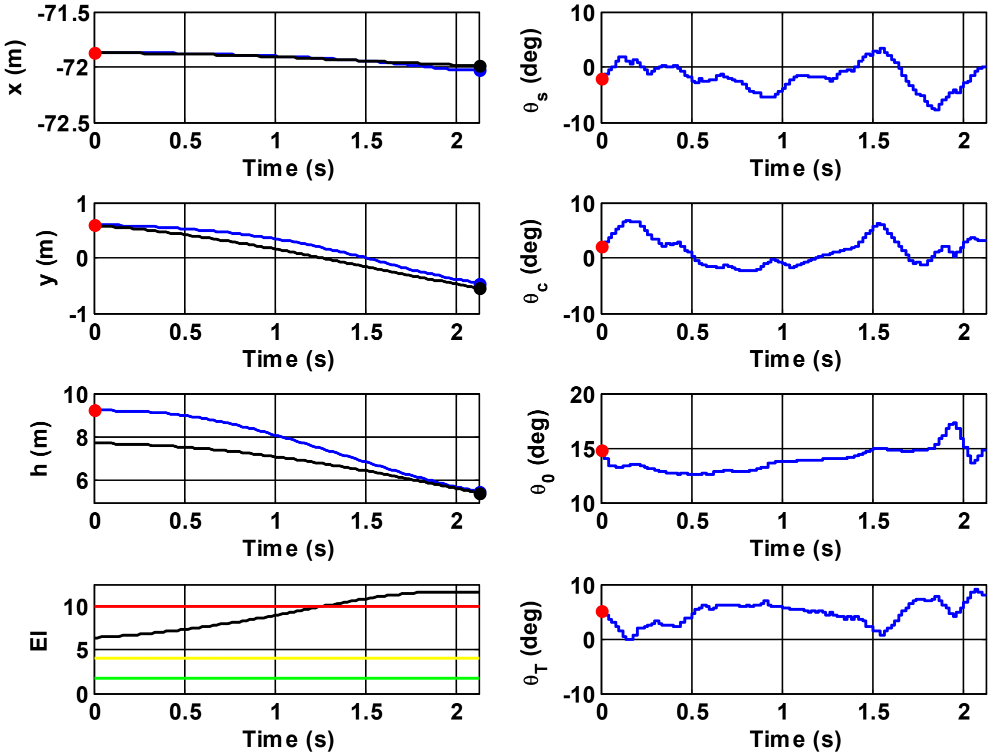

Fig. C.10 Position and control input histories (blue lines) of the helicopter during the landing on the downstroke moving deck (black lines) starting from Time = 187 s in the third sample of the ship motion, airwake is included

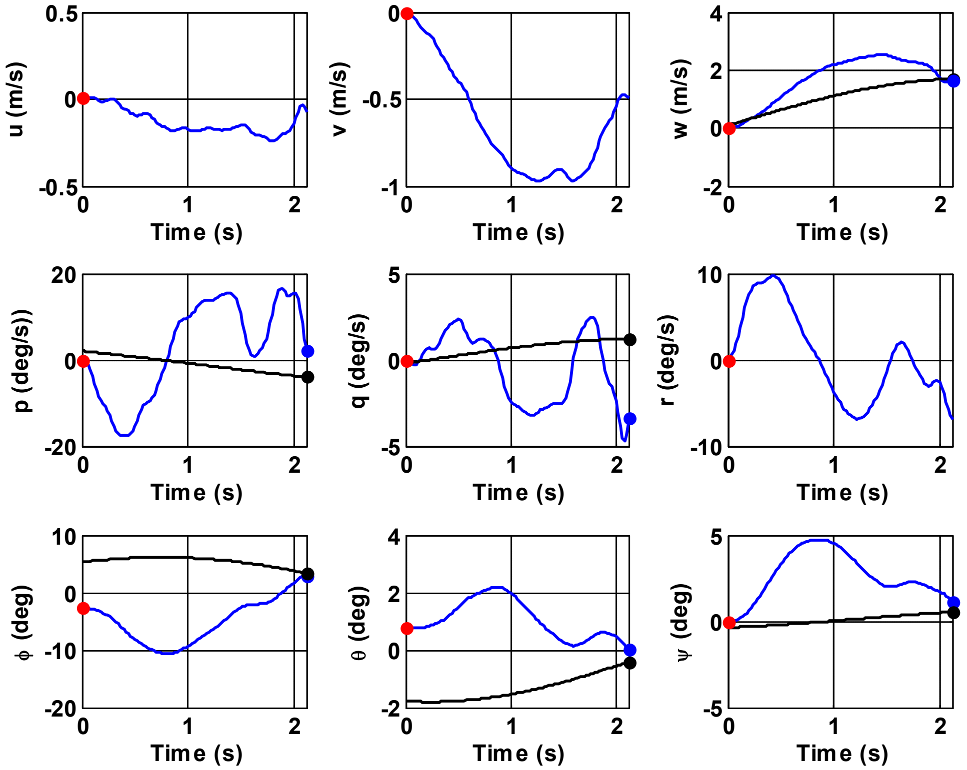

Fig. C.11 Fuselage state responses of the helicopter during the landing starting from Time = 187 s

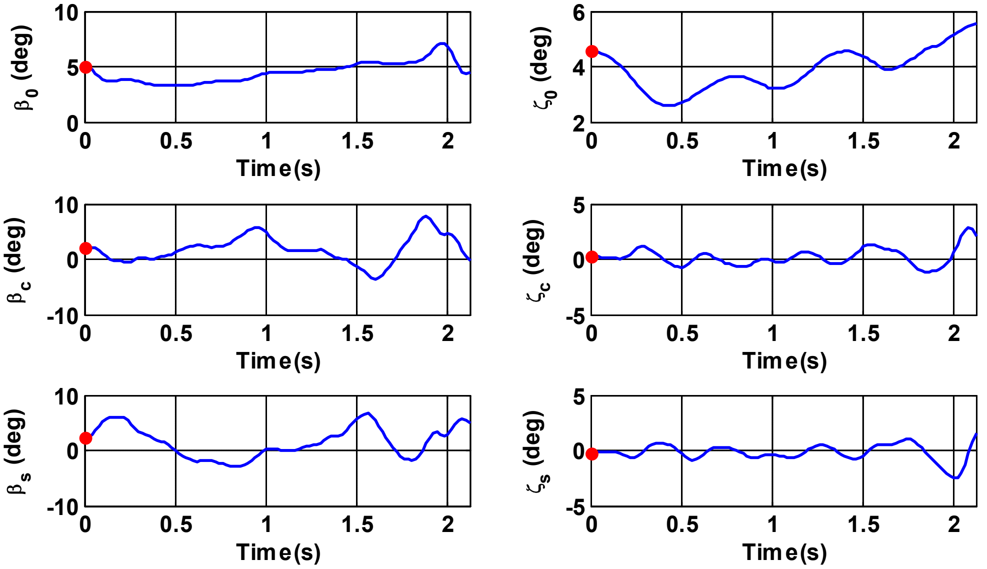

Fig. C.12 Flapping, lead-lagging states of the main rotor during the landing starting from Time = 187 s

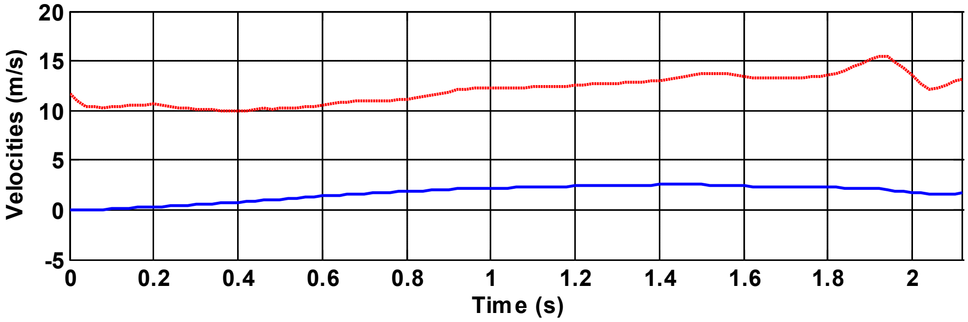

Fig. C.13 Induced inflow (dashed line) and rate of descend (solid line) during the landing starting from Time = 187 s

References

[1] Bemporad, A., and Morari, M., “Robust Model Predictive Control: A Survey,” Robustness in Identification and Control, Lecture Notes in Control and Information, Vol. 245, Springer, London, 1999, pp. 207-226.

[2] Roscoe, M. F., and Wilkinson, C. H., “DIMSS-JSHIP’s Modeling and Simulation Process for Ship/Helicopter Testing and Training,” *AIAA Modeling and Simulation Technologies Conference and Exhibit*, Monterey, California, 5-8 Aug. 2002.

[3] Kääriä, C. H., Wang, Y., Padfield, G. D., Forrest, J. S., and Owen, I., "Aerodynamic Loading Characteristics of a Model-Scale Helicopter in a Ship’s Airwake," *Journal of Aircraft*, Vol. 49, No. 5, September–October 2012.

[4] Kääriä, C. H., "Investigating the Impact Superstructure Aerodynamics on Maritime Helicopter Operations," Ph.D. dissertation, School of Engineering, The University of Liverpool, August 2014.

[5] Lee, D., Sezer-Uzol, N., Horn, J. F., and Long, L. N., "Simulation of Helicopter Shipboard Launch and Recovery with Time-Accurate Airwakes," *Journal of Aircraft*, Vol. 42, No. 2, March–April 2005.

[6] Lee, D., "Simulation and Control of a Helicopter Operating in a Ship Airwake," Ph.D. Dissertation, Department of Aerospace Engineering, The Pennsylvania State University, 2005.

[7] Horn, J. F., Bridges, D. O., and Lee, D., "Flight Control Design for Alleviation of Pilot Workload during Helicopter Shipboard Operations," presented at the American Helicopter Society 62nd, Annual Forum, Phoenix, AZ, May 9-11, 2006.

[8] Lusardi, J. A., Tischler, M. B., Blanken , C. L., and Labows, S. J., "Empirically Derived Helicopter Response Model and Control System Requirements for Flight in Turbulence," *Journal of the American Helicopter Society*, Vol. 49, No. 3, 2004.

[9] Lusardi, J. A., "Control Equivalent Turbulence Inputs Model for the UH-60,” Ph.D. Dissertation, Department of Mechanical and Aeronautical Engineering, Univ. of California, Davis, Davis, CA, 2004.

[10] Hess, R. A., "Simplified Technique for Modeling Piloted Rotorcraft Operations Near Ships," *Journal of Guidance, Control, and Dynamics*, Vol. 29, No. 6, November–December 2006.

[11] Hess, R. A., "A Simplified and Approximate Technique for Scaling Rotorcraft Control Inputs for Turbulence Modeling," *Journal of the American Helicopter Society*, Vol. 49, No. 3, 2004.

[12] MIL-STD-1797A, "Flying Qualities of Piloted Aircraft," Department of Defense, 1990, pp. 678.

[13] McFarland et al., "System and Method for Finite Element Simulation of Helicopter Turbulence", United States Patent No. 5860807, Jan.19, 1999.

[14] Voskuijl, M., Padfield, G. D., Walker, D. J., Manimala, B. J., and Gubbels, A. W., "Simulation of Automatic Helicopter Deck Landings Using Nature Inspired Flight Control," *The Aeronautical Journal of the RAeS*, Vol. 114, No. 1151, 2010, pp. 25-34.

[15] Peters, D. A., and He, C. J., "Finite State Induced Flow Models Part II - Three-dimensional Rotor Disc," *Journal of Aircraft*, Vol. 32, No. 2, 1995, pp. 323-333.
doi: 10.2514/3.46719

[16] Oh, S. R., Pathak, K., Agrawal, S. K., Pota, H. R., and Garratt, M., "Approaches for a Tether-Guided Landing of an Autonomous Helicopter," *IEEE Transactions on Robotics*, Vol. 22, No. 3, Jun. 2006.

[17] Scherer, S., Chamberlain, L., and Singh, S., "First Results in Autonomous Landing and Obstacle Avoidance by a Full-Scale Helicopter," *IEEE International Conference on Robotics and Automation*, Saint Paul, MN, May 2012, pp. 951-956.
doi: 10.1109/ICRA.2012.6225215

[18] Scherer, S., Chamberlain, L., and Singh, S., "Autonomous Landing at Unprepared Sites by a Full-scale Helicopter," *Journal of Robotics and Autonomous Systems,* Vol. 60, No. 12, 2012, pp. 1545-1562.
doi: 10.1016/j.robot.2012.09.004

[19] Ferrier, B., Duncan, J., Ludwig, M. D. J., and Sandberg, W. C., "Air Vehicle Deck Limit Calculation as a Function of Ship Environment Characterization," *Proceeding of the American Society of Naval Engineering*, Washington, 2009.

[20] Lee, D., Sezer-Uzol, N., Horn, J. F., and Long, L. N., "Simulation of Helicopter Shipboard Launch and Recovery with Time-Accurate Airwakes," *Journal of Aircraft*, Vol. 42, No. 2, 2005.
doi: 10.2514/1.6786

[21] Kim, H. J., Shin, D. H., and Sastry, S. S., "Nonlinear Model Predictive Tracking Control for Rotorcraft-based Unmanned Aerial Vehicles," *Proceedings of the American Control Conference*, Vol. 5, 2002, pp. 3576-3581.
doi: 10.1109/ACC.2002.1024483

[22] Chung, H., and Sastry, S. S., "Autonomous Helicopter Formation using Model Predictive Control," *AIAA Guidance, Navigation, and Control Conference and Exhibit*, 21-24 August 2006, Keystone, Colorado, AIAA Paper 2006-6066, 2006.
doi: 10.2514/6.2006-6066

[23] Chung, H., "Autonomous Formation Flight of Helicopters: Model Predictive Control Approach," Ph.D. Dissertation, University of California, Berkeley, 2006.

[24] Avanzini G., Thomson D., and Torasso A., "Model Predictive Control Architecture for Rotorcraft Inverse Simulation," *Journal of Guidance, Control, and Dynamics*, Vol. 36, No. 1, 2013, pp. 207-217.
doi: 10.2514/1.56563

[25] Jung, Y. C., and Hess, R. A., “Precise Flight-Path Control using a Predictive Algorithm,” *Journal of Guidance, Control, and Dynamics,* Vol. 14, No. 5, Sep-Oct 1991, pp. 936-942.
doi: 10.2514/3.20734

[26] Oktay, T., "Constrained Control of Complex Helicopter Models," Ph.D. Dissertation, Department of Aerospace & Ocean Engineering, Virginia Polytechnic Institute and State University, May 2012.

[27] Oktay T., and Sultan C., "Constrained Predictive Control of Helicopter," *Aircraft Engineering and Aerospace Technology*: *An International Journal*, Vol. 85, No. 1, 2013, pp. 32-47.
doi: http://dx.doi.org/10.1108/00022661311294021

[28] Oktay, T., and Sultan C., "Simultaneous Helicopter and Control-System Design," *Journal of Aircraft*, Vol. 50, No. 3, 2013, pp. 911-925.
doi: 10.2514/1.C032043

[29] Oktay, T., and Sultan C., "Modeling and Control of a Helicopter Slung-Load System," *Aerospace Science and Technology*, Vol. 29, No. 1, 2013, pp. 206-222.
doi: 10.1016/j.ast.2013.03.005

[30] Oktay, T., and Sultan, C., "Flight Control Energy Saving via Helicopter Rotor Active Morphing," *Journal of Aircraft*, Vol. 51, No. 6, 2014, pp. 1784-1804. doi: 10.2514/1.C032494.

[31] Ngo, T. D., and Sultan, C., "Nonlinear Helicopter and Ship Models for Predictive Control of Ship Landing Operations," *AIAA Guidance, Navigation, and Control Conference*, 13-17 January 2014, National Harbor, Maryland, AIAA Paper 2014-1298, 2014.

[32] Ngo, T. D., and Sultan, C., "Modeling the Airwake in Helicopter Ship Landing Operations from a Control Perspective," *American Helicopter Society 70th Annual Forum Proceedings*, Montreal, Quebec, Canada, May 20-22, 2014.

[33] Ngo, T. D., and Sultan, C., "Simulation of Helicopter Shipboard Operations with Spatial Velocity Gradients in the Ship's Airwakes," presented at American Helicopter Society 71st Annual Forum, Virginia Beach, Virginia, May 5-7, 2015.

[34] Kuwata, Y., Teo, J., Fiore, G., Karaman, S., and Frazzoli, E., "Real-time motion planning with applications to autonomous urban driving," IEEE T. Control Systems Technology, vol. 17, no. 5, Sep. 2009.

[35] Frazzoli, E., Dahleh, M. A., and Feron, E., "Real-time motion planning for agile autonomous vehicles," AIAA J. Guidance, Control, and Dynamics, vol. 25, no. 1, Jan-Feb. 2002.

[36] Frazzoli, E., Dahleh, M., and Feron, E., "Trajectory tracking control design for autonomous helicopters using a backstepping algorithm," American Control Conference, vol. 6, IEEE, New York, 2000, pp. 4102–4107.

[37] Koo, T., and Sastry, S., "Output tracking control design of a helicopter model based on approximate linearization," Proceedings of the IEEE Conference on Decision and Control, vol. 4, IEEE, New York, 1998, pp. 3635–3640.

[38] Frazzoli, E., Dahleh, M. A., and Feron, E., "Maneuver-based motion planning for nonlinear systems with symmetries," IEEE T. Robotics, vol. 21, no. 6, Dec. 2005.

[39] Hehn, M., and D'Andrea, R., "Real-time trajectory generation for quadrocopters," IEEE Trans. Robotics, vol. 31, no. 4, pp. 877-892, Aug. 2015.

[40] Richards, A., and How, J. P., “Robust variable horizon model predictive control for vehicle maneuvering,” International J. Robust & Nonlinear Control, vol. 16, Feb. 20016, pp. 333-351.

[41] Richards, A., Schouwenaars, T., How, J. P.,and Feron, E., “Spacecraft trajectory planning with avoidance constraints using mixed-integer linear programming,” Journal of Guidance, Control, and Dynamics, vol. 25, no. 4, Jul.-Aug. 2002.

[42] Park, J., Karumanchi, S., and Iagnemma, K., “Homotopy-based divide-and-conquer strategy for optimal trajectory planning via mixed-integer programming,” IEEE Transactions on Robotics, vol. 31, no. 5, Oct. 2015.

[43] Schouwenaars, T., “Safe trajectory planning of autonomous vehicles,” Ph.D. dissertation, Aero. & Astro. Dept., MIT. Univ., Cambridge, MA, 2006.

[44] Schouwenaars, T., Mettler, B., Feron, E., and How, J., “Hybrid model for trajectory planning of agile autonomous vehicles,” AIAA J. Aerospace Computing, Information, and Communication, vol. 1, Dec. 2004.

[45] Kuwata, Y., “Trajectory planning for unmanned vehicles using robust receding horizon control,” Ph.D. dissertation, Aero. & Astro. Dept., MIT. Univ., Cambridge, MA, 2007.

[46] Bopardikar, S. D., Englot, B., and Speranzon, A., “Multiobjective path planning: localization constraints and collision probability,” IEEE Trans. Robotics, vol. 31, no. 3, Jun. 2015.

[47] LaValle, *Planning algorithms*, Cambridge, U.K.: Cambridge Univ. Press, 2006.

[48] Hass, K., “Assessment of Energy Production Potential from Ocean Currents along the United States Coastline”, Technical Report, Georgia Tech Research Corp., Atlanta, GA, 2013.

[49] Machado, M. C. P. M., VanZwieten, J.H., and Pinos, I. “A Measurement Based Analyses of the Hydrokinetic Energy in the Gulf Stream” Journal of Ocean and Wind Energy, vol 3(1): pp 25-30, 2016.

[50] VanZwieten, J. H., Duerr, A. E. S., G. M. Alsenas, and Hanson, H. P. “Global Ocean Current Energy Assessment: an Initial Look” in Proceedings of the 1st Marine Energy Technology Symposium (METS13) hosted by the 6th annual Global Marine Renewable Energy Conference, Washington D.C, April 10-11, 2013.

[51] Davis, B. V., Farrell, J. R. , Swan, D. H. , and Jeffers, K. A. , “Generation of Electric Power from the Florida Current”, in Proc. 18th Annual Offshore Technology Conference, Houston, TX, May 5-8, 1986, no. OTC-5120.

[52] SNMREC, “SNMREC Turbine Tow Test 1 Video Posted,” 2014. Available: http://snmrecwebext.eng.fau.edu/news/snmrec-turbine-tow-test-1-video-posted

[53] Swales, H., Coakley, D., Gupta, S., and Way, S., “Stability and Loads Validation of an Ocean Current Turbine,” in Proc. 2nd Marine Energy Technology Symp., Seattle, WA,April 15-18, 2014.

[54] Bolin, W. D., “Ocean Stream Power Generation: Unlocking a Source of Vast, Continuous, Renewable Energy,” in Proc. 2nd Marine Energy Technology Symp., Seattle, WA, April 15-18, 2014.

[55] VanZwieten, J. H., Vanrietvelde, N., and Hacker, B. L., “Numerical Simulation of an Experimental Ocean Current Turbine,” IEEE Journal of Oceanic Engineering, vol. 38, no. 1, Jan. 2013.

[56] VanZwieten, J. H., Driscol, F. R., Leonessa, A., and Deane, G., “Design of a Prototype Ocean Current Turbine—Part I: Mathematical Modeling and Dynamics Simulation,” Ocean Eng., vol. 33, pp. 1485–1521, Aug. 2006.

[57] VanZwieten, J. H., Driscoll, F. R., Leonessa, A., and Deane, G., “Design of a Prototype Ocean Current Turbine—Part II: Flight control system,” Ocean Eng., vol. 33, pp. 1522–1551, Aug. 2006.

[58] Ngo, T. D., and Sultan, C., "Model Predictive Control for Helicopter Shipboard Operations in the Ship's Airwakes," AIAA Journal of Guidance, Control, and Dynamics, 2015, in press. http://arc.aiaa.org/doi/abs/10.2514/1.G001243

[59] Ngo, T. D., and Sultan, C., "Mixed Integer Model Predictive Control for Helicopter Precision Landing on Moving Decks," in preparation for the IEEE Transactions on Robotics.

[60] Ngo, T. D., Sultan, C., VanZwieten, J. H., and Xiros, N. I., "Integration of Variance Constrained Cyclic Blade Control for Moored Ocean Current Turbine Flight Control," in preparation for the IEEE Transactions on Control System Technology.

[61] VanZwieten, J. H., Pyakurel, P., Ngo, T., Sultan, C., and Xiros, N. I., “An Assessment of Using Variable Blade Pitch for Moored Ocean Current Turbine Flight Control,” International Journal of Marine Energy, vol. 13, pp. 16-26, 2016.

[62] Ngo, T. D., Sultan, C., VanZwieten, J. H., and Xiros, N. I., "Variance Constrained Cyclic Blade Control of Moored Ocean Current Turbines," to be presented at the American Control Conference, Boston, MA, July 6-8, 2016.

[63] Padfield, G. D., *Helicopter Flight Dynamics*, AIAA Education Series, AIAA, Reston, VA, 2007, Chaps. 2, 3, 6, 7.

[64] Leishman, J. G., *Principles of Helicopter Aerodynamics*, Cambridge University Press, 2006, pp. 160.

[65] Klein V., and Morelli E. A., *Aircraft System Identification-Theory and Practice*, AIAA, Reston, VA, 2006, Chap. 9.

[66] Shannon, C. E., "Communication in the Presence of Noise," *Proceedings of the IEEE*, Vol. 86, No. 2, 1998, p. 447-457.

[67] Motora, S., "On the Measurement of Added Mass and Added Moment of Inertia of Ships in Steering Motion," First Symposium on Ship Maneuverability, David Taylor Model Basin, Report 1461, Oct. 1960.

[68] Fossen T. I., *Marine Control Systems: Guidance, Navigation and Control of Ships, Rigs and Underwater Vehicles*, Trondheim, Norway: Marine Cybernetics AS, 2002, Chap. 3.

[69] Lewandowski, E. M., *The Dynamics of Marine Craft Maneuvering and Sea Keeping*, Advanced Series on Ocean Engineering, World Scientific, Vol. 22, 2003, Chap. 5.

[70] St Denis, M., and Pierson, W. J., "On the Motions of Ships in Confused Seas," *Transactions of the Society of Naval Architects and Marine Engineers*, Vol. 61, 1953.

[71] Program PDSTRIP: Public Domain Strip Method, pdstrip.sourceforge.net, 2013-04-22

[72] O'Reilly, P. J., "Aircraft/Deck Interface Dynamics for Destroyer," *Marine Technology*, Vol. 24, No. 1, 1987, pp. 15-25.

[73] Ferrier, B., and Manning, T., "Simulation and Testing of the Landing Period Designator (LPD) Helicopter Recovery Aid," *Naval Engineers Journal*, Vol. 110, No. 1, 1998, pp. 189-205.

[74] Sherman, B. W., "The Examination and Evaluation of Dynamic Ship Quiescence Prediction and Detection Methods for Application in the Ship-Helicopter Dynamic Interface", Master Thesis, Virginia Polytechnic Institute and State University, 2007.

[75] Maciejowski, J. M., *Predictive Control with Constraints*, Prentice Hall, Pearson Education, 2001, Chap. 6.

[76] Prouty, R., *Helicopter Performance, Stability and Control*, PWS Publishers, 1986, pp.684.

[77] Anonymous, "Handling Qualities Requirements for Military Rotorcraft," U.S. Army Aviation and Missile Command ADS-33E-PRF, Aviation Engineering Directorate, Redstone Arsenal, Alabama, Mar. 2000.

[78] Bemporad, A., Morari, M., and Ricker, N. L., Model Predictive Control Toolbox User's Guide, MathWorks, Massachusetts, Sept. 2012, pp. 2.17–2.21.

[79] Tate, S. and Padfield, G.D., "Simulating Flying Qualities at the Helicopter/Ship Dynamic Interface," Proceedings of the 50th Annual Forum of the American Helicopter Society, Washington, D.C., May 1994.

[80] FAA, "Helicopter emergencies and hazards," Chapter 11. https://www.faa.gov/regulations_policies/handbooks_manuals/aviation/helicopter_flying_handbook/media/hfh_ch11.pdf

[81] Driscoll, F. R., Alsenas, G. M., Beaujean, P. P., Ravenna, S., Raveling, J., Busold, E., and Slezycki, C., "A 20 kw Open Ocean Current Test Turbine," in *Proc. MTS/IEEE Oceans Conference*, Quebec City, Canada, September 15-18, 2008, no. OCEANS.2008.5152104.

[82] Drela, M., and Youngren, H., "XFoil Subsonic Airfoil Development System," Available: http://web.mit.edu/drela/Public/web/xfoil/ Last modified 07-April-2008; accessed 22-Feb.-2011.

[83] Hansen, C., "AirfoilPrep" NWTC Design Codes, Available: http://wind.nrel.gov/designcodes/preprocessors/airfoilprep/ Last modified 09-March-2010; accessed 22-Feb.-2011.

[84] Hansen, M. O. L., Aerodynamics of Wind Turbines. London, UK: Earthscan, 2008, pp. 49, 52, 53, 55, 85-100.

[85] Bossanyi, E. A., “Individual Blade Pitch Control for Load Reduction,” Wind Energy, vol. 6, pp. 119-128, 2003.

[86] Skelton, R. E., and Lorenzo, M. D., “Space Structure Control Design by Variance Assignment,” Journal of Guidance, Control, and Dynamics, vol. 8, no. 4, pp. 454-462, 1985.

[87] Zhu, G., Grigoriadis, K. M., and Skelton, R. E., “Covariance Control Design for Hubble Space Telescope,” Journal of Guidance, Control, and Dynamics, vol. 18, no. 2, Mar.-Apr. 1995.

[88] Skelton, R. E., and Sultan, C., “Controllable Tensegrity, a New Class of Smart Structures,” SPIE Intl. Symposium on Smart Structures and Materials, San Diego, CA, 1997.

[89] Sultan, C., and Skelton, R. E., “Integrated Design of Controllable Tensegrity Structures,” in ASME Intl. Mechanical Engineering Congress and Exposition, Dallas, TX, 1997.

[90] Oktay, T., and Sultan, C., “Comfortable Helicopter Flight Via Passive/Active Morphing,” IEEE Transactions on Aerospace and Electronic Systems, to appear in October 2016.

[91] Zhu, G., M. Rotea, A., and Skelton, R., “A Convergent Algorithm for the Output Covariance Constraint Control Problem,” SIAM Journal of Control Optimization, vol. 35, no. 1, pp. 341-361, Jan. 1997.

[92] Hsieh, C., Skelton, R., and Damra, F. M., “Minimum Energy Controllers with Inequality Constraints on Output Variances,” Optimal Control Applications and Methods, vol. 10, pp. 347-366, 1981.